Development of Flow Reactors for Tuneable Gold Nanoparticle Synthesis: Towards Continuous Manufacturing

Spyridon P. Damilos

Department of Chemical Engineering
University College London

A thesis submitted for the degree of
Doctor of Philosophy of University College London

April 2020

I, Spyridon P. Damilos, confirm that the work presented in this thesis is my own.
Where information has been derived from other sources, I confirm that this has been indicated in the thesis.

_____
Signature

_____
Date

Abstract

Gold nanoparticles (Au NPs) are gaining increasing attention in various sectors, such as electronics, catalysis and biomedicine. However, nanomaterial synthesis is considered a bottom-up process, which means that the desired particle structure, size and yield depend on the thermodynamics and kinetics of the fabrication process. Therefore the current challenges in nanomaterial manufacturing are related to understanding, controlling and integrating different operating units for continuous operation, while maintaining narrow particle size distribution, uniform size and high yield. This thesis is aimed at investigating the use of microwave heating for the flow synthesis of gold nanoparticles and developing a manufacturing platform for the continuous synthesis of high quality Au NPs of desired sizes.

Initially, an alternative form of heating using microwaves was investigated to address the control of the longitudinal temperature profile and evaluate the heating efficiency in a milli-scale tube by varying the process parameters. The study was conducted both experimentally and computationally – by developing a finite element method (FEM) model – in a commercial single-mode microwave applicator. Varying the input microwave power, the medium (water) temperature inside the tube increased. However, the temperature profile plateaued and remained unaffected by the increase of the input microwave power beyond a certain value, as there was an excess of microwave power which could not be absorbed by the system. Microwave efficiency increased by increasing the inlet flow rate, due to the volumetric nature of microwave heating, without decreasing the temperature profile significantly. Changing the tube orientation both the microwave absorption and temperature profile decreased, while increasing the system pressure (from 1 bara to 2.3 bara), the temperature of the medium increased (by ~ 20 ^{o}C). The outcomes of this study provide in-depth understanding of the operating parameters on the temperature profile and energy efficiency of microwave-assisted flow synthesis systems.

Then, the potential of microwave heating for the synthesis of spherical Au NPs via the reduction of the gold precursor (tetrachloroauric acid) by trisodium citrate (namely *Turkevich* method) was investigated. For that reason, two synthesis platforms were developed, using microwave heating only (one-stage system) or using microwaves for reaction initiation and conventional heating in series as growth stage (two-stage system). In the latter system, increasing the microwave power from 0 (only conventional heating) to 25 W, the particle size varied between 20 – 25 nm. A

Welch's unpaired t-test was conducted indicating that the particle sizes obtained at different input microwave powers were statistically significant. Varying the residence time under microwave heating had no significant effect on final particle size, despite a small change on the temperature profile inside the microwave reactor. The large particle size distribution (> 18 %) of the synthesised Au NPs in flow under microwave heating was attributed to the non-isothermal longitudinal temperature profile, the particle deposition on reactor walls and the residence time distribution deviating from a plug flow reactor profile. The aforementioned results indicate the shortcomings of the microwave technology for nanoparticle synthesis in flow.

Existing mathematical models describing the kinetics of Au NPs synthesis via the *Turkevich* method were not applicable for designing continuous milli-fluidic flow reactors due to the complexity of the synthesis route. Therefore, two statistical correlations were developed for the estimation of the particle size and reaction time for the targeted synthesis of 10 – 20 nm Au NPs. The influence of order of reactant addition and synthesis pH on the particle size and reaction time was investigated. The developed models take into account the reactant speciation, concentrations and temperature, while the final pH of the colloidal solution was ~ 5.6, to ensure highly reproducible synthesis, yielding targeted spherical and monodisperse Au NPs. The developed statistical correlations could be used as a tool to engineer the flow process for a tuneable Au NPs synthesis.

Finally, based on the developed statistical correlations a continuous milli-scale manufacturing platform was constructed for citrate-capped Au NPs synthesis (*Turkevich* method) under conventional heating. Using a two-phase flow system (using heptane as continuous phase) prevented the fouling in the reactor walls. A membrane separator and a UV-Vis spectrometer were integrated into a single standalone flow platform. The in-house designed membrane separator allowed the downstream separation of the organic and the aqueous streams, while the inline UV-Vis spectrometer ensured the quality control in flow via online monitoring of the synthesised particles (size, yield and process stability). Recycling of the heptane was tested, showing that re-using the collected heptane without further purification, increased the polydispersity of the colloidal solutions (~ 23 %). This platform is considered as a viable option towards scalable continuous manufacturing of nanoparticles.

Impact statement

Over the past decades, gold nanoparticles (Au NPs) have gained increasing attention and interest as they can be used in a variety of applications, including catalysis, electronics, imaging and point-of-care diagnostics. The Au NPs properties depend on their size and shape, as well as, their capping ligand on the particle surfaces and can be further functionalised to meet the specific application requirements. Therefore, the development of robust and scalable continuous manufacturing synthetic processes is of paramount importance to provide high quality materials based on the application specifications.

The state-of-art Au NPs production concerns the synthesis in batch reactors using conventional heating systems. Although successful, these systems provide low to non-existent manufacturing control and discontinuous processes, while large production volumes are required in order the production to be economically attractive. This PhD project was focused on the adaptation of continuous flow processes for Au NPs synthesis in milli-scale reactors, which provide control over the operational parameters, enhanced heat and mass transfer and scalability. Additionally, implementation of the microwave technology was investigated as an alternative to conventional heating, due to the reported advantages regarding rapid and selective heating.

Highlights:

(1) The efficiency of microwave heating and heat transfer was investigated in continuous flow reactors. The temperature and the electric field profile over the tube length were studied using ultra-pure water of known dielectric properties. Microwave heating is gaining increasing popularity in chemical engineering and manufacturing platforms due to its advantages over the conventional heating, especially when selective heating is preferred. The outcomes of this study could instigate the application of microwave technology on chemical reactions and process intensification of flow systems, as well as optimisation of the existing applications.

(2) The use of microwave-assisted reactors for gold nanoparticle synthesis highlighted the mechanisms affecting the synthesis. The combination of the microwave and conventional heating in series allowed insight whether there were non-thermal effects on the heating of Au NPs under microwave radiation. In case of

microwave-assisted syntheses, the current study addressed several factors influencing the final results (particle size and shape) including the non-isothermal temperature profile, particle deposition on reactor walls (fouling) and the dominant convective forces over diffusion as particles were being formed over the reactor length.

(3) A statistical semi-empirical correlation was developed in batch for the estimation of the process parameters (reactant concentrations and temperature) for targeted 10 – 20 nm Au NPs synthesis, as well as the required reaction time. Prior to the model development, the effect of order of reactant addition and the solution pH were also examined to ensure the construction of a robust model. The targeted pH of the colloidal solution was then set at ~ 5.6, as it was previously reported to result in highly reproducible synthesis due to the reactant species present in the Au NPs synthesis. Hence, the developed semi-empirical correlation accounted also for reactant speciation, as well as the ratio and concentration of the reducing agent compounds (citric acid and trisodium citrate) to adjust the synthesis within the high reproducibility zone (pH = ~ 5.6). The results from this study provide a valuable tool for the process design for continuous synthesis of targeted and monodisperse gold nanoparticles.

(4) A continuous manufacturing platform was engineered for the translation of 10 – 20 nm citrate-capped Au NPs synthesis from batch to flow. A two-phase flow system was designed and commissioned to prevent fouling inside the reactor, while an in-house designed Teflon membrane separator allowed the in-flow separation of the organic and the aqueous streams and the collection of the colloidal solution. The reactant concentrations and the residence time were estimated via the developed semi-empirical correlation in batch. Inline UV-vis spectrometry was used for the online quality control of the synthesised particles (particle size and process yield) and manufacturing stability. Recycling of the used heptane was also investigated to improve the sustainability of the developed system. The highlights of this study address the challenges and the potentials of manufacturing platforms for the formation of Au NPs in flow.

Beyond the academic research, the particles obtained via the aforementioned studies are of great interest in healthcare and biomedical applications either as-synthesised or to be used as seeds for a seeded-growth process for the synthesis of larger Au NPs (> 20 nm) which can find application in biolabeling and bioimaging and surface-

enhanced Raman spectroscopy (SERS). It is worth noting that the final application of the synthesised Au NPs depends on both the size and shape, as well as the capping ligand on the particle surface for the appropriate functionalisation. These gold nanoparticles can be used in diagnostic devices – lateral flow and point-of-care (POC) testing (such as immunoassays for diagnostics of pathogens biomarker testing). Furthermore, the translation of the developed synthesis platform towards commercialisation has been supported by a successful EPSRC IAA Discovery-to-Use enterprise grant application along with an industrial partner organisation (*Pilot platform development for the continuous manufacturing of gold nanoparticles for diagnostic applications*).

Acknowledgements

First, I would like to express my deepest gratitude to my primary supervisor Professor Asterios Gavriilidis for his continuous enthusiasm, guidance and support all these years to complete this work. I feel really proud to be part of his group. Also, I would like to thank my secondary supervisor Professor Junwang Tang, who supported my work and helped me with the necessary information on the microwave-assisted synthesis and Dr Georgios Dimitrakis from University of Nottingham whose profound knowledge, especially in microwave technology, filled the missing pieces of my research apart from the chemical engineering perspective.

A special mention goes also to the academics and members of the MAFuMA research project. I would like to thank Professor Peter Dobson, Professor Nguyen Thi Kim Than, Professor Ivan Parkin, Professor Charalambos Makatsoris and Professor Quentin Pankhurst for their advice on my research all these years. It has been a great honour to collaborate with the elites from different fields. Also, I would like to acknowledge and thank all the researchers of the MAFuMa project and the members of Professor's Gavriilidis group. Dr Razwan Baber, Dr Hendrik du Toit, Dr He Huang, Dr Gaowei Wu who shared their knowledge and experience and helped me develop my research skills and complete this work successfully. Also, I would like to thank Luca Panariello and Dr Ioannis Alissandratos who spent countless hours discussing and optimising the developed systems and helped me with my research. Thanks to Dr Enhong Cao, Dr Katerina Loizou, Dr Maximilian Besenhard, Conor Waldron, Gleb Valitov and Georgios Gkogkos for their help in both research and life. Needless to say, I would like to thank Dr Anand N. P. Radhakrishnan, Baldassarre Venezia and Ilaria Gimondi for their continuous support in both research and academic life, always keeping me positive in working hours and enjoying the PhD life.

I would like to thank my brother Dimitris and my parents Anastasios and Georgia for their unconditional love and support through all my student life. Finally, I would like to express my greatest gratitude and appreciation to my fiancée Maria Athanaseli – without her love and support all these years none of it would have been possible.

Contents

List of figures

List of tables

Nomenclature

Latin symbols

A	Light absorbance ($a.u.$)
$\boldsymbol{B}$	Magnetic flux density vector (Wb/m^2)
Bo	Bond number (-)
c	Speed of light in vacuum (299,792,458 m/s)
Ca	Capillary number (-)
C	Concentration (M)
C_p	Specific heat capacity (J/kgK)
CV	Coefficient of variation
d	Diameter (m)
De	Dean number (-)
$\boldsymbol{D_e}$	Electric flux density vector (C/m^2)
DF	Degrees of freedom
D_m	Molecular diffusivity (m^2/s)
d_p	Penetration depth (m)
$\boldsymbol{E}$	Electric field vector (V/m)
f	Microwave frequency (Hz)
$\boldsymbol{H}$	Magnetic field vector (A/m)
h_{air}	Heat transfer coefficient for natural convection (W/m^2K)
$\boldsymbol{J}$	Electric current density vector (A/m^2)
k	Thermal conductivity (W/mK)
L	Length (m)
l	Optical path length (cm)
m	Mass of workload (kg)
MS	Mean square
N	Total sample number
p	System pressure (Pa)
P_d	Microwave power density (W/m^3)
Pe	Péclet number (-)
P_{in}	Input microwave power (W)
P_{total}	Absorbed microwave power in the medium (W)

Q	Heat flux (W/m)
R^2	Coefficient of determination (-)
R_{adj}^2	Adjusted coefficient (-)
Re	Reynolds number (-)
r	Cluster radius
r_c	Critical radius
SS	Sum of squares
T	Temperature (℃)
t	Time (s)
$tan\delta$	Loss tangent ($tan\delta = \varepsilon'/\varepsilon''$)
$\boldsymbol{u}$	Fluid velocity field vector (m/s)
u_0	Average fluid velocity (m/s)
$\dot{V}$	Inlet flow rate (m^3/s)
We	Weber number (-)
wf	Water fraction (-)
X	Experimental factor
Y_d	Yield of colloidal solution (%)
$\hat{Y}$	Response of the regression model (m)
ΔG	Gibbs free energy
ΔG_c	Activation energy
ΔG_v	Bulk free energy per unit volume

Greek symbols

β_0	Intercept of the regression model
γ	Surface energy per unit area
δ	Film thickness (m)
ε	Surface emissivity (-)
ε_{ext}	Extinction coefficient ($M^{-1}cm^{-1}$)
ε_m	Extent of mixing
ε_0	Electric permittivity of vacuum ($8.854 \cdot 10^{-12}\ F/m$)
ε_r	Relative complex permittivity ($\varepsilon_r = \varepsilon' - j\varepsilon''$) (-)
ε'	Dielectric constant (-)
ε''	Dielectric loss (-)

η	Dynamic viscosity ($Pa \cdot s$)
λ_0	Microwave wavelength in vacuum (m)
λ	Microwave wavelength in the waveguide (m)
μ_0	Magnetic permeability of vacuum ($4\pi \cdot 10^{-7}\ H/m$)
μ_r	Relative complex permeability ($\mu_r = \mu' - j\mu''$) (-)
μ'	Real part of complex permeability (-)
μ''	Imaginary part of complex permeability (-)
ρ	Density of the material (kg/m^3)
ρ_m	Electric charge density (C/m^3)
σ	Stefan–Boltzmann constant ($5.67 \cdot 10^{-8}\ W/m^2K^4$)
σ_d	Standard deviation of the particle size distribution (m)
σ_e	Electrical conductivity (S/m)
τ	Characteristic time (s)

Subscripts

air	Air and ambient environment
$Aqueous$	Aqueous phase
$blue$	Blue dye
$calc$	Calculated values
$conv$	Convection
D	Droplet
$diff$	Diffusion
est	Estimated values based on numerical models
exp	Experimentally measured values
$HAuCl_4$	Tetrachloroauric acid
$Heptane$	Heptane
i,j	Index numbers (levels of experimental factors)
$model$	Model values
$organic$	Organic phase
$residual$	Residual values
s	Support structure
SPR	Surface plasmon resonance
t	Tubing/capillary (m)
$total$	Total values

$water$	Water medium
400	400 nm wavelength in the UV-Vis spectra
450	450 nm wavelength in the UV-Vis spectra

CHAPTER 1. Introduction

This chapter describes the synthetic routes, the characteristics and applications of the gold nanoparticles, and presents the motivation and objectives of this thesis. The outline structure of the thesis is also discussed.

1.1. Motivation and objectives

Over the past years, there has been an increasing research interest for the use of gold nanoparticles (Au NPs) in various applications, including imaging, catalysis and healthcare due to their physicochemical properties and surface functionalization. These properties depend on the shape and size of the nanoparticle and several synthetic routes have been examined and proposed for the synthesis of monodisperse particles[1]. Specific shapes of Au NPs, such as nanospheres and nanorods have been proposed for various applications including surface-enhanced Raman scattering (SERS)[2, 3], *in vivo* molecular imaging[4] and selective photothermal therapy of cancer cells[4, 5], due to the enhanced resonant electromagnetic field on the surface of the particles. Spherical-shaped Au NPs are, also, used in different applications based on the particle diameter. Ultra-small gold nanoparticles (1 – 3 nm range) are being used in catalytic reactions[6, 7] or antimicrobial applications[8]. Larger spherical Au NPs are gaining increasing interest in drug delivery[9] and gene therapy[10], as well as in health care applications, including lateral flow testing[11, 12] and point-of-care diagnostics[13]. The gold nanoparticles are desirable for biomedical applications as gold is biocompatible and they exhibit unique physical and chemical properties suitable for drug and gene delivery[14].

The Au NPs application is also subject to particle functionalization as well as the ligands - capping agent - used during the particle synthesis. Citrate-capped Au NPs are widely used in biomedical applications, as the negative charge on the particle surface allows electrostatic interactions with the positive charged biomolecules[15]. Other hydrophilic ligands, such as polyethylene glycol (PEG) and polyvinylpyrrolidone (PVP) are being used in nanomedicine for targeted drug delivery (antibodies)[16, 17]. Thiol-capped hydrophobic ligands find application in cancer research[18, 19], diagnostics[20, 21] and antimicrobial surface activation[8, 22]. Bimetallic Au NPs (i.e. core-shell nanoparticles) are gaining increasing interest in hyperthermia for cancer therapy[23, 24], catalysis[25-27] electronics[28] and imaging[29, 30].

The characteristics and the stability of the synthesised nanoparticles depend on the (i) synthesis route, (ii) the manufacturing technique and (iii) the quality control of the process[31]. There is a plethora of different synthesis routes for the production of colloidal Au NPs particles of different sizes, such as *Brust-Schiffrin*[32], *Martin*[33] and *Turkevich method*[34], as well as the synthesis methodologies developed by Brown *et al.*[35] and Li *et al.*[36] The citrate-reduction method (*Turkevich*) is the most common

synthetic route for production of spherical colloidal Au NPs, as the citrate capping agent can easily react and bond with the desired ligands and molecules in further functionalisation steps[37]. During the citrate-reduction method, the reducing agent (citric acid and trisodium citrate) reacts with the gold precursor (tetrachlorauric acid), while the citrate acts as a reducing agent, capping agent and pH meditator[38]. Previous literature studies have examined the synthesis of gold nanoparticles in either batch or flow systems, revealing a number of parameters affecting final particle characteristics, such as reaction temperature[39] and pH[40], as well as which reactant species, concentrations and capping agent were used[38, 41].

Although batch synthesis is widely used for chemical synthesis, it has been previously reported that there are some limitations of batch processing, since the required mixing time to achieve homogenous mixtures is comparable to the reaction time, while during mixing particle nucleation and growth steps take place[42]. This results in variations on the pH in the batch reactors and broad particle size distributions, low batch-to-batch reproducibility and limited scalability[42]. Hence, there have been extensive studies on developing continuous manufacturing platforms offering reliable, reproducible and robust systems for the synthesis of monodisperse and high quality colloidal Au NPs[42]. Microreactors provide the required heat and mass transfer advantage, as the synthetic routes are described by fast reaction rates, while the diffusivity of the formed particles changes due to the particle growth[43-45]. However, scaling up the synthetic process can result in insufficient reactant mixing, yielding large particle size distribution. Multiphase flow systems in micro- and milli-scale reactors (i.e two-phase segmented flow using an organic substance as continuous phase and the aqueous colloidal solution as disperse phase) exhibit excellent mixing inside the droplet due to internal circulation and very narrow residence time distribution profiles resembling ideal plug flow conditions[42, 45, 46].

Many synthesis routes have been studied for the initiation of the synthetic reaction and production of Au NPs including heating laser[47] and UV radiation[48, 49], ultrasound waves[50], conventional heating using water or oil baths[38, 51] and microwave (MW) radiation[52, 53]. Microwave technology is considered an integral technology of process intensification because of the controllable dielectric heating, the reduction of the reaction time and the “greener” approach in manufacturing processes[54]. There have been several studies employing microwave heating (MWH) in batch systems for Au NPs synthesis (using either the *Turkevich method* or other synthetic routes)[15, 52, 55-58]. The studies showed promising results of narrow particle size distribution and targeted

particle size, due to the rapid heating and the higher achieved temperatures. However, there is very limited use of this technology for Au NPs in continuous flow systems (there is currently only one study by Bayazit *et al.*[53]). During the past decade several studies have described the benefits and limitations of MWH in flow systems[59-61]. Additionally, the literature studies have outlined the scalability of these systems from laboratory scale towards pilot plants acknowledging the "volumetric nature" of MWH and the advantage of radial uniform temperature profile in comparison to conventional heating systems[62, 63].

The thesis aimed to investigate the use of microwave heating – as an alternative to conventional heating – as a tool for the intensification of Au NPs manufacturing, as well as to investigate the synthesis mechanisms and derive the appropriate statistical correlations of the operating parameters for the development of continuous flow manufacturing set-ups. The developed platforms would be deployed for the delivery of tunable, high quality and monodisperse Au NPs, which can be used in biomedical applications. In this regard, the specific objectives of the thesis are:

- To study the heat transfer and microwave efficiency in continuous flow microwave heating systems.
- To design a gold nanoparticle synthesis system using milli-scale reactors, continuous flow processing and microwave technology.
- To investigate the parameters influencing the particle size distribution of gold nanoparticles under continuous microwave processing.
- To develop statistical correlations for gold nanoparticle size and reaction time estimations based on process parameters.
- To integrate a well-characterised capillary flow system with an efficient heat transfer under conventional heating and an inline quality control unit into a single standalone continuous synthesis platform.
- To examine the stability and robustness of the developed system for the development of a continuous manufacturing platform for Au NPs synthesis.

1.2. Thesis outline

In Chapter 1, the background, applications and motivation of researching process routes of gold nanoparticles are introduced. The thesis motivations and objectives are also described.

In Chapter 2, an introduction to the synthetic mechanism of gold nanoparticles is provided, as well as the advancements of the synthesis from batch to flow, followed by examples of continuous gold nanoparticle syntheses. Also, the background and advantages of microwave heating and examples of microwave technology introduced in nanoparticle synthesis and processing are outlined.

In Chapter 3, the efficiency of the microwave heating was investigated by varying four major process parameters – input microwave power, inlet flow rate, system orientation and pressure – using water as the medium in a microwave-assisted flow system. Temperature profile plateaued above a certain value, as the absorbed microwave power remained unaffected, while microwave efficiency was improved by increasing the flow rate. Microwave heating is descripted as volumetric in nature, since increasing the workload volume, the microwave absorbance and thereby the microwave efficiency increases. A finite element method (FEM) model was developed to track the temperature and the electric field profiles of the medium.

In Chapter 4, the gold nanoparticle production via microwave-assisted synthesis was explored. The use of a growth stage using conventional heating was required for the completion of the reaction. Inlet flow rate in the microwave reactor had negligible effect on particle size, while varying the input microwave power the particle size ranged between 20 – 25 nm. The challenge using microwave technology for Au NPs synthesis lies on the non-isothermal temperature profile, the particle deposition on the reactor walls, and the high convective to diffusive forces as the particle size increases, which shifts the residence time distribution (RTD) from plug flow towards the pure convection regime.

In Chapter 5, a semi-empirical correlation was developed for the estimation of the experimental conditions (reactant concentrations and temperature) for the targeted synthesis of citrate-capped gold nanoparticles. Based on previously published data, there is a highly reproducible zone of Au NPs synthesis at pH 5.6. Upon completing a preliminary study on the effect of pH and the effect of the order of reactant addition in the final particle size, two regression models were developed for the particle size and reaction time. The empirical correlations consist of a response surface model which estimate the concentration of the gold precursor, reactant molar ratio and temperature for the targeted Au NPs sizes and the required reaction time.

Additionally, the developed correlation calculate the concentrations of trisodium citrate and citric acid (reducing agents) to maintain the final pH at 5.6. The model was tested for the reproducible successful targeted synthesis of 10 – 20 nm Au NPs in batch.

In Chapter 6, using the semi-empirical correlations developed in Chapter 5, a flow setup was developed for the continuous synthesis of citrate-capped Au NPs. A two-phase flow was used by introducing heptane as the continuous phase and the aqueous colloidal solution was the dispersed phase. Heptane prevented the particle deposition on the reactor walls, ensuring continuous synthesis, while a hydrophobic membrane separator ensured the separation of the two phases in flow. The aim was the development of a system towards continuous manufacturing of 10 – 20 nm Au NPs. An inline UV-vis spectrometer allowed the online monitoring of particle size, process yield and manufacturing stability of the system. The potentials of recycling the heptane for the continuous Au NPs synthesis were also investigated.

In Chapter 7, the conclusions of the thesis are summarised and the future work is outlined.

CHAPTER 2. Literature review

This chapter presents the background and advantages of microwave technology as a tool for process intensification, as well as examples of microwave-assisted synthesis of nanocrystals in batch and continuous flow systems. The synthetic routes of gold nanoparticles are also presented, focusing on the citrate-reduction method. The synthesis in single-phase and multi-phase flow systems is also reviewed.

2.1. Gold nanoparticle formation

2.1.1. Particle size and colloidal stability

The term nanoparticle refers to the particles ranging between 1 and 100 nm. These nano-size materials differ from larger particle regarding their physical and chemical properties[64]. Their size is their most important characteristic and they exhibit unique optical, magnetic, electric, etc. properties, high surface areas, mechanical strength and specific magnetization, thus they are proposed for various technological applications[64-66].

Particle size and shape are dependent on the reaction stoichiometry, kinetic control or thermodynamic stability. The first attempt of understanding and predicting the mechanism of particle formation was the work of Becker and Döring (1935), stated hereafter as the classical nucleation theory (CNT)[67, 68]. Herein, nucleation is thermodynamically driven by the appearance of a new phase – stated as nucleus – and the overall system shifts towards thermodynamic equilibrium. The CNT describes the spontaneous homogenous nucleation occurring when the system is in supersaturation with simultaneous minimisation of the Gibbs free energy[68, 69]. The Gibbs free energy of the formation of spherical nucleus is given by the following equation (Equation 2-1)[70], while a graphical representation is displayed in Figure 2-1:

$$\Delta G = -\frac{4}{3}\pi r^3 |\Delta G_v| + 4\pi r^2 \gamma \qquad \text{Eq. 2-1}$$

Where r is the cluster radius, ΔG_v is the bulk free energy per unit volume and γ is the solid-liquid interfacial energy.

The first term in Gibbs free energy represents the reduction of the bulk free energy due to bonding of monomers (volume term), while the second term represents the increase in the surface energy with the cluster size (surface term)[68, 70, 71]. Given Equation 2-1 and Figure 2-1, there is a critical cluster size r_c (Equation 2-2) which corresponds to the maximum of the ΔG ($d\Delta G/dr = 0$) resulting in ΔG_c called the activation energy (Equation 2-3). For cluster sizes below the critical radius, because of the interplay of the surface energy and bulk free energy, the cluster radius is unstable, while for clusters of radius above that critical value there is a decrease in the Gibbs free energy and nucleation and growth process are favorable[68].

$$r_c = \frac{2\gamma}{|\Delta G_v|} \quad \text{Eq. 2-2}$$

$$\Delta G_c = \frac{4\pi {r_c}^2 \gamma}{3} \quad \text{Eq. 2-3}$$

Where r_c is the critical cluster radius, ΔG_v is the bulk free energy per unit volume, ΔG_c is the activation energy and γ is the solid-liquid interfacial energy.

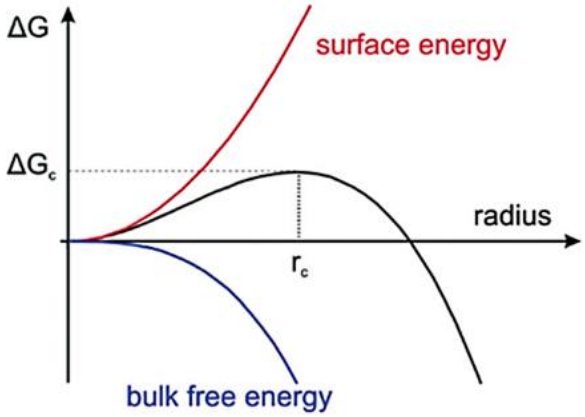

Figure 2-1 Schematic of the Gibbs free energy of the formed nucleus, the surface energy and the bulk free energy as a function of the cluster radius. The critical radius $\boldsymbol{r_c}$ and the respective activation energy $\Delta \boldsymbol{G_c}$ are also displayed. Adapted with permission from Ref.[69] under Creative Commons Attribution 3.0 Unported Licence. Copyright 2015 Royal Society of Chemistry.

The above concept of the CNT describes the homogeneous nucleation process of the target nanoparticles, while further growth of the formed particle should be studied by additional processes. In nanoparticle synthesis, heterogeneous nucleation – nucleation on sites or surfaces which cause reduction to the surface energy and subsequently to the activation energy – is also possible and it should be taken into account in the seed formation or in seeded-growth processes[69].

The concept of *burst nucleation* or *LaMer theory* (shown in Figure 2-2) was investigated by LaMer and co-workers describing the simultaneous homogenous nucleation followed by a subsequent growth without further nucleation[69, 72, 73]. According to LaMer theory, the nucleation and growth process is separated in three phases:

- In phase I, upon reduction of the precursor and the formation of monomers, their concentration is increasing in time passing the critical supersaturation level C_s, where homogeneous nucleation can be realised.
- As the monomer concentration is increasing, it reaches a level (C_{min}) at which the activation energy for homogeneous nucleation can be overcome, leading to a burst nucleation (phase II). Due to the rapid self-nucleation, the monomer concentration starts to decrease after reaching a maximum supersaturation point.
- In phase III, the monomer concentration drops to the critical supersaturation level, where particle growth and/or heterogeneous nucleation take place by diffusion of the monomers on the particle surface.

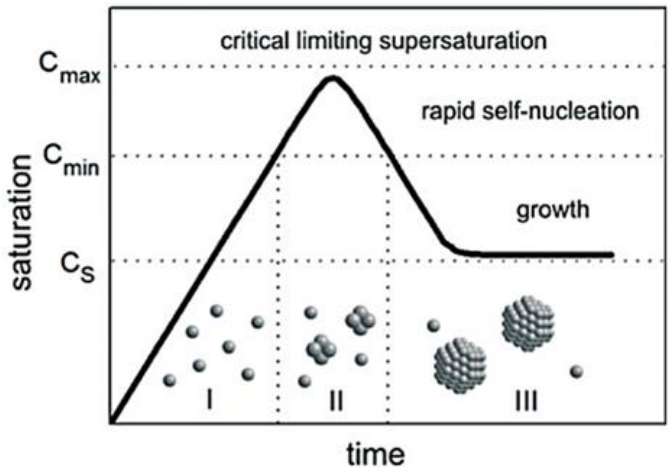

Figure 2-2 Schematic the LaMer model phases over time and the key-points of the monomer saturation levels. Adapted with permission from Ref.[69] under Creative Commons Attribution 3.0 Unported Licence. Copyright 2015 Royal Society of Chemistry.

The LaMer model describes the particle nucleation and growth as a function of the reduction rate and the monomer supersaturation level. As a consequence, the faster the reduction rate and the higher the nucleation phase, the smaller the final particle sizes[69]. Although, LaMer model describes the nucleation and the growth stage process of the nanoparticle synthesis, it fails to predict the final particle size and distribution. Additionally, another phenomenon which can been reported to occur during the particle growth is the Ostwald ripening, where smaller particles are likely to re-dissolve and provide their atoms as monomers for the growth of the larger and more stable particles[74, 75]. Polte[69] has reviewed several kinetic models for the prediction of the final particle size, however, the main drawback is the lack of

experimental data on the effect of reactant concentration and synthesis conditions (such as temperature and pH) on the particle size[69].

In colloidal systems such as the nanoparticle solutions, particle aggregation and subsequently the stability of the formed colloids are subject to the inter-particle attractive and repulsive forces[69, 76]. The attractive forces are the van der Waal forces between the synthesized nanoparticles. Between two particles, the magnitude of the van der Waals forces is inversely proportional to the second power of the inter-particle distance[76]. The repulsive forces are determined by the electromagnetic interactions of the surrounding ions on the particle surface – the so-called electric double layer (EDL)[69, 76]. EDL consists of two layers, the compact immobile inner layer of ions which are adsorbed on the particle surface (Stern layer) and a second diffuse layer. The surface potential decreases from the particle surface along the distance of the EDL and the thickness of the EDL depends on the ion concentration in the solution; the higher the ion concentration in the solution the lower the EDL. Figure 2-3a shows a schematic of the interaction potential of the repulsive, attractive and total forces between two identical nanoparticles, while Figure 2-3b displays the EDL of a nanoparticle and the electric potential along the distance from the particle surface. In cases of higher ion concentration or smaller particle sizes, the length of EDL decreases and van der Waals attractive forces prevailing with a simultaneous decrease of the aggregation barrier; in other words, larger particles are colloidally more stable. The particle stabilization as the summary of the van der Waals and EDL forces is called electrostatic stabilization.

In addition, steric stabilization is subject to the adsorption of polymeric or surfactant molecules on the particle surfaces[69, 76]. These molecules act as repulsive forces since the higher the molecular density in the inter-particle distance, they lower the entropy of the system making the agglomeration thermodynamically unfavorable. The steric stabilization is subject to the polymeric chain and the temperature. The combination of the aforementioned electrostatic and the steric stabilization is described by the DLVO theory (named by Derjaguin – Landau[77] and Verwey – Overbeek[78]) which provides a quantitative analysis of the aggregation barrier and the rate of agglomeration of the colloidal solution[67].

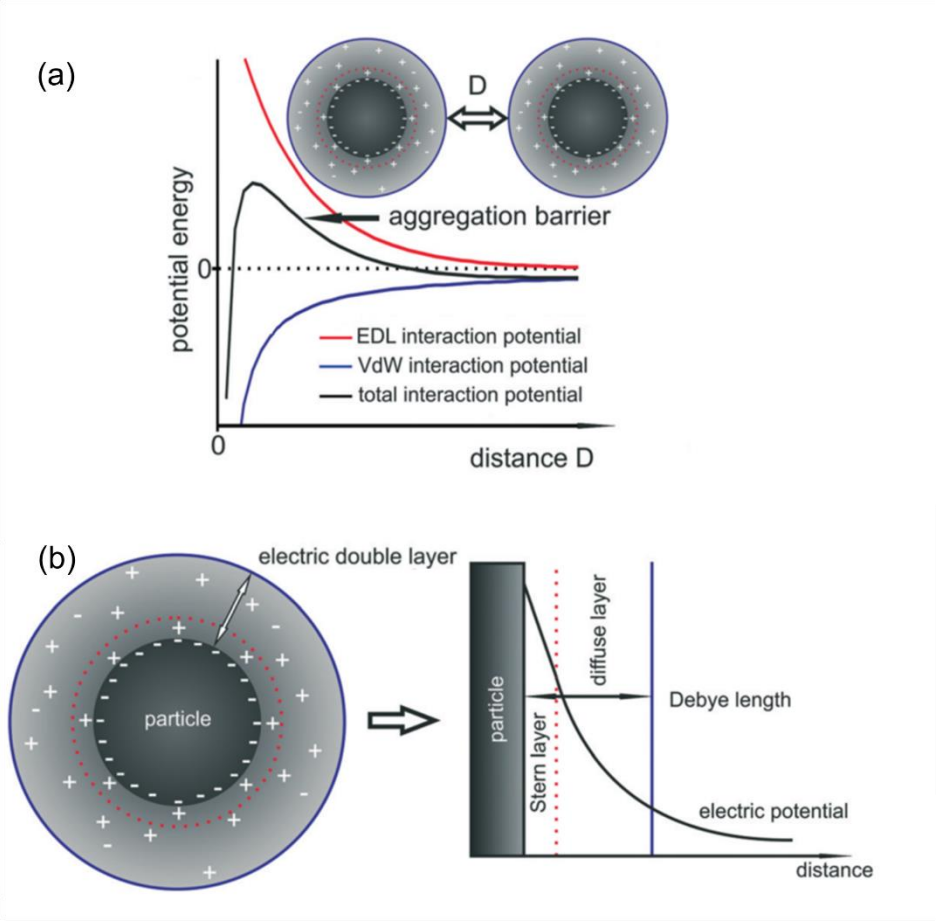

Figure 2-3 a) Graphical representation of the van den Waals (VdW), electric double layer (EDL) and total interaction potential between two identical nanoparticles with regards to the distance between them. b) *Left* The electric double layer around a nanoparticle. Red dotted line depicts the Stern layer and solid blue line depicts the boundaries of the diffuse layer. *Right* The electric potential over the distance from the particle surface. Adapted with permission from Ref.[69] under Creative Commons Attribution 3.0 Unported Licence. Copyright 2015 Royal Society of Chemistry.

Physical and chemical properties of metal nanoparticles depend strongly on their size and shape. Synthesis and manufacturing of uniform compositional nanocrystals of narrow particle size distribution and shape depends on controlling the nucleation and growth steps of the particle formation process[31]. When external electromagnetic field is applied on non-charged metal particles, i.e. UV light, it causes the free electrons on the metal surface to oscillate. In case of dispersed metal nanoparticles, when the external applied light is of wavelength larger than the particle size, then the free electrons oscillate collectively on the particle surface and its localized plasmon is named localized surface plasmon resonance (SPR) (Figure 2-4a)[64]. The wavelength, position and intensity of SPR depend on the size, shape and structure of

nanoparticles, as well as the dielectric constant and quality of the substrate (Figure 2-4b). In case of spherical Au NPs, SPR band varies between ~ 520 – 550 nm and if the solution is irradiated with a visible light of the same wavelength the solution will display a red-purple colour, while the green part of the spectrum will be absorbed[64, 79].

As discussed in this Section, the stages of nanoparticle formation are nucleation, seed formation and growth[79]. Preparation of monodispersed nanoparticles can be achieved by a rapid nucleation step followed by slow growth step. The smaller the particle size the higher the surface energy, thus the use of dispersing agents should be used to stabilize the size of the desired particle. For a given system, size is controlled through heating, hence rapid heating of the substrate, results in rapid precursor reduction to monomers, quick cluster or seed formation and finally to the formation of the nanocrystals. The higher the number of seeds due to rapid heating and *burst nucleation* the less the monomers and so the smaller the size of the final nanoparticles[75, 80]. Metal nanoparticles tend to be synthesised in a variety of different shapes, such as spheres, cubes, rods or wires, tetrahedron, thin plates with a triangular, hexagonal, or circular profiles, pyramids, etc. The shape of these particles plays an important role in its properties as well as the SPR band. Different shapes and sizes shift the band accordingly[64, 79, 81].

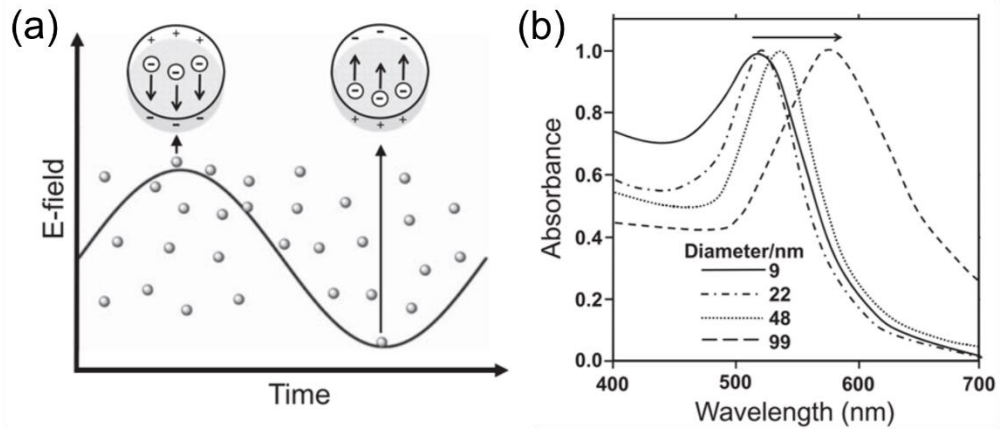

Figure 2-4 a) Mechanism of the surface plasmon resonance (SPR) on the nanoparticle surface in case of an incident electric field. b) Red-shifting of the SPR of Au NPs by increasing the nanoparticle size. Reprinted with permission from John Wiley and Sons and Copyright Clearance Center. Ref.[64] Copyright 2013.

2.1.2. The mechanism of citrate reduction method (*Turkevich* method)

Turkevich method is described as the simplest method for Au NPs fabrication[34]. According to the methodology, tetrachloroauric acid ($HAuCl_4$) is reduced with trisodium citrate ($Na_3C_6H_5O_7$ or Na_3Ct). The advantage of this method is the production of citrate-capped and stable gold nanoparticles. Turkevich method is a multi-step reaction process, with reactions occurring in series and in parallel. Kumar *et al*.[65] compared the effect of citrate/gold ratio to final particle diameter of 5 different independent research groups, showing that increasing the ratio up to 7/1 the final size decreases. However, Chow and Zukoski[82] kept citrate concentration constant and decreased the precursor concentration, showing that by increasing the ratio, final size initially decreased, up to 7/1 ratio. It is worth mentioning that the less reactive the gold complexes, the larger the final size of the particles, as reaction rates (nucleation and growth) decrease. Increase of citrate, increases the pH of the solution, deactivating the gold precursor, although the higher the citrate the smaller particles. When dissolved, by increasing pH, chloride ions Cl^- of the $AuCl_x^-$ complex are substituted by hydroxyl groups OH^-, resulting to less reactive formations $AuCl_x(OH)_{(4-x)}^-$. The speciation of the tetrachloroauric acid and citrate are as follows[38, 52]:

$$AuCl_4^- \rightleftarrows AuCl_3(OH)^- \rightleftarrows AuCl_2(OH)_2^- \rightleftarrows AuCl(OH)_3^- \rightleftarrows Au(OH)_4^-$$

$$H_3Ct \rightleftarrows H_2Ct^- \rightleftarrows HCt^{2-} \rightleftarrows Ct^{3-}$$

Kumar *et al.*[65] summarized the overall mechanism of gold nanoparticles following *Turkevich* method, while the steps are also shown in Figure 2-5. Initially, citrate is oxidised to dicarboxy acetone (DCA), and the precursor is reduced from Au^{3+} to Au^{1+}, to form a multimolecular complex with DCA, which has been formed by oxidization of citrate. Then, the auric salt is reduced to aurous salt and the aurous species are dispropotionated to gold atoms (Au^0). For the disproportionation step, three aurous chloride molecules are required to combine[65]. Disproportionation step is followed by the particle formation and can occur on the formed particle surfaces, as well. However, at high temperatures DCA transforms to acetone and no longer plays a role in the overall reaction mechanism. The gold atoms produced by disproportionation are absorbed by the particle, resulting in the growth of gold

nanoparticles. Following that model, proposed citrate-to-gold ratio for complete conversion from precursor to gold nanoparticle is above 1.5. However, Frens[83] stated the stoichiometric citrate-to-gold ratio at 0.43, without proposing the respective mechanism.

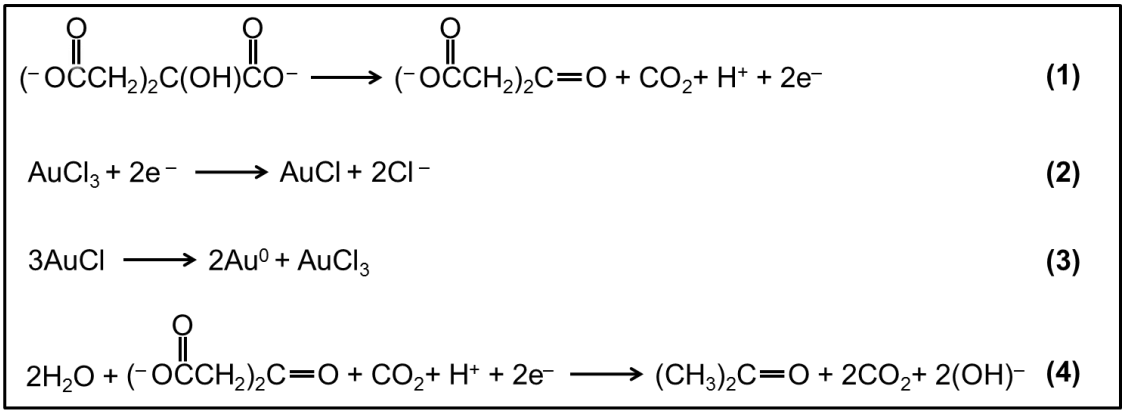

Figure 2-5 Reaction mechanism of *Turkevich* method. (1) oxidation of citrate to dicarboxy acetone, (2) reduction of auric salt to aurous salt, (3) aurous species to gold atoms and (4) dicarboxy acetone to acetone[65].

Further experimental studied conducted by Polte's group via XANES and SAXS data[38, 40, 69, 84, 85] analysed the citrate reduction mechanism for the formation of gold nanoparticles and their analysis is summarised as shown in Figure 2-6. The steps of *Turkevich* method are (i) the reduction of a part of precursor and formation of nuclei and clusters (AuX_4^-), (ii) the formation of seeds based on the nuclei within the first seconds of the synthesis process, (iii) slow and (iv) fast growth of the seed particles up to the desired size, as the remaining precursor in the solution is being attached on the electric double layer of the particles, thus the reaction continuous (precursor reduction) on the EDL of the seeds, leading to the particle growth. During the steps (iii) and (iv) no further particles are formed and the particle number remains constant, while size is determined during steps (i) and (ii).

According to the *Turkevich* method, Na_3Ct acts as reducing and capping agent and pH mediator[40]. $[HAuCl_4]/[Na_3Ct]$ ratio and pH levels affect the Au nanoparticle synthesis. Kettemann *et al.*[40] described the high stability and reproducibility of citrate species HCt^{2-} within 5.5 – 6.0 pH range, characterizing it as "typical Turkevich synthesis range". Also, increasing citrate concentration results in smaller gold nanoparticles as citrate acts as a reducing and stabilizing agent of the formed particles[65, 86]. It should be noted that above a certain citrate concentration, Na_3Ct

could lead to larger Au NPs, due to the high ionic strength from citrate reduced species causing particle aggregation.[38] Regarding the precursor, the higher its concentration, the smaller the particle sizes as it leads to increased number of monomers (Au^0), that is increased number of seeds, which means Au NPs of smaller sizes[38].

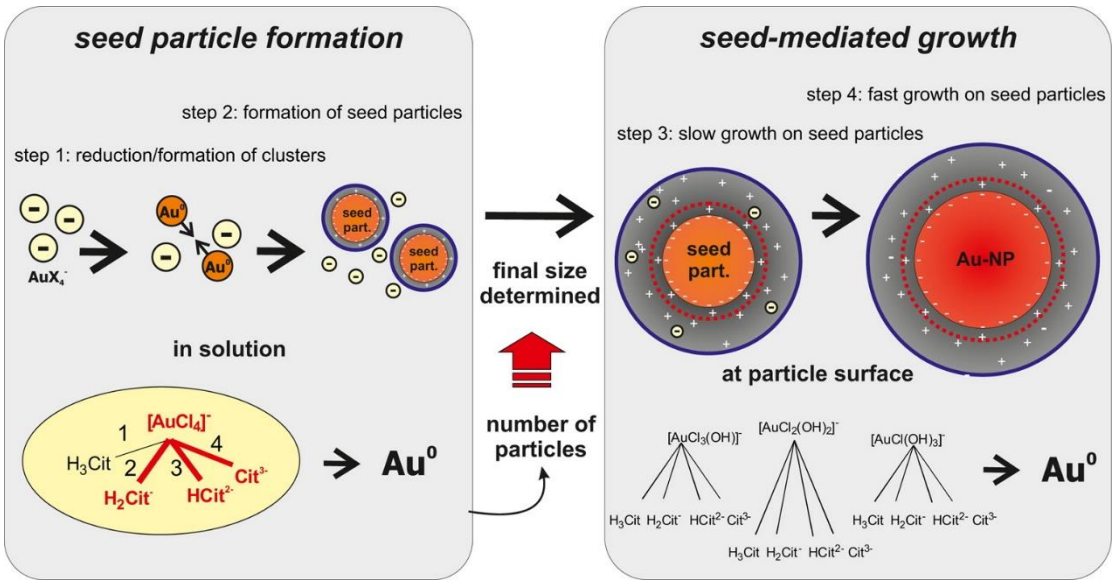

Figure 2-6 General growth mechanism of gold nanoparticles, according to the *Turkevich* method. Reprinted with permission from Ref.[40] Copyright 2016 American Chemical Society.

2.2. Characterisation techniques

A series of characterisation analysis techniques have been introduced and implemented in the literature for gold nanoparticle synthesis. The most common techniques are the UV-Vis spectroscopy due to the information acquired based on the SPR peak (height, width, wavelength) and the transmission electron microscopy for the evaluation of both size and shape of the nanoparticles. Additionally, differential centrifugal sedimentation offers a rapid estimation of the particle size distribution. However, due to the limitations of each characterisation method, multiple or combination of several techniques is required for the global and accurate evaluation of the sample and the final particles. A brief introduction to the most common characterisation techniques which were used in this project is given in the following paragraphs.

2.2.1. Ultraviolet-Visible (UV-Vis) spectroscopy

Ultraviolet-Visible (UV-Vis) spectroscopy is the most common and widely used technique for the analysis of gold nanoparticles, due to its simplicity and rapid analysis, without coming in contact or damaging the sample. In principle a UV-Vis lamp emits light in the UV spectrum (100 – 400 nm) and the visible spectrum (400 nm – 700 nm) up to ~ 800 nm (margins of near-infrared electromagnetic spectrum). The set-up consists of the UV-Vis light source, the sample holder and the spectrometer for data recording. The sample is placed in a designated cuvette and the absorbed photons causing electronic excitation on the molecular electrons. For a given wavelength, the light absorption is proportional to the sample's extinction coefficient, concentration and optical path, as described by Beer-Lambert's law[41]:

$$A = \varepsilon_{ext} l C \qquad \text{Eq. 2-4}$$

Where ε_{ext} is the extinction coefficient (or the molar attenuation coefficient), l is the optical path length and C is the sample concentration.

UV-Vis spectroscopy offers a plethora of information regarding the reactant (prior to the synthesis), the synthesis reaction and the final colloidal gold sample. Regarding the citrate-reduction mechanism, the absorbance at 200 nm wavelength offers information on the monitoring of the protonation of the citrate species[38]. Concerning the gold precursor ($HAuCl_4$), the peak at 222 – 226 nm and 313 nm is related to the ${AuCl_4}^{-}$[38, 87], while the drop of the absorbance at the 313 nm can be used to monitor the kinetics of the hydroxylation equilibrium ($AuCl_{4-x}(OH)_x^-$)[38]. Particle size can be estimated by conjugating the obtained information from the UV-Vis spectra (SPR peak varies between 515 nm – 590 nm for sizes 5 nm – 120 nm) with the light scattering mathematical models (Mie theory)[88, 89] or statistical regression models[90, 91]. Finally, Hendel *et al.*[84] described a linear dependence between the particle concentration and the absorbance of the UV-Vis spectra at 400 nm fitted with the Beer-Lambert Law, as the extinction coefficient of the particles varies with the Au NPs size.

2.2.2. Differential centrifugal sedimentation (DCS)

Differential centrifugal sedimentation (DCS) measures the size of the particles in a colloidal solution by applying centrifugal force in a rotating disc. The sample of the

colloidal solution (~ 0.1 ml) is injected in the centre of the rotating disc and the particles are forced to travel through a density gradient medium towards the edge of the disc and they are being detected by a photodetector positioned near the disc edge[92]. According to Stoke's law, the velocity (and time) of sedimentation of a spherical particle is proportional to the diameter and density of the particle, as well as the density and viscosity of the medium[93].

In differential sedimentation, the photodetector records the intensity from the monochromatic beam (i.e. 405 nm) at the edge of the disc. As the particles of the colloidal solution sediment, from the centre of the disc to the edge, passing in front of the photodetector, the recorded light intensity decreases, therefore – based on the particle and fluid density and the sedimentation time – it calculates the particle diameter via Mie theory mathematical modelling. However, in order to avoid the simultaneous sedimentation of different diameter particles (namely as *streaming*), which can hinder the analysis of the particle size distribution, the medium comprises of a density gradient where the density increases from top to bottom[94].

For Au NPs analysis, the particle density can be assumed constant and equal to 12.3 g/ml for 8 – 30 nm citrate-capped gold nanoparticles[49]. For high density particles (such as aqueous Au NPs) the density gradient comprises of a mixture of two sucrose solutions (8 % - low density and 24 % - high density). Also, a film of dodecane (~ 0.5 ml in volume) prevents the evaporation of water from the density gradient, increasing the stability of the mixture. The 180 nm silica particles (179 ± 16 nm, non-functionalized NanoXact^{TM} Silica, nanoComposix) is used as a calibrant for the Au NPs analysis. In comparison with UV-Vis spectrometry, DCS provides detailed information on the particle size distribution (i.e. sample polydispersity), while it provides higher accuracy on the average particle size than TEM due to the difference in the order of magnitude of the analysed particles (particles counted by DCS is ~ 10^{11} compared to ~ 10^{2} by TEM). However, the accuracy of the sample analysis depends on the stability of the density gradient (which can last up to 6 hours of continuous operation) and particle size, since the lowest Au NPs that can be measured by DCS is 3 nm; below 3 nm Au NPs particle sedimentation is difficult due to Brownian motion.

2.2.3. Transmission electron microscopy (TEM)

Transmission electron microscopy (TEM) allows the evaluation of both nanoparticle size and shape and estimation of sample polydispersity. TEM set-up consists of the electron gun, the electromagnetic lenses, the sample holder with the specimen grid, the phosphorescent screen and the charge-coupled camera devise[95]. The electron beam generated by the gun travels in a vacuum chamber through a series of electromagnetic lenses which focus the electrons on the sample grid (Au NPs sample is placed on a thin carbon coated copper grid). Then, the beam travels through the specimen and with the help of a series of electromagnetic lenses, the electrons reach the phosphorescent screen or the photosensitive film of the camera, projecting an image of the particles on the sample. The areas of the sample where the beam is being absorbed appear black, otherwise appear light (i.e. grey). The Au NPs interact strongly with the electron beam, since gold is a heavy element, hence particles appear as dark shades on the detector.

TEM can be used for the estimation of size and shape of ultra-small particles (< 2 nm)[96], while High-Resolution TEM provides visualisation of the lattice structure down to single atom[95]. However, quantification of the sample population is strongly dependant on the magnification focusing on the sample. Lower magnification offers the visualisation of large population and rapid sample analysis, however, hinders the size estimation. On the other hand, higher magnification increases the particle resolution, while limiting the measured nanoparticle population which can lead to improper and biased statistical analysis of the particle size distribution[97].

2.3. Gold nanoparticles synthesis in flow systems

2.3.1. Single-phase flow

Single-phase micro- and milli-reactors have been investigated for the translation of gold nanoparticle synthesis from batch to flow due to the rapid heat and mass transfer, minimising the particle size distribution[98]. Wagner and Köhler[99] used a glass-silicon split and recombine microreactor for the synthesis of 5 – 50 nm PVP-capped Au NPs using ascorbic acid as reducing agent (Figure 2-7a). Increasing the inlet flow rate from 1 ml/min to 8 ml/min, the gold particle size decreased from 35 nm to 24 nm, due to the severe fouling observed on the reactor walls at lower flow rates, influencing both particle size and polydispersity. Operating at high concentration of

the reducing agent and high pH led to the formation of smaller sizes, due to the increasing nucleation rate and redox potential, respectively, while elevated pH suppressed the particle deposition on reactor walls. Increasing the concentration of the stabilising agent from 0.025 % to 0.25 %, resulted in synthesis of < 6 nm Au NPs, due to the stabilisation of the smaller particles by the large molecule of PVP. Köhler *et al.*[100] also used a similar glass-silicon split and recombine micro-chip reactor for the rapid mixing of tetrachloroauric acid, ascorbic acid, poly(vinyl alcohol) (PVOH), sodium metasilicate and Fe(II) sulfate for the synthesis of Au NPs. Varying the feed and concentration of the reagents, they were able to synthesise gold nanoparticles of different configurations and size, including spherical, core–shell particles and hexagonal nanocrystallites. Wagner *et al.*[101] optimised the micro-chip design via the addition of multiple micromixers in series and residence loop for the multi-step reactant addition and minimisation of fouling on the reactor walls (Figure 2-7b). The reduction of tetrachloroauric acid with sodium borohydride ($NaBH_4$) yielded reproducible Au NPs within 4 – 7 nm without observed fouling. Decreasing the reactant concentrations led to the formation of smaller particle sizes.

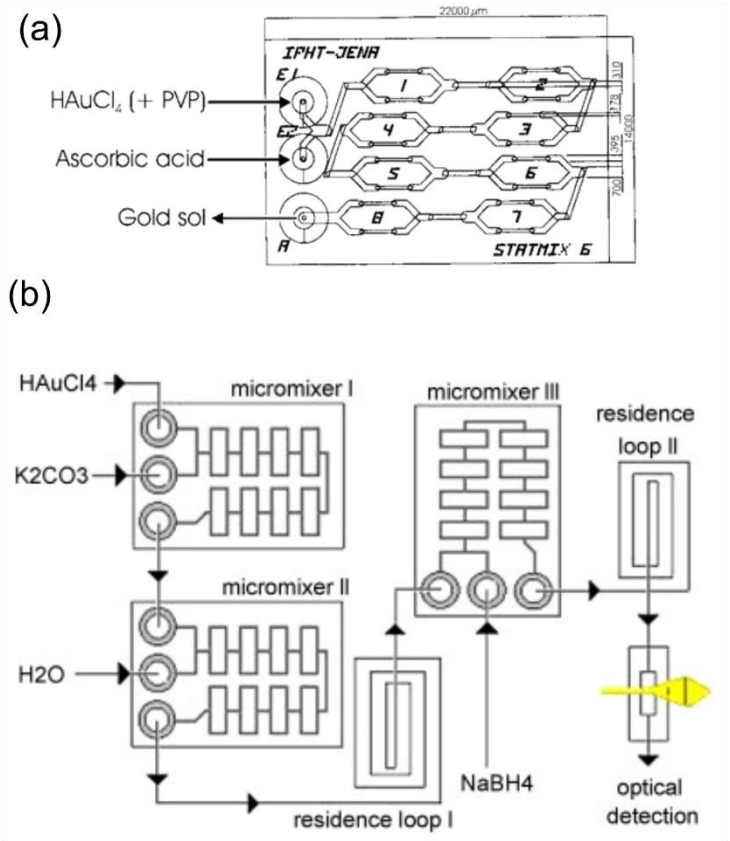

Figure 2-7 a) Schematic of the glass-silicon split and recombine mixer for the of PVP-capped gold nanoparticles using ascorbic acid as reducing (reprinted with permission from Ref.[99] Copyright 2005 American Chemical Society). b) Modular microreactor with split and recombine micromixer arrangement and residence loops with multi-step reactant addition for gold nanoparticles synthesis (adapted with permission from Ref.[101] Copyright 2008 Elsevier).

Ftouni *et al.*[102] synthesised ultra-small Au NPs (< 2 nm) via the *Turkevich* method using a T-junction for rapid reactant mixing prior to the fused-silica capillary reactor (inner diameter: 200 µm) at 100 ^{o}C (Figure 2-8). Taking advantage of the rapid mixing, heating and quenching of the synthesis set-up, the synthesis was realised at 35 – 50 s residence time in the reactor. Increasing the residence time up to 94 s, the size of the colloidal solution increased up to 3 nm. Sugano *et al.*[103] fabricated a microfluidic chip for the Au NPs synthesis consisting of a Y-shaped mixer and two piezoelectric valveless micropumps for the mixing of $HAuCl_4$ and Na_3Ct at room temperature (Figure 2-9). Increasing the switching frequency up to 200 Hz, mixing was realised within 95 ms, while decreasing the frequency resulted in increased mixing times. At 100 Hz, they presented the successful formation of 40 nm Au NPs with ~ 10 % coefficient of variation of the particle size distribution.

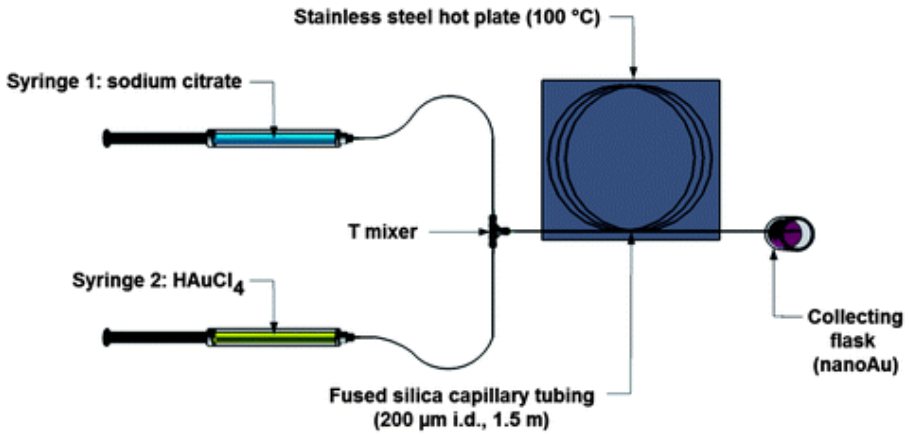

Figure 2-8 Single-phase microfluidic set-up comprising of a T-junction for mixing of the reactants and a fused-silica capillary reactor for the synthesis of gold nanoparticles via the *Turkevich* method. Reprinted with permission from Ref.[102] Copyright 2012 Royal Society of Chemistry.

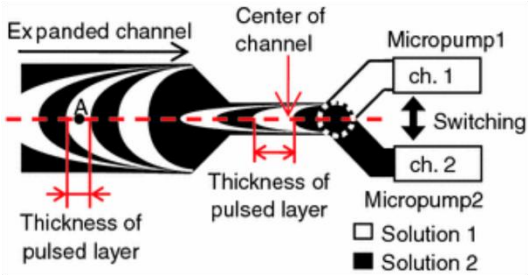

Figure 2-9 Schematic of the Y-shape pulsing micromixer for the synthesis of citrate-capped gold nanoparticles. Reprinted with permission from Ref.[103] Copyright 2010 Springer.

Milli-fluidic devises can be used for the scale-up of nanoparticle flow synthesis, increasing the channel dimension by one order of magnitude, providing similar control over fluid flow and residence time distribution and presenting the similar advantages as the microfluidic systems[104]. Lohse *et al.*[105] implemented a milli-fluidic reactor comprising of a polyethylene Y-mixer connected to a TYGON poly vinyl tubing (inner diameter: 2.7 mm) and an inline UV-Vis spectrometer on the outlet of the reactor for the monitoring of the synthesised gold nanoparticles (Figure 2-10). The reactor could be used for the synthesis of aqueous spherical citrate-, ω-functionalized thiol- and CTAB-stabilised gold nanoparticles (2 – 40 nm in size) via $NaBH_4$ reduction of $HAuCl_4$, as well as for the synthesis of gold nanorods 15-50 nm in length and aspect ratio between 1.5 – 4 and gold nanocubes. Varying the length of the tubing (and subsequently the volume of the reactor), the residence time could be varied between 3 – 30 min. Baber *et al.*[106] examined the synthesis of citrate-capped

Au NPs via *Turkevich* method using a coaxial flow reactor (CFR) comprised of an outer glass tube (inner diameter: 2 mm) and an inner glass tube (inner diameter: 0.8 mm) to minimise the fouling observed during Au NPs synthesis (Figure 2-11). A coil flow inverted comprised of a PTFE tube (inner diameter: 1 mm) was used in series with the CFR to improve the residence time distribution. Increasing the flow rate from 0.25 ml/min to 3 ml/min particle size increased from 17.9 ± 2.1 nm to 23.9 ± 4.7 nm, while particle size distribution increased from 11 % up to 20 %. Varying the synthesis temperature between 60 – 100 ^{o}C, the minimum particle size observed at 80 ^{o}C (17.9 ± 2.1 nm).

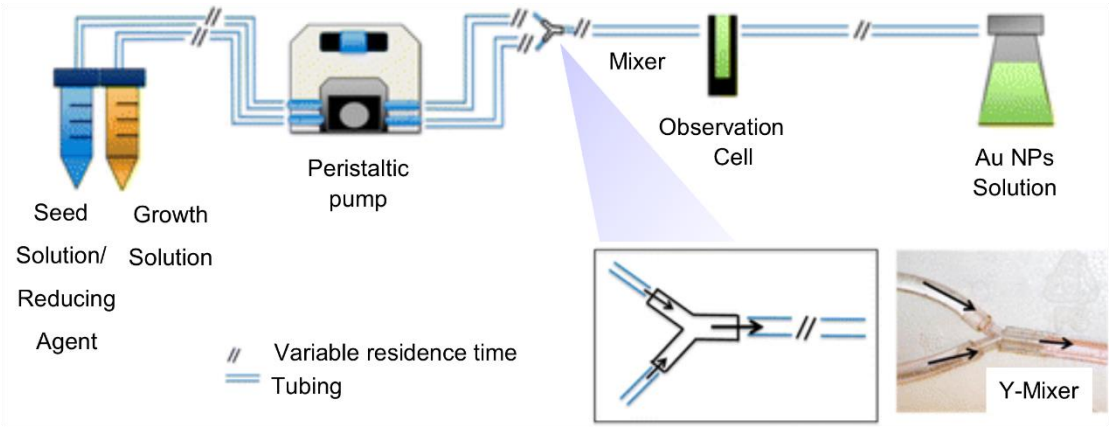

Figure 2-10 Schematic of the integrated millifluidic reactor set-up used for gold nanoparticle synthesis. The set-up comprises of the feed reacting streams, a peristaltic pump, a Y-shape mixer, an inline UV-Vis monitoring spectrometer and the collection of the colloidal solution. Magnified area: schematic and photograph of the Y-shape polyethylene micromixer. Adapted with permission from Ref.[105] Copyright 2013 American Chemical Society.

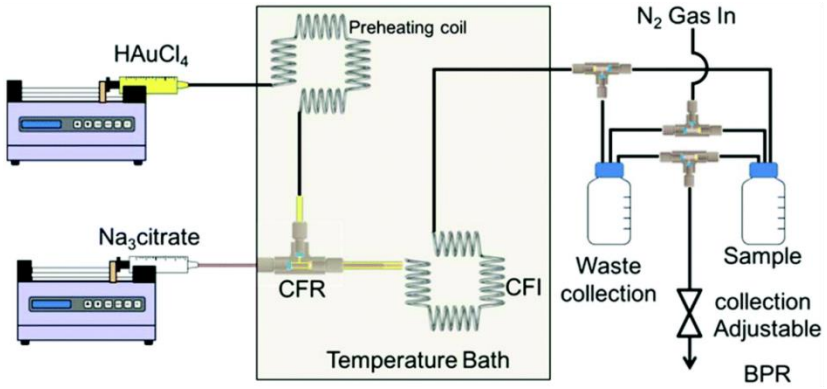

Figure 2-11 Schematic of the experimental setup for gold nanoparticle synthesis via the *Turkevich* method, using a coaxial flow reactor (CFR) and a coil flow inverter in series. Reprinted with permission from Ref.[106] under Creative Commons Attribution 3.0 Unported Licence. Copyright 2017 Royal Society of Chemistry.

Huang *et al.*[96] investigated the parameters influencing the synthesis of ultrasmall citrate-capped Au NPs (< 2 nm) in millifluidic reactors (Figure 2-12). In their study they varied both the capillary material (polytetrafluoroethylene, fluorinated ethylene propylene, polyetheretherketone and fused silica) using capillaries of different diameters (inner diameter varied between 0.3 – 1 mm), residence time (1.5 – 30 min) and synthesis temperature (70 – 100 ^{o}C). Decreasing the capillary diameter down to 0.3 mm (increasing the surface-to-volume ratio) particle size was 1.9 ± 0.2 nm, while particle size was similar (2 – 3 nm) regardless of the reactor material. However, fouling was observed on the capillary walls due to the interaction between the positive charged citrate-gold precursor species and the negative charge tubings and the van der Waals forces between the synthesised particles and capillary walls.

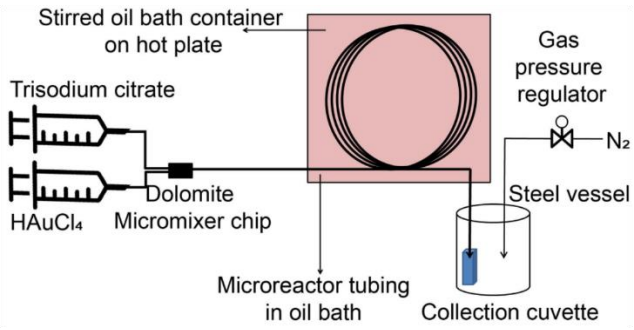

Figure 2-12 The Schematic of the experimental set-up for the continuous synthesis of ultrasmall gold nanoparticles in a capillary reactor using tetrachloroauric acid and trisodium citrate. Reprinted with permission from Ref.[96] under Creative Commons CC-BY. Copyright 2018 Elsevier.

2.3.2. Multi-phase flow

The use of multi-phase flow by introduction of an immiscible phase (i.e. organic solvent) has been studied for the elimination of fouling on the reactor walls due to the formation of a surrounding film around the slugs (or droplets). Another limitation of the single-phase flow systems is the residence time distribution (RTD) describing a the probability density function of the time each fluid element spends in the reactor. The RTD is related to the particle size distribution (PSD) of the nanoparticle synthesis; as RTD deviates from the plug-flow profile ("wider" RTD), the polydispersity of the nanoparticle sample increases ("wider" PSD)[107]. The formed droplets can be considered as individual plug-flow reactors, hence optimising the residence time distribution[43], as well as enhancing the mixing efficiency of the reactants due to the internal vortex circulation (Taylor flow)[108]. Sebastian Cabeza *et al.*[44] studied the reduction of $HAuCl_4$ by $NaBH_4$ for the synthesis of Au NPs (aqueous phase) in a silicon microreactor (channel depth x width: 0.4 mm x 0.4 mm) segmented by air, toluene or silicone oil (Figure 2-13). Due to the hydrophilicity of the silicon channels, water was the continuous phase. The smallest particles were synthesised in the air-water system (2.8 ± 0.2 nm), while the silicon oil-water system resulted in a bimodal particle size distribution (7.8 ± 6.5 and 15.5 ± 3.1 nm). Air-water system provided the best internal recirculation in the aqueous slugs, improving the residence time distribution. Kulkarni and Sebastian Cabeza[109] compared the toluene-water two-phase flow in a hydrophobic PTFE capillary reactor (inner diameter: 2.5 mm) and a hydrophilic microreactor (similar to Sebastian Cabeza *et al.*[44]) for the biphasic synthesis of Au NPs using different organic reducing agents (triethylamine (TEA), butyl amine (BA), ethyle amine (EA), octadecylamine, chloropyridine and piperidine). Using a hydrophobic capillary, aqueous phase is the disperse phase forming droplets surrounded by toluene acting as the continuous phase (Figure 2-14 a – c). According to their findings, particles accumulated at different location for different wettability of the reactor wall, influencing the size and shape of the Au NPs. In the hydrophilic channels, particles were dispersed in the aqueous phase and were accumulated at the low pressure in the rear of the organic slugs (Figure 2-14 d – e). In that case, the particle formed sharp hexagonal bipyramidal particles of ~ 42 nm in size. In case of the hydrophobic channels, the particles were in the dispersed aqueous droplets, while synthesis initiated at the front-end of the droplets and then moved and accumulated at the low-pressure region located at the back-end of the

droplet (Figure 2-14 f – g). The internal recirculation in the aqueous droplets enhanced the mixing yielding in smaller spherical Au NPs of ~ 12 nm in size.

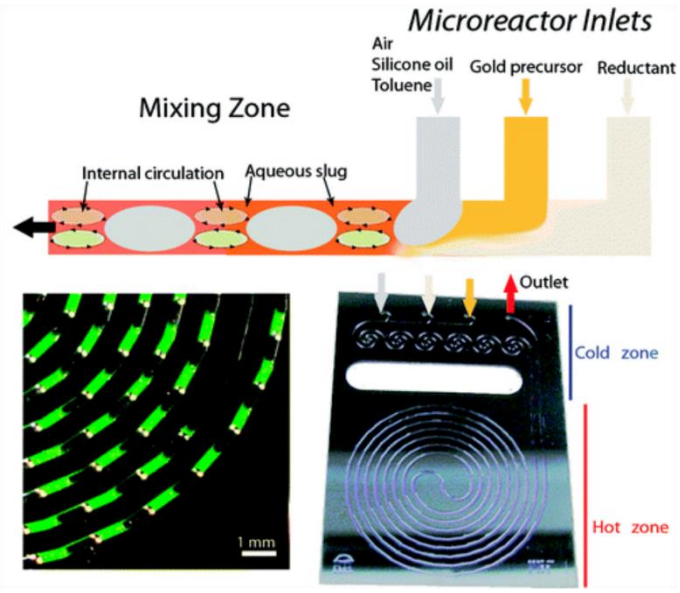

Figure 2-13 Gold nanoparticle formation in a segmented flow system using a glass-silicon micoreactor. Reprinted with permission from Ref.[44] Copyright 2012 American Chemical Society.

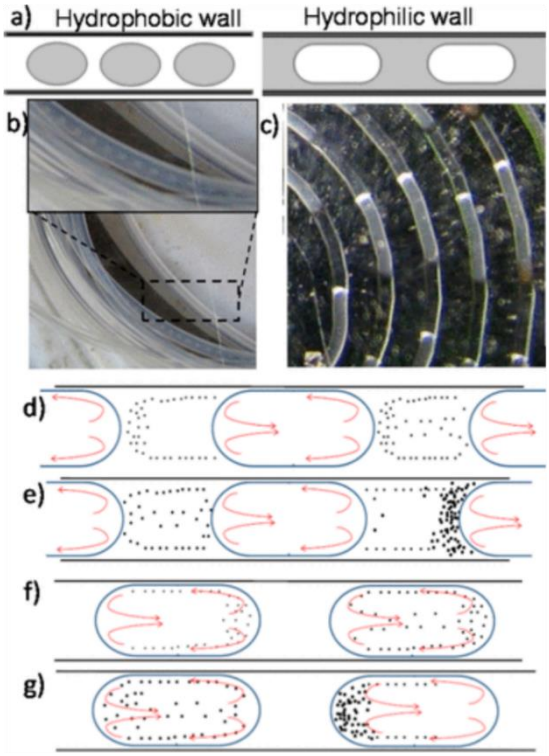

Figure 2-14 a) Schematic and b) photograph of the two-phase flow in hydrophobic (left) and hydrophilic (right) microchannels (grey: aqueous phase, white: organic phase). d-e) formation and accumulation of synthesised gold nanoparticle in a hydrophilic reactor. f-g) formation and accumulation of synthesised gold nanoparticle in a hydrophobic reactor. Reprinted with permission from Ref.[109] Copyright 2017 American Chemical Society.

Duraiswamy and Khan[110] used a poly(dimethyl siloxane) (PDMS) microfluidic device (depth x width: 155 μm x 300 μm), for the anisotropic synthesis of gold nanostructures (Figure 2-15a). A T-junction allowed the simultaneous addition of the three streams (gold seeds, premixed gold precursor with capping agent (CTAB) and the ascorbic acid acting as reducing agent) forming homogeneous droplets using silicon oil as the segmenting fluid. Silicon oil was the continuous phase preventing fouling on the reactor walls, while reactant mixing was enhanced in the formed droplets due to chaotic advection (Figure 2-15b). Varying reactant concentrations and flow rates resulted in a tunable synthesis of gold nanorods and nanospheres, as well as cubes, tetrapods, and four-edged stars.

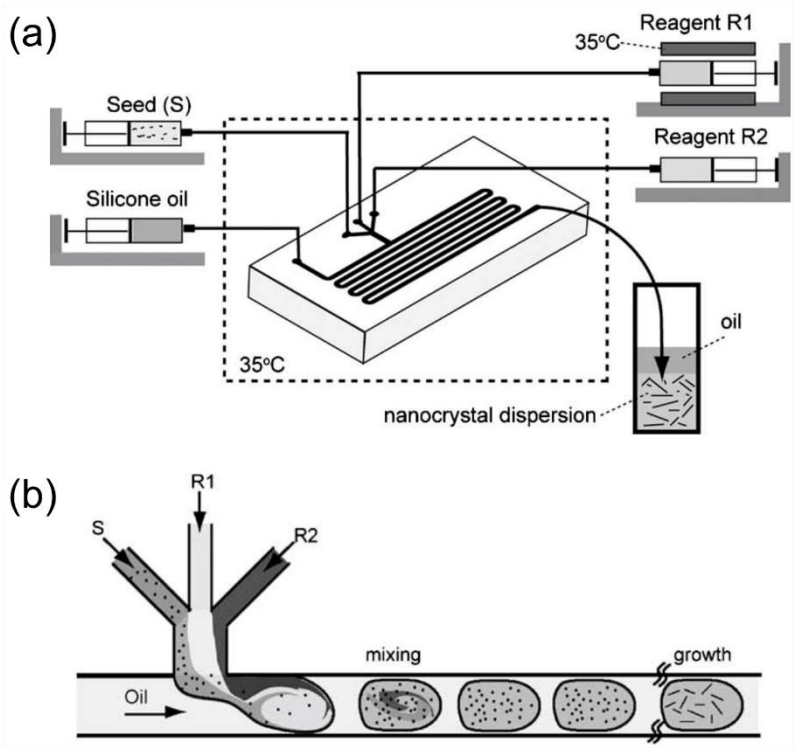

Figure 2-15 a) Schematic of the experimental set-up and b) schematic of reactant mixing and droplet formation in the microfluidic chip for the tunable synthesis of gold nanocrystals. Adapted with permission from John Wiley and Sons and Copyright Clearance Center. Ref.[110] Copyright 2013.

Du Toit *et al.*[49] synthesised citrate-capped Au NPs in an aqueous-heptane flow system. Nucleation was enhanced in a glass capillary (inner diameter: 0.8 mm) via a series of UVC lamps of varying UV intensity, followed by an FEP tube (inner diameter) placed in a glycerol bath at constant temperature (90 ^{o}C) for controllable particle growth (Figure 2-16). Varying the UV intensity at constant 10 s exposure time and 20 min growth time, Au NPs ranged between 6.6 ± 0.8 nm (at 60 ^{o}C growth temperature) to 36.1 ± 6.9 nm (at 100 ^{o}C growth temperature). Carino *et al.*[111] developed a segmented flow tubular reactor (SFTR) for the synthesis of citrate-capped spherical Au NPs. Operating at 95 ^{o}C with 5 min residence time, yielded in monodisperse particles of ~ 15 nm in size, while estimating that the throughput can potentially increase up to 5 g/day, followed by ultrafiltration and dialysis for sample purification.

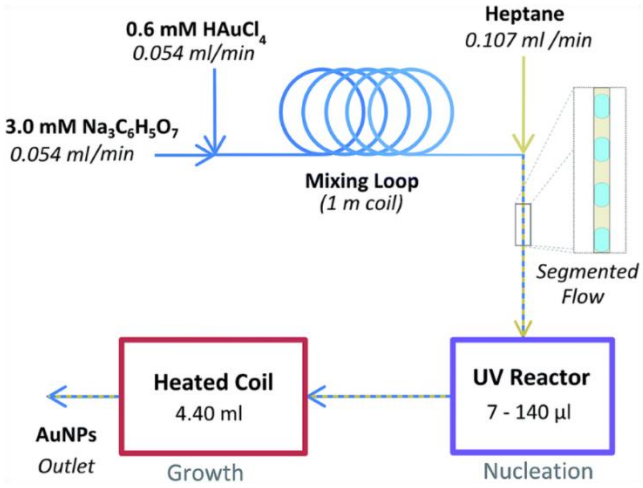

Figure 2-16 Schematic of the set-up for the UV-induced citrate-capped gold nanoparticle synthesis (*Turkevich* method) in a two-phase flow reactor. Reprinted with permission from Ref.[49] under Creative Commons Attribution 3.0 Unported Licence. Copyright 2017 Elsevier.

2.4. Microwave technology

2.4.1. Introduction

Microwave technology has been studied and implemented over the past decade in organic chemistry and inorganic synthesis as a method to intensify the existing commercial processes, while there has been extensive research towards optimisation of the microwave-assisted reactor for efficient energy delivery, lower capital cost and increasing the safety of the microwave systems by preventing the microwave leakage outside the reactor[112]. Microwaves cover the frequency (f) range between 300 MHz and 300 GHz of the frequency spectrum. The respective wavelengths (λ) in vacuum are in the range of 1 m and 1 mm ($\lambda = {}^{c}/_{f}$; c: speed of light in vacuum). The following figure (Figure 2-17) shows the electromagnetic spectrum in the range between the visible light and the longwave radio signal.

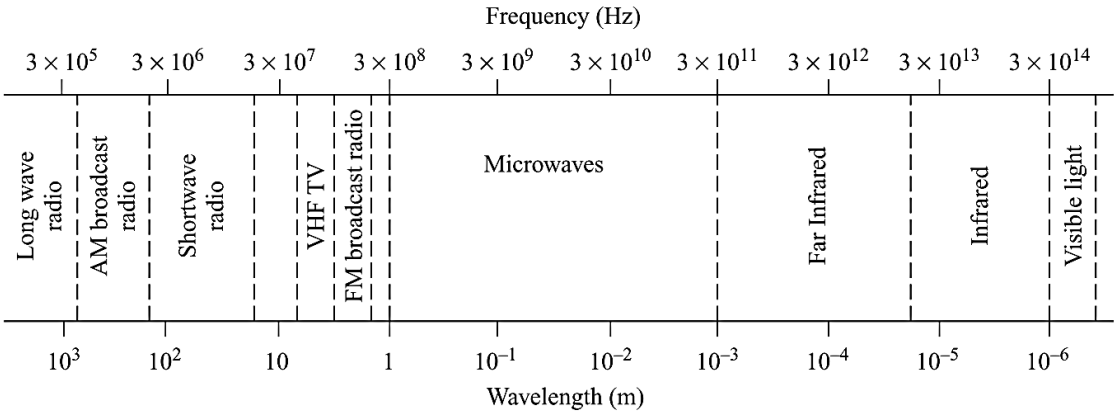

Figure 2-17 The electromagnetic spectrum. Range: Visible Light to Longwave Radio Signals. Adapted with permission from John Wiley and Sons and Copyright Clearance Center. Ref.[113] Copyright 2012.

Due to legislation boundaries, to avoid interference with radio signals and telecommunication frequencies, the common frequencies used in chemical process design are 915 MHz, 2.45 GHz and 5.85 GHz (customarily at the Industrial Scientific and Medical (ISM) frequency of 2.45 GHz)[112, 114]. The methodology that microwaves interact with the medium depends on the medium's physical state, liquid or solid. Nevertheless, microwave photon energy in this frequency region is approx. 0.0016 eV, insufficient to cause breakage or rearrangement of chemical bonds[54]. For liquid systems, the key factor is the polarity of the molecules. In case of polar molecules (e.g. water or ethanol) or ions (e.g. salts), which present permanent dipole moments, they rotate in the presence of a rapidly alternating electric field of microwave radiation. This rotational motion causes an internal friction in the medium, which results in heating[114] (Figure 2-18). Microwave heating is described as "volumetric" in nature, as it depends on the volume of the reactor (workload), as well as the dielectric properties of the medium and its permittivity to microwaves, which they function of the temperature and electromagnetic frequency[115]. In other words, this heating method is described by Maxwell's equations (Section 2.4.2.), based on the electromagnetic field distribution in time and space, as well as the properties of the medium, for the transformation of the electromagnetic energy to heat[113, 114].

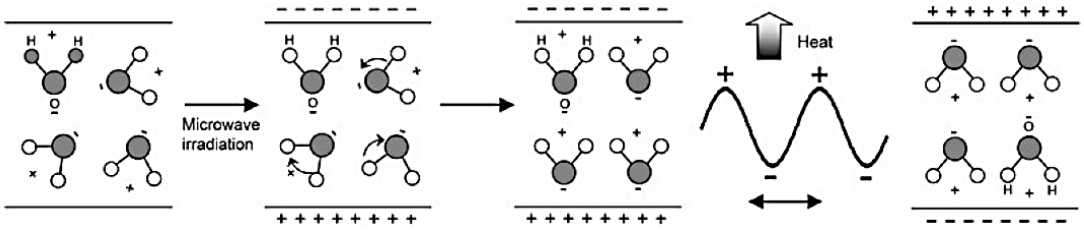

Figure 2-18 Heating mechanism of H_2O by microwave irradiation. Reprinted with permission from John Wiley and Sons and Copyright Clearance Center. Ref.[116] Copyright 2005.

Reports of microwave heating for chemical synthesis are dated back in 1980s. The area of microwave heating application includes organic or polymer synthesis, biomedical or biochemical reactions, nanotechnology and nanoparticle synthesis[75, 117, 118]. Microwave heating has been used due to its advantages over accelerating reaction rates and reducing reaction times[112]. In case of nanoparticle synthesis, microwave-assisted fabrication provides various advantages, over conventional heating methods, such as rapid and selective heating, superheating above solvents' boiling point and high pressure reactions in sealed vessels[54]. These parameters are related to particle size distribution and shape, composition and structure. These parameters control and tune the properties of synthesized nanoparticles[66, 75, 79]. Literature findings on microwave-assisted nanoparticle synthesis include the formation of single-metal nanocrystals, metal oxides, oxide or no-oxide semiconductors and core-shell configurations[75]. Although both batch and continuous flow nanoparticle synthesis have been examined, microwave-assisted synthesis is believed not to have yet reached its full potential[75, 119, 120].

2.4.2. Background of microwave heating

Electromagnetic theory is described by Maxwell's equations, which describe the electromagnetic field intensity in the time-dependent form as[113, 115]:

$$\nabla \cdot \boldsymbol{B} = 0 \qquad \text{Eq. 2-5}$$

$$\nabla \cdot \boldsymbol{D}_e = \rho_m \qquad \text{Eq. 2-6}$$

$$\nabla \times \boldsymbol{E} = -\frac{\partial \boldsymbol{B}}{\partial t} \qquad \text{Eq. 2-7}$$

$$\nabla \times \boldsymbol{H} = \boldsymbol{J} + \frac{\partial \boldsymbol{D}_e}{\partial t} \qquad \text{Eq. 2-8}$$

together with the auxiliary equations:

$$\boldsymbol{J} = \sigma_e \boldsymbol{E} \quad \text{Eq. 2-9}$$

$$\boldsymbol{D_e} = \varepsilon_0 \varepsilon' \boldsymbol{E} \quad \text{Eq. 2-10}$$

$$\boldsymbol{B} = \mu_0 \mu' \boldsymbol{H} \quad \text{Eq. 2-11}$$

Where $\boldsymbol{B}$ is the magnetic flux density, $\boldsymbol{D_e}$ is the electric flux density, $\boldsymbol{E}$ is the electric field, $\boldsymbol{H}$ is the magnetic field density, $\boldsymbol{J}$ is the electric current density, σ_e is the electrical conductivity, ε_0 is the electric permittivity of vacuum, μ_0 is the magnetic permeability of vacuum, ε' is the dielectric constant and μ' is the real term of complex permeability.

Temperature distribution in a material subject to microwave heating depends on the electromagnetic field. There are two ways to approach the microwave power absorption to assess field intensity – by using Maxwell's equations or Lambert's Law. In the former approach absorbed microwave power is calculated based on the spatial distribution of the electromagnetic field, while according to Lambert's Law the absorbed microwave power depends on the penetration depth of the microwaves in the medium. The penetration depth of the microwaves in the medium is described as the depth at which the power density falls to e^{-1} of its initial value (~36.7%) at the surface and is given by the following equation[114, 121]:

$$d_p = \frac{\lambda_o}{2\pi\sqrt{2\varepsilon'}} \frac{1}{\sqrt{\sqrt{1 + \left(\varepsilon'/\varepsilon''\right)^2} - 1}} \quad \text{Eq. 2-12}$$

Where ε' is the dielectric constant, ε'' is the dielectric loss and λ_0 is the microwave wavelength in vacuum.

Lambert's Law is used for high volume samples, where the reactor size is larger than the penetration depth of the electromagnetic wave[121, 122]. However, in case of micro-reactors and milli-reactors, where the penetration depth of the materials and solvents is much larger than the tube diameter, the electromagnetic field distribution is calculated by Maxwell's equations and the absorbed microwave heating is assumed to be homogeneous across the cross sections.

Materials are characterized by their complex relative permittivity ε_r and their complex relative permeability μ_r to the respective microwave radiation. Complex relative permittivity can be described by the following equation:

$$\varepsilon_r = \varepsilon' - j\varepsilon'' \qquad \text{Eq. 2-13}$$

Where ε' is the dielectric constant and ε'' is the dielectric loss. ε' is dependent on the material and describes its potential to store the microwave energy and thus be polarized by the electromagnetic field. ε'' describes the efficiency of converting electromagnetic energy into heat. The higher the dielectric loss, the higher is the amount of electromagnetic energy which will be converted into heat (i.e. leading to a higher final temperature).

Loss tangent $tan\delta$ is the ratio of dielectric loss to dielectric constant and describes the dissipation of microwaves in the medium. Similarly to the dielectric loss factor, the higher the value of loss tangent, the higher the amount of electromagnetic energy which will convert into heat (higher final temperature):

$$tan\delta = \frac{\varepsilon''}{\varepsilon'} \qquad \text{Eq. 2-14}$$

Tables 2-1 and 2-2 present the dielectric properties of common materials and solvents. These materials/solvents can be described as *high absorbing, medium absorbing, low absorbing* or *microwave transparent* according to their loss tangent value, following the rule-of-thumb[54]:

Highly Absorbing:	$tan\delta$ > 0.5
Medium Absorbing:	0.1 < $tan\delta$ < 0.5
Low Absorbing:	$tan\delta$ < 0.1
Microwave transparent:	$tan\delta$ ≈ 0

Table 2-1 Dielectric constant ($\boldsymbol{\varepsilon'}$), dielectric loss ($\boldsymbol{\varepsilon''}$), and loss tangent ($\boldsymbol{tan\delta}$) of common materials at 25 ^{o}C[114].

Material	$\boldsymbol{\varepsilon'}$	$\boldsymbol{\varepsilon''}$	$\boldsymbol{tan\delta}$
Vacuum	1	0	0
Air	1.0006	0	0
Glass (Pyrex)	4.82	0.026	0.0054 (3 GHz)
Styrofoam	1.03	0.0001	0.0001 (3 GHz)
PTFE	2.08	0.0008	0.0004 (10 GHz)

Table 2-2 Loss tangent ($\boldsymbol{tan\delta}$) of common solvents at 25 ^{o}C and 2.45 GHz[54].

Solvent	$\boldsymbol{tan\delta}$	**Solvent**	$\boldsymbol{tan\delta}$
ethylene glycol	1.350	DMF	0.161
Ethanol	0.941	1,2-dichloroethane	0.127
DMSO	0.825	Water	0.123
2-propanol	0.799	chlorobenzene	0.101
formic acid	0.722	chloroform	0.091
Methanol	0.659	acetonitrile	0.062
nitrobenzene	0.589	ethyl acetate	0.059
1-butanol	0.571	acetone	0.054
2-butanol	0.447	tetrahydrofuran	0.047
1,2-dichlobenzene	0.280	dichloromethane	0.042
N-methyl-2-pyrrolidinone (NMP)	0.275	Toluene	0.040
acetic acid	0.174	Hexane	0.020

In terms of time-varying properties, the microwave power density is defined by the following equation[113, 114]:

$$P_d = 2\pi f \varepsilon_o \varepsilon'' |\boldsymbol{E}|^2 + 2\pi f \mu_o \mu'' |\boldsymbol{H}|^2 \qquad \text{Eq. 2-15}$$

Where f is the frequency of the electromagnetic field, ε_o is the electric permittivity of vacuum, ε'' is the dielectric loss and $|\boldsymbol{E}|$ is the electric field intensity, μ_o is the magnetic permeability of vacuum, μ'' is the imaginary part of complex permeability and $|\boldsymbol{H}|$ is the magnetic field intensity. For non-magnetic materials which their properties depend only on the electric field, the second term on the right hand side is neglected.

Considering an adiabatic system where energy is dissipated uniformly in the reactor volume, the heat generation can be expressed by the following equation in batch[115]:

$$P_d = mC_p \frac{dT}{dt} \quad \text{Eq. 2-16}$$

and in continuous-flow process:

$$P_d = \frac{dm}{dt} C_p \Delta T \quad \text{Eq. 2-17}$$

Where ρ is the density, Cp is the specific heat capacity, T is the temperature, m is the workload mass and t is the time.

In microwave-assisted synthesis, the temperature increase is proportional to the heat generation (microwave power density), the material dielectric properties and the electric field profile. On the contrary, as it can be observed from Equations 2-16 and 2-17, temperature increase is inversely proportional to the mass or volume of the medium or workload; thereof microwave heating is described "volumetric" in nature. In a continuous flow system, when a sample is heated under volumetric microwave heating, temperature rise depends on the coupling of Maxwell's equations and heat transfer to the medium (see Chapter 3).

2.4.3. Microwave heating simulations

Several studies were conducted in the past implementing computational modelling in order to simulate the temperature profile of solid materials[121], liquids (in batch or in flow)[59, 123] and liquid-solid particle systems[124]. Modelling studies of microwave heating use either the finite element method (FEM)[59, 123, 125-127] or the finite-difference time-domain (FDTD)[117, 128] techniques to couple and simultaneously solve the electromagnetic field, heat transfer and fluid flow to describe the system. Salvi *et al.*[125] compared results obtained by FEM modelling with experimental results for continuous flow of water in a polytetrafluoroethylene (PTFE) tube placed inside a TE10 microwave applicator. Modelling overestimated the temperature of the medium (Figure 2-19), resulting in 5 – 20 ^{o}C discrepancies between experimental and computational results at the edges of the tube. These discrepancies were attributed to the no-slip boundary conditions resulting in zero fluid velocity at the tube walls,

intensifying the electric field and thereby, the final temperature. However, another possible reason explaining those discrepancies was the insufficient meshing of the domains[125, 129]. Yousefi *et al.*[122] simulated the temperature profiles of water under continuous flow conditions in a vertical tube, undergoing microwave heating through a rectangular waveguide. They coupled heat transfer and fluid flow physics and discussed the effects of the inlet water velocity and applicator dimensions on the temperature profiles. Tuta and Palazoğlu[127] coupled Maxwell's equations, Fourier's heat transfer equation and Navier-Stokes equation to optimise the microwave energy uptake to achieve greater and more uniform temperature increase of fluids in a pilot-scale, continuous flow, coiled PTFE tube under microwave heating. Varying dielectric properties and the presence of secondary flow (Dean vortices) were included in their studies. Robinson *et al.*[130] investigated the microwave dissipation on the walls of a microwave absorbing vessel (such as silicon carbide), resulting in elevated temperatures in the medium, as opposed to "microwave transparent" vessels.

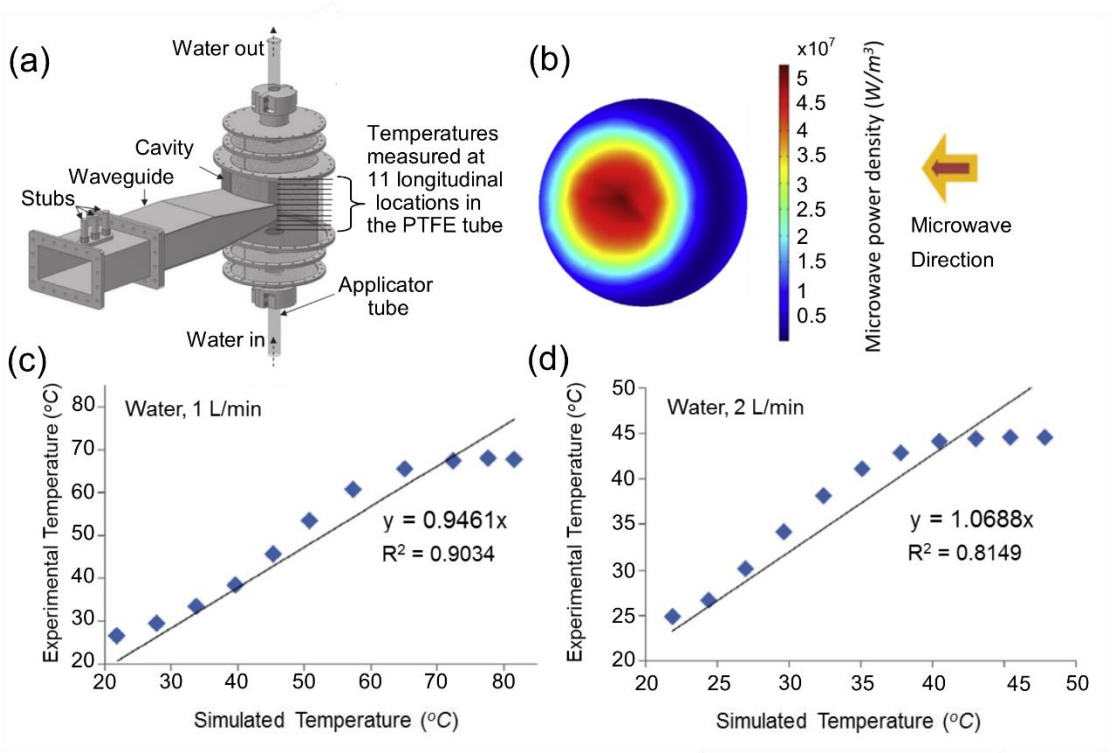

Figure 2-19 a) Continuous flow single-mode microwave system, b) Cross section of the spatial distribution of microwave power density in the flowing water in the PTFE tube, c-d) average experimental versus simulated temperature for 1 L/min and 2 L/min water flow rates, respectively. Adapted with permission from Elsevier and Copyright Clearance Center. Ref.[125] Copyright 2011.

From previous studies[59, 61, 126, 131] it is evident that the temperature profile depends on the geometry, dimensions and materials of the reactor, as well as reactor position and flow rate of the medium. Morgan *et al.*[131] described the presence of electric field depolarisation on a Teflon microfluidic chip on horizontal and perpendicular orientation, focussing on the reactor and medium characteristics rather than liquid flow (Figure 2-20). In their analysis they altered the orientation of the chip and observed higher heating efficiency when the electric field was parallel to the long dimension of the straight channels of the chip. Computational modelling of the electromagnetic waves and subsequent microwave heating allows better understanding of the parameters affecting final results and temperature profile under microwave power. Although microwave energy results in rapid and selective heating, the main drawback of this technology is the non-uniform temperature profile inside the material or the medium[60]. Several researchers and case studies were conducted in the past, implementing computational modelling design, in order to simulate the temperature profile of solid materials,[121] liquids (in batch or in flow)[59, 123] and suspended particles[124].

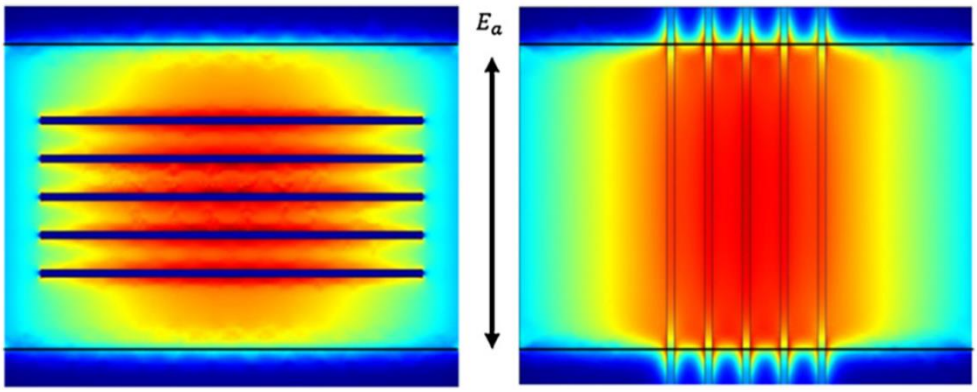

Figure 2-20 Depolarisation of the electric field E_a in a microfluidic chip. When the channels are placed vertically to the electric field profile (left) depolarisation takes place, while there is no depolarisation of the electromagnetic field in horizontal channels (right). Color mapping depicts the electric field intensity (blue: low intensity, red: high intensity). Reprinted with permission from Elsevier and Copyright Clearance Center. Ref.[131] Copyright 2013.

2.4.4. Microwave vs conventional heating

There are two types of microwave apparatus, single-mode and multi-mode applicators, as shown in Figure 2-21. In single-mode (or monomode) applicators a

single-standing wave is generated in the cavity and the sample is positioned in the maxima of the magnitude of microwave energy. Single-mode applicators exhibit higher electromagnetic field densities, than multi-mode ones, resulting in higher heating rates. However, the small cavity volume is a limiting factor. In multi-mode applicators[114], a rotating deflector ensures the electromagnetic waves to be spread and reflected inside the cavity, thus generating multiple microwaves of different amplitude to increase the effective surface area of heating. However non-uniformity of electric field and temperature profile, due to the large number of different electromagnetic waves, act as the main disadvantages of this mode[54, 114].

Table 2-3 summarizes the main differences between microwave and conventional heating. Microwave heating is described as rapid, volumetric and heats up the centre of the medium, avoiding the process of heating the walls of the tube or vial first and then the medium, resulting in temperature gradients in the cross-sectional area[114, 132]. Another aspect is the selectivity of microwave heating, as a function of the $tan\delta$ of the medium or material. This results in increased heating rates of the lossy medium and highest product quality and purification, without affecting "microwave transparent" materials and excess energy losses[75]. Also, since the temperature of the walls is lower than that of the medium, the material deposition potentially decreases[133]. Although microwave heating is considered an alternative to conventional heating, there have reactor designs where the reactor is heated by microwave radiation for selective heating surrounded by a cooling jacket[120].

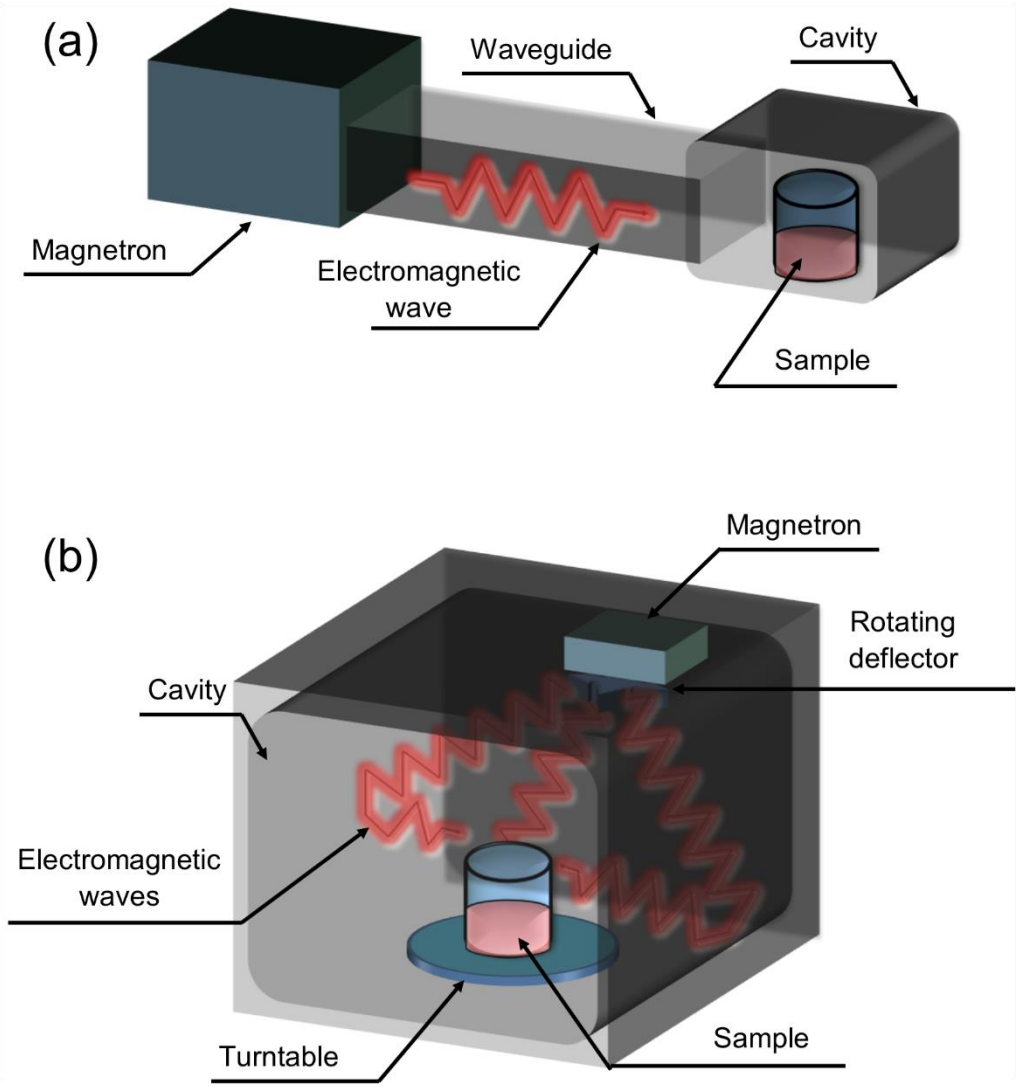

Figure 2-21 Schematic of a) single-mode and b) multi-mode microwave applicators for batch synthesis.

The increased temperature rates are related to the microwave energy potential to accelerate chemical reactions. According to reaction kinetics and the Arrhenius Law, rate constants are proportionally related to temperature and a decrease in the activation energy results in increased reaction rates. However, the increased reaction rates are usually mentioned as part of the non-themal effects of microwave energy, due to polarization of molecules (which can potential increase the nucleation rates in nanoparticle synthesis), rather than increase of medium temperature[114, 134]. Validation of non-thermal effects could be achieved only through testing the reaction rates and product syntheses under different microwave frequencies, while maintaining the same final temperature[75, 112]. Nevertheless, non-thermal effects are currently a debatable subject[75].

In conventional heating, highest reachable temperature is limited by the boiling point of the solvent. However, in microwave heating, temperature can exceed the boiling point by a small degree due to superheating[135, 136]. Nevertheless, superheating might result in rapid and significant increase of vapour pressure[54, 137]. Hot-spot formation due to components of different dielectric properties can affect selectivity of desired products[54, 132]. Temperature control still remains one of the major issues of microwave heating as temperature rises at constant microwave irradiation[60]. There have been attempts of temperature control through external cooling jacket of "microwave transparent" fluids, controlling the fluid velocity or microwave power in continuous or batch syntheses[52, 60, 120, 122].

Table 2-3 Differences between microwave and conventional heating[54, 75, 112, 114, 132-134, 137, 138].

Microwave Heating	Conventional Heating
Electromagnetic waves.	Thermal or electrical sources.
Coupling at molecular level.	Superficial heating.
Heating mechanism involves dipolar polarization or ionic conduction.	Heating mechanism involved conduction and convection.
Volumetric heating of the centre of reactor.	Heating gradually from reactor walls to the centre of reactor.
No physical contact with power source.	Reactor In contact with power source.
Temperature rise depends on the dielectric properties of the material.	Highest temperature is limited by boiling point of substrates.
Superheating (temperature rise above the boiling point of the medium).	All components of the mixture are heated almost equally.
Selective heating depending on the dielectric properties of the material.	Slow heating rates.
Possible hot-spots.	
Rapid heating rates.	

2.5. Microwave-assisted nanoparticle synthesis

2.5.1. Examples of nanoparticle synthesis in batch

Microwave heating has been used for the synthesis of single metal or core-cell nanoparticles, metal oxides and luminescent nanocrystals among others, due to its

advantages over conventional heating[75, 139-143]. Thermal effects are related to kinetics and reaction rates due to rapid volumetric heating and higher reaction temperatures. Since final temperature, precursor and reagents types and concentration remain the same, the advantages of microwave over conventional heating for nanoparticle synthesis lie on the rapid heating provided by microwaves, instead of the slow heating-up process of oil-baths. However, results may be similar if same conditions are being used[75, 118]. Recent use of ionic liquids in nanoparticle synthesis suggest that their dielectric properties may be a promising option over other synthesis methodologies, due to their high dielectric loss factor, resulting in high temperature ramping (over 200 ^{o}C, within seconds)[75, 144].

On the other hand, the observed advantages of microwave over conventional heating, may be the result of other specific effects, related to the thermal effects, but cannot be duplicated by conventional heating[52, 75]. Increased heating rates, hot spots and superheating are considered as thermal effects for nanoparticle formation which result in burst nucleation and growth of nanocrystals. However, they cannot be duplicated by conventional heating and are related to microwave properties, such as the frequency of the field[118]. Frequency is related to the relative permittivity of the materials, affecting the heating rate and penetration depth[145].

In case of Zhu *et al.*[139] the use of microwave heating in microfluidic set-up increased the overall yield and purity of desired products (LaF_3/$LaPO_4$:Ce, Tb nanocrystals) in comparison with oil-bath heating. The results were attributed to the specific effects related to the dielectric properties of the medium and the polarisation of the molecules due to the microwave field increasing the nucleation rate. Similarly, since microwave heating is selective it triggers the formation of hot-spots, which increase the overall production rate and reduces the fouling of reactors, as microwave heat-up the centre of the bulk, leaving the inner walls in a lower temperature, thus avoiding the formation of nanoparticles on the surface. These two properties are considered important assets for microreactors, since the available space is limited and the intensification of the process is increased. The study of Horikoshi *et al.*[133] for silver nanoparticle synthesis (Ag NPs), showed that microwave heating resulted in narrower particle size distribution and reduced fouling in the reactor when compared to conventional heating (Figure 2-22).

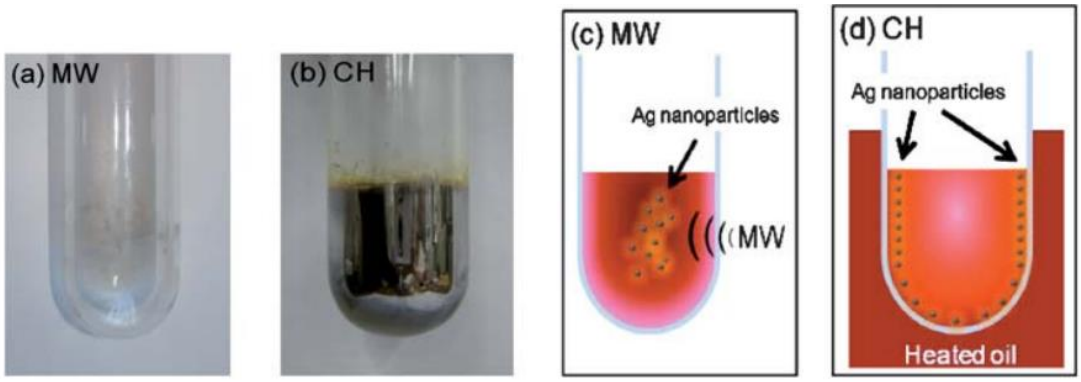

Figure 2-22 Image and schematic of the reactor after silver nanoparticle synthesis a) after 4 min of microwave irradiation, and b) after 5 min of oil bath heating. Schematic: nanoparticle synthesis in the reactor c) after the 4 min of microwave heating, and d) after the 4 min of oil bath heating. Reprinted with permission from Ref.[133] Copyright 2010 Royal Society of Chemistry.

Non-thermal effects are derived from microwave electric field without resulting in any changes in the temperature profile of the molecules. In other words, non-thermal effects affect the polarization of molecules to the electric field. This polarization could enhance (i) the pre-exponential factor *A* in Arrhenious equation and decrease the activation energy of reaction mechanisms and enhance the (ii) reactivity and product crystallization due to increased polarization or instantaneous dipole moments[52, 75, 116]. However, non-thermal effects are strongly related to the frequency of the field, as it affects the effective collision frequency of the primary clusters, which later result in the desired nanoparticles. Horikoshi *et al.*[58] tested the fabrication of gold nanoparticles under varying microwave frequency (2.45 GHz and 5.8 GHz) and residence time (7 min and 15 min) via organic and polyol/aqueous process routes. For the case of organic synthesis (Figure 2-23), Au NPs were produced only under 5.8 GHz for 7 min and 15 min residence time based on the surface plasmon resonance band (see Section 2.1.2) appearing at 528 nm wavelength, as a result of the higher temperatures reached during synthesis for the case of 5.8 GHz (Figure 2-23a). On the other hand, during the polyol-based process, system temperature was similar in both studied frequencies and there was no effect of the varying frequency on the particle size. As the dielectric properties of the materials and the substrate are related to the electric field frequency, the most appropriate series of tests would be maintaining same temperature, at different field frequencies, taking into account limiting factors such as penetration depth.

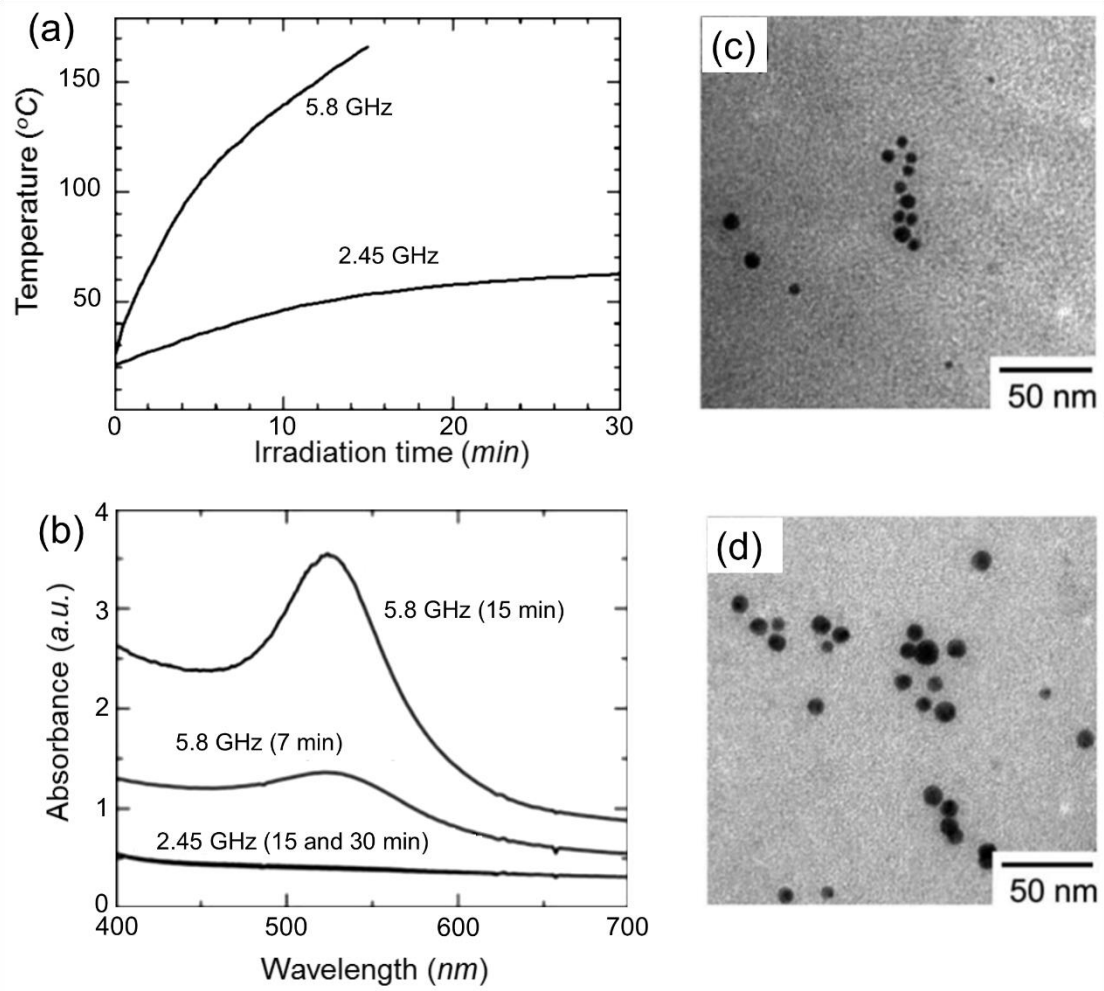

Figure 2-23 a)Temperature increase over time of the organic-based aurochloric acid/oleylamine mixture exposed to 2.45 GHz and 5.8 GHz microwave radiation at 45 W input power. b) UV–vis absorption spectra of the produced gold nanoparticles. c-d) TEM images of the synthesised nanoparticles under 5.8 GHz after 7 min and 15 min residence time indicated, respectively. Adapted with permission from Ref.[58] Copyright 2011 Royal Society of Chemistry.

The use of external cooling jacket, with a “microwave transparent” liquid or gas, could be described as an enhancement in the microwave-assisted synthesis. The cooling liquid could support the temperature control, due to absorbance of heat by the cooling liquid and controlling its flow rate[120] or to reduce the impurities on the reactor wall, by maintaining its temperature lower than that of the bulk. Horikoshi *et al.*[133] studied the synthesis of Ag NPs in batch mode, using three protocols:

i. Microwave heating using 170 W input microwave power without external cooling (MW-170W)
ii. Microwave heating using 170 W input microwave power with external cooling (MW-170W/Cool)

iii. Microwave heating using 390 W input microwave power with external cooling (MW-390W/Cool)

As showed by the results (Figure 2-24), temperature increase was similar for protocols MW-170W and MW-390W/Cool, however the average diameter of the nanoparticles produced in the MW-390W/Cool and MW-170W protocols were 1 – 2 nm and 1.4 – 3.6 nm, respectively and the particle size distribution was narrower during the former protocol. In the MW-390W/Cool protocol the temperature increase was nearly 0.51 ^{o}C/min, while in the MW-170W/Cool protocol, the temperature increase was nearly 0.27 ^{o}C/min and no nanoparticles were formed (Figure 2-24).

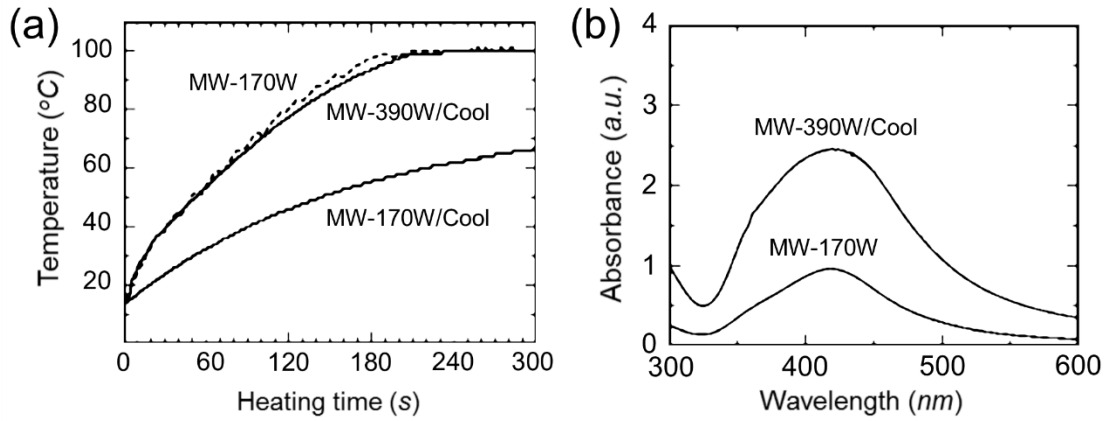

Figure 2-24 a) Temperature–time profiles of the aqueous solution for the synthesis of silver nanoparticles under the studied protocols (MW-170W, MW-170W/Cool and MW-390W/Cool). b) Plasmon resonance absorption of the silver nanoparticles synthesised under the studied protocols (MW-170W and MW-390W/Cool). Adapted with permission from Ref.[133] Copyright 2010 Royal Society of Chemistry.

2.5.2. Examples of continuous nanoparticle synthesis

Microwave heating has been used for nanoparticle synthesis in both batch and continuous flow reactors. The use of “microwave transparent” materials, like PTFE or quartz, allows microwaves to penetrate the medium, while reactor walls do not absorb energy and their temperature remains lower than that of the bulk. The reactor material has been investigated to affect the synthesis in non-polar solvents rather than in “lossy” mediums (i.e polar solvents), due to the temperature increase on the reactor walls, subsequently leading to heating up the “microwave transparent” solvents, interfering with the reaction kinetics and the equilibrium data[130, 146]. Thus, in

microwave-assisted continuous flow synthesis, microwave absorbing solvents build-up in temperature and achieve the desired synthesis in shorter times.

Continuous MW-assisted synthesis has already been examined for metal nanoparticles and nanocrystals fabrications. Nishioka *et al.*[147] examined the fabrication of silver nanoparticles in a single-mode, MW-assisted, coiled-flow, tubular PTFE reactor. They used silver nitrate ($AgNO_3$) and poly(N-vinylpyrrolidone) (PVP) dissolved in ethylene glycol. Outlet temperature was set 160 ^oC and the flow rate varied between 10-600 ml/h, showing that increasing the flow rate, resulted in smaller particles and narrower particle size distributions; the average particle size was 14.3 ± 3.1 nm at 10 ml/h and 9.8 ± 0.9 nm at 100 ml/h. Figure 2-25 shows the UV-Vis spectra of the Ag NPs synthesized by varying the flow rate of reaction solution and the TEM images of the silver nanoparticles synthesized with the above flow rates of 10 ml/h and 100 ml/h. Dzido *et al.*[66] studied the effect of precursor's reactivity in nanoparticle size, using a coiled flow PTFE reactor in a single-mode MW applicator. As they observed, silver acetate led to faster formation of small Ag NPs (10-20 nm) than silver nitrate, due to the former's lower solubility in ethylene glycol which allows separation of *growth* from *nucleation* stage. Tu and Liu[148] used a coiled glass reactor, in a domestic microwave oven for the continuous synthesis of platinum (Pt NPs) and palladium (Pd NPs). The nanoparticles produced at 750 W and residence time 25 s were 1.46 ± 0.25 nm for Pt NPs and 1.50 ± 0.32 nm for Pd NPs. It was also observed that continuous flow synthesis had a positive effect on platinum small size particles comparing to the batch mode synthesis, due to the formation of more crystal nuclei and smaller cluster formation. Bondioli *et al.*[149] studied the formation of zirconium oxide nanoparticles (ZrO_2 NPs) in a multi-mode applicator, by varying the flow rate. Decreasing the flow rate from 100 ml/min to 50 ml/min resulted in larger and more spherical nanoparticles, 10 ± 5 nm and 100 ± 20 nm, respectively.

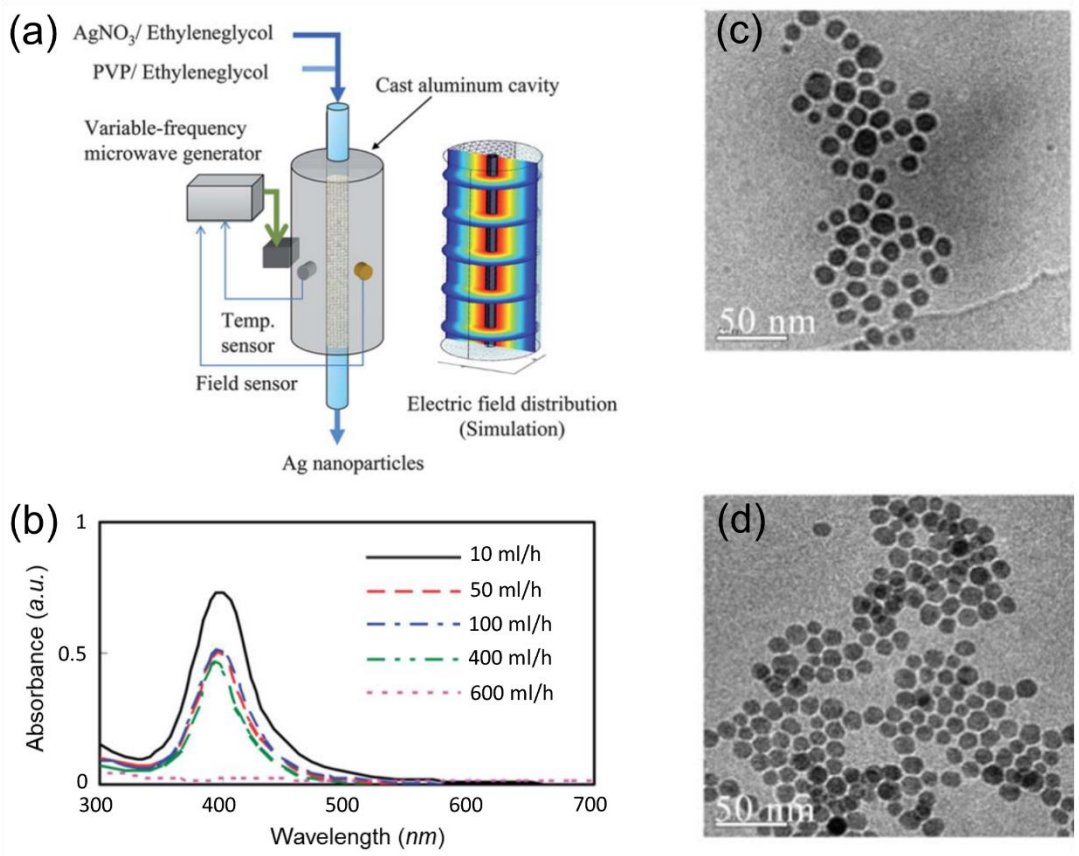

Figure 2-25 a) Schematic of the microwave-assisted flow reactor system. b) UV-Vis spectra of silver nanoparticle synthesized by varying the flow rate of reaction solution and c-d) TEM images of the silver nanoparticles synthesised at 10 ml/h and 100 ml/h flow rates, respectively. Adapted with permission from Ref.[147] Copyright 2011 Royal Society of Chemistry.

The use of a droplet-like segmented flow was also investigated to allow fouling prevention and intensification of the nanoparticle synthesis under microwave heating. Koziej *et al.*[150] studied the use of a segmented microwave-assisted reactor using a PDMS microfluidic device (Figure 2-26) for the synthesis of tungsten oxide nanoparticles (WO_3 NPs). Despite the expected de-polarisation of the electromagnetic field due to the difference in the dielectric properties between the two phases, the proposed set-up showed enhancement of the reaction synthesis, when compared to previously used in-flow reactor. Hostetler *et al.*[140] examined the synthesis of colloidal lead selenide nanoparticles (PbSe NPs) in a two-stage multi-phase continuous flow PTFE reactor (inner diameter: 1.6 mm). Reaction initiation/nucleation started in a single-mode microwave heating (MWH) reactor zone followed by a conventional heating (CH) reactor zone (oil-bath). Varying the input microwave power, the temperature in the MWH zone ranged between 124 – 159 ^{o}C,

while maintaining the temperature at the CH zone constant at 140 ^{o}C. The initial stage of the MWH zone was beneficial for the PbSe NPs synthesis, as increasing the temperature in the MW reactor resulted in smaller nanoparticle sizes (average size decreased from 13.9 nm to 11.2 nm, by increasing the temperature from 124 ^{o}C to 159 ^{o}C), while particle size distribution was constant at ~ 15 – 16 %. Similarly, Kim *et al.*[151] introduced a two-phase flow system using a PTFE milli-scare reactor (inner diameter: 1.59 mm) for the synthesis of ternary $CuInSe_2$ NPs. In their study they introduced argon gas as the segmenting fluid preventing particle deposition on the reactor walls and improving the residence time distribution. Their set-up was based on the hot-injection method, therefore the synthesis was initiated under MWH and completed in a CH reactor at constant temperature (247 ^{o}C) (Figure 2-27). The set-up allowed the synthesis of 14 – 17 nm nanocrystals by varying the reactant molar ratio, while without the growth stage it allowed the production of uniform and small (< 3 nm) quantum dots within 5 s under microwave heating. Table 2-4 summarises the key-findings of the literature case studies of the microwave-assisted synthesis of NPs.

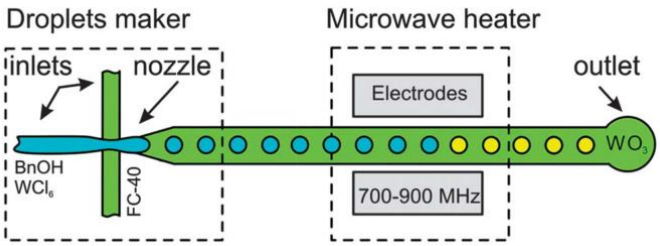

Figure 2-26 Schematic of the two-phase microwave-assisted flow reactor system for the tungsten oxide nanoparticles (WO_3 NPs) synthesis. Continuous phase: fluorinert electronic liquid FC-40 (FC-40 oil), disperse phase: benzyl alcohol droplets. Reprinted with permission from Ref.[150] Copyright 2013 Royal Society of Chemistry.

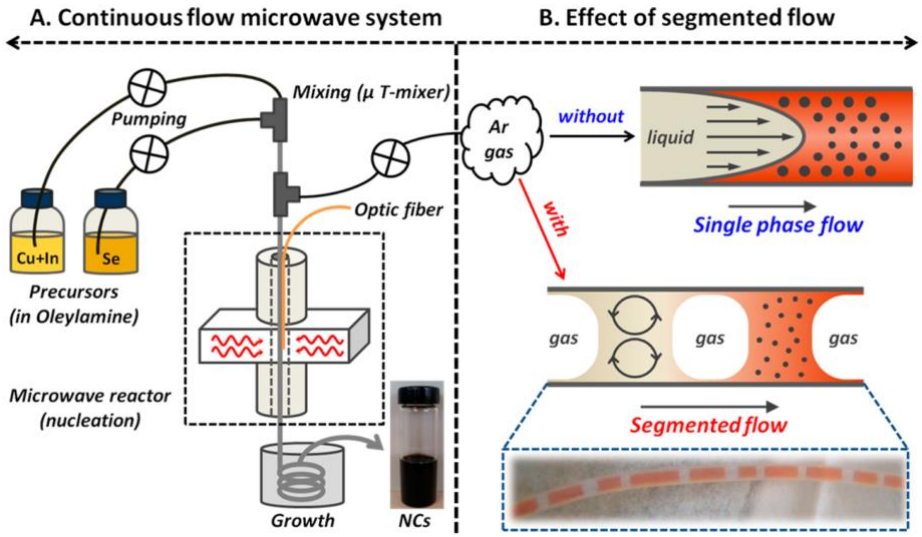

Figure 2-27 Schematic of the *(Left)* two-stage continuous flow system for the $CuInSe_2$ NPs synthesis (nucleation: microwave heating reactor, growth: conventional heating reactor) and *(Right)* the flow profile with (bottom) and without (top) segmented flow using argon gas. Reprinted with permission from Ref.[151] Copyright 2014 American Chemical Society.

Table 2-4 Case studies of continuous nanoparticle synthesis in microwave-assisted reactors.

Reference	Target nanoparticles	Highlights	MW applicator mode
Bondioli *et al.*[149]	ZrO_2 NPs	10 ± 5 nm (at flow rate: 100 ml/min) and 100 ± 20 nm (at flow rate: 50ml/min) Decrease of flow rate resulted in more spherical NPs.	Multi-mode
Dzido *et al.*[66]	Ag NPs	Reactivity of precursors: AgOAc >>$AgNO_3$ AgOAc: 28±0.6 nm (*T*: 150 ^oC), $AgNO_3$: 15-20 nm (*T*: 171 ^oC)	Single-mode
Hostetler *et al.*[140]	PbSe NPs	Two stage synthesis (microwave and conventional heating in series) 13.9 ± 2.1 nm (at MW *T*: 124 ^oC) and 11.2 ± 1.7 nm (at MW *T*: 159 ^oC) In all scenarios: CH *T:* 140 ^oC	Single-mode
Kim *et al.*[151]	$CuInSe_2$ NPs	Two stage segmented-flow synthesis (microwave and conventional heating in series) 16.6 ± 3.2 nm (ratio: Cu/In/Se : 1:1:2, MW residence time: 5s, CH growth time: 20 min) 17.1 ± 2.6 nm (ratio: Cu/In/Se : 1:1:1, MW residence time: 5s, CH growth time: 20 min) 14.3 ± 3.0 nm (ratio: Cu/In/Se : 1:1:1, MW residence time: 5s, CH growth time: 10 min) In all scenarios: MW *T*: 247 ^oC and CH *T* = 210 ^oC	Single-mode
Koziej *et al.*[150]	WO_3 NPs	Electric field intensity: 700 – 900 MHz, MW *T*: 50 ^oC in the droplets, residence time: 64 ms Nanoparticle size < 3 nm (without washing with ethanol)	Single-mode
Nishioka *et al.*[147]	Ag NPs	MW outlet *T*: 160 ^oC 14.3 ± 3.1 nm at 10 ml/h and 9.8 ± 0.9 nm at 100 ml/h Increasing the flow rate, resulted in smaller particles and narrower particle size distributions	Single-mode
Tu and Liu[148]	Pt NPs Pd NPs	Microwave power: 750 W, residence time: 25 s Pt NPs: 1.46 ± 0.25 nm, Pd NPs: 1.50 ± 0.32 nm	Multi-mode

2.5.3. Microwave-assisted gold nanoparticle synthesis

Since the desired properties of the gold nanoparticles are a function of their size and shape there are literature reports concerning the synthesis of spherical and nanorods particles, as well as other crystalline gold nanostructures, including nanogears, nanobelts, icosahedrons and nanoplates[80] using microwave radiation. Kundu *et al.*[152] managed to synthesize in batch, for the first time, gold nanospheres, nanorods and nanoprims of various aspect ratios, in the presence of a cationic surfactant cetyltrimethylammonium bromide (CTAB), using a domestic microwave oven (DMO). As it was observed, precursor concentration, stirring and heating procedures were the key issues for the synthesis of each type. In case of nanospheres, they were produced through seed-mediated growth techniques, by mixing different solutions in different growth steps. The final nanospheres were 40-45 nm in diameter, with the solution exhibiting a plasmon resonance peak at 535-540 nm. Additionally, Tsuji *et al.*[116] studied the parameters affecting the formation of spherical, single crystalline polygonal plates, sheets, rods, wires, tubes, and dendrites nanoparticles, in rapid MW-assisted synthesis in batch. They managed to produce triangular and polygonal nanoplates when used $HAuCl_4$ reduced in ethylene glycol (EG) and PVP at 198 ^{o}C. To examine if non-thermal effects were responsible, they duplicated the same procedure using MW heating of either continuous wave or a pulse-mode and an oil-bath. According to TEM images obtained for the three procedures, it was shown that all three had the same types of nanoplates and spherical nanoparticles. However, in the MW heating of continuous wave the nanospheres were smaller than the ones during oil-bath heating (approx. 100-190 nm), similarly to the pulse-mode MW heating (approx. 120-160 nm).

Ngo *et al.*[15] and Seol *et al.*[52] studied the fabrication of Au NPs using the citrate method (*Turkevich method*), in batch mode, however the former used a multi-mode applicator while the latter a single-mode. Both tests show similar results, a LSPR peak at approx. 520 nm. Seol *et al.*[52], managed to synthesize spherical Au NPs of 12.04 ± 1.35 nm, maintaining uniform temperature profile by adjusting the microwave power and keeping pH above 6.1. In that way they maintained uniform temperature profiles which is suggested as a key-factor for particle size distribution[153] (Figure 2-28). The study of Ngo *et al.*[15] indicate the formation of spherical uniform nanoparticle 14.0 ± 3.0 nm in size, based on UV-Vis and TEM data, while zeta-potential test indicated negative charges on the Au NPs surface (-23.9 mV), due to the presence of citrate, which acts as both reducing and stabilizing agent.

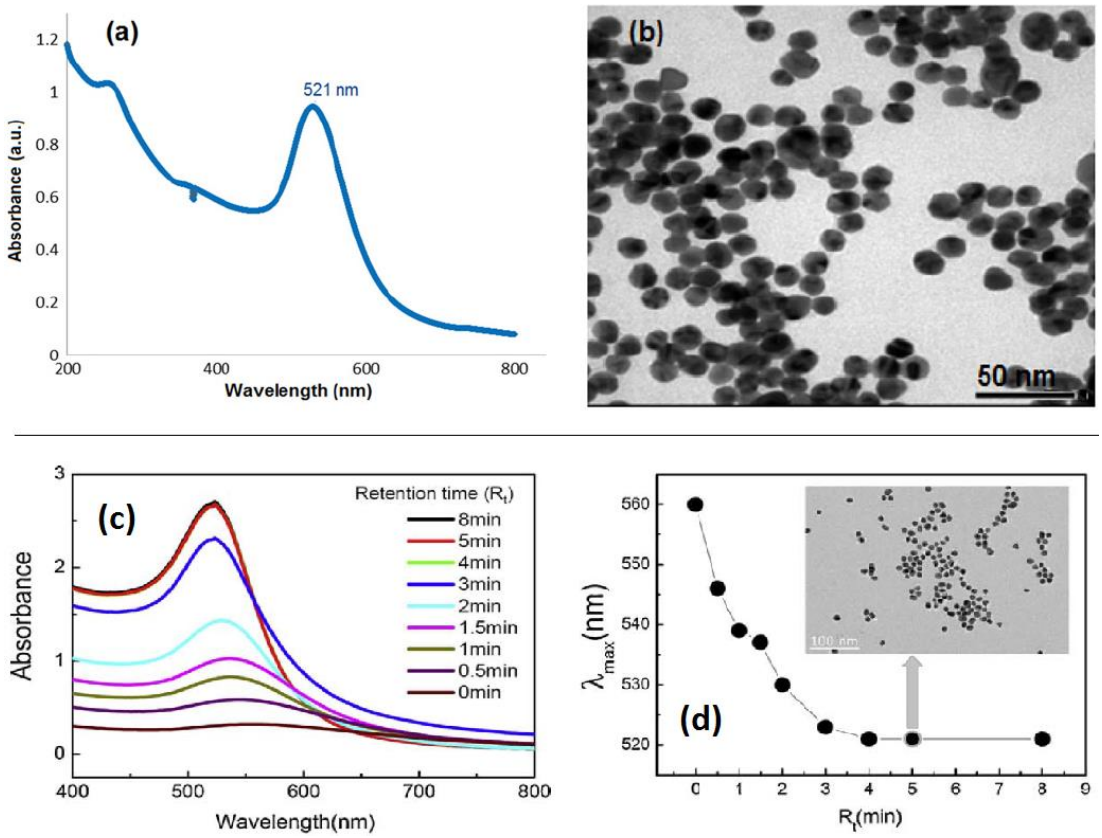

Figure 2-28 Microwave-assisted AuNPs synthesis. (a-b): a) UV–vis absorption spectra, b) TEM images and of synthesized AuNPs by microwave heating (adapted with permission from Ref.[15] (doi: 10.1088/2043-6262/6/3/035015) under Creative Commons Attribution 3.0 licence. Copyright 2015 IOP Science. (c-d): c) UV–Vis absorption (temperature ~ 95 ^{o}C, temperature ramping rate ~ 157.5 ^{o}C/min), d) TEM image of the synthesized colloidal AuNPs after residence time ~ 5 min (adapted with permission from Elsevier and Copyright Clearance Center. Ref.[52] Copyright 2011).

Uppal *et al.*[154] examined the effect of $[HAuCl_4]/[Na_3Ct]$ ratio (*Turkevich* method) on nanoparticle size and compared microwave-heating synthesis with sonolysis, UV-Vis light and themal (conventional) heating methods. Their findings suggest the importance of citrate in reduction synthesis[38, 75], while the increase of citrate in the solution resulted in reducing the mean diameter of the nanoparticles down to approx. 11 nm. Results were similar to that of conventional heating (11.0–11.9 nm). UV-Vis spectra, comparing microwave and conventional heating, suggested similar results, as the SPR peak was around 519 – 520 nm. It was suggested that microwave heating was more efficient and rapid but could not explain the low tendency to the formation of small spherical nanocrystals and tetrachloroauric acid consumption, assuming that reduction and growth mechanism were taking place simultaneously on

one site. Table 2-5 summarises the key-findings of the literature case studies of the microwave-assisted synthesis of Au NPs.

Table 2-5 Case studies of gold nanoparticle synthesis in microwave-assisted reactors in batch.

Author	Method	Results	MW Mode	Evaluation Technique
Tsuji *et al.*[116]	$HAuCl_4$ and PVP	Nanoparticles: spherical, triangular, square, pentagonal, and hexagonal nanoplates. Diameters or edge lengths of 30–90 nm	Multi-mode	UV-Vis, TEM
Kundu *et al.*[152]	$HAuCl_4$ and PVP	Spherical NPs : 5–25 nm (MW power: 1000 W, RT: 5-60 s)	Multi-mode (DMO)	UV-Vis, TEM
Uppal *et al.*[154]	*Turkevich method*	Spherical NPs: 11.3 – 17.2 nm Preparation of 4 different solutions ($[HAuCl_4]/[Na_3Ct]$ ratio) Comparison with sonolysis, UV light and themal heating methods	Multi-mode (DMO)	UV-Vis, TEM
Seol *et al.*[52]	*Turkevich method*	Spherical NPs: 12.04 ± 1.35 nm Increase of heating or pH produce more uniform and spherical NPs. Isothermal conditions, by adjusting the MW power	Single-mode	UV-Vis, TEM
Ngo *et al.*[15]	*Turkevich method*	Spherical NPs: 14 ± 3 nm Uniform temperature distribution narrows the PSD	Multi-mode	UV-vis, TEM Zeta-potential

RT: Residence time, **DMO:** Domestic microwave oven, **UV-Vis:** Ultraviolet-visible spectrometry, **TEM:** Transmission electron microscopy.

CHAPTER 3. Experimental and computational investigation of heat transfer in a microwave-assisted flow system*

Various operational parameters - microwave power, inlet flow rate, tube orientation and pressure – were examined and the investigation concerned their effect on the electric field and temperature profiles of water flowing in a PTFE tube (2.4 mm internal diameter), placed in a commercial single-mode microwave applicator. A finite element model was developed to estimate the longitudinal temperature profiles and the absorbed microwave power, while *in situ* temperature monitoring was performed by a fibre optic probe placed at multiple locations inside the tube. The water temperature inside the tube increased by increasing the microwave power input and temperature profiles stabilised beyond 20 W, while the percentage absorbed microwave power showed the inverse trend. When changing the tube orientation or decreasing the inlet flow rate, microwave absorption decreased significantly. When the pressure was increased to 2.3 bara, water temperature increased by ~ 20 ^{o}C. Results from this study provide valuable insights on achievable temperature profiles and energy efficiency of microwave-assisted flow synthesis systems.

* This chapter has been published in *Chemical Engineering and Processing - Process Intensification*:
S. Damilos, A. N. P. Radhakrishnan, G. Dimitrakis, J. Tang and A. Gavriilidis, *Chemical Engineering and Processing - Process Intensification*, 2019, 142, 107537.

3.1. Introduction

Microwave heating has been studied over the past decades as an alternative to conventional heating. The main advantages of microwave technology are rapid heat transfer, selective heating (depending on the dielectric properties of the medium), superheating of the solvents and providing a renewable and sustainable heating source, since electricity can be sourced from renewable means[54]. These advantages have made microwave heating attractive in various areas including organic and polymerisation reactions[60, 134, 155], bioelectromagnetic studies[156], food processing[121], nanoparticle synthesis[75, 119], catalytic processes[120, 157], adsorption processes[158], reactive distillation[159] and microreactor processing[138, 160, 161]. Microwave heating is generally described as volumetric heating in nature, as it usually takes place over the entire workload volume and depends on the dielectric properties of the medium, which are also a function of temperature and frequency[115]. Therefore, for certain conditions and dielectric property values, microwave energy is deposited directly into the entire workload volume and the heating mechanism is not driven by conduction and convection, as in conventional heating[59, 119]. Microwave and conventional heating can be combined by exploiting the rapid energy transfer of microwave power and the readily-controllable heat exchange by conventional heating to maintain the targeted temperature[120]. An interesting feature of this technology is the inverse temperature profile inside the heated medium[60], which is due to the temperature gradient between the medium and the container and the heat loss to the surrounding medium. When the container dimensions are smaller or comparable to the microwave penetration depth, the cross sectional temperature distribution could be uniform. Microwave heating has also received attention for large-scale or industrial systems, aiming to intensify chemical processes[158, 162]. This task requires optimisation of the microwave cavity for the targeted application, along with the microwave generators and the available reactors, to couple the electromagnetic phenomena with the heat generation in the scaled-up system[162].

Temperature distribution in a medium subject to microwave heating depends on the electromagnetic field. In the case of micro-reactors and milli-reactors, the penetration depth - the distance from the medium surface, to the point where the microwave power drops to ~ 37 % of the initial value at the surface - is much larger than the tube diameter[114]. Thus, microwave heating can be assumed to be homogeneous in the

cross section and the spatial distribution of the electromagnetic field is described by Maxwell's equations. In this chapter, the effects of various operational parameters on the temperature profile were investigated numerically and experimentally in a milli-scale tube placed in a commercial single-mode microwave applicator. An FEM model was developed to simulate the temperature and electric field profiles along the tube length and the absorbed microwave power and used it to study the effect of various operating parameters.

3.2. Experimental section

3.2.1. Materials & methods

Ultra-pure water (15 MΩ·cm) was used for all experiments. PTFE tubes (1 mm I.D., VICI Jour) were used for all fluidic parts and polyether ether ketone (PEEK) ferrules and fittings (Upchurch) were used for all connections. Dielectric constant and dielectric loss of water were experimentally evaluated for the temperature range 20-95 ^{o}C at atmospheric pressure, following the methodology previously described in literature[146], and are shown in Table A-1 (Appendix A). The measurements showed that the water dielectric properties were almost constant for each measured temperature between 2.45 GHz and 2.47 GHz, which is within the magnetron specifications. PTFE was assumed to be microwave transparent in the studied conditions ($\varepsilon_{r,PTFE} = 2.1 - 0j$)[115].

3.2.2. Experimental set-up

A commercial single-mode microwave applicator (Discover SP, CEM) was used for microwave generation. A U-shape tube (VICI Jour) of total volume 0.75 ml (inner diameter, I.D. 2.4 mm, outer diameter, O.D. 3.175 mm, length: 165 mm) on a flat-plate support structure was placed into the microwave cavity, allowing entrance and exit of the flowing medium from the top. The tube and the support structure were made of polytetrafluoroethylene (PTFE), which is considered a "microwave transparent" material due to its low dielectric loss factor. The input power ranged from 5 W to 35 W. The effect of the U-shape tube orientation on the temperature profile was studied by placing the support structure parallel and perpendicular to the microwave port, hereafter referred as "parallel-to-port" and "perpendicular-to-port", respectively. The flow rates of water were 0.5 ml/min, 0.7 ml/min and 1.5 ml/min,

resulting in mean residence times of 0.5-1.5 min, and were controlled using syringe pumps (Legato 270P, KD Scientific) with 25 ml glass syringes (25MDR-LL-GT, Scientific Glass Engineering). The pressure inside the tube was regulated with a K-type backpressure regulator (maximum 4 barg, Swagelok). Immediately after switching on the microwave power, the temperature rapidly increased and reached the target temperature, but extra time was allowed before taking the temperature readings (5 min) in order to ensure there were no temperature fluctuations over time. Temperature was monitored via a fibre optic temperature sensor (O.D. 1.7 mm, T1s, Neoptix) with direct temperature measurements at 5 different positions throughout the tube length. The fibre optic sensor was inserted from the tube outlet, to avoid flow disturbances and measurement inaccuracy[59]. Temperature measurements were performed at 36 mm (point 1), 70 mm (point 2), 83 mm (point 3), 95 mm (point 4) and 135 mm (point 5) from the tube inlet (point 0) (see Figure 3-1).

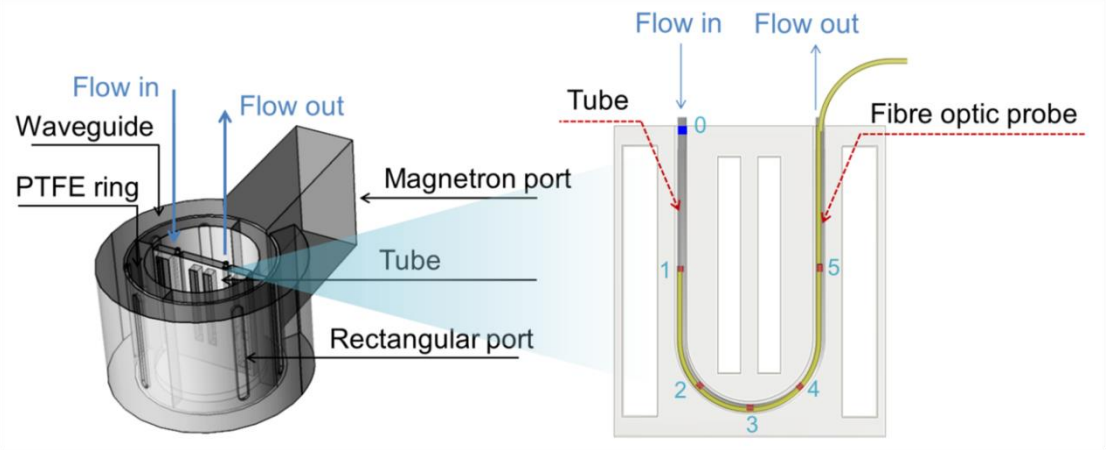

Figure 3-1 (Left) schematic of inner parts of the CEM Discover SP microwave applicator. (Right) the tube with the PTFE support structure. The tube is displayed in grey colour and the fibre optic temperature probe is displayed in yellow colour. The blue mark indicates the tube inlet (point 0) and the red marks indicate the points of temperature measurements made by inserting the probe from the tube outlet (point 1: 36 mm, point 2: 70 mm, point 3: 83 mm, point 4: 95 mm, point 5: 135 mm from tube inlet). Images are not to scale.

3.3. Mathematical model development

The model geometry is a representation of the geometrical features of the single-mode microwave applicator, as shown in Figure 3-1. The microwave generator

utilised a magnetron set at 2,460 MHz (+/- 10 MHz) having microwave power range 1-300 W. The computational modelling considered only the cavity and the tube with the support structure. The cavity was made of stainless steel and contained a PTFE protective ring. Within the metallic cavity there were 6 rectangular ports, providing uniform electromagnetic field to the load placed in the cavity. The geometry of the applicator and the tube are displayed in Figure 3-1.

The analysis of the electromagnetics and heat transfer in the system was carried out in COMSOL Multiphysics software (v.5.3a, COMSOL Inc.), similar to the methodology described by Sturm *et al.*[123], and computational analysis was divided into two steps. A diagram of the interconnected computational steps is shown in Figure 3-2. In the first step, the Helmholtz representation of Maxwell's electromagnetic field equation was solved (see Equation 3-1) using the Electromagnetic Waves module for the estimation of the electric field throughout the length of the tube, by keeping the dielectric properties (dielectric constant ε' and dielectric loss ε'') of water constant at 20 ^{o}C (Figure 3-2, Step 1) including all domains (the metal cavity, the contained PTFE protective ring, air, the PTFE support structure, the PTFE tube and the water flowing inside the tube). The Helmholtz representation of Maxwell's electromagnetic field equations is described by[163]:

$$\nabla^2 \boldsymbol{E} + \varepsilon_r \left(\frac{2\pi f}{c}\right)^2 \boldsymbol{E} = 0 \qquad \text{Eq. 3-1}$$

where $\boldsymbol{E}$ is the electric field vector of the time-harmonic oscillating microwave field, f is the frequency of the electromagnetic field, c is the speed of light in vacuum and ε_r is the relative complex permittivity, which consists of the dielectric constant ε' and dielectric loss ε'' ($\varepsilon_r = \varepsilon' - j\varepsilon''$). ε' is dependent on the material and describes its potential to store the microwave energy and thus be polarized by the electromagnetic field. ε''describes the efficiency of the material in converting electromagnetic energy into heat. The higher the dielectric loss, the higher is the amount of electromagnetic energy which is converted into heat (i.e., leading to a higher final temperature).

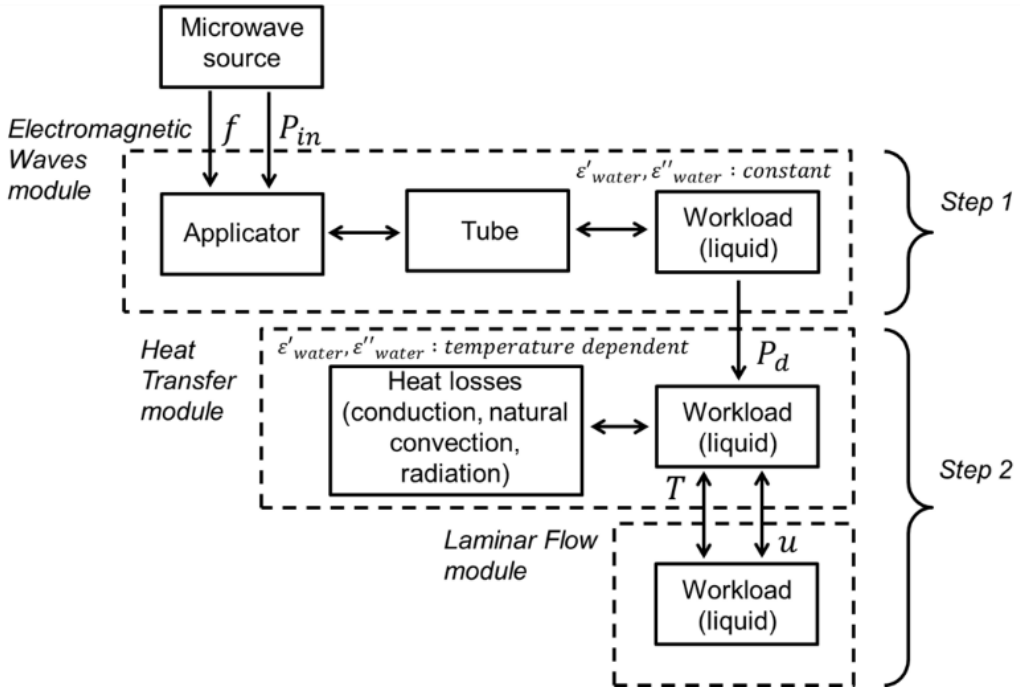

Figure 3-2 Diagram of the interconnected modules and variables for the two steps of the Finite Element Method model developed in COMSOL Multiphysics. In Step 1, the Electromagnetic Waves module computed the electric field profile throughout the tube length. In Step 2, the Heat Transfer and Laminar Flow modules were coupled for the computation of temperature profile. The microwave power density in Step 2 was calculated as a function of the electric field output from Step 1.

No fluid flow was taken into account at Step 1. Due to the difference in transmitted and reflected microwave energy[123] and the lack of control over matching impedance, a parametric sweep over the magnetron frequency was conducted under the respective experimental conditions. The parametric sweep was performed over the frequency of the magnetron which varied between 2,450 MHz and 2,470 MHz at a 5 MHz step, for each microwave power. In the second step, Fourier's heat transfer and Navier-Stokes equation were solved (see Equations 3-2 and 3-3, respectively) – by coupling the Heat Transfer and the Laminar Flow modules – for the computation of the temperature profile of water in the tube, for the corresponding laminar flow conditions (Figure 3-2, Step 2). Fourier's heat transfer equation is described by[117, 122]:

$$\rho C_p(\boldsymbol{u} \cdot \nabla T) = \nabla Q + P_d \qquad \text{Eq. 3-2}$$

Where ρ is the density, Cp is the specific heat capacity, Q is the heat flux, $\boldsymbol{u}$ is the fluid velocity field vector inside the tube, T is the temperature and P_d is the microwave power density. The term on the left hand side describes the contribution of convection to heat transfer. The first term on the right hand side describes the contribution of conduction to heat transfer and the second term is the heat generation in the medium.

The fluid flow profile was computed using the Laminar Flow module, as shown in Step 2 (Figure 3-2), by solving the momentum balance equation (incompressible Navier–Stokes equation) described by[164]:

$$\rho[\boldsymbol{u} \cdot \nabla \boldsymbol{u}] - \eta \nabla \cdot [\nabla \boldsymbol{u} + (\nabla \boldsymbol{u})^T] + \nabla p = 0 \qquad \text{Eq. 3-3}$$

and the continuity equation for incompressible fluids:

$$\rho(\nabla \cdot \boldsymbol{u}) = 0 \qquad \text{Eq. 3-4}$$

Where ρ is the density of the medium, η is the dynamic viscosity, $\boldsymbol{u}$ is the fluid velocity field vector, T is the temperature and p is the pressure. The first term in the momentum balance equation is the inertial forces, the second term is the viscous forces and the third term is the pressure gradient. No slip boundary condition was set on the inner tube wall in contact with the liquid. Temperature and fluid velocity were obtained via the coupled calculation in Step 2 between Heat Transfer and Laminar Flow module (Figure 3-2). The values of the various parameters used in the simulations are given in Table A-3 in the Appendix A.

Heat losses were also taken into account. The heat flux through the tube wall and support structure is given by Equation 3-5, while the heat loss to the ambient environment due to natural convection and radiation is given by Eq. 3-6:

$$Q = k \nabla T \qquad \text{Eq. 3-5}$$

$$Q = h_{air}(T_{air} - T) + \varepsilon\sigma({T^4}_{air} - T^4) \quad \text{Eq. 3-6}$$

Where ρ is the density, Cp is the specific heat capacity, Q is the heat flux, $\boldsymbol{u}$ is the fluid velocity field vector inside the tube, T is the temperature, P_d is the microwave power density, k is the thermal conductivity, T_{air} is the air ambient temperature, h_{air} is the heat transfer coefficient for natural convection, ε is the surface emissivity and σ is the Stefan–Boltzmann constant.

Temperature rise in the medium depends on the coupling of Maxwell's equations and Fourier's heat transfer equation. The microwave power density in the medium is described by[115, 123]:

$$P_d = 2\pi f \varepsilon_o \varepsilon'' |\boldsymbol{E}|^2 \quad \text{Eq. 3-7}$$

Where ε_o is the electric permittivity of vacuum, f is the frequency of the electromagnetic field, ε'' is the dielectric loss and $|\boldsymbol{E}|$ is the electric field intensity.

The model assumptions and boundary conditions for Step 1 are included in Section A.3 in Appendix A. The water thermal properties and other parameters used in the model are provided in Tables A-3 and A-4 in Appendix A.

Varying electric field profiles for each set of microwave power and respective magnetron frequency (from the parametric sweep) were obtained in Step 1 and used in Step 2. The magnetron frequency which resulted in the highest power absorption was estimated by comparing the experimental and computational results of the temperature for each set of frequencies; the frequency value at which we observed maximisation of the absorbed microwave power and minimum discrepancy between experimental and computational results was denoted as the optimum magnetron frequency, and was found to be 2.47 GHz for all cases. For the three different flow rates studied, the Reynolds number for water at 20 ^{o}C was in the range 4.96-14.9, confirming the existence of laminar flow in the U-shape tube.

Meshing for Step 1 was set at "Coarse" (element size max: 16.5 mm, min: 5.07 mm) for the metal cavity, the contained PTFE protective ring and the air domains, "Fine"

(element size max: 6.71 mm, min: 1.27 mm) for the PTFE support structure and the PTFE tube, and “Extra fine” (element size max: 2.91 mm, min: 0.19 mm) for the water flowing inside the tube, resulting in 1,442,208 elements. The simulations were carried out in “Frequency Stationary” mode, as steady state conditions were assured during the experimental procedure. Meshing for Step 2 was set at “Fine” (element size max: 6.71 mm, min: 1.27 mm) for the PTFE support structure and the PTFE tube, and “Extra fine” (element size max: 2.91 mm, min: 0.19 mm) for the water flowing inside the tube, resulting to 356,826 elements. The computer used was equipped with an Intel® Xeon® CPU E5-2637 V3, at 3.50 GHz (2 processors), with 192 GB RAM, running on 64-bit Windows® Server 2016. Total simulation time was ca. 26 min for both Step 1 and Step 2. Calculations using finer meshing showed that results were mesh-independent.

3.4. Results & discussion

3.4.1. Influence of process parameters on temperature profile

The microwave field is influenced in general by the dielectric properties of the materials used, the level of the microwave power and the flow conditions. These interactions result in different temperature profiles throughout the tube length which affect the reaction rates. Microwave power, flow rate and tube orientation with respect to the microwave port were investigated for their effect on the temperature profile over the tube length. Finally, the effect of system pressure on dielectric properties and temperature profiles was investigated, since elevated pressures, commonly used in chemical syntheses, increase the boiling point of the liquid in the system.

3.4.1.1. Effect of microwave power on temperature profile

Figure 3-3 shows the temperature profile in the centre of the tube along its length, at different input microwave powers. All experiments were conducted at atmospheric pressure and for that reason maximum temperature achieved experimentally was around 100 ^{o}C (boiling point of water). For the cases of 25 W, 30 W and 35 W, the maximum temperature reached 100.8 ± 0.5 ^{o}C, exceeding that of water boiling point. Although this could be related to a slight increase in the ambient pressure – which could affect the boiling point of the medium – previous studies have also discussed

the superheating effect of water under a microwave field, due to lack of bubble nucleation sites in case of smooth surfaces, resulting in a small increase in the boiling point[135, 136]. Increasing microwave power from 5 W to 35 W resulted in temperature profiles with similar trends, despite the higher energy intensity. Comparing the experimental temperature profiles between 5 W to 15 W, an upward trend for the same measurement positions can be observed (Figure 3-3a). Close to the outlet of the tube (at point 5), there was a ~ 30 ^{o}C increase when the microwave power increased from 5 W to 15 W. However, when increasing microwave power from 20 W to 35 W, there was no further temperature increase at the same measurement positions (Figure 3-3b). This behaviour can be explained by the absorbed microwave power being similar at different microwave power inputs, as described in Section 3.4.2.2. Note that for 15 – 35 W input power, the temperature at point 5 varied between 87-89 ^{o}C and it was lower than the maximum temperature measured in the middle of the tube (Figures 3-3a and 3-3b). Reasons for the observed temperature drop were the heat losses via conduction (to the exterior of the PTFE tube and the support structure), radiation and natural convection, as well as the lower electric field intensity towards the outlet of the tube[165]. Another factor contributing to this temperature drop was phase change. When water reached the boiling point – as described above – in the middle of the tube, vapour bubbles formed, which have different dielectric properties than liquid water[166], and reflected the microwave radiation, subsequently leading to perturbation of the electric field[131].

Although there was satisfactory agreement between experimental and computational results, discrepancies were observed. The longitudinal temperature profile provided by the FEM model was similar – qualitatively – to the temperature trend across the tube length obtained by the experimental measurements. As shown in Figure 3-3, both in the experimental and computational results, there was a steep increase in temperature across the tube length (from the tube inlet to the centre) followed by rapid drop. Following the parametric study on the magnetron frequency, the optimum magnetron frequency was 2.47 GHz, resulting in maximum microwave power absorbance and minimum difference between experimental and computational results on the temperature profile. The FEM model underestimated the temperature close to the inlet (point 1) by ~ 2.5 ^{o}C up to 25 W and it increased in the middle of the tube (points 2 – 4) varying between 1.5 ^{o}C (30 W) to 25 ^{o}C (15 W). The difference between experimental and numerical results was similar as previous literature models – where the reported discrepancies varied between 5 – 20 ^{o}C[120, 125, 146] –

showing that the developed model was satisfactory for the evaluation of the longitudinal profile.

The observed discrepancies by the developed model were not constant throughout the tube length, but varied with microwave power and position in the tube, related to the non-uniform longitudinal electric field leading to non-isothermal heating (see Section 3.4.2). They could be associated with unstable magnetron behaviour due to overheating and the effect of reflected microwaves on applicator cavity and the magnetron[61, 123]. Salvi *et al*.[125] observed that FEM modelling overestimated the temperature of the medium both at the centre and the walls of the tube, and attributed the latter to high electromagnetic density as a result of zero liquid velocity (no slip boundary condition) imposed on the walls. It is worth noting in order to improve the prediction of the temperature profile in this analysis, the coupling of the Electromagnetic and Heat Transfer module in the FEM model was performed on the 3-dimensional electric field intensity inside the water phase and not only on the longitudinal electric field profile in the centre of the tube. Regarding phase change and subsequently bubble formation, Salvi *et al.*[125] modified their model to account for this phenomenon and their model seemed to overpredict the temperature at higher temperature regions. In our study, we accounted for phase change by assuming the dielectric loss of water $\varepsilon'' = 0$ when the temperature reached 100 ^{o}C at 1 bara, and therefore no microwave absorption occurred. Experimentally, bubbling was observed from 95 ^{o}C and hence ε'' values were measured only up to 95 ^{o}C (see Table A-1, Appendix A). Therefore, in the FEM modelling a linear interpolation was performed by COMSOL software between ε'' at 95 ^{o}C (where bubbling occurred experimentally) and $\varepsilon'' = 0$ at 100 ^{o}C.

Cherbański and Rudniak[126] also discussed the sources of the discrepancies between experimental and computational results. According to their study, the shift in the magnetron frequency was the primary parameter affecting the experimental results. The type of the fibre optic sensor and the assumption of constant dielectric properties could enhance the observed discrepancies. However, Robinson *et al.*[146] examined the effect of a fibre optic probe in batch conditions, showing negligible changes on electric field distribution because of the probe. We compared the simulated temperature profiles with and without the fibre optic, and even though the fibre optic

affected the electric field intensity locally, the temperature profile was not affected (see Figures A-2 and A-3, Appendix A).

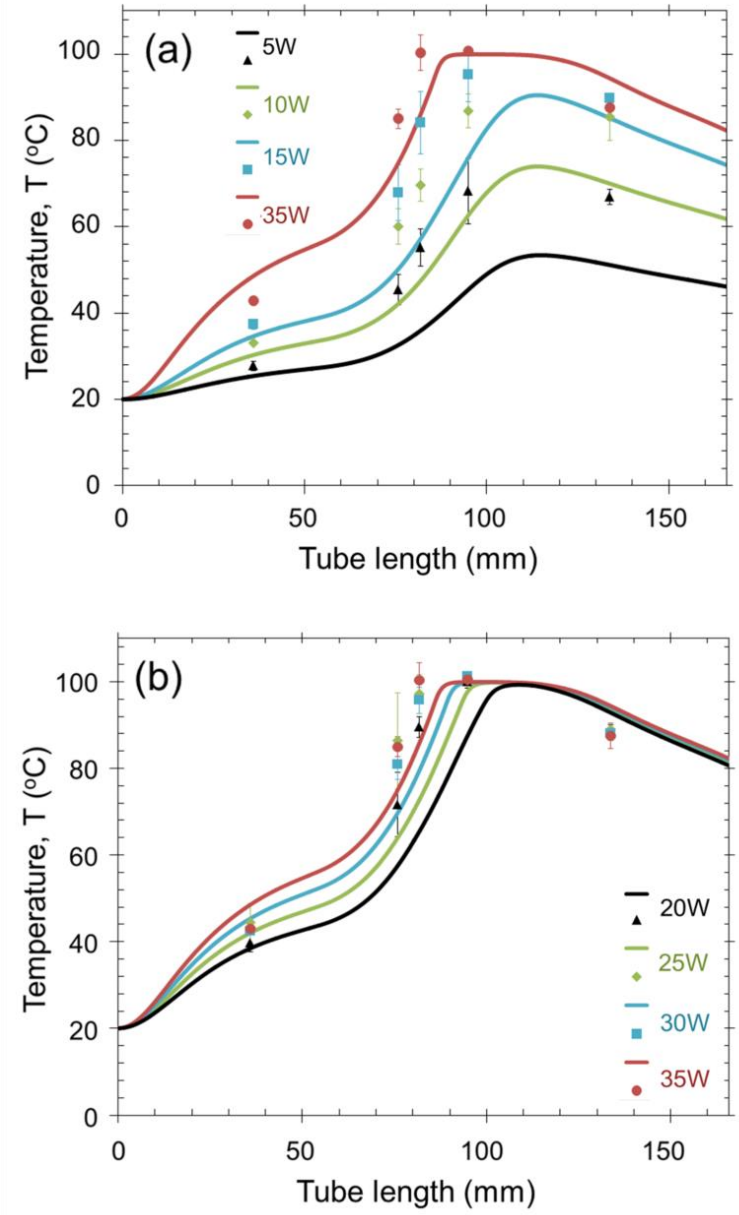

Figure 3-3 Experimental and computational results of the temperature profile inside the tube, when varying microwave power a) 5-35 W, b) 20-35 W. Flow rate, 0.7 ml/min; tube orientation: parallel-to-port; system pressure, 1 bara; frequency, 2.47 GHz (marks: experimental results; lines: computational results). Error bars correspond to the standard deviation of three experimental measurements at each point. Computational results correspond to the temperature profile in the centre of the tube (water domain).

3.4.1.2. Effect of tube orientation on temperature profile

Tube orientation was studied by placing the tube assembly parallel (parallel-to-port) and perpendicular (perpendicular-to-port) to the microwave port, as shown in Figure 3-4.

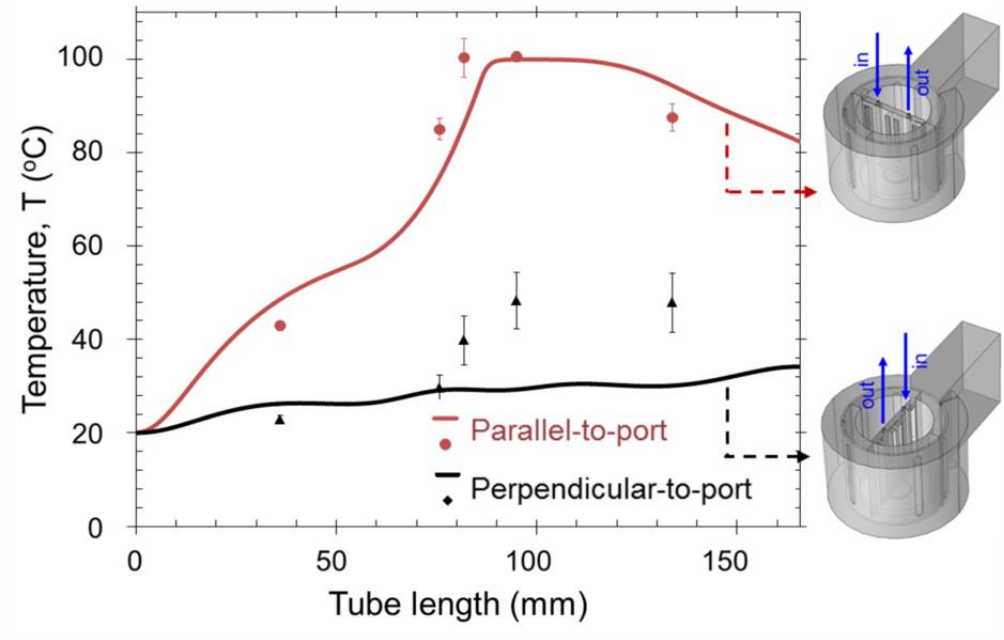

Figure 3-4 Experimental and computational results of the temperature profile inside the tube, when varying the tube orientation. Flow rate, 0.7 ml/min; microwave power, 35 W; system pressure, 1 bara; frequency, 2.47 GHz (marks: experimental results; solid lines: computational results). Error bars correspond to the standard deviation of three experimental measurements at each point. Computational results correspond to the temperature profile in the centre of the tube (water domain).

The temperature profile inside the tube was affected by the orientation of the tube with respect to the microwave port, leading to a 50 ^{o}C difference in the maximum temperature reached (Figure 3-4). Morgan *et al.*[131] discussed the effect of the depolarisation of the electric field when the microwave radiation crosses the boundaries of materials of different dielectric properties, as well as its dependence on the material geometry and orientation in the cavity. In our study, the maximum unperturbed electric field intensity was observed in the centre of the applicator (Figure 3-5a) and for this reason the tube was placed in the centre of the cavity, similar to previous studied microwave-assisted syntheses for maximum microwave power absorbance[156]. Due to the geometrical characteristics of the cavity of the

Discover SP – considering the 6 rectangular ports on the metallic cavity – both straight inlet and outlet parts of the U-shape tube were always parallel to the sidewalls of the cavity whereas a minor area of the curved part was parallel to port. Therefore, the observed differences on the temperature profile and heating rate were the result of the interaction of the U-shape tube with the minima and maxima of the resonant electric field. These interactions of the tube with the electric field affected the temperature profile experienced by the liquid. Figure 3-5b and 3-5c show the different electric field profiles inside the tube when placed in parallel-to-port and perpendicular-to-port orientation, respectively.

The microwave power density was one order of magnitude higher when the tube was placed parallel-to-port (Figure 3-6a), instead of perpendicular-to-port (Figure 3-6b). In parallel-to-port orientation, the maximum power density was located at the curved part of the tube, which was parallel to the applied field, resulting in the maximum observed temperature. Considering the electric field profiles and the microwave power density along the tube, changing the tube orientation to perpendicular-to-port position resulted in significant depolarisation which lessened the heating efficiency, as described by Morgan *et al.*[131]. Experimental results of the temperature profile for perpendicular orientation showed a steep increase in the middle of the tube, while the temperature profile obtained from the simulations for the same conditions showed a steady temperature increase throughout the tube length (see Figure 3-4). The temperature difference between experimental and computational results in the perpendicular-to-port orientation, was between 0.3 – 18.8 ^{o}C, which was comparable to that in the parallel-to-port orientation (0.7 – 26.9 ^{o}C).

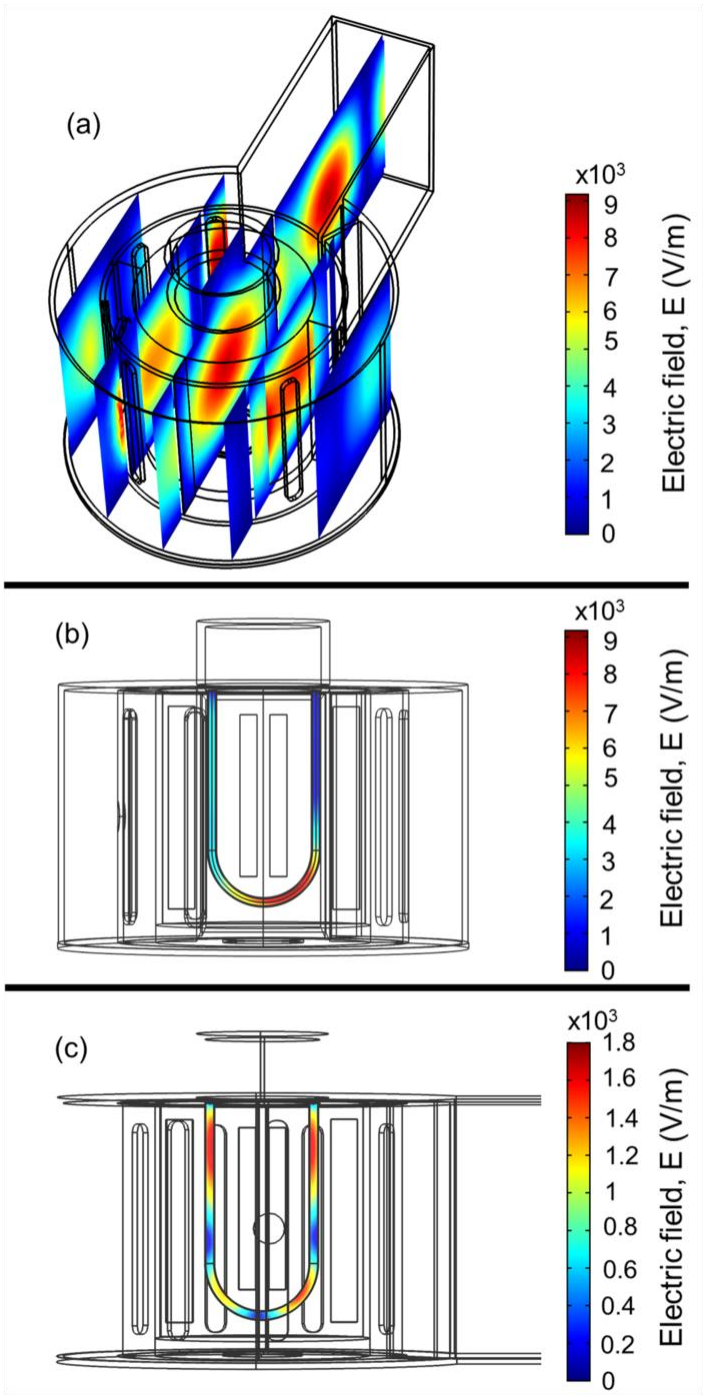

Figure 3-5 Electric field maps inside the a) empty cavity and the tube for b) parallel-to-port and c) perpendicular-to-port tube orientation inside the microwave cavity. Flow rate, 0.7 ml/min; microwave power, 35 W; system pressure, 1 bara; frequency, 2.47 GHz.

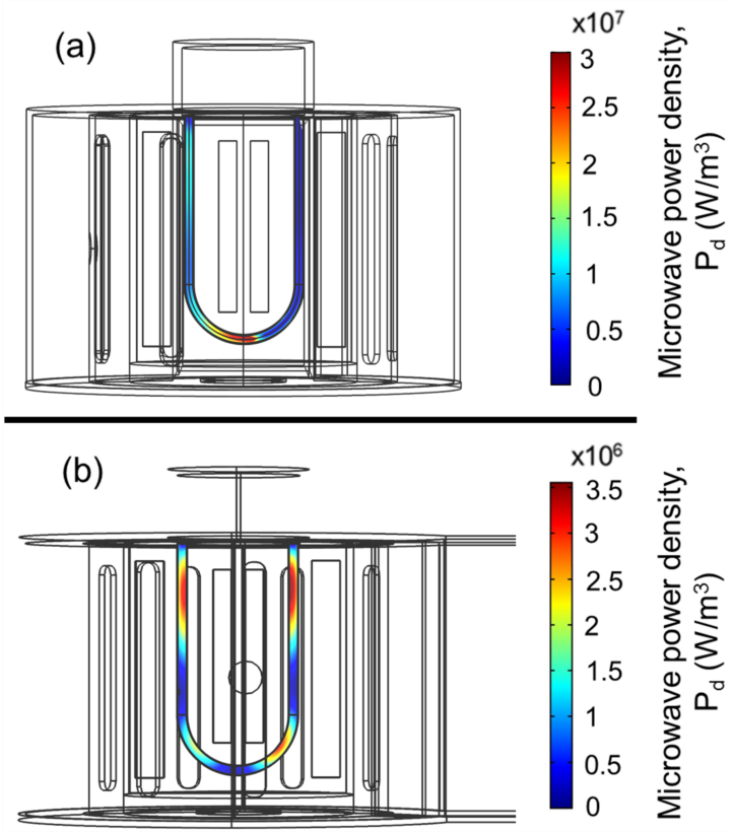

Figure 3-6 Microwave power density inside the tube for a) parallel-to-port and b) perpendicular-to-port tube orientation inside the microwave cavity. Flow rate, 0.7 ml/min; microwave power, 35 W; system pressure, 1 bara; frequency, 2.47 GHz.

3.4.1.3. Effect of inlet flow rate on temperature profile

Microwave heating is related to the volume of the workload (volume of the medium) under the electromagnetic radiation and consequently the volumetric flow rate or the residence time of the medium[114, 115]. The effect of medium velocity was studied by varying the inlet flow rate from 0.5 ml/min to 1.5 ml/min and the results are shown in Figure 3-7. It has previously been shown that increasing the flow rate of the medium results in decreasing temperature at the outlet, due to the volumetric nature of the microwave heating[122]. Salvi *et al.*[165] increased the tap water flow rate by 2–fold in a vertical tube, resulting in a gradually decreasing temperature in the centre of the tube. In this study, the effect of residence time on the axial temperature profile was examined by increasing the flow rate of water by 3-fold at atmospheric pressure, under constant microwave power at 35 W and parallel-to-port orientation. Decreasing the flow rate from 0.7 ml/min to 0.5 ml/min, a small difference was observed in the

experimental results on the water temperature profile (Figure 3-7). This could be related to the similar electric field profile and consequently same microwave power density in the tube for these two conditions. On the other hand, decreasing the flow rate from 1.5 ml/min to 0.7 ml/min, the experimentally measured temperature at points 1- 3 increased by ~ 10 – 20 ^{o}C. With regards to the 1.5 ml/min flow rate experiment, the temperature close to the outlet (point 5) remained close to 100 ^{o}C, which is higher compared with the results obtained for 0.5 ml/min and 0.7 ml/min. The absorbed microwave energy was used to maintain the temperature near the boiling point and overcome the temperature drop associated with heat losses due to conduction, radiation and microwaves reflection due to bubble generation.

The FEM model allowed tracing the temperature profile at different flow rates. It is worth noting that the difference between experimental and theoretical temperature profiles obtained at 0.5 ml/min and 0.7 ml/min flow rates was similar. For all flow rates studied, the temperature discrepancies between experiments and simulations were of the same order of magnitude, similar to the previous cases (Sections 3.4.1.1 and 3.4.1.2).

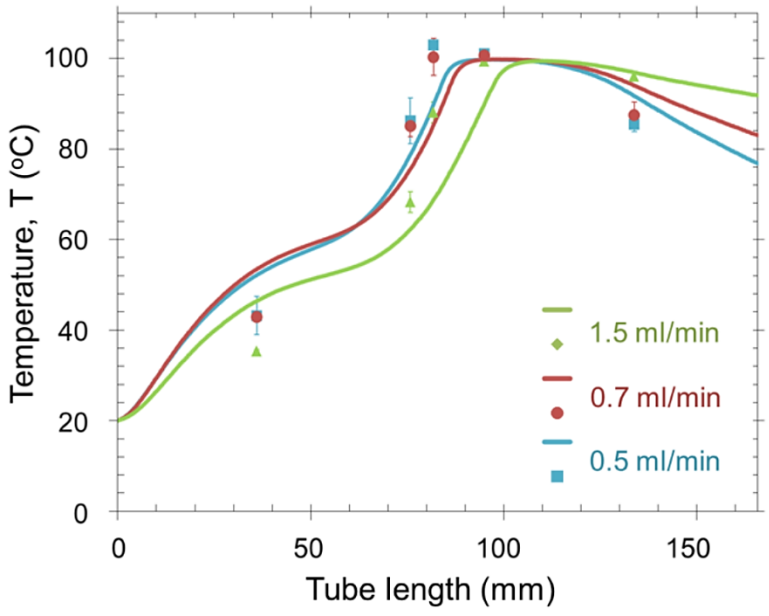

Figure 3-7 Experimental and computational results of the temperature profile inside the tube, when varying the water flow rate. Microwave power, 35 W; tube orientation, parallel-to-port; system pressure, 1 bara; frequency, 2.47 GHz (marks: experimental results; lines: computational results). Error bars correspond to the standard deviation of three experimental measurements at each point. Computational results correspond to the temperature profile in the centre of the tube (water domain).

3.4.1.4. Effect of operating pressure on temperature profile

The temperature profile inside the tube was examined at higher pressure, 2.3 bara, and various microwave input powers. An important parameter which defines the dielectric properties is relaxation time and describes the rate of increase and collapse of polarisation[167, 168]. For polar liquids, relaxation time is a function of temperature and viscosity, as dipoles are affected and oriented by the random molecular movement due to the thermal motion[114]. Researchers developed empirical formulas describing the dielectric properties and relaxation times of water as a function of temperature for given microwave frequencies, while studies on polar solvents considered pressure as another variable[169-173]. The effect of pressure on the dielectric constant of polar solvents was attributed to the increased compression of the liquid under pressure[169, 173]. The study of Schornack and Eckert[169] showed the importance of system pressure on the dielectric properties of polar solvents. Bradley and Pitzer[174] and Floriano and Nascimento[175] developed empirical correlations to relate the dielectric constant of water to the system temperature and pressure. These correlations show that there is an insignificant increase in the dielectric constant when increasing the pressure to 2.3 bara (see Table A-2, Appendix A). Increasing the system pressure the boiling point increases; the boiling point of water is 125 ^{o}C at 2.3 bara. In order to simulate the system at 2.3 bara, the dielectric constant and dielectric loss of water were extrapolated from the experimentally measured properties at atmospheric pressure (see Figure A-1, Appendix A). As described in Section 3.4.1.1, to account for the phase change above boiling point conditions, we assumed that the dielectric loss of water became zero, when the temperature reached 125 ^{o}C at 2.3 bara pressure. As bubbling was observed from 120 ^{o}C at 2.3 bara, the experimentally measured ε'' values were extrapolated only up to 120 ^{o}C. A linear interpolation was then performed between ε'' at 120 ^{o}C to $\varepsilon'' = 0$ at 125 ^{o}C by COMSOL.

Figure 3-8 shows computational results of the temperature profile throughout the tube length at 2.3 bara pressure. Although there was limited quantitative agreement between model and experiments for 5 W and 15 W under pressure, there was satisfactory agreement for 25 W. A temperature drop was observed at the tube outlet, similar to the results obtained at atmospheric pressure (1 bara). Comparing the experimental results shown in Figures 3-3 and 3-8, for the same input microwave

power, there was a 3-15 ^{o}C temperature increase at 5 W and up to 20 ^{o}C increase at 15 W and 25 W, when increasing the pressure to 2.3 bara. The temperature difference was higher towards the middle and near the outlet of the tube, where rapid temperature increase and higher temperatures were observed. Nevertheless, the temperature profile remained qualitatively similar.

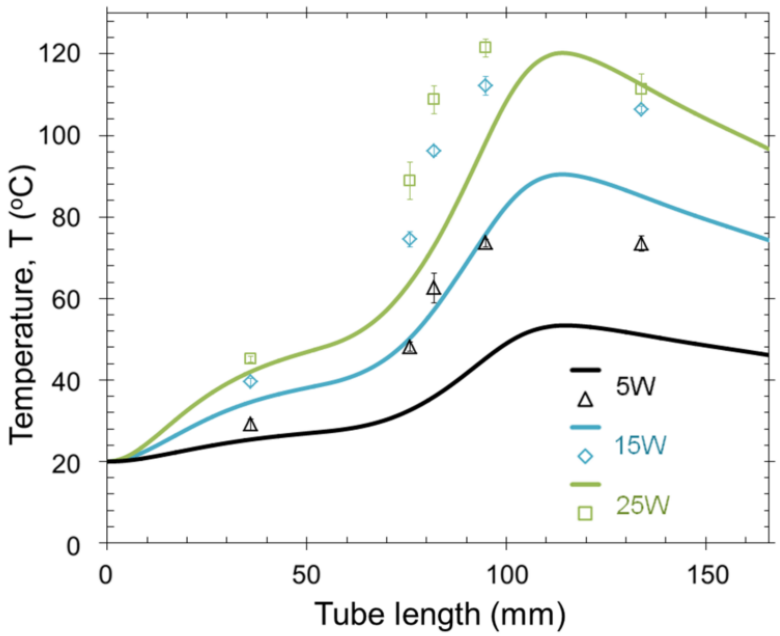

Figure 3-8 Experimental and computational results of the temperature profile inside the tube at 2.3 bara pressure, when varying microwave power in the range 5-25 W. Flow rate, 0.7 ml/min; tube orientation, parallel-to-port; frequency, 2.47 GHz (marks: experimental results, lines: computational results). Error bars correspond to the standard deviation of three experimental measurements at each point. Computational results correspond to the temperature profile in the centre of the tube (water domain).

3.4.2. Modelling of the electric field and absorbed power under microwave irradiation

The electric field inside the tube under microwave heating was simulated using the FEM model. The temperature profile was conjugated with the electric field profile, as the electromagnetic field governs the microwave absorbance and the observed temperature profile and vice versa, due to the dependency of the dielectric properties on temperature. Therefore, the developed model could offer an insight on the electromagnetics inside the tube and the energy balance of the system. A detailed

discussion on the electric field profile and the absorbed microwave power is presented in the following sections.

3.4.2.1. Electric field and temperature profile in the tube

The electric field profile inside the cavity and tube is of major importance, as it is directly related to the microwave power density (Eq. 3-7). When the tube was placed in the cavity, it caused perturbation of the electric field. This perturbation was dependent on the geometry of the cavity and the dielectric properties of the materials, as well as the tube orientation, as previously discussed in Section 3.4.1.2. Figure 3-9 shows the electric field throughout the tube length, for parallel-to-port and perpendicular-to-port orientation. For parallel-to-port, there was an electric field maximum close to the middle of the tube. However, when the tube was placed perpendicularly to the applied field, the field fluctuated around an average value (1 kV/m), affected by the field perturbation[131]. The electric field profile is also affected by the input microwave power. Figure 3-9 shows the electric field and theoretical temperature profile along the tube length for two input microwave powers (5 W and 35 W). For both cases, the temperature profile was not along the tube length, while water temperature increased rapidly and reached its maximum value around the middle of the tube, at ca. 90 mm, corresponding to the point where the curve of the tube was located and maximum electric field intensity was observed. Increasing the microwave power from 5 W to 35 W for parallel-to-port orientation, the electric field intensity increased from 3.4×10^3 V/m (5 W) to 9×10^3 V/m (35 W) and the maximum temperature increased from ~ 55 ^{o}C (5 W) to ~ 100 ^{o}C (35 W).

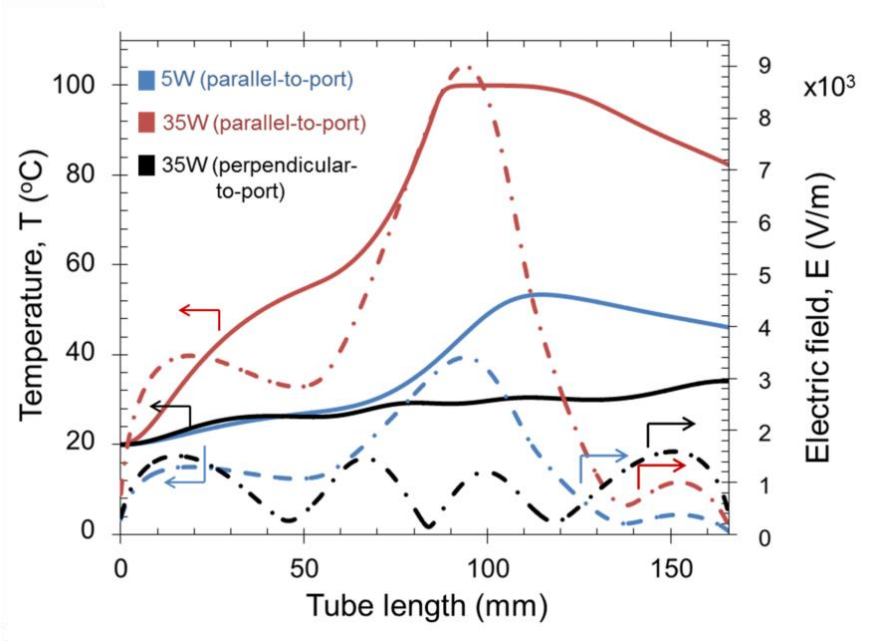

Figure 3-9 Computational results of the electric field and temperature profiles inside the tube for parallel-to-port orientation for 5 W and 35 W and for perpendicular-to-port orientation for 35 W. Flow rate, 0.7 ml/min; system pressure, 1 bara; frequency, 2.47 GHz (solid lines: temperature profile, dash dotted lines: electric field profile). Computational results correspond to the electric field and temperature profiles in the centre of the tube (water domain).

3.4.2.2. Effect of the process parameters on absorbed microwave power

The developed model allows the estimation of the power absorbed by the continuous flow system and evaluation of the desired process parameters for achieving the targeted temperature profile and minimising energy usage. The lack of monitoring of reflected power in the microwave cavity makes the computational model a necessary tool to estimate the energy required. The absorbed microwave power was calculated via volume integration of the tube[128], in the Step 2 of the computational methodology:

$$P_{total} = \iiint_V P_d \, dxdydz \qquad \text{Eq. 3-8}$$

where P_d is the microwave power density generated inside the tube and x, y, z are the respective coordinates.

Increasing the input microwave power to 20 W, the absorbed power reached 4.6 W. Further increase of the input power up to 35 W led to plateauing of the microwave absorption at 5 W, as it is a function of both the electric field intensity and the dielectric properties, which are temperature dependent. Therefore, given the temperature profile results in Figure 3-3a and Figure 3-3b, in which temperature increased by increasing the input power up to 20 W and it remained constant up to 35 W, increasing the input microwave power led to an excess of microwave power which could not be absorbed by the system (Table 3-1).

There was a dramatic decrease on the microwave absorbance from 8.7 W to 5 W, corresponding to 25 % and 14 % of absorbed over input microwave power, respectively, when decreasing the flow rate from 1.5 ml/min to 0.7 ml/min at 35 W microwave power. Decreasing the flow rate further to 0.5 ml/min resulted in further drop to 12 % in the absorbed over input microwave power ratio. These results demonstrate the enhancement of the microwave efficiency at higher flow rates which could be a result of water dielectric properties change and possible bubble formation due to evaporation, causing perturbation to the electric field. Increasing the water temperature, the dielectric properties decrease causing alterations to the field perturbations, while water at lower dielectric loss values couples weakly with the applied microwave field. On the other hand, for the case study of tube orientation (***D*** in Table 3-1) the absorbed microwave power for perpendicular-to-port orientation showed a 80 % decrease, as compared to parallel-to-port orientation, since parts of the U-tube coinciding with the minima and maxima of the applied electric field in resonant mode, affected the electric field profile and thereby the power density inside the tube. By increasing the pressure from 1 bara to 2.3 bara, the absorbed microwave power was unaffected, despite the significant temperature increase (***E*** in Table 3-1), indicating the need for accurate dielectric data of water under pressure.

Table 3-1 Absorbed microwave power by water inside the tube for different experimental conditions (values in parentheses display the percentage of the absorbed over the input microwave power).

Input microwave power, P_{in}	**Absorbed microwave power P_{total} (W)**				
	A	***B***	***C***	***D***	***E***
5 W	-	1.9 (38 %)	-	-	1.9 (38 %)
10 W		3.1 (31 %)			-
15 W		4.0 (27 %)			4.0 (27 %)
20 W		4.6 (23 %)			-
25 W		4.8 (19 %)			5.8 (23 %)
30 W		4.9 (16 %)			-
35 W	8.7 (25 %)	5.0 (14 %)	4.1 (12 %)	1.0 (3 %)	-

***A**:* Flow rate, 1.5 ml/min; tube orientation, parallel-to-port; pressure, 1 bara; frequency, 2.47 GHz

***B**:* Flow rate, 0.7 ml/min; tube orientation, parallel-to-port; pressure, 1 bara; frequency, 2.47 GHz

***C**:* Flow rate, 0.5 ml/min; tube orientation, parallel-to-port; pressure, 1 bara; frequency, 2.47 GHz

***D**:* Flow rate, 0.7 ml/min; tube orientation, perpendicular-to-port; pressure, 1 bara; frequency, 2.47 GHz

***E**:* Flow rate, 0.7 ml/min; tube orientation, parallel-to-port; pressure, 2.3 bara; frequency, 2.47 GHz

3.5. Conclusions

In this chapter, microwave heating of water continuously flowing in a small diameter tube was investigated. Microwave power played a significant role in the temperature profile and temperature increase throughout the tube length. When increasing the input microwave power up to 20 W, the longitudinal temperature increased for the same axial position, due to the increasing absorbed microwave power. Further increase of the input microwave power up to 35 W, resulted in an insignificant increase in the temperature profile, since the electric field intensity increased only to a low extent and the absorbed power remained constant. Changing the orientation of

the tube from parallel to perpendicular position towards the microwave port led to 50 ^{o}C decrease of the maximum temperature and 80 % reduction of the absorbed microwave power, due to perturbation of the electric field. Decreasing the water flow rate from 1.5 ml/min to 0.5 ml/min resulted in the same final maximum temperature; however, the microwave absorbance reduced dramatically by 53 % due to the volumetric nature of the microwave heating. Increasing the pressure from 1 bara to 2.3 bara, which raised the water boiling point to 125 ^{o}C, resulted in higher temperatures for the same microwave power, despite the same qualitative temperature profile. The developed computational FEM model showed sufficient qualitative and quantitative agreement with experimental data as compared with previously reported literature models. Thereby the developed model establishes a robust methodology for tuning the operating conditions of microwave-assisted reactors to trace the temperature and electric field profiles and calculating the power absorption.

CHAPTER 4. Investigation of citrate-capped gold nanoparticle synthesis in continuous flow microwave-assisted reactors

Microwave heating is gaining increasing interest for the synthesis of colloidal nanoparticle solution as a tool for process intensification. However, the challenges transferring the synthesis from batch to flow have not been fully addressed. In this study two operating systems were developed using either only a commercial single-mode microwave applicator (one-stage synthesis) or microwave heating and a conventional heating in series (two-stage synthesis) for the synthesis of gold nanoparticles in a PTFE tube (2.4 mm internal diameter). In the one-stage synthesis, varying the input microwave power had negligible effect on the average particle size (size fluctuating around 20 nm), while the reactant molar ratio was the deciding factor. However, in the one-stage system, the particles were unstable upon collection when the residence time was lower than 20 min. In the two-stage system, nucleation was initiated under microwave heating followed by a conventional heating reactor for the particle growth. Thus, the effect of nucleation temperature on the particle size, shape and dispersity could be evaluated at different microwave powers or residence times in the microwave reactor. Increasing the microwave power from 0 (only conventional heating) up to 15 W, the particle size increased from 19.8 ± 3.3 nm to 24.9 ± 4.3 nm and decreased upon further increase of the input power. On the other hand, varying the residence time under microwave heating had no significant effect on final particle size (ranging between 18 – 20 nm), despite a small change on the temperature profile inside the microwave reactor. In all cases, the observed high particle dispersity (> 18%) was correlated to the parabolic laminar flow profile as the residence time distribution approaches the pure convection regime, the non-isothermal temperature profile under the microwave heating and the loss of unreacted species due to particle deposition on the tube walls. These results provide in-depth understanding of the challenges for the development of microwave-assisted continuous synthesis platforms for colloidal gold solutions.

4.1. Introduction

Ngo *et al.*[15] and Seol *et al.*[52] studied the fabrication of spherical Au NPs using the citrate-reduction method in batch, using multi-mode and single-mode microwave applicators, respectively, obtaining similar results, while the analysis via UV-Vis spectroscopy showed that the surface plasmon resonance (SPR) peak of the synthesised Au NPs was at ~ 520 nm. The SPR band is the characteristic localised surface plasmon resonance signal of the Au NPs and depends – among other factors – on the particle size, shape and concentration; thus it can be used for comparison between nanoparticles of similar morphology and chemical composition[84]. Seol *et al.*[52]*,* managed to synthesize spherical Au NPs of 12.04 ± 1.35 nm maintaining the temperature constant at 95 ^{o}C by adjusting the microwave power and keeping pH above 6.1[153]. The study of Ngo *et al*. [15] has shown the formation of spherical uniform nanoparticle 13 – 15 nm in size within 10 min, based on the UV-Vis and TEM data, using a domestic microwave oven, without recording the synthesis temperature. Uppal *et al.*[154] examined the effect of $[Na_3Ct]/[HAuCl_4]$ ratio on nanoparticle size in batch and compared microwave-heating synthesis (MWH) with sonolysis, ultra-violet (UV) radiation and themal (conventional) heating (CH) methods. The findings on the microwave-assisted synthesis suggested the final particle size was influenced primarily by the concentration of Na_3Ct in reduction synthesis, rather than the microwave power input, as already stated in the literature[38, 75]. Also, increasing the concentration of Na_3Ct in the solution resulted in smaller nanoparticles down to ~ 11 nm, comparable to that of conventional heating. Comparing MWH and CH, the synthesis under conventional heating completed faster than the microwave-assisted process, but UV-Vis spectra suggested similar results, as the SPR peak was around 519 – 520 nm. Liu *et al.*[176] investigated the synthesis of citrate-capped gold nanoparticles using a multi-mode microwave applicator by increasing the synthesis temperature from 50 – 150 ^{o}C or the temperature ramping rate from ~ 5 – 80 ^{o}C/min. In their study, particle size decreased from 80 nm to 20 nm and standard deviation of the particle size decreased from 19 nm to 2 nm, due to the increased nucleation and growth rates at higher temperatures. Bayazit *et al.*[53] studied the synthesis of Au NPs from batch to flow under microwave heating using a PTFE tube reactor investigating the effect of microwave power, $[Na_3Ct]/[HAuCl_4]$ ratio and residence time on the particle size and length-to-width particle aspect ratio. The findings suggested that varying the microwave power had minor effect on the particle size and aspect ratio,

while increasing the $[Na_3Ct]/[HAuCl_4]$ ratio the particle formation changed significantly from nanowire-like structures to spherical particles.

Former studies have explored multiple parameters of Au NPs in batch (using both MWH and CH), however, there is limited information on the key parameters and the challenges for transferring the synthesis to flow under MWH. In this chapter, the effect of the operational process parameters on the final size, shape and dispersity of the Au NPs was investigated experimentally, using a single-mode microwave applicator in a one-stage and a two-stage reaction process (MWH – CH reactors in series). Additionally, a finite element method model provided insight on the temperature profile along the reactor length, allowing the correlation of the heating profile on the formed Au NPs. Finally, it was attempted to identify the major challenges affecting the particle disprersity for transferring the synthesis of Au NPs from batch to flow utilising a continuous microwave reactor.

4.2. Experimental section

4.2.1. Materials & methods

The reactants used were trisodium citrate dihydrate (Sigma-Aldrich, $Na_3C_6H_5O_7 \cdot 2H_2O$) and Gold (III) chloride trihydrate (Sigma-Aldrich, $HAuCl_4 \cdot 3H_2O$ 99.9+%) and were of analytical grade. Ultra-pure water (15 MΩ·cm) was used for all aqueous solutions. Polytetrafluoroethylene (PTFE) tubing (1 mm ID, VICI Jour) was used for all fluidic tubing and ferrules and fittings made of polyether ether ketone (PEEK) (Upchuch) were used for all required connections in the experimental set-up.

The synthesised nanoparticles were characterised using UV-Vis absorption spectroscopy (UV-vis) (Spectrometer: USB2000+UV-VIS-E and light source: DT-MINI-2-GS, Ocean Optics, Inc), TEM imaging (Jeol 2010–200 kV) and differential centrifugal sedimentation (DCS) (CPS 24 000 Disc Centrifuge, CPS Instruments). For the UV-Vis absorption spectra, the Au NPs sample (~3 ml) was placed in a polypropylene cuvette (path length: 1 cm) and spectral analysis was performed in the range of 200-800 nm. The samples were recorded immediately after the sample collection and in daily or regular basis until they were stabilised. TEM samples were prepared by dipping a drop of the sample solution, when stabilised, onto a carbon film 200 mesh copper grid (C200 Cu, EM Resist Ltd) and let it dry in air. Particle

counts from the TEM image analysis was performed via Pebbles software to ensure accurate and unbiased particle sizing[177]. Au NPs samples were analysed via DCS, once stable, (~0.1 ml injected per sample). The assumed nanoparticle density for the DCS analysis was 12.3 g/ml as it was shown to provide comparable results with TEM image analysis for the range of 8 – 30 nm citrate-capped Au NPs[49].

4.2.2. Experimental set-up

Gold nanoparticles were synthesised using the citrate-reduction method (*Turkevich method*), in which the gold precursor ($HAuCl_4$) was reduced and stabilized by trisodium citrate (Na_3Ct). The precursor stock solution that was used was 5 mM $HAuCl_4$ and a freshly prepared stock solution of 50 mM Na_3Ct. For the evaluation of the influence of microwave heating on the gold nanoparticle synthesis, two different set-ups were developed. In the first set-up the reactants were premixed in one-stage microwave-assisted synthesis, following the experimental protocol previously developed by Bayazit *et al.*[53] (Figure 4-1). In the second set-up, a two-stage process was developed comprising a microwave and a conventional heating reactor in series.

In detail, in the one-stage synthesis, the reactor used was a coiled flow reactor of 6 ml volume (inner diameter: 2 mm, outer diameter: 3.175 mm, length: 1.9 m) made of PTFE placed in the centre of the cavity of the commercial microwave applicator (Discover SP, CEM). $HAuCl_4$ and Na_3Ct were premixed at room temperature and the input mixture was injected immediately through a 60 ml plastic syringe (BD Plastipak) using a syringe pump (Legato 270P, KD Scientific) at 4 ml/min resulting in 90 s residence time. The applied microwave power varied between 25 – 45 W and [Na_3Ct]/[$HAuCl_4$] ratio varied between 1/1 to 60/1, while the concentration of the gold precursor after mixing was constant and equal to 0.25 mM; thus [Na_3Ct] after mixing ranged between 0.25 – 15 mM. The temperature of the heated solution was measured via a K-type thermocouple (TJC1, Omega), introduced from the reactor outlet in contact with the solution and positioned at 5 cm from the outlet of the microwave cavity, to avoid interference with the electromagnetic field inside the cavity. The reactor was under 2.3 bara – using an air cylinder – and the pressure was established with a backpressure regulator (BPR) (20 psi, Upchurch). In all experimental series, the solution was passed through an ice bath to quench the reaction prior to collection.

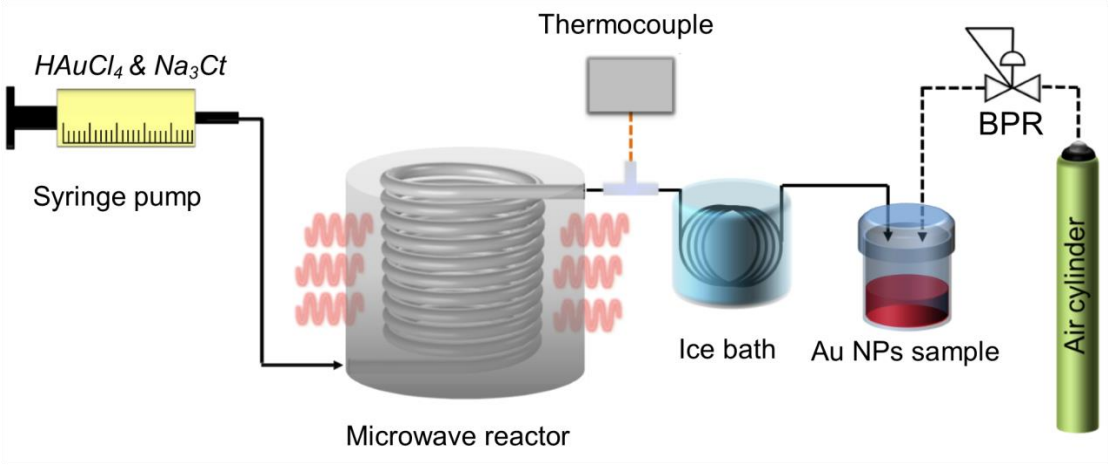

Figure 4-1 Setup of the one-stage microwave-assisted continuous synthesis of citrate-capped gold nanoparticles.

In the two-stage synthesis (Figure 4-2), the procedure included two stages, using a MWH reactor for the initial stage and a CH reactor for the second stage. Firstly, the two reactants were prepared by filling the two 25 ml glass syringes (25MDR-LL-GT, Scientific Glass Engineering), one with 0.5 mM $HAuCl_4$ and the other with 3.0 mM Na_3Ct. The flow of the two solutions was regulated by a syringe pump (Legato 270P, KD Scientific) and they were mixed using a glass split and recombine mixer of 4.64 µl volume (Micromixer Chip, Dolomite Microfluidics). For the first stage, a U-shape tube reactor 0.75 ml (inner diameter: 2.4 mm, outer diameter: 3.175 mm, length: 165 mm) made of PTFE was placed in the centre of the single-mode commercial microwave applicator (Discover SP, CEM) in a parallel-to-port orientation. The two solutions were delivered at the same flow rate depending on the targeted residence time inside the microwave heating reactor. The flow rates for each stream ($HAuCl_4$ and Na_3Ct) were 0.35 ml/min, 0.25 ml/min and 0.1875 ml/min, resulting in mean residence times of the mixed stream ca. 1 – 2 min. Applied microwave power was set at 3 different levels 5 W, 15 W and 25 W. All components inside the microwave cavity were made of PTFE, due to its low dielectric loss factor (microwave transparent material)[115].

For the second heating stage, a glycerol bath on a hot plate with an integrated magnetic stirrer (Stuart UC152D, Cole-Parmer Ltd) was used including a coiled flow tubular reactor (inner diameter: 2.4 mm, outer diameter: 3.175 m) reactor made of PTFE. The temperature and residence time under conventional heating remained constant at 90 ^{o}C and 20 min, respectively, using the tube reactor of appropriate volume (7.5 ml, length: 1,658 mm; 10 ml, length: 2,210 mm; 14 ml, length: 3,095 mm)

based on the total set flow rate of the mixed stream. The temperature homogeneity in the glycerol bath was evaluated by immersing an external thermocouple at various positions and depths during the synthesis process; there were no temperature variations of more than 1 ^{o}C from the set temperature of 90 ^{o}C. The overall procedure was carried out at 2.3 bara pressure established with a backpressure regulator (BPR) (max. 4 bar K-type, Swagelok). The use of a polycarbonate 3-way valve (Large-Bore Luer Stopcocks, Cole-Parmer Ltd) allowed the sample collection after only the microwave reactor (MW sample) and after both the microwave and the conventional heating reactor (MW/CH sample).

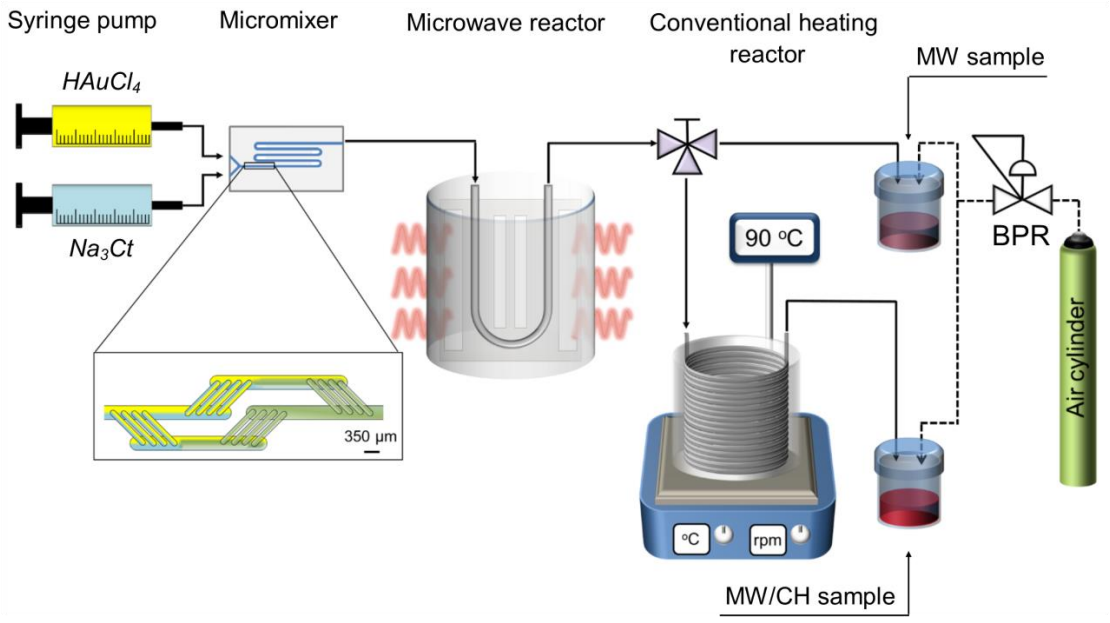

Figure 4-2 Setup of the two-stage microwave-assisted continuous synthesis of citrate-capped gold nanoparticles. MW sample: sample collected after only the microwave reactor, MW/CH sample: sample collected after both the microwave and the conventional heating reactor.

4.2.3. Temperature measurements

The temperature inside the microwave reactor was monitored via a fibre optic temperature sensor (T1s, Neoptix Inc.) with direct temperature measurements at 5 different positions throughout the tube length. In order to avoid deposition of gold nanoparticles on the sensing tip of the fibre optic probes, which could interfere with our measurements, only ultra-pure water was used as the medium for the temperature measurements, under the desired microwave power and total input flow

rate in the U-shape tube. In the microwave frequency range, the microwave absorption in the water is dominant over the absorption in the diluted spherical gold nanoparticles[178]. Additionally, according to previous published findings on radiofrequency heating, gold nanoparticles have low to negligible contribution to final temperature of the medium[179, 180]. To ensure that the use of ultra-pure water would be representative as a medium for the experimental investigation of the temperature profile under microwave heating, the temperature ramping of the reacting mixture ($HAuCl_4$ and Na_3Ct) was tested and it was proved similar to that observed for only Na_3Ct at the same concentration or ultra-pure water (Section B.1, Appendix B).

As described in Chapter 3, temperature measurements were performed at five different points over the U-shape reactor: 36 mm (point 1), 70 mm (point 2), 83 mm (point 3), 95 mm (point 4) and 135 mm (point 5) from the inlet. The diameter of temperature monitoring probes (1.3 mm) was significant with respect to the inner diameter of the reactor tube (2.4 mm). For that reason, the fibre optic sensor was inserted from the tube outlet, to avoid flow disturbances and measurement inaccuracy[59]. For the temperature monitoring in the second stage (glycerol bath), a temperature controller (Stuart SCT1, Cole-Parmer Ltd) was connected to the hot plate, allowing simultaneous reading and regulation of the glycerol temperature at 90 ^{o}C inside the bath.

4.3. Results & discussion

4.3.1. Preliminary results on microwave-assisted synthesis

In order to evaluate the feasibility of Au NPs synthesis under microwave heating and the parameters affecting the synthesis, a parametric study was conducted in one-stage process under microwave heating, based on the experimental protocol proposed by Bayazit *et al.*[53]. A range of different microwave powers and mixtures of $HAuCl_4$ and Na_3Ct were passed through the single-mode applicator. Collected samples were stored in a dark container at room temperature and they were analysed using UV-Vis spectroscopy in regular intervals to estimate their stability upon collection. Once stable, Au NPs were analysed using TEM and DCS. Figure 4-3a shows the stability of the colloidal Au NPs, which was collected after the synthesis under microwave radiation (90s residence time at 36 W input power), by regular monitoring of the UV-Vis spectra of the collected sample. Results were compared

with the UV-Vis spectra of a control sample synthesised using the same reactant concentrations ([Na_3Ct] = 1.5 mM and [$HAuCl_4$] = 0.25 mM) by simply mixing the reactants at room temperature. Comparing the UV-Vis spectra of the sample after collection and when it was stable (after 168 h), there was a significant 351 % increase in the absorbance at 400 nm, which is directly related to the concentration of Au^0 [84], and a shift of surface plasmon resonance band, which is related to the formed citrate-capped gold nanoparticles. When particles were stable, the SPR band blue-shifted compared to the respective peak after collection. One explanation for this phenomenon could be a decrease on the particle length-to-width aspect ratio as particles become spherical[53, 89]. However, previous studies have shown that polydisperse samples – depending on the temperature, ligands and particle size distribution amongst other factors – are likely to go through digestive Ostwald ripening as a size-focusing route, where the large particles dissolve in favour of thermodynamically stable smaller particles[181-183]. Thus, it is evident that although reaction initiated in the reactor under microwave heating, the complete reduction of the gold precursor to stable particles was not completed within the proposed residence time of 90 s and the reaction continued at room temperature. Once the sample was stable, it was analysed via TEM imaging, as shown in Figure 4-3b, which showed that the particle size was 21.8 ± 3.6 nm and the Au NPs were relatively spherical (~ 1.2 length-to-width aspect ratio).

The wider distribution of the SPR of the control experiment (dashed line in Figure 4-3a) in comparison with the spectra of the stable sample band – as given by the UV-vis spectra analysis – was a clear indication that microwave heating has a positive effect on the particle size distribution, towards the synthesis of spherical and monodisperse Au NPs[86]. The temperature was measured using a thermocouple placed in the centre of the tube introduced from the outlet, in order to avoid any disturbances in the flow[59]. Due to the interference of the electromagnetic field by the metal parts of the thermocouple, it was positioned at 5 cm from the microwave cavity outlet and the temperature reading was fluctuated around ~ 116 ^oC for the different applied microwave power (25 – 45 W). However, taking into account the heat loss from the reactor outlet until the measuring point, it could be estimated that the temperature on the outlet of the microwave reactor ranged between 120 – 128 ^oC for the studied input microwave powers (Table B-1, Appendix B). Hence, rapid nucleation and seed formation must have started under microwave heating and an uncontrollable growth was achieved as the samples were stored at room

temperature. Higher temperatures favour the rapid reduction of $[AuCl_4^-]$ to Au^0 monomers resulting to rapid formation of nuclei[38], allowing less available reactant species for the growth step, which indicated the positive effect of short residence time under microwave on the lower polydispersity of the final gold particles compared with the control sample.

Increasing the microwave power from 25 – 45 W under constant $[Na_3Ct]$/$[HAuCl_4]$ ratio equal to 6/1 and 90 s residence time, particles resulted in approximately similar Au NPs sizes varying between 20 – 25 nm and the polydispersity of the 25 – 45 W samples varied between 12 – 25 %, as shown in Figure 4-3c. In all cases, the particles were allowed to stabilise at room temperature, exhibiting similar length-to-width aspect ratio (1.2 – 1.3), which translates to spherical morphology, for applied microwave power between 25 – 45 W, as shown by TEM imaging (Figure B-3, Appendix B). Figure 4-4 shows the particle size distribution of the synthesised Au NPs by increasing the residence time from 90 s up to 20 min under 25 W microwave power. As the residence time increased to 20 min, the colloidal solution was stable upon collection, however, the longer residence time under microwave radiation did not have a significant effect on the particle size resulting in 23.8 ± 4.3 nm (which was comparable with the Au NPs sizes shown in Figure 4-3c). The results in Chapter 3 indicated that above a certain value of residence time or microwave power, the temperature profile in the medium remained constant. Since the estimated temperature on the microwave outlet was ~ 125 ^{o}C (boiling point of water at 2.3 bara) for 90 s residence time at 25 W input microwave power, the same temperature was expected for 20 min residence time at the same power. It is worth noting that for 20 min residence time, the distribution was skewed due to the synthesis of larger particle sizes (> 35 nm) and polydispersity increased from 14 % (for 90 s residence time) to 18%. This phenomenon could be attributed to the particle deposition (fouling) on the reactor walls as it is later discussed in Section 4.3.3.

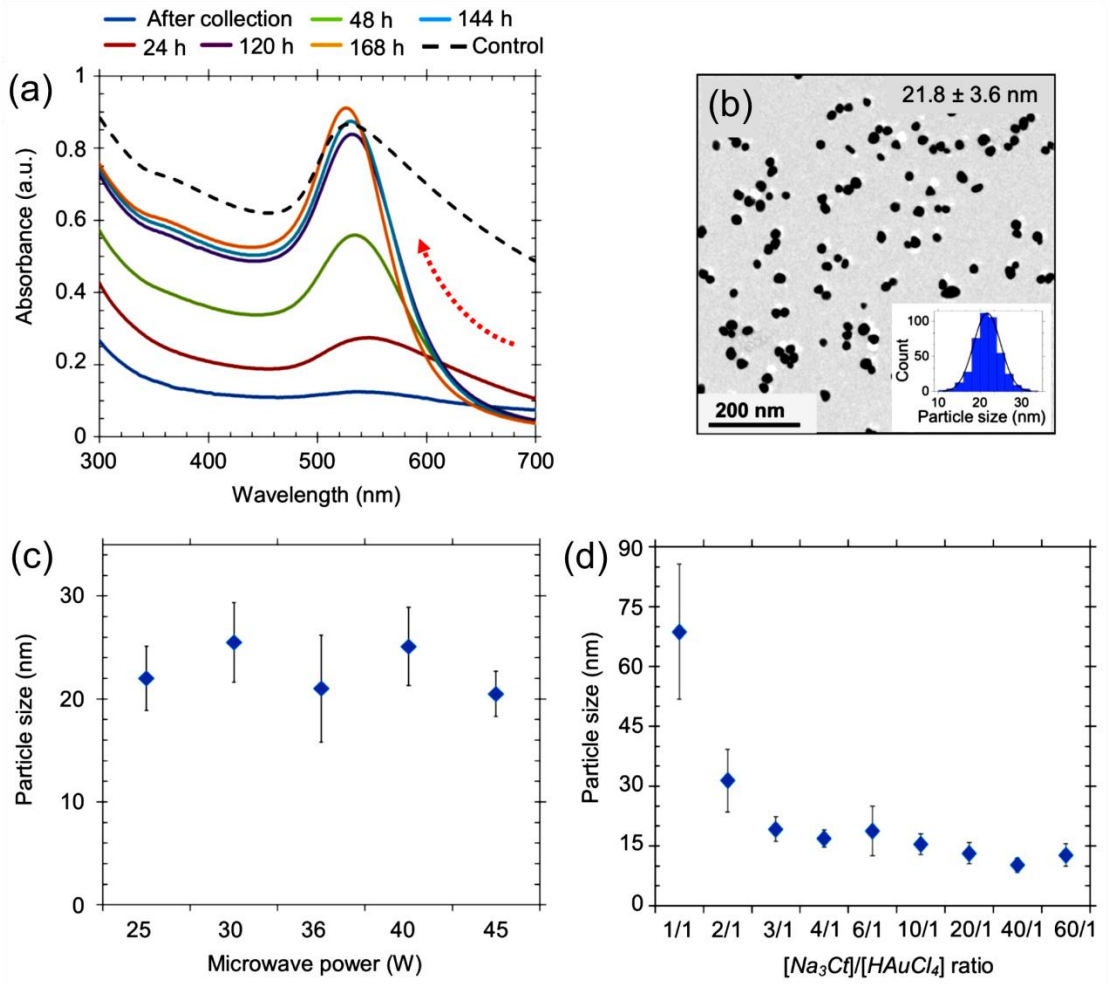

Figure 4-3 a) UV-Vis spectra of the Au NPs sample synthesised – under 36 W microwave heating and $[Na_3Ct]/[HAuCl_4]$ ratio = 6/1– taken after regular intervals to assess the stability of the collected sample and comparison with the batch control sample (synthesised at room temperature under similar reactant molar ratio) noted with the dashed line. Dotted red arrow indicates the increase of the surface plasmon resonance band of the collected sample with time. b) TEM image of the sample described in (a) when stable (after 168 h from collection). c) Particle size of the stable synthesised Au NPs in flow for 25 – 45 W microwave power and 6/1 $[Na_3Ct]/[HAuCl_4]$ ratio. d) Particle size of the stable synthesised Au NPs in flow for 36 W microwave power and 1/1 – 60/1 $[Na_3Ct]/[HAuCl_4]$ ratio. In (c) and (d) samples were left at room temperature for approx. 5 days for colloidal particles to stablise prior to TEM and DCS analysis. In (a) – (d): One-stage microwave-assisted gold nanoparticles synthesis; $[HAuCl_4]$ (after mixing), 0.25 mM; reactor volume, 6 ml; inlet flow rate, 4 ml/min; residence time under microwave heating, 90s; system pressure, 2.3 bara. Particles sizes in (c) and (d) were obtained based on DCS. Error bars correspond to the standard deviation of the particle distribution.

Additionally, increasing the $[Na_3Ct]/[HAuCl_4]$ ratio from 1/1 to 60/1 (Figure 4-3d) particle size decreased, which is related to citrate acting as both reducing and stabilising agent[65]. Results also showed that 1/1 $[Na_3Ct]/[HAuCl_4]$ ratio resulted in large and polydispese Au NPs (73.6 ± 18.8 nm), while increasing the reactant molar ratio above 3/1, size and polydispersity decreased and particle size fluctuated between 15 – 20 nm, similarly to previously reported results using conventional heating[38, 40, 82, 184, 185], confirming the great impact of the concentration of the reducing agent on the particle size[38]. Again, the temperature on the outlet of the microwave cavity was estimated equal to ~ 125 ^{o}C, as the power was kept constant at all studied reactant molar ratios and due to the strong absorption of the microwave radiation by the medium (water). Hence, the Na_3Ct would undergo the similar speciation ($H_xCt^{(3-x)-}$) resulting in similar pH (~ 6.5), suggesting that the synthesis condition would be similar in the studied $[Na_3Ct]/[HAuCl_4]$ ratio range. Figure 4-3d shows that at 40/1 $[Na_3Ct]/[HAuCl_4]$ ratio there seemed to be a minimum on the synthesised particle size, while size increased for 60/1 $[Na_3Ct]/[HAuCl_4]$ ratio. Although further examination on higher $[Na_3Ct]/[HAuCl_4]$ ratios is required, it has been previously discussed that at high $[Na_3Ct]$ particle size is expected to increase due to the high ionic strength and the instability of the formed Au NPs[38].

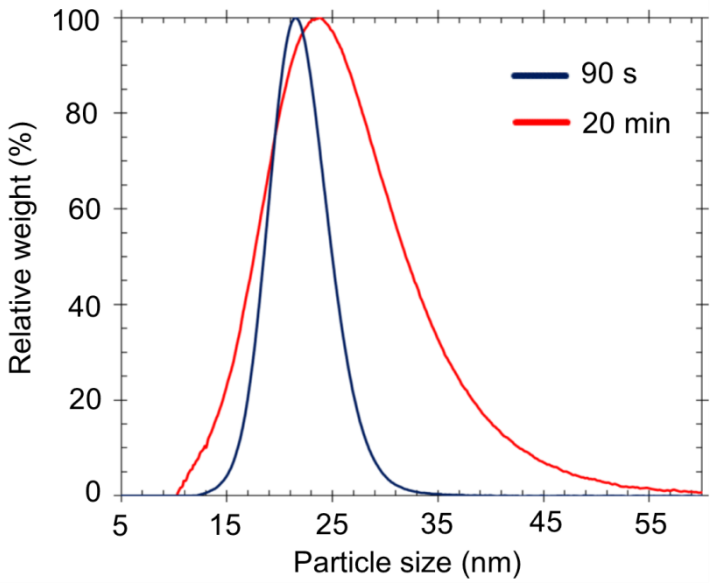

Figure 4-4 Particle size distribution of Au NPs synthesised in the one-stage process under microwave heating for 90 s and 20 min. Sizes were given by DCS. Microwave power, 25 W; reactor volume, 6 ml; inlet flow rate, 0.3 – 4 ml/min; $[HAuCl_4]$ (after mixing), 0.25 mM; $[Na_3Ct]$ (after mixing), 1.5 mM; system pressure, 2.3 bara.

4.3.2. Two-stage microwave-assisted gold nanoparticles synthesis

Chemical synthesis under microwave heating is influenced by the reactant species and concentrations, the dielectric properties of the materials used and the operating conditions. It is worth noting that these operating parameters and interactions result in different electric field and subsequently temperature profiles inside the tube reactor in the microwave cavity, which affect the final product and yield. The study was further aided by simulating the electric field and the temperature profile throughout the reactor length using a finite element model (FEM) model to understand the uniformity of the temperature during the operating conditions. A two-stage process was designed including a microwave-assisted initiation stage and a controllable growth stage. Microwave heating is considered "volumetric" in nature, thus microwave power and flow rate were investigated for their effect on the temperature profile over the reactor length and the synthesis of the final product. Au NPs were collected and compared after only the first stage (microwave heating only) or only the second stage (conventional heating only), as well as after microwave followed by conventional heating, to monitor the influence of the electromagnetic heating to initiate nucleation and subsequently final size of the Au NPs.

4.3.2.1. Effect of growth stage on particle size

The influence of a growth stage after the microwave reactor was investigated using a conventional heating tube reactor ensuring the residence time and temperature were constant and equal to 20 min and 90 ^{o}C, respectively. A U-shape PTFE reactor was used in the microwave reactor (first stage), positioned parallel to the microwave port. Du Toit *et al.*[49] showed that operating between 90 – 100 ^{o}C for 20 min residence time, the average particle size remained unaffected by the reaction temperature. At the same time, Wuithschick *et al.*[38] examined the Au NPs synthesis at different temperatures, showing that there was no significant decrease on reaction time or increase on the particle size above 90 ^{o}C. Figure 4-5 shows the synthesised gold nanoparticles obtained after the microwave reactor only (MW sample) and after the microwave reactor followed by the conventional heating stage (MW/CH sample) at 5 W microwave power and 0.5 ml/min total inlet flow rate, for [Na_3Ct]/[$HAuCl_4$] ratio equal to 6/1. The MW sample was left at room to temperature to stabilise for approx. 5 days prior to the TEM and DCS analysis. As shown in Figure 4-5, the stable MW

sample showed a bimodal distribution in which the two peaks were located at ~ 20 nm and ~ 40 nm. However, after the addition of the growth stage, the colloidal solution was stable upon collection, while the particle distribution of the MW/CH sample shifted to smaller sizes, resulting in a monomodal distribution and the average particle size was 19 nm. Based on the particle distribution of the two samples, it can be estimated that reaction was initiated in the microwave reactor, but the growth stage at constant temperature affected both the size and the polydispersity of the Au NPs colloidal solution.

Wuithschick *et al.*[38] studied the effect of reaction temperature concluding that this parameter is associated with the reduction of the reactive $AuCl_4^-$ to $AuCl_{3-x}OH_{1+x}{}^-$ which influences the seed formation and subsequently to Au^0 determining the amount of supplied monomers. Examining the TEM images of the MW sample and MW/CH sample, both the shape and size of the synthesised particle can be seen, where for the MW sample there were elongated and aggregated particles. Similar shapes have been previously reported by Ji *et al.*[86], Frens *et al.*[83] and Bayazit *et al.*[53], referring to particles during the initial stages of the synthesis. It can be assumed that in the case of the MW sample, the uncontrollable growth at room temperature (including the reduction and growth mechanisms of the Au NPs synthesis) resulted in the observed larger particle sizes and bimodal distribution. Of course, the non-isothermal profile inside the microwave reactor[186] (increasing from 20 ^{o}C up to 90 ^{o}C along the reactor length) could hinder the reduction of the reactive $AuCl_4^-$, resulting in the polydispersity observed for the MW sample. However, comparing the TEM images and the DCS results of the MW and MW/CH samples, the addition of a second growth stage (conventional heating) in series with the microwave reactor allowed the completion of the Au NPs in a controllable environment (constant temperature at 90 ^{o}C) and the formation of spherical particles.

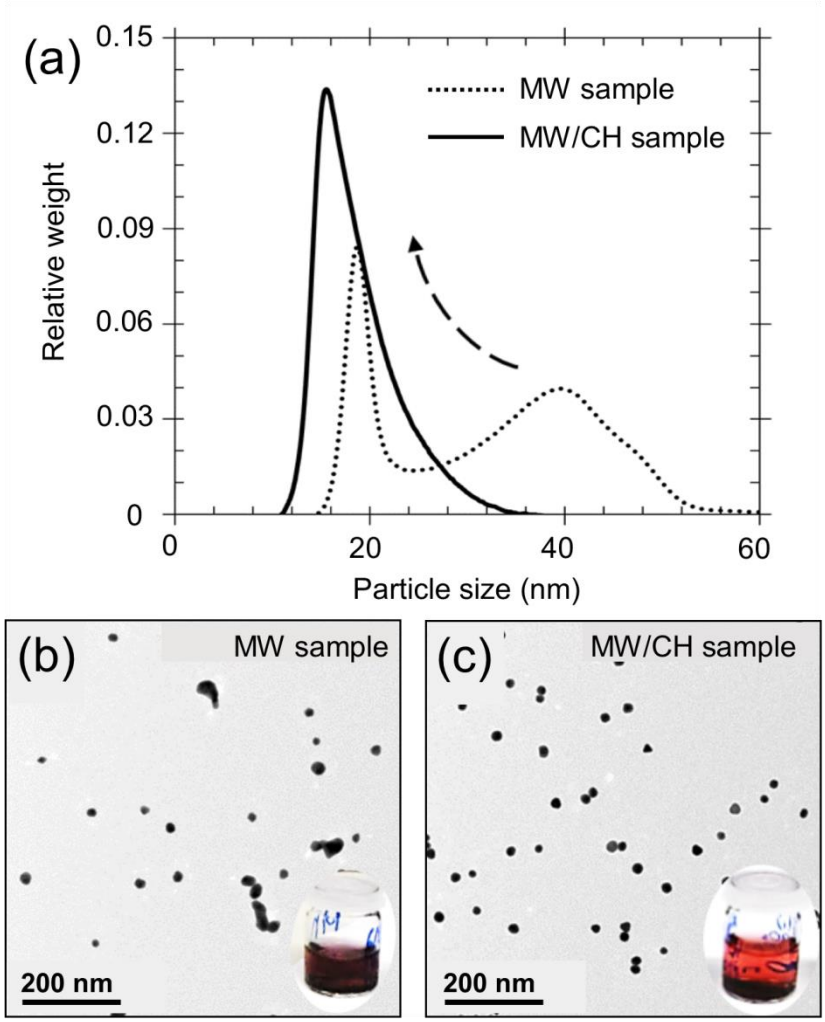

Figure 4-5 a) Particle size and distribution – obtained by DCS – of the stable sample collected after the microwave reactor (MW sample) and stable sample collected after the microwave reactor followed by the conventional heating stage (MW/CH sample). b) The TEM image of the stable MW sample. c) The TEM image of the stable MW/CH sample. MW sample was left at room temperature after collection to stabilise for approx. 5 days prior to TEM and DCS analysis. MW/CH sample was stable upon collection. Pictures in (b) and (c) display the stable colloidal solution of the MW sample and MW/CH sample, respectively. [$HAuCl_4$] (after mixing), 0.25 mM; [Na_3Ct] (after mixing), 1.5 mM; microwave power, 5 W; total inlet flow rate, 0.5 ml/min; microwave heating reactor volume, 0.75 ml, residence time in microwave reactor, 90 s; conventional heating reactor volume, 10 ml, residence time in conventional heating reactor, 20 min; temperature in conventional heating reactor, 90 ^{o}C; system pressure, 2.3 bara.

4.3.2.2. Effect of microwave power on particle size

The effect of the microwave heating in the two-stage process for Au NPs synthesis was studied by varying the input power of the microwave reactor from 5 W to 25 W keeping the total inlet flow rate constant at 0.5 ml/min, while the growth step in series was set at 20 min residence time and temperature at 90 ^{o}C. Figure 4-6 shows the temperature and electric field profile throughout the tube length, at different microwave power levels (5 W – 25 W) for 90 s residence time in the microwave reactor. Simulations of the microwave heating inside the U-shape reactor were performed using the FEM tool following the methodology described in Chapter 3. Based on the findings displayed in Figure 4-6, it can be confirmed that temperature was not uniform along the tube length in the microwave reactor during the operation. Increasing the microwave power, the temperature profile increased and the maximum temperature achieved experimentally was 85.7 ± 1.0 ^{o}C for 5 W and 125.2 ± 1.0 ^{o}C for 25 W. In case of 15 W and 25 W, temperature decreased towards the reactor outlet, which was related to the heat losses – via conduction, natural convention and radiation – as well as the lower electric field intensity at the reactor outlet as simulated by the FEM model[186]. Vapour formation inside the reactor was expected to lead to further decrease on the simulated electric field, due to the perturbation of the electric field caused by the reflectance of the microwave radiation by the vapour bubbles[131, 186]. The maximum electric field and subsequently a steep temperature increase was observed in the middle of the capillary – on the curve of the reactor – since this position is in parallel to the microwave port resulting in maximum energy dissipation[131].

Figure 4-7a shows the average final sizes of the Au NPs synthesised in the two-stage process under 0 – 25 W input microwave power, while Figures 4-7b – e show the TEM images of the synthesised Au NPs. Increasing the input microwave power from 5 W to 15 W, average particle size increased up to ~ 20 % (from 20.7 ± 3.0 nm to 24.9 ± 4.3 nm) and dropped to 18.0 ± 3.5 nm at 25 W (Figure 4-7a). There seemed to be a level of control of the Au NPs particle size in respect to the input microwave power in the two-stage synthesis process. A statistical analysis was performed for the different particle sizes obtained from TEM imaging for 5 – 25 W input microwave power, via the Welch's unpaired t-test[187] – due to the unequal sample variances – at 95 % confidence level ($p - value$ threshold: < 0.05)[188].

The mean particle size of the experimentally measured synthesised gold nanoparticles (via TEM imaging) is given by:

$$\bar{d}_{exp} = \frac{\sum d_i}{N} \quad \text{Eq. 4-1}$$

and the standard deviation of the particle size distribution is given by:

$$\sigma_d = \sqrt{\frac{\sum \left(d_i - \bar{d}_{exp}\right)^2}{N-1}} \quad \text{Eq. 4-2}$$

Where d_i is the measured particle size and N is the number of the measured particles of the sample.

The statistic t showing the difference of the samples' means relative to samples' variations (expressing the magnitude of discrepancy from null hypothesis) is calculated by[187]:

$$t_{ij} = \frac{\bar{d}_{exp,i} - \bar{d}_{exp,j}}{\sqrt{\frac{\sigma_{d,i}^2}{N_i} + \frac{\sigma_{d,j}^2}{N_j}}} \quad \text{Eq. 4-3}$$

Where $\bar{d}_{exp,i}$, $\sigma_{d,i}$ and N_i are the mean particle size, the standard deviation and the sample size of sample i.Similarly for sample j.

The degrees of freedom of the variance are estimated by[187]:

$$DF_{ij} = \frac{\frac{\sigma_i^2}{N_i} + \frac{\sigma_j^2}{N_j}}{\frac{\sigma_i^4}{DF_i N_i^2} + \frac{\sigma_j^4}{DF_j N_j^2}} \quad \text{Eq. 4-4}$$

Where DF_i is the degrees of freedom of the sample i, equal to $v_i = N_i - 1$. Similarly for sample j.

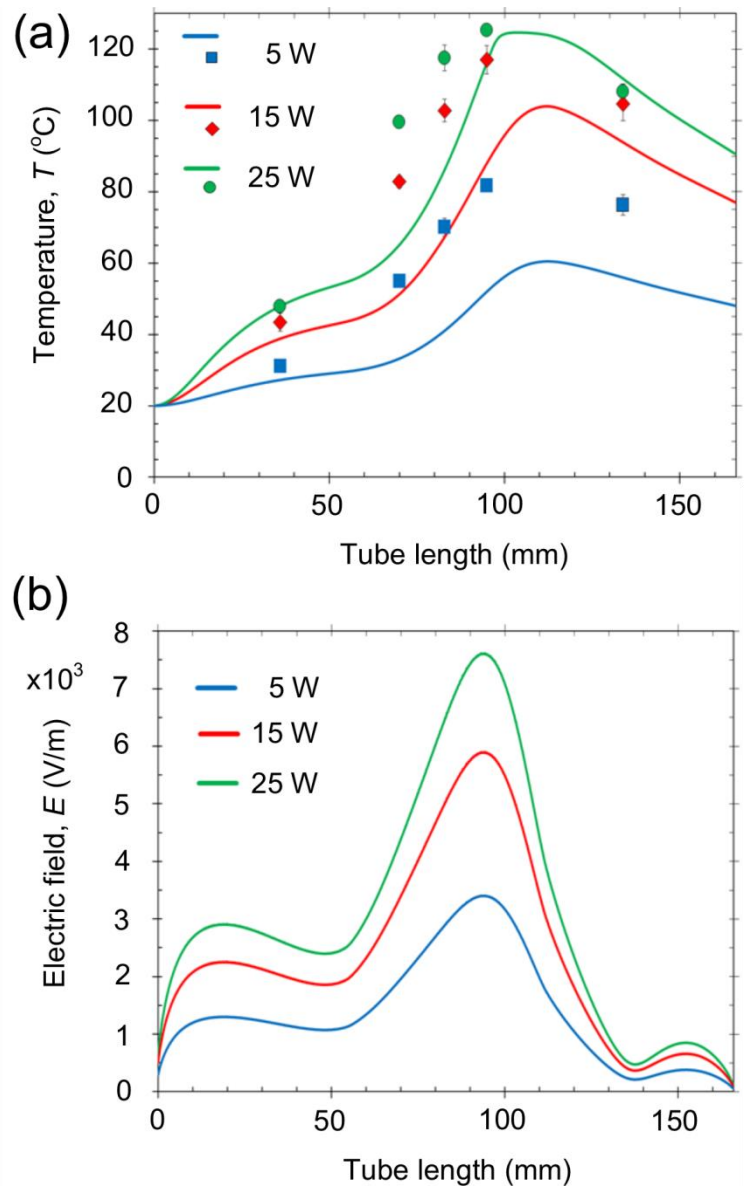

Figure 4-6 a) Temperature and b) electric field profile throughout the tube length, using water as medium (solid lines: computational results, markers: experimental results). Microwave power, 5 – 25 W; inlet flow rate, 0.5 ml/min; residence time under microwave heating, 90s; system pressure, 2.3 bara; frequency, 2.47 GHz (error bars indicate the standard deviation between 3 repeats).

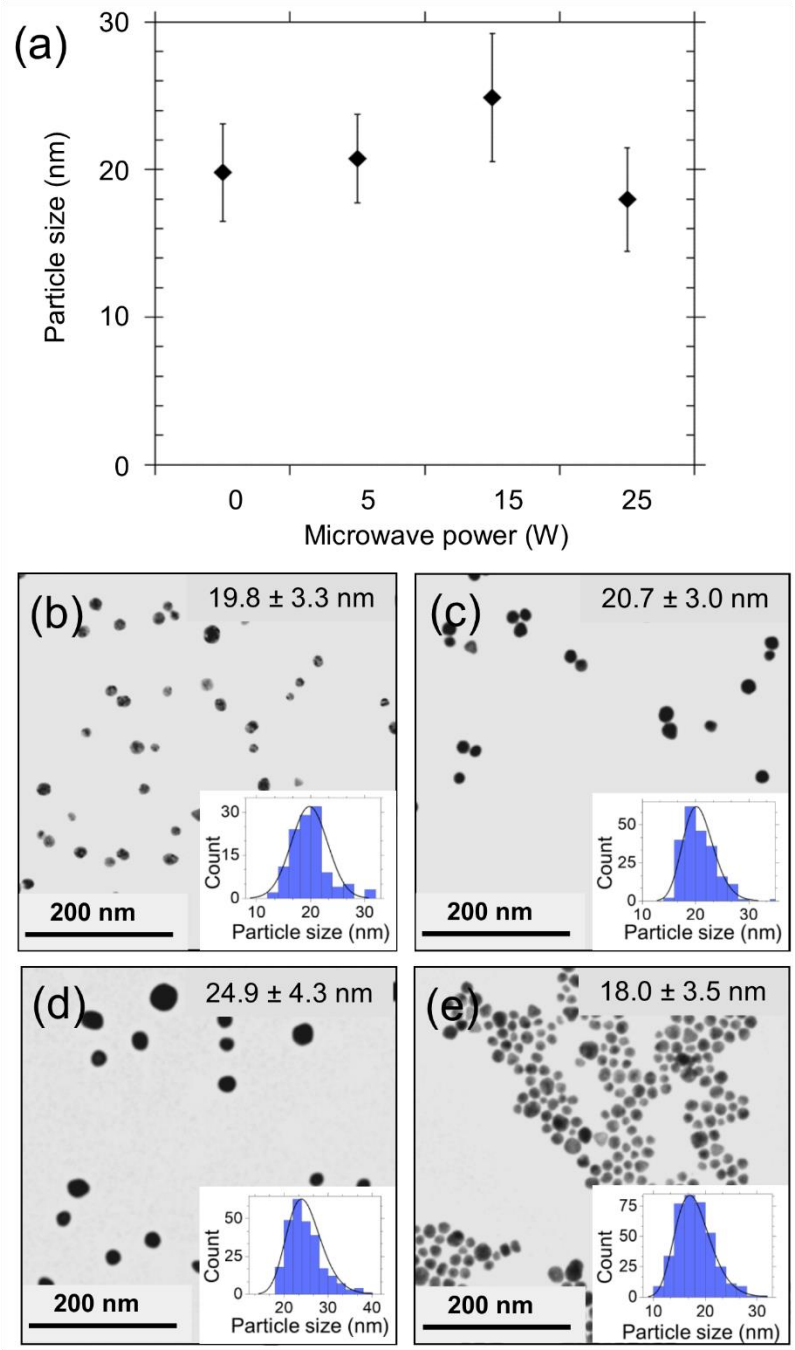

Figure 4-7 a) Particle size of gold nanoparticles synthesised under different input microwave powers in the two-stage system, given by TEM. TEM image of the gold nanoparticles synthesised at b) 0 W (only conventional heating), c) 5 W, d) 15 W, e) 25 W microwave power. Histograms display the particle size distribution given by TEM. [$HAuCl_4$] (after mixing), 0.25 mM; [Na_3Ct] (after mixing), 1.5 mM; total inlet flow rate, 0.5 ml/min; microwave heating reactor volume, 0.75 ml, residence time in microwave reactor, 90 s; conventional heating reactor volume, 10 ml, residence time in conventional heating reactor, 20 min; temperature in conventional heating reactor, 90 ^{o}C; system pressure, 2.3 bara.

Table 4-1 includes the parameters and the $p-values$ of the Welch's unpaired t-test for the particle sizes obtained for 5 – 25 W microwave power, showing that the obtained Au NPs sizes via TEM imaging were statistically significant comparing all three different microwave power levels ($p-value <$ 0.05). Considering the temperature profile inside the microwave reactor depicted in Figure 4-6, increasing the input microwave power, the electric field and subsequently the longitudinal temperature increased. Although, the nucleation rate increases at higher temperatures resulting in more nuclei and subsequently smaller particle sizes[38], in this study the nucleation and growth rates should be highly affected by the non-uniformity of the longitudinal temperature profiles. The observed larger particle size synthesised at 15 W input microwave power compared to the respective Au NPs for 25 W, could be attributed to: 1) the non-isothermal temperature profile in the tube, which affects strongly the nucleation and growth rates and 2) the particle deposition on the tube walls affecting the synthesis due to loss of Au^{3+} and Au^{0} . It should be noted that the fouling was realised at a greater extent under 25 W, and although unclear, it could be possibly related to the higher temperatures achieved along the reactor length. It cannot be estimated at which position of the tube particle growth could start, however, both the nucleation and growth rates should vary along the tube length as they temperature dependant[38, 189]. There has also been an extensive discussion in the literature, regarding the possibility of non-thermal effects of the microwave radiation on the synthesis reactions[75]. Due to the electromagnetic nature of the microwave heating, it is assumed that microwave radiation could interact with the reacting molecules and compounds enhancing the synthesis, although it still remains a controversial issue[190]. Here, non-thermal effects of the microwave heating were not considered to affect the Au NPs synthesis, due to the strong polarisation of the medium (water)[178] (Section B.1, Appendix B).

Table 4-1 Analysis of Welch's unpaired t-test of the gold nanoparticle sizes obtained under the 3 different input microwave power (P_{in}) levels via the two-stage synthesis.

$\boldsymbol{t_{5W-15W}}$	12.53	$\boldsymbol{t_{5W-25W}}$	9.93	$\boldsymbol{t_{15W-25W}}$	21.54
$\boldsymbol{DF_{5W-15W}}$	463	$\boldsymbol{DF_{5W-25W}}$	501	$\boldsymbol{DF_{15W-25W}}$	483
$\boldsymbol{p-value}$	$2.42 \cdot 10^{-30}$	$\boldsymbol{p-value}$	$1.41 \cdot 10^{-21}$	$\boldsymbol{p-value}$	$1.55 \cdot 10^{-72}$

$\boldsymbol{P_{in}}$ = 5W: $\bar{\boldsymbol{d}}_{\boldsymbol{exp,5W}}$ = 20.7 nm; $\boldsymbol{\sigma_{5W}}$ = 3.0 nm; $\boldsymbol{N_{5W}}$ = 215 particles

$\boldsymbol{P_{in}}$ = 15W: $\bar{\boldsymbol{d}}_{\boldsymbol{exp,15W}}$ = 24.9 nm; $\boldsymbol{\sigma_{15W}}$ = 4.3 nm; $\boldsymbol{N_{15W}}$ = 262 particles

$\boldsymbol{P_{in}}$ = 25W: $\bar{\boldsymbol{d}}_{\boldsymbol{exp,25W}}$ = 18.0 nm; $\boldsymbol{\sigma_{25W}}$ = 3.5 nm; $\boldsymbol{N_{25W}}$ = 382 particles

Comparing with the synthesis under only conventional heating at 90 ^{o}C for 20 min residence time (0 W at Figure 4-7), the Au NPs average particle size was 19.8 ± 3.3 nm (Figure 4-7b) and it was comparable to the results obtained by the two-stage synthesis where microwave radiation was present at 5 W and 25 W. However, when the input microwave power was 15 W, average particle size was ~ 5 nm larger than the results at 0 W. This indicates that varying the microwave power, and therefore the temperature profile, may affect the final particle size, although the growth stage is a more decisive factor for the completion and final size of the Au NPs. Hostetler *et al.*[140] and Kim *et al.*[151] examined the synthesis of colloidal lead selenide nanoparticles (PbSe NPs) and ternary $CuInSe_2$ NPs, respectively, in two-stage multi-phase continuous flow reactors. In their studies reaction initiation/nucleation started in a single-mode microwave heating (MWH) reactor zone followed by a conventional heating (CH) reactor zone (oil-bath). According to their findings, varying the input microwave power and the temperature in the MWH stage provided better control on the particle size and crystallinity of the final structures.

For the estimation of the productivity of Au NPs under the studied conditions, we examined the Au^0 concentration on the produced Au NPs based on the absorbance of the UV-Vis spectra at 400nm (A_{400}), based on the work of Hendel *et al.*[84] and Yue *et al.*[191]. The estimated yield for the two-stage process increased from 65 % for 0 W (only conventional heating) up to 79 % for 25 W input microwave power (Figure B-4, Appendix B). It is worth noting that the lower productivity could be related to the particle deposition on the reactor walls, showing the positive effect of MWH on the synthesis process. The extinction coefficient is expected to increase as the particle

size increases[84], thereof the absorbance A_{400} and subsequently the concentration of the Au^0 is subject to the particle size distribution. This methodology is sufficient in the current estimation due to the similar particle sizes and polydispersity of the synthesised samples between the 0 W to 25 W input microwave power.

4.3.2.3. Effect of residence time under microwave radiation on particle size

The effect of residence time under microwave heating in the two-stage process for Au NPs synthesis was studied by varying the total flow rate of the inlet streams from 0.375 ml/min to 0.7 ml/min (corresponding to 120 s and ~ 60 s residence time under microwave heating, respectively), while keeping the input microwave power constant at 25 W. The growth step in series was set at 20 min residence time and temperature at 90 ^{o}C. Figure 4-8 shows the temperature profile throughout the tube length, at different microwave power levels total inlet flow rates. Simulations of the microwave heating inside the U-shape reactor were performed using the FEM tool following the methodology described in Chapter 3. Increasing the inlet flow rate, the residence time under microwave heating decreases, which lowers the temperature profile by 5 – 20 ^{o}C due to the volumetric nature of microwave heating. Temperature was higher for 0.375 ml/min total inlet flow rate (due to the longer residence time in the tube) resulting in greater drop closer to the tube outlet. It is worth noting that the observed discrepancies between the experimental and numerical results are similar as previously described (see Chapter 3). Interestingly, the efficiency of the microwave system increased by increasing the inlet flow rate from 0.375 ml/min to 0.7 ml/min, as the calculated absorbed microwave power by the medium in the reactor – based on the FEM model – increased from 4.1 W to 5 W.

Figure 4-9 shows the average final sizes of the Au NPs synthesised in the two-stage process under 0.375 ml/min to 0.7 ml/min total inlet flow rate and the respective TEM images of the synthesised Au NPs. The effect of the residence time under microwave heating was studied in the two-stage process, to evaluate any effect of the microwave heating step when followed by the conventional heating in series. The concentration of the $HAuCl_4$ after mixing was kept constant at 0.25 mM and the $[Na_3Ct]/[HAuCl_4]$ ratio was 6/1. Although the inlet flow rate and subsequently the residence time in the MWH reactor was varied, the residence time under

conventional heating was kept constant at 20 min, by varying the reactor length (see Section 4.2.2). Figure 4-9a shows the average particle size obtained after the two-stage synthesis using both microwave and conventional heating. The average Au NPs size was similar for all inlet flow rates studied and it fluctuated around ~ 19 nm (ranging between 18 – 20 nm) while dispersity was 18 – 21 % (Figure 4-9 b – d). Hence, varying the residence time inside the microwave reactor did not have a major effect on the synthesis process presumably because in all flow rates similar maximum temperatures were reached (i.e. 120 – 125 ^{o}C) and the residence time inside the microwave reactor was not sufficient to affect the nanoparticle synthesis. Therefore the particle size remained unaffected by the residence time as the synthesis is dependent on the temperature, while longer residence times under MWH indicate that particle growth took place in the microwave reactor but the effect on the particle size was negligible.

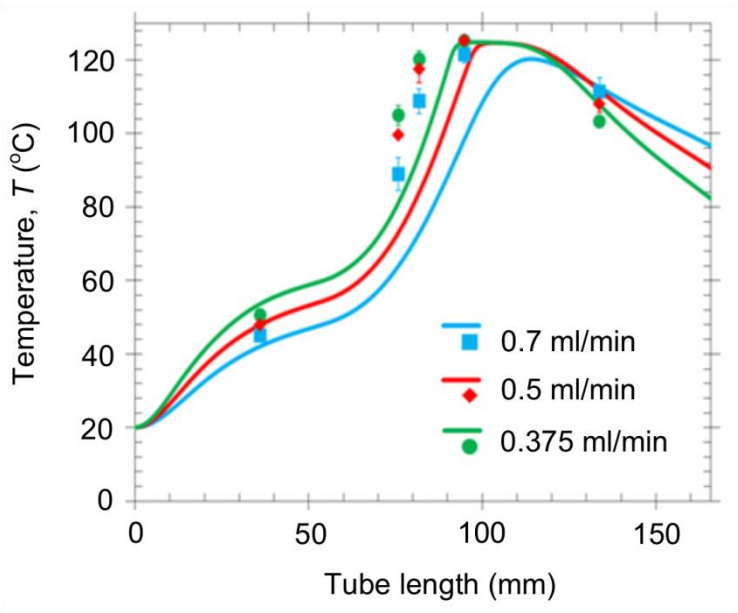

Figure 4-8 Temperature profile throughout the tube length, using water as medium (solid lines: computational results, markers: experimental results). Inlet flow rate, 0.375 – 0.7 ml/min; microwave power, 25 W; residence time under microwave heating, 90s; system pressure, 2.3 bara; frequency, 2.47 GHz (error bars indicate the standard deviation between 3 repeats). The results of the temperature profile for 0.7 ml/min were obtained from Damilos *et al.*[186]

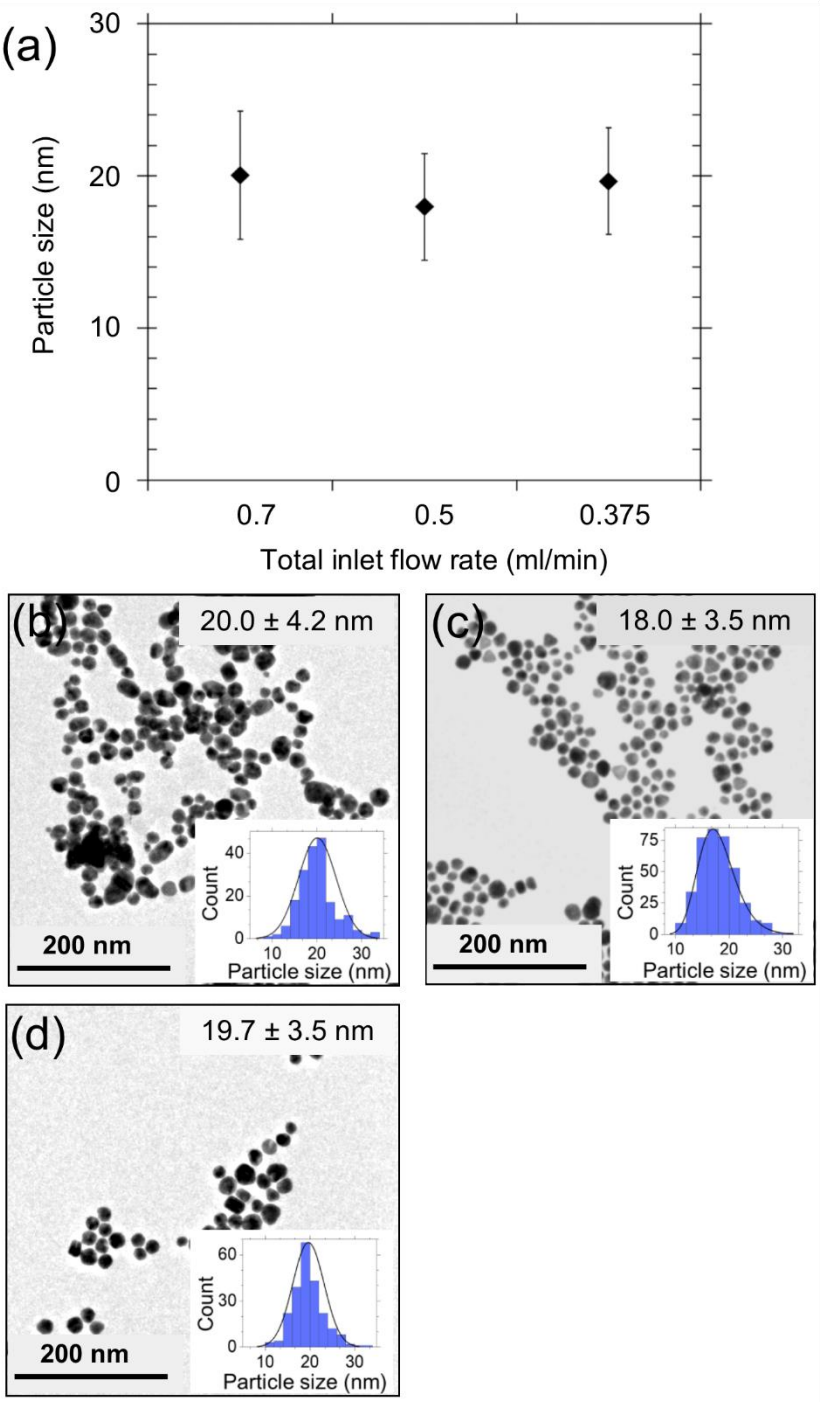

Figure 4-9 a) Particle size of gold nanoparticles synthesised under different inlet flow rates in the two-stage system, given by TEM. TEM image of the gold nanoparticles synthesised at b) 0.7 ml/min, c) 0.5 ml/min and d) 0.375 ml/min total inlet flow rate. Histograms display the particle size distribution given by TEM. [$HAuCl_4$] (after mixing), 0.25 mM; [Na_3Ct] (after mixing), 1.5 mM; microwave heating reactor volume, 0.75 ml, residence time in microwave reactor, 90 s; conventional heating reactor volume, 7 – 14 ml, residence time in conventional heating reactor, 20 min; temperature in conventional heating reactor, 90 ^{o}C; system pressure, 2.3 bara.

4.3.3. Factors influencing particle polydispersity under microwave heating

In all above synthesis scenarios, the synthesised Au NPs were of similar size and high dispersity despite the varying input microwave power and the inlet flow rate. There are three factors that could be influencing the final synthesised Au NPs under microwave heating:

1) The residence time distribution in the tube reactor
2) The non-uniform longitudinal temperature profile
3) The particle deposition (fouling) on the reactor walls

Although the flow profile was laminar in the discussed flow rates with Reynolds number varying between 3.8 – 7.1, the residence time distribution (RTD) resembled the laminar flow reactor profile rather than the plug flow reactor (PFR) behaviour describing the milli- and micro-reactors[192]. In nanoparticle synthesis the diffusivity changes over time or more appropriately over the length of the reactor. The diffusion coefficient of the aqueous reactants is in the order of ~ 10^{-9} m^2/s. At the same time, the respective coefficient of the synthesised Au NPs – calculated by the Stokes-Einstein equation – decreases by the increase of the particle size reaching down to ~ 10^{-11} m^2/s for 20 nm Au NPs (Section B.4, Appendix B). As particle size increase, the transport rates of convection over diffusion increase and they are estimated via the Bodenstein number (Bo) for a given reactor (L/d_t: reactor length over inner tube diameter):

$$Bo = \frac{ud_t}{D_m} \qquad \text{Eq. 4-5}$$

Where u is the liquid velocity in the tube, d_t is inner tube diameter and D_m is diffusion coefficient.

Figure 4-10 shows the determination of the residence time distribution of the Au NPs for various sizes as well as the gold precursor in the MW and the CH reactor[193]. In case of the microwave reactor (filled marks), as the precursor was being reduced to the formation of nuclei (2 nm Au NPs)[65, 194] the flow remained within the intermediate regime between axial dispersion and pure convection. However, as the particles grew further to their final size (10 nm and 20 nm), the flow fell within the pure

convection regime, indicating negligible molecular diffusion without intermixing between the flow streamlines. A similar issue was addressed by Panariello *et al.*[43] studying the RTD of the synthesis of silica nanoparticles, showing that in a single phase micro-reactor the growing particles fell within the same regime (pure convection) explaining the larger particle size distribution observed in continuous flow in comparison with the batch synthesis. In this study, the use of a micromixer prior to the MWH and CH reactors ensured the complete mixing of the two reactants. However, the RTD inside the MWH reactor was far from the plug flow reactor behavior. In the initial stages of gold nanoparticle synthesis – reduction of the gold precursor to Au^0 and the formation of nuclei of ~ 2 nm – the RTD fell within the intermediate regime between the pure convection and axial dispersion. Thus, as the reduction and nucleation takes place, there is limited axial diffusion between the streamlines, minimising the diffusion of the gold species and Au^0, potentially hindering the homogeneous nucleation of gold particles. As the particles grow (i.e. 10 nm or 20 nm), their diffusion coefficient decreases and the RTD moves to the pure convection regime, thereafter every streamline behaves as an individual plug flow reactor without cross sectional micromixing along the stream lines leading to non-homogenous particle growth[43, 193]. Considering the coiled formation of the growth CH reactor, the RTD fell within the intermediate regime between the pure convection and axial dispersion; thus it could be assumed that molecular diffusion was not negligible, but the convective forces were still prevailing over the diffusive forces. Also, in the CH reactor, the calculated Dean number was 0.7 – 1.2 for the studied inlet flow rates, showing that the viscous forces were dominant and there was no effect of the centrifugal forces which could enhance the radial mixing[195, 196] (Table B-2, Appendix B). Shalom *et al.*[197] used a microfluidic chip for the synthesis of 2 – 4 nm thiol-capped Au NPs, where they addressed the importance of the residence time distribution with respect to the particle polydispersity, explaining the high particle size distribution (20 – 24 %) when their system was operating as a laminar flow reactor. To approach the PFR conditions, Sebastian Cabeza *et al.*[44] used a two-phase flow system in a microfluidic device for the synthesis of monodisperse aqueous Au NPs (3 – 5 nm) using toluene, resulting to 7 – 8 % dispersity. The use of two-phase flow via the introduction of an immiscible continuous organic solvent would result in a droplet-like flow pattern, in which each aqueous droplet would act as a plug flow reactor optimising the RTD and minimising the particle dispersity[43]. However, the use of two liquids of different dielectric properties (polar and non-polar) would increase the

depolarization of the electromagnetic field in the MWH reactor decreasing the efficiency of the microwave heating[131].

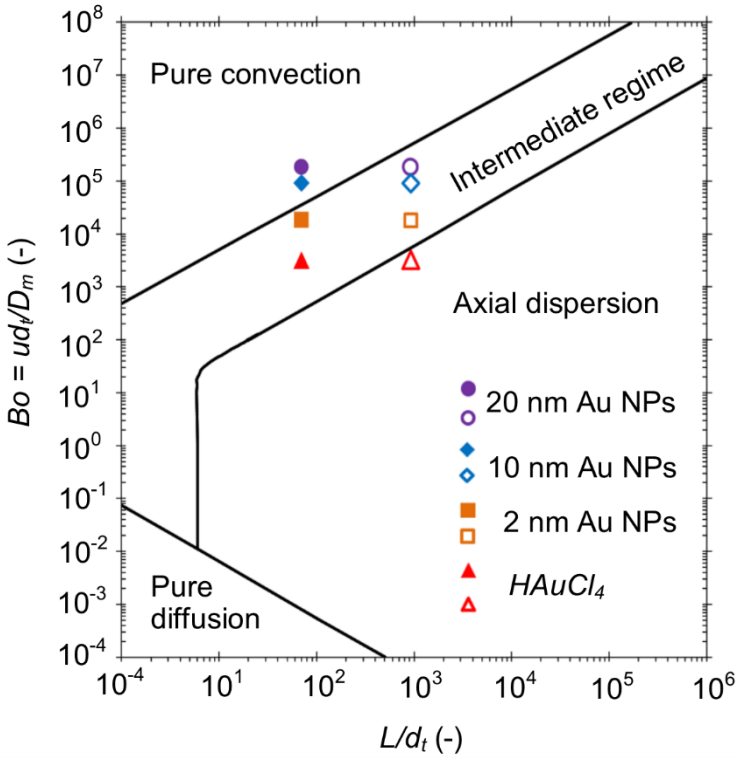

Figure 4-10 Residence time distribution determination for the gold precursor ($HAuCl_4$), the gold nuclei (2 nm Au NPs) and the synthesised gold nanoparticles of 10 – 20 nm in the microwave reactor (filled marks) and the conventional heating reactor (empty marks). (see Section B.4, Appendix B).

The work of Turkevich *et al.*[34] and Wuithschick *et al.*[38] investigated experimentally the effect of temperature on particle size showing a minimum particle size obtained at 80 ^{o}C and 60 ^{o}C, respectively, depending on the process parameters. Following the work of Wuithschick *et al.*[38], as the temperature increases from room temperature to 60 ^{o}C, the nucleation rate increases, producing more nuclei and reducing the amount of precursor for growth; final particle size decreases as the nucleation rate becomes higher[69]. However, above 60 ^{o}C particle aggregation is also observed, resulting in larger particles[38, 194]. It should be noted that the above studies concerned batch systems of uniform temperature, showing the effect of temperature on the final particle size. As explained in Figures 4-6 and 4-8, the temperature profile is non-uniform across the length inside the MWH reactor resulting to a maximum close the middle of the reactor length, due to the electric field profile. As the temperature changes on the axial direction, the nucleation and growth rates would not be

homogenous in the reactor, but they will vary along the reactor length or even not completed at all, hindering the formation of nuclei or uniform particles under MWH. It is worth noting that the above results could affect also the growth stage under CH, despite the uniform temperature both in the radial and axial direction.

Another parameter affecting the nucleation and growth rates is the loss of material (gold precursor) on the reactor wall due to particle deposition. Wagner and Köhler[99] addressed this issue on the synthesis of Au NPs in microreactors, while Huang *et al.*[96] investigated the particle deposition during the continuous Au NPs synthesis via *Turkevich method* and divided the fouling into two categories, namely "dark fouling" and "pink fouling". The former consists of positively charged gold ions and citrate-gold complexes, as well as Au^0 caused by the electrostatic attraction from the negatively charged PTFE tube. The "pink fouling" consists of synthesised negatively charged citrate-capped Au NPs which are irreversibly attached to the wall via van der Waals forces and can be removed only via the use of aqua regia. In this study particle deposition was observed as "dark fouling", "pink fouling" or even as elemental gold being deposited on the tube walls (Section B.5, Appendix B). Since fouling is related to loss of material, the loss of unreacted gold and citrate and Au^0 are expected to affect the propagation of nucleation and growth process (based on the proposed model by Kumar *et al.*[65] and Agunloye *et al.*[189] and the particle size and dispersity), whilst the loss of stable Au NPs via fouling will result only to loss of material lowering the process yield. The schematic in Figure 4-11 illustrates the expected particle formation and the RTD in the studied system, due to the non-isothermal temperature profile, poor micromixing related to the diffusivity of the particles and the fouling on the reactor walls.

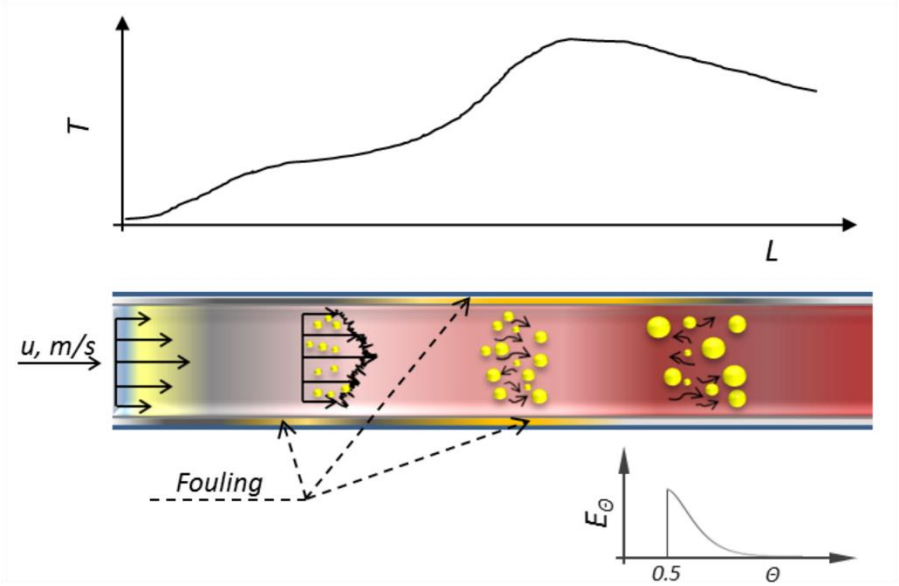

Figure 4-11 Schematic of gold nanoparticle synthesis illustrating the polydispersity in the formed colloidal solution in a milli-scare reactor under microwave heating. Temperature profile in non-uniform across the reactor length. Diffusion coefficient varies with the Au NPs size, resulting in flow within the pure convection regime. During the synthesis, gold nanoparticle deposition is observed on the inner reactor walls (fouling).

4.4. Conclusions

In this chapter the continuous synthesis of spherical citrate-capped gold nanoparticles using microwave heating was investigated. In the one-stage synthesis, where a single-mode microwave reactor was used, microwave power had negligible effect on the final particle size. However, to ensure completion of the reaction and stable colloidal solutions upon collection in the one-stage synthesis, the residence time under constant microwave power (25 W) increased from 90 s to 20 min. On the other hand, increasing the reactant ratio ($[Na_3Ct]/[HAuCl_4]$ ratio), particle size decreased and plateaued at ~ 15 nm between 3/1 – 20 /1 reactant molar ratio, showing similar results with previously reported studies in batch using conventional heating. Transferring the synthesis to a two-stage process, the reaction nucleation and initiation was realised in the microwave reactor, while growth was completed in the second stage under conventional heating ensuring completion of the reaction and production of stable Au NPs. In the two-stage synthesis, the reactants were mixed

using a micromixer without preheating and speciating to avoid fouling i4n the mixer. Varying the input microwave power between 0 W (only conventional heating) and 25 W, there was a maximum on the average particle size for 15 W input power (24.9 nm), which could be attributed to the longitudinal temperature profile inside the MWH reactor. Increasing the inlet flow rate from 0.375 ml/min to 0.7 m/min under constant microwave power at 25 W, the residence time under microwave radiation decreased from 120 s to 60 s, resulting in a small decrease on the temperature profile. However, there was no observed variation on the particle size, despite the lower residence time in the MWH for reaction nucleation and initiation of growth. In the two-stage process, the particle size distribution in all cases ranged between 18 – 20%, which is similar to preciously reported Au NPs synthesis in single-phase flow reactors. This was proposed to be the combined outcome of the dominant convective forces over diffusion inside the reactor, the non-uniform longitudinal temperature profile under microwave heating and the loss of unreacted material due to the particle deposition (fouling) on the reactor walls. The aforementioned results provide adequate information on the benefits of microwave heating for gold nanoparticle synthesis, while outlining the challenges that need to be overcome for the development of a continuous synthesis platform and transferring the synthesis from batch to flow utilising a microwave heating reactor.

CHAPTER 5. Development of a predictive model for the targeted synthesis of citrate-capped gold nanoparticles

The challenge of high quality gold nanoparticles (Au NPs) for various applications has driven the research toward the investigation of robust mathematical models. A statistical correlation was developed for the determination of the process parameters (reactant concentrations and temperature) for targeted Au NPs size as well as the required reaction time. An extended semi-empirical model was also developed accounting for the reactant speciation, as well as the ratio of the citric acid to trisodium citrate concentration to adjust the synthesis pH at ~ 5.6 and ensure a highly reproducible synthesis. The effect of order of reactant addition and the solution pH were also examined to ensure the construction of a robust empirical correlation. Response surface models for the particle size and reaction time showed that only the gold precursor concentration and reactant ratio were statistically significant for the determination of the particle size, while the reaction time depended on the precursor concentration and the synthesis temperature. In the pH-adjusted *Turkevich* synthesis, where the pH was equal to ~ 5.6, the order of reactant addition had no effect on the synthesis results, while increasing the solution pH both particle size and reaction time increased. Results from this study provide a valuable tool for the process design for continuous synthesis of targeted and monodisperse gold nanoparticles.

5.1. Introduction

The increasing interest of nanotechnology in commercials products and their application in catalysis, electronic and biomedicine, has shifted the research to investigate the development of robust, sustainable processes for the production of high quality nanoparticles[31]. Gold nanoparticles (Au NPs) find application in healthcare and medicine after appropriate functionalisation which allow them to be used in drug and protein delivery[14], diagnostics[10], point-of-care diagnostic devices[13] and antimicrobial applications[8]. The unique properties of Au NPs depended on their size and shape, thus the research goal is the development of robust synthesis protocols and manufacturing models for targeted and monodisperse particles[79, 198].

In the past, various researchers have tried to conduct parametric studies and propose mathematical models for the synthesis of the desired Au NPs. Frens[83] studied the synthesis of 16 – 150 nm Au NPs by varying the concentration of the reducing agent and keeping the gold precursor concentration constant. On the other hand, Chow and Zukoski[82] decreased the gold precursor concentration under constant citrate amount, showing the reduction in the particle size by increasing the $Na_3Ct/HAuCl_4$ molar ratio. Similar parametric studies were conducted by other researchers such as Abid[184], Zabetakis *et al.*[199] and Schulz *et al.*[200] to understand the effect of process parameters on the final particle size and shape. Ji *et al.*[86] evaluated the effect of the solution pH on the particle size, showing that increasing the pH above 6.5, both particle size and reaction time increase. Kumar *et al.*[65] developed population balance numerical models to characterise the nucleation-growth mechanism of *Turkevich* method, resulting in limited agreement with the experimental results – as described by Agunloye *et al.*[194] – since the reactant speciation was excluded in their analysis. The work of Wuithschick *et al.*[38] and Kettermann *et al.*[40] provided detailed information on the role of reactant speciation on the particle size and reaction time, as well as explaining the effect of pH on both particle dispersity and reproducibility. Agunloye *et al.*[189] developed a mechanistic model predicting the size of seeds and final particles, however, the developed model could not provide the evolution of gold nanoparticles in time for the calculation of the required residence time for the targeted synthesis.

In the established *Turkevich* method (use of only $HAuCl_4$ and Na_3Ct), the order of the reactant addition seems to affect both the final particle size and the time required for the completion of the reaction. Wuithschick *et al.*[38] evaluated the effect of the reactant addition following the *Turkevich method* ([$HAuCl_4$] = 0.25 mM and [Na_3Ct] = 2.5 mM after mixing at 85 ^{o}C). According to their findings, during the *inverse Turkevich* method, the particle size was ~ 14 nm and the reaction time was ca. 35 min, while in the *direct Turkevich* method the particle size and the reaction time increased up to ~ 18 nm and ca. 50 min, respectively. This behaviour was related to the higher amount of $AuCl_4^-$ in the non-speciated gold precursor which was added in the preheated Na_3Ct during the *inverse* synthesis; preheating of the gold precursor shifts the speciation equilibrium towards its hydrolysed (passivated) forms resulting in less Au^0 and subsequently larger Au NPs. Oliveira *et al.*[90] developed a response surface model for the citrate-capped gold nanoparticles synthesis based on UV-Vis spectroscopy data, where the input variables were the concentration of trisodium citrate and the synthesis time. According to their findings and the developed model, the higher the concentration of the reducing agent and the synthesis time, the particle dispersity decreases as observed from the full-width at half-maximum (FWHM) of the surface plasmon resonance (SPR) peak. However, the developed model could not provide the necessary information for the targeted nanoparticle synthesis or the required reaction time.

In this chapter the development of a statistical correlation for the targeted synthesis of Au NPs within the range of 10 – 20 nm is presented, enabling the calculation of the experimental parameters required for the targeted synthesis of monodisperse Au NPs, as well as the estimation of the required reaction time. The proposed model takes into account the reactant speciation, the order of reactant addition and the solution pH, providing the necessary information for the design of continuous flow reactors.

5.2. Experimental section

5.2.1. Materials and methods

The reactants used were citric acid monohydrate (H_3Ct, $C_6H_8O_7 \cdot H_2O$, Sigma-Aldrich), trisodium citrate dihydrate (Na_3Ct, $Na_3C_6H_5O_7 \cdot 2H_2O$, Fisher Scientific) and Gold (III) chloride trihydrate ($HAuCl_4$, Sigma-Aldrich). Hydrochloric acid (HCl) 37% v/v, nitric

acid (HNO_3) and sodium hydroxide ($NaOH$, 2 M) used were supplied by Sigma-Aldrich. All chemicals were of analytical grade. Ultra-pure water (15 MΩ·cm) was used for all aqueous solutions throughout the experimental series. The UV-Vis absorption measurements and the time resolved UV-Vis spectra were carried out using a USB2000+UV-VIS-E spectrometer (Ocean Optics) connected to a DT-MINI-2-GS deuterium/tungsten halogen lamp light source (Ocean Optics) via the appropriate fibre optics. For the UV-Vis absorption spectra, the sample was placed in a 3 mL quartz cell (10.00 mm QS, Hellma Ltd), and spectral analysis was performed in the range of 200-800 nm. The cuvette and the polytetrafluoroethylene (PTFE)-coated magnetic stirrer (6 mm, Agilent Technologies) were cleaned with freshly prepared aqua regia solution (HCl:HNO_3, 3:1 molar ratio) followed by $NaOH$ for neutralisation and then rinsed thoroughly with water before each use, to ensure there was no particle deposition on the cuvette walls or on the magnetic stirrer.

The pH measurements were performed with a SevenCompact pH meter S220 (Mettler Toledo) equipped with an InLab Micro glass electrode (Mettler Toledo). The synthesised nanoparticles were characterised via transmission electron microscopy (TEM) imaging (JEM 2010–200 kV, JEOL) and differential centrifugal sedimentation (DCS) (CPS24000 Disc Centrifuge, CPS Instruments). TEM samples were prepared by dipping a drop of the sample solution onto a carbon film 200 mesh copper grid (C200 Cu, EM Resist Ltd) and letting it dry in air. Particle counts from the TEM image analysis was performed via Pebbles software to ensure accurate and unbiased particle sizing[177]. DCS analysis was performed by injecting ~ 0.1 ml of the colloidal Au NPs solution and the rotating speed was set at 24000 rpm. The assumed density of the citrate-capped Au NPs was 12.3 g/ml as it was shown to provide comparable results with TEM image analysis within 8 – 30 nm[49].

5.2.2. *In-situ* UV-Vis measurements

The data on the evolution of the particle size of gold nanoparticle and the construction of the regression models regarding the particle size and the reaction time were based on the *direct Turkevich* synthesis protocol described by Kettemann *et al.*[40]. In their study they varied the $HAuCl_4$ concentration and the reactant molar ratio, by keeping the pH of the colloidal solution at room temperature ~ 5.6[40]. According to their study, there is a “highly reproducible synthesis zone” at pH ~ 5.6,

which is related to the citrate species and the $HAuCl_4$ present during the reaction. The stock solutions used were a 5 mM $HAuCl_4$, as well as two freshly prepared solutions of 50 mM H_3Ct and 50 mM Na_3Ct. The H_3Ct and Na_3Ct solutions were mixed at a specific molar ratio (noted thereafter as $Citrate$) – prior to their addition to the reacting solution – to ensure the pH after mixing was ~ 5.6 for a given $HAuCl_4$ concentration (Table 5-1). Kettemann *et al.*[40] observed that there was no significant increase on the Au NPs size by increasing the gold precursor concentration after mixing above 0.5 mM, therefore the maximum [$HAuCl_4$] considered in this study was 0.5 mM. The reaction time data required for a targeted Au NPs synthesis were acquired using a peltier-based temperature-controlled cuvette sample compartment (Qpod 2e, Quantum Northwest) connected to the UV-Vis spectrometer. The equipment was calibrated for the temperature range, the desire volume, the cuvette used and the target stirring speed, thereby the set temperature was equal to $T_{set} = 1.015 \cdot T_{medium}$, where the T_{medium} is the desired temperature of the medium.

Table 5-1 Molar ratio of H_3Ct and Na_3Ct ($H_3Ct : Na_3Ct$) and final concentration of the two components in the freshly prepared $Citrate$ stock solution for different $HAuCl_4$ concentration and [$Citrate$]/[$HAuCl_4$] ratios. Adapted from Kettemann *et al.*[40]

[$HAuCl_4$] (mM)	[$Citrate$]/[$HAuCl_4$]	$H_3Ct : Na_3Ct$	[H_3Ct] (mM)	[Na_3Ct] (mM)
0.125	6/1	0.65 : 5.41	5.36	44.64
0.25		0.60 : 5.45	4.96	45.04
0.5		0.55 : 5.45	4.58	45.42
0.125	12/1	1.10 : 4.90	9.17	40.83
0.25		1.08 : 4.92	9.00	41.00
0.5		1.00 : 5.00	8.33	41.67

The graphical representation of the experimental procedure is displayed in Figure 5-1, where the gold precursor (aged for several days in the fridge at 4 ^{o}C, away from light) was added on a preheated volume of water stirring at maximum speed of 3000 rpm (without the formation of vortexes), and it was heated for 2 min to ensure the speciation of the gold precursor (*direct Turkevich* synthesis method). The freshly

prepared mixture of $Citrate$ (or Na_3Ct in case of the *standard Turkevich* synthesis) was then added and the reacting solution reached a final volume of 1.5 ml. The synthesis conditions are shown in Table 5-2. There was no reflux due to limitations of the set-up. Instead, a PTFE cap was placed on the top of the quartz cuvette to avoid water evaporation. The synthesis temperature was varied between 85 – 95 ^{o}C, since previous literature[38, 85] showed a dependency of the particle size and reaction time by temperature.

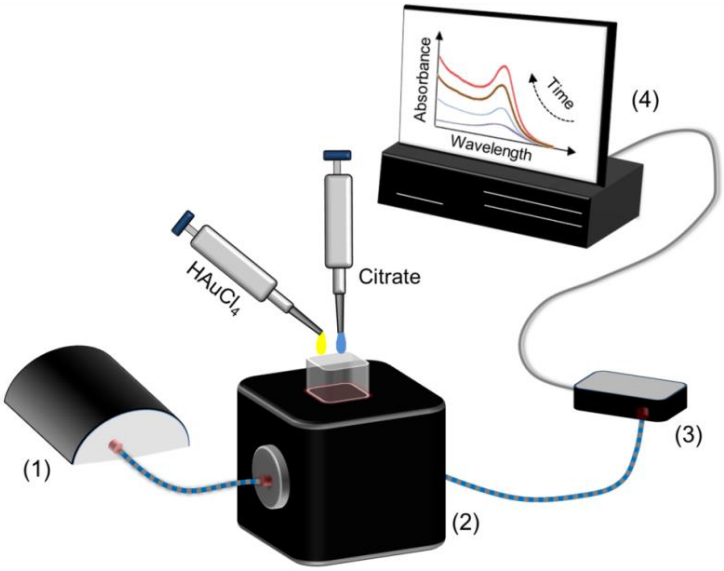

Figure 5-1 The experimental setup used for the gold nanoparticle synthesis *in situ* with UV-vis spectroscopy consisted of a (1) UV-Vis light source, (2) temperature–controlled sample compartment for particle synthesis, (3) spectrophotometer and (4) computer for the data acquisition.

Similar to the experimental procedure of the *direct Turkevich* synthesis and the graphical representation in Figure 5-1, the water was preheated at the target temperature, however, in the *inverse Turkevich* method, the reducing agent was added first and it was let to speciate for 2 min, followed by the addition of the aged gold precursor. The final volume of the reacting solution was again 1.5 ml. Additionally, in the *both speciation Turkevich* method, the reducing agent (either Na_3Ct only or the mixture of Na_3Ct and H_3Ct) was preheated at the target temperature, quenched and cooled at room temperature, to ensure the speciation of the reducing agent. For the Au NPs synthesis in this *Turkevich* method, the gold precursor was added on the preheated water solution and it was let to speciate for 2 min prior to the addition of the speciated reducing agent. The reactant concentrations

and synthesis conditions used for the evaluation of particle size and reaction time via the *direct, inverse and both speciated Turkevich* synthesis methods are shown in Table 5-2 for [$HAuCl_4$] = 0.25 mM and [$Citrate$]/[$HAuCl_4$] = 6/1 at 95 ^{o}C

Table 5-2 Final reactant concentrations in the cuvette and required volumes from the stock solutions of $HAuCl_4$ and $Citrate$ (5 mM and 50 mM, respectively) and water (H_2O) in the 1.5 ml batch experiments for the gold nanoparticle synthesis, as well as the final pH of the synthesised colloidal solutions, varying the [$HAuCl_4$] at different [$Citrate$]/[$HAuCl_4$] ratios. Adapted from Kettemann *et al.*[40]

[$HAuCl_4$] (mM)	[$Citrate$]/ [$HAuCl_4$]	[H_3Ct] (mM)	[Na_3Ct] (mM)	V_{HAuCl_4} (µl)	$V_{Citrate}$ (µl)	V_{H_2O} (µl)	pH
0.125	6/1	0.08	0.67	38	23	1440	5.64
0.25		0.15	1.35	75	45	1380	5.67
0.5		0.28	2.73	150	90	1260	5.65
0.125	12/1	0.28	1.23	38	45	1418	5.73
0.25		0.54	2.46	75	90	1335	5.66
0.5		1.00	5.00	150	180	1170	5.65

The UV-Vis data acquisition started 1 min before the addition of the reactants in the preheated water, to ensure the detection of the gold speciation and the Au NPs synthesis; the spectra acquisition time was set at 500 ms. Reaction time was estimated via a Python script* (Python Software v. 3.6)[201-204], indicating the completion of the reaction. Reaction time was estimated by monitoring the evolution of the wavelength and the absorbance of the surface plasmon resonance peak and it was corresponded to the time when these values plateaued and the variation of the absorbance of the SPR peak compared to its asymptotical value was less than 1%.

* The Python script was developed by Dr Hendrik du Toit and Dr Anand N. P. Radhakrishnan (Department of Chemical Engineering, UCL)

5.2.3. Statistical analysis

A statistical analysis was performed using the JMP Pro software (v.14.1.0, SAS Institute Inc) using analysis of variance (ANOVA) method at 95% confidence level and least square fit. A factorial analysis was performed to assess the effect of different factors and the interactions between the multifactor experiments on the target response. The developed response surface models (RSM) allowed the screening of the effects of individual factors or the interplay of multiple factors at several levels on a particular response, as well as optimisation of the synthesis conditions due to the interconnection of the various parameters for a targeted response[90, 205]. This analysis justified the adequacy of the derived regression models[90, 206-208]. The mathematical model relating factors and responses for a typical regression problem takes the following form[205]:

$$\hat{Y} = \beta_0 + \sum_{i=1}^{K} \beta_i X_i + \sum_{i=1}^{K} \beta_{ii} X_i^2 + \sum_{i=1}^{K} \sum_{j=2}^{K} \beta_{ij} X_i X_j + \epsilon \qquad \text{Eq. 5-1}$$

Where $\hat{Y}$ is the response (in this case the mean size of the synthesised gold nanoparticles or the synthesis reaction time), X_i and X_j are the independent variables (experimental factors), β_0 is the intercept of the regression model, β_i are the coefficients of the linear terms, β_{ii} are the coefficients of the quadratic terms, β_{ij} are the coefficients of the interaction terms and ϵ is the stochastic error term. The regression model for three factors (X_1, X_2 and X_3) transforms in the second order equation:

$$\hat{Y} = \beta_0 + \beta_1 X_1 + \beta_2 X_2 + \beta_3 X_3 + \beta_{12} X_1 X_2 + \beta_{13} X_1 X_3 + \beta_{23} X_2 X_3 + \beta_{11} {X_1}^2 + \beta_{22} {X_2}^2 + \beta_{33} {X_3}^2 \qquad \text{Eq. 5-2}$$

Due to their effect on the particle size and reaction time as described in the literature[38, 40], the selected factors in the present study were the gold precursor concentration after mixing (X_1), the reactant molar ratio [$Citrate$]/[$HAuCl_4$] (X_2) (where $Citrate$ is the mixture of H_3Ct and Na_3Ct) and the synthesis temperature (X_3). In order to ensure high reproducibility of the synthesis, the model was constrained at pH equal to 5.6.The final pH depends on the concentration of both H_3Ct and Na_3Ct

as well as of $HAuCl_4$. Hence the RSM includes only the $Citrate$ as a mixture of H_3Ct and Na_3Ct and the final concentration of the two individual components would be estimated either experimentally[40] or using a supplementary model for calculation of all concentrations for the targeted synthesis (see Section 5.3.3.2). The levels of the gold precursor concentration after mixing that was used in this study was 0.5 mM, 0.25 mM and 0.125 mM. The levels for the $Citrate/HAuCl_4$ molar ratio was 6/1 and 12/1 and the levels for the synthesis temperature was 85 ^{o}C and 95 ^{o}C.

The fitting test within the 95 % significance against the null hypothesis (that the regression coefficients β_i, β_{ii} and β_{ij} are zero and there is no relationship between the factors and the response), was examined by the Fisher's statistical test (F-test), the coefficient of determination R^2 and the adjusted coefficient R^2_{adj}. The degrees of freedom (DF) representing the number of independent values that can vary for each source of variation (model, residual and total) are given by:

$$\begin{cases} DF_{model} = k \\ DF_{total} = n - 1 \\ DF_{residual} = DF_{total} - DF_{model} \end{cases} \quad \text{Eq. 5-3}$$

Where k is the number of model parameters (excluding the intercept) and n is the number of experimental runs.

The sum of squares (SS) for each source of variation (model, residual and total) are given by:

$$\begin{cases} SS_{residual} = \sum_{i=1}^{n} \left(\hat{Y}_i - Y_{actual,i}\right)^2 \\ SS_{total} = \sum_{i=1}^{n} \left(\hat{Y}_i - \bar{Y}\right)^2 \\ SS_{model} = SS_{total} - SS_{residual} \end{cases} \quad \text{Eq. 5-4}$$

Where, $\hat{Y}_i$ is the response value for the run i, $\bar{Y}$ is the sample mean and $Y_{actual,i}$ is the actual value for the run i. SS_{total} represents the total variation of the response value from the average response. $SS_{residual}$ shows the variability of the response that

cannot be explained by the regression model. SS_{model} shows the variability of the model.

The mean square (MS) for each source of variation (model and residual) are given by:

$$\begin{cases} MS_{model} = \dfrac{SS_{model}}{DF_{model}} \\ MS_{residual} = \dfrac{SS_{residual}}{DF_{residual}} \end{cases} \quad \text{Eq. 5-5}$$

The $F - value$ of the developed model is given by:

$$F - value = \frac{MS_{model}}{MS_{residual}} \quad \text{Eq. 5-6}$$

The F-test includes the comparison of the model's $F - value$ with the critical value at 95% confidence considering the model and the residual degrees of freedom: $F_{0.95}(DF_{model}, DF_{residual})$. $F - value > F_{0.95}(DF_{model}, DF_{residual})$ describes an adequate model indicating a good predictability. The values of $F_{0.95}(DF_{model}, DF_{residual})$ can be found by the F-distribution tables for the given confidence and DF_{model} and $DF_{residual}$ values[209].

The coefficient of determination (R^2) representing the variability of the model and therefore the model's accuracy, is given by:

$$R^2 = \frac{SS_{model}}{SS_{total}} \quad \text{Eq. 5-7}$$

The adjusted coefficient (R^2_{adj}) of the developed model represents the variation of the model's accuracy with respect to the model parameters to evaluate the improvement of the model predictability by increasing the number of factors and is given by:

$$R^2_{adj} = 1 - \frac{MS_{residual}}{SS_{total}/DF_{total}} \quad \text{Eq. 5-8}$$

Additionally, the $p-value$ (probability of error) of individual factors was examined to evaluate the significance of each factor on individual response. The $p-value$ ranges between 0 – 1 and for the 95 % confidence considered in this study, the $p-value$ of each factor of the RSM models should be $p-value \leq 0.05$ to indicate that the factor has significant contribution on the response value. The developed models were

The mean particle size of the experimentally measured synthesised gold nanoparticles is given by:

$$\bar{d}_{exp} = \frac{\sum d_i}{N} \quad \text{Eq. 5-9}$$

Where d_i is the measured particle size and N is the number of the measured particles of the sample.

The standard deviation of the particle size distribution is given by:

$$\sigma_d = \sqrt{\frac{\sum\left(d_i - \bar{d}_{exp}\right)^2}{N-1}} \quad \text{Eq. 5-10}$$

and the coefficient of variation of the particle size distribution is given by:

$$CV = \frac{\sigma_d}{\bar{d}_{exp}} \quad \text{Eq. 5-11}$$

5.3. Results & discussion

5.3.1. Preliminary results on the effect of order of reactant addition

Prior to the development of the statistical model for the targeted colloidal gold synthesis, the order of reactant addition was examined. This allowed the evaluation of possible effects of the addition order on the particle size and the reaction time when the reducing agent consisted of H_3Ct and Na_3Ct (*pH adjusted Turkevich* method) and the pH of the colloidal solution was ~ 5.6. Any possible effects would affect the developed model, determining the use of a specific *Turkevich* method for

the model development or considering the order addition as an extra variable in the system.

The citrate-reduction method or *Turkevich* method describes the reaction between the gold precursor ($HAuCl_4$) and the Na_3Ct, which acts as reducing and stabilising agent and pH meditator[86]. As it has been discussed in the literature, there are two forms of *Turkevich* method depending on the order of addition of the two reactants [38]:

- The *direct Turkevich* method in which the reducing agent is added on preheated gold precursor.
- The *inverse Turkevich* method in which gold precursor is added on preheated reducing agent.

However, there is also the possibility of premixing the two components and heating the solution afterwards[49] or even preheating both reactants prior to mixing[200]. In any case, as described by Kettemann *et al.*[40] and Wuithschick *et al.*[38], preheating the reactants leads to their speciaton and driving which species being present in the reaction. This affects the final particle size and reaction time. In the stock solution of the gold precursor the expected pH is ~ 3.3 and $AuCl_4^-$ is the dominant species. The addition of the reducing agent increases the pH from acidic towards basic and shifts the gold equilibrium towards less reactive gold complexes ($AuCl_{3-x}(OH)_{1+x}^-$). Similarly, the reducing agent can act as an acid-base buffer and speciate via protonation/deprotonation. During the Au NPs synthesis, the citrate speciates reversibly ($Cit^{3-} + xH^+ \rightleftarrows H_xCit^{(3-x)-}$), or even be thermally and irreversibly oxidised to dicarboxy acetone (DCA) and acetone[40, 65]. The citrate species are also dependent on the pH of the solution; in the mild acidic conditions of the *Turkevich* method (pH ca. 4.8 – 6.5) HCt^{2-} is the dominant species, while in more acidic or basic conditions the dominant species are H_2Ct^- and Ct^{3-}, respectively[40]. DCA acts as a reducing agent for the gold precursor, which can affect the seed formation or the particle growth rate, but has negligible effect on the final particle size[38].

Two sets of experiments were performed on Au NPs synthesis with and without pH adjustment to 5.6 (where the reducing agent consisted of a $H_3Ct{:}Na_3Ct$ mixture or Na_3Ct only, respectively) – under similar conditions – keeping the reactant molar ratio ($[Citrate]/[HAuCl_4]$ or $[Na_3Ct]/[HAuCl_4]$) equal to 6/1 and the precursor concentration at 0.25 mM after mixing. Experiments ran at 95 ^{o}C with *in situ* UV-Vis

spectroscopy to assess the reaction time in all cases. The results of the *both speciated Turkevich* method on the particle size and reaction time were compared with the respective results using the *direct* and the *inverse Turkevich* methods. Figure 5-2a shows the results on reaction time required for the Au NPs synthesis with and without pH adjustment to 5.6, in which the reaction time was significantly lower (~ 4 min) in the pH adjusted system for all cases. In the *direct Turkevich method*, the gold precursor was left to speciate for 2 min upon its addition, which was sufficient to ensure the reactant speciation at 95 ^{o}C prior to the addition of the reducing agent as shown in Figure C-1 (Appendix C). As it can be seen from Figure 5-2a for the synthesis without pH adjustment (Na_3Ct only), the reaction time for the *inverse* and the *both* speciated *Turkevich* method resulted in similar reaction times (11.3 min) and lower than in the *direct Turkevich* method (12.3 min). At the same time, in case of the pH adjusted synthesis (H_3Ct:Na_3Ct mixture in Figure 5-2a), the reaction time fluctuated around 4.6 min in all three studied *Turkevich* methods. The absorbance and the peak of the SPR band for all studied conditions are shown in Figure C-2 (Appendix C). The larger difference in the reaction time between pH adjusted and classical *Turkevich* synthesis was related to the pH of the reducing agent. The pH of the solution in the classical *Turkevich* synthesis (where only Na_3Ct was present) was ~ 6.5, therefore the addition of the reducing agent shifts the gold equilibrium towards higher hydroxylation state (where $AuCl(OH)_3^-$ species is dominant), in comparison with pH adjusted synthesis (pH ~ 5.6), where the dominant species are $AuCl(OH)_3^-$ and $AuCl_2(OH)_2^-$ [40]. The hydroxylation of the gold precursor in all cases can be verified by the drop of the absorbance at the 313 nm wavelength of the UV-vis spectra (Figure C-1, Appendix C).

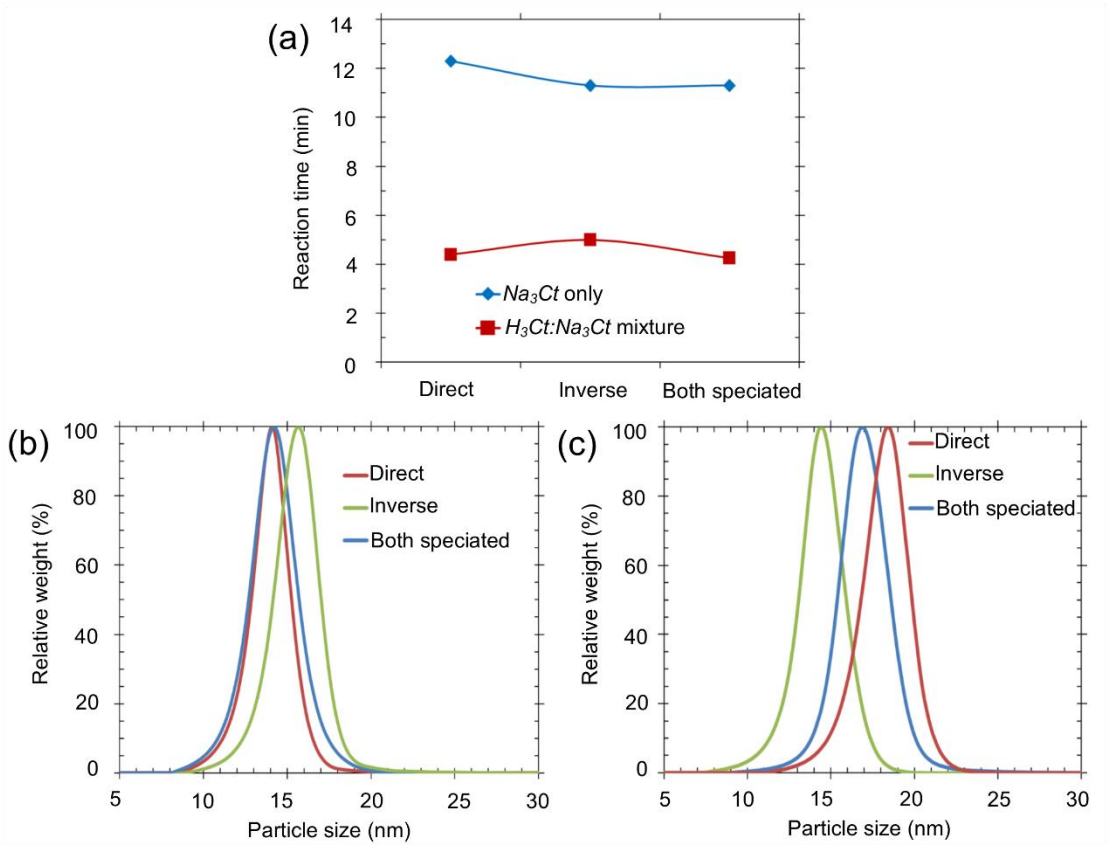

Figure 5-2 a) Reaction time required for the completion of the gold nanoparticle synthesis with ($\boldsymbol{H_3Ct}$:$\boldsymbol{Na_3Ct}$ mixture) and without ($\boldsymbol{Na_3Ct}$ only) pH adjustment to ~ 5.6, for *direct*, *inverse* and *both direct Turkevich* methods, obtained by *in situ* UV-Vis spectroscopy. Particle size distribution of the synthesised gold nanoparticles b) with and c) without pH adjustment to ~ 5.6, for *direct*, *inverse* and *both direct Turkevich* methods, from DCS. *Direct Turkevich* method: addition of the reducing agent at preheated gold precursor. *Inverse Turkevich* method: addition of the gold precursor at preheated reducing agent. *Both speciated Turkevich* method: addition of the preheated reducing agent at preheated gold precursor. Gold precursor concentration $\boldsymbol{HAuCl_4}$ (after mixing), 0.25 mM; reducing agent, $\boldsymbol{H_3Ct}$:$\boldsymbol{Na_3Ct}$ mixture concentration (after mixing): [$\boldsymbol{H_3Ct}$] = 0.15 mM, [$\boldsymbol{Na_3Ct}$] = 1.35 mM or $\boldsymbol{Na_3Ct}$ only concentration (after mixing): [$\boldsymbol{Na_3Ct}$] = 1.5 mM; temperature, 95 ^{o}C. Solid lines in (a) are used for visual aid.

Figures 5-2b and 5-2c show the particle size distribution for the pH adjusted and non-adjusted synthesis, respectively. During the synthesis without pH adjustment (Na_3Ct only), there was a ~ 4 nm difference in particle size between *direct* and *inverse* synthesis (particle size was 14.4 ± 1.6 nm for the *inverse* and 18.1 ± 10.5 nm for the *direct Turkevich* method), as shown by the DCS results. On the contrary, in the pH

adjusted synthesis there was a ~ 1 nm difference between *direct* and *inverse* synthesis (14.2 ± 1.4 nm and 14.9 ± 1.5 nm, respectively). Comparing the UV-Vis spectra over time between the pH adjusted *direct* and *inverse Turkevich* methods*,* it can be confirmed that the evolution of the absorbance at 313 nm and at the SPR peak were similar in both scenarios, confirming that the conditions during the reaction were similar in both cases (Figure C-3, Appendix C). Figure C-4 a – c (Appendix C) shows the reproducibility of the three pH adjusted *Turkevich* methods (*direct*, *inverse* and *both direct Turkevich* method), showing that the pH adjusted synthesis is reproducible for all three methods (*direct*, *inverse* and *both speciated*). As shown from the preliminary study, when operating at the pH adjusted system, the order of the reactant addition had no significant effect on the reaction time, the particle size or the particle dispersity, due to the gold and citrate species present. Therefore, any of the *Turkevich* methods (*direct, inverse* or *both speciated*) can be used for the development of the statistical correction for the estimation of particle size and reaction time for the completion of the Au NPs synthesis.

5.3.2. Preliminary results on the effect of solution pH on gold nanoparticle synthesis

pH has a vital role in the gold nanoparticle synthesis due to its relation with the reactant speciation. In the current study, the development of the predictive model for the colloidal gold synthesis was focused on the pH adjusted *Turkevich* method. However, increasing the synthesis pH using a basic solution ($NaOH$) offered an important insight on the synthesis tolerance (reaction time and particle size) on the variations of the pH. In order to evaluate the influence of the pH on the final particle size and particle dispersity, following the pH adjusted *Turkevich method,* the pH of reducing agent (H_3Ct:Na_3Ct mixture) increased with $NaOH$ addition prior to mixing with the gold precursor. In that way, the effect of the pH on the development of the predictive model could be evaluated. Adjusting the pH of reducing agent (H_3Ct:Na_3Ct mixture) prior to mixing with the $HAuCl_4$ affected the protonation of the citrate species without altering the speciation of the gold precursor. Ji *et al.*[86] investigated the variation of the colloidal gold particle size by increasing the pH of the solution, however, in their study, the additions of the HCl or $NaOH$ were carried out in the solution when only the gold precursor was present (before the Na_3Ct addition). This methodology affected the speciation of the precursor and the existence of the Au(III)

species which are critical for the determination of the particle size[96]. The study of Ketteman *et al.*[40] confirmed that both Au(III) complex equilibrium and the protonation of the reducing agent (H_3Ct:Na_3Ct mixture) are important for the final particle size, particle dispersity and reproducibility.

Figure 5-3 presents the reaction time (Figure 5-3a) and the particle size distribution (Figure 5-3b) where the pH of the final colloidal Au NPs solution increased from 5.6 to 7.9, using the *direct Turkevich* method. A small amount of $NaOH$ ($[NaOH]$ = 30 mM) was added in the reducing agent (H_3Ct and Na_3Ct mixture) prior to the mixing with the gold precursor (100 μL and 130 mL for pH = 6.9 and pH = 7.9, respectively). The studied synthesis conditions were 0.25 mM concentration of the gold precursor $HAuCl_4$ (after mixing) and 12/1 $[Citrate]/[HAuCl_4]$ ratio at 95 ^{o}C; the ratio of Na_3Ct and H_3Ct is given in Tables 5-1 and 5-2. The addition of the $NaOH$ increased the pH of the synthesis mixture above the threshold of 6.5, where the Au(III) complexes shift from the $AuCl_4^-$ / $AuCl_3(OH)^-$ species (pH = 3.7 – 6.5) to $AuCl_2(OH)_2^-$ / $AuCl(OH)_3^-$ (pH = 6.5 – 7.7)[86]. The change in the complex species affects both nucleation and growth steps. Increasing the solution pH the reaction time increased significantly from 5.3 minutes (for pH=5.6) to 49 min (for pH=7.9 min), which is directly related to the passivation of the gold precursor and the shift of the Au(III) towards less reactive higher hydroxylated species[40, 86]. Figure C-5 in Appendix C shows the absorbance and the wavelength of the SPR peak in time for all pH conditions studied, for the calculation of the reaction time. At the same time, increasing the pH in this range, the average particle size – provided by the DCS – increased from 14.0 ± 1.3 nm (pH=5.6) to 28.4 ± 11.4 nm (pH=6.9) and 37.9 ± 12.2 nm (pH=7.9).

Figures 5-3 c – e show the TEM images of the synthesised particles at the studied pH range, confirming the observations by the DCS that increasing the pH, both the particle size and the particle dispersity increase. Increasing the pH above the highly reproducible zone (pH between 5.4 – 6.5) the ionic strength increases, decreasing the colloidal stability of the formed seeds and of the synthesised particles, resulting in particle agglomeration. Additionally, at high pH, the nucleation rate decreases due to the lower amount of $AuCl_4^-$. All the above reasons lead to larger and non-uniform particle formation and the synthesis of particles of large polydispersity[38], as it can be seen from Figure 5-3e (sample synthesised at pH=7.9). The larger distribution observed at high pH could also be related to Ostwald ripening, where the smaller

particles dissolve to their monomers and atoms once the existent monomers are depleted and the dissolved atoms are then received by the larger particles[74]. Polte *et al.*[69] commented on this phenomenon since particle coalescence and Ostwald ripening can lower the particle concentration in favour of larger particle size. As shown from the preliminary study, operating at the pH equal to ~ 5.6 results in faster synthesis, smaller sizes and narrower particle size distributions than operating at higher final solution pH.

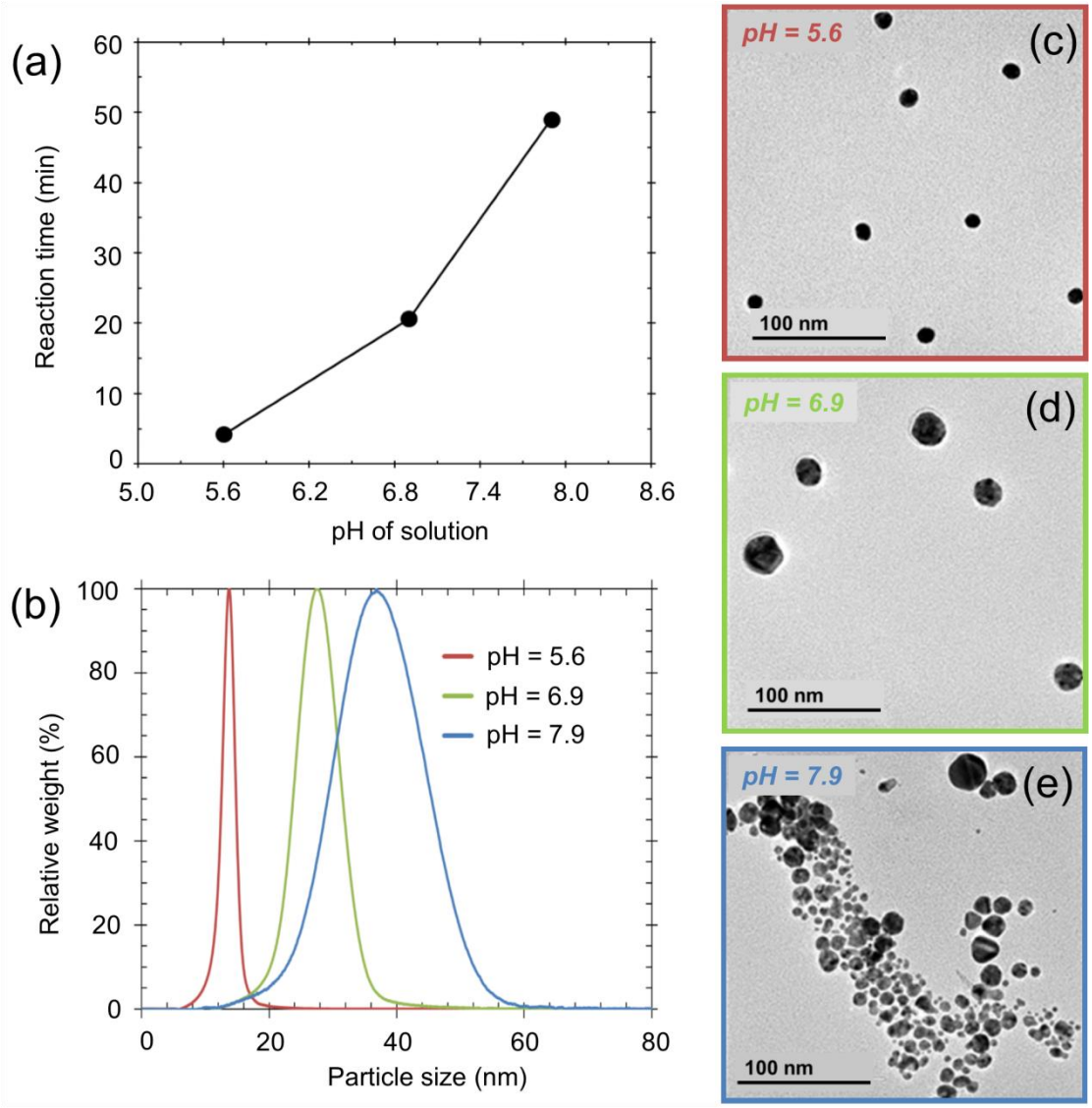

Figure 5-3 a) Reaction time and b) particle size distribution (obtained by DCS) of gold nanoparticle synthesis for different final pH using the *direct Turkevich* method. c-e) TEM images of the synthesied gold nanoparticles at pH = 5.6 (c), pH = 6.9 (d) and pH = 7.9 (e). Gold precursor concentration $\boldsymbol{HAuCl_4}$ (after mixing), 0.25 mM; reducing agent ($\boldsymbol{H_3Ct}$:$\boldsymbol{Na_3Ct}$ mixture) concentration (after mixing), [$\boldsymbol{H_3Ct}$] = 0.54 mM, [$\boldsymbol{Na_3Ct}$] = 2.46 mM, temperature, 95 ^{o}C. Solid line in (a) is used for visual aid.

5.3.3. Development of a predictive regression model for particle size and reaction time

Based on the preliminary results on the effect of the results on the order of reactant addition, both *direct* and *inverse Turkevich* methods resulted to similar particle sizes when the pH of the colloidal solution was ~ 5.6 and the kinetic data can be acquired based on the *direct Turkevich* methodology following the synthesis protocol described by Kettemann *et al.*[40]. The kinetic data – based on TEM imaging and *in situ* UV-Vis spectrometry – were obtained by varying the precursor concentration and the reactant molar ratio, as shown in Table 5-1. Varying the temperature between 80 – 100 ^{o}C has low effect on particle size[210] (particle size changes significantly by lowering the temperature to 60 ^{o}C[211]), however, the reaction time shows more than a 2-fold increase from 100 ^{o}C to 60 ^{o}C[211]. Thus, the studied temperature was set at 85 ^{o}C and 95 ^{o}C, to estimate the particle size and reaction time for each condition (shown in Table 5-1), while maintaining a rapid Au NPs synthesis. Two response surface models (RSM) were developed for the particle size and the reaction time as a function of gold precursor and $Citrate$ (H_3Ct and Na_3Ct mixture) concentration after mixing and temperature. An additional semi-empirical model was developed to calculate the molar ratio of the H_3Ct and Na_3Ct after mixing in the targeted synthesis to ensure the pH to be equal to ~ 5.6 in the targeted synthesis.

5.3.3.1. Response surface model for the gold nanoparticle size and reaction time

Table 5-3 displays the results of the particle size and reaction time for the *direct Turkevich* method at 85 ^{o}C and 95 ^{o}C for 6/1 and 12/1 [$Citrate$]/[$HAuCl_4$] ratio and [$HAuCl_4$] between 0.125 – 0.5 mM based on the factorial analysis described in Section 5.2.3. TEM imaging indicated that the synthesised Au NPs were spherical and monodisperse with an average coefficient of variation ~ 8% (Table C-1 and Figures C-6 – C-7, Appendix C), while the evolution of the SPR peak wavelength and absorbance for the estimation of the reaction time via *in situ* UV-Vis spectrometry is given in Figures C-8 – C-9 (Appendix C). Increasing the gold precursor concentration from 0.125 mM to 0.5 mM, the particle size and reaction time decreased. This trend is directly related to the higher amount of $AuCl_4^-$, resulting in more nuclei being produced (burst nucleation) increasing the number of the produced seeds, thereby

decreasing the Au NPs size. Similarly, the higher the $AuCl_4^-/AuCl_{3-x}(OH)_{1+x}^-$ ratio, the more acidic are the synthesis condition and the reaction time decreases due to the higher monomer supply (mainly provided by the reduction of the $AuCl_4^-$) resulting in faster reaction rates. Figures C-8a and C-9a (Appendix C) display the decreasing trend of the reaction time by increasing the $HAuCl_4$ concentration at 85 °C and 95 °C for 6/1 and 12/1 $[Citrate]/[HAuCl_4]$ ratio.

Table 5-3 The experimental runs of the Au NPs synthesis with the three factors along with the experimental response on the mean particle size $\bar{d}_{exp}$ and standard deviation of the particle size distribution σ_d (based on TEM), and average reaction time $\bar{t}_{exp}$ (based on in situ UV-vis spectrometry). X_1: $[HAuCl_4]$ (mM), X_2: $[Citrate]/[HAuCl_4]$ and X_3: Temperature (°C).

Run	Experimental factors			Experimental results	
	X_1	X_2	X_3	Mean particle size, $\bar{d}_{exp} \pm \sigma_d$ (nm)	Average reaction time, $\bar{t}_{exp}$ (min)
1	0.125	6	85	18.5 ± 1.7	16.1
2	0.25	6	85	13.9 ± 1.6	8.8
3	0.5	6	85	12.6 ± 1.0	5.4
4	0.125	12	85	16.1 ± 1.8	11.4
5	0.25	12	85	12.4 ± 1.1	7.3
6	0.5	12	85	11.8 ± 0.8	4.9
7	0.125	6	95	17.8 ± 1.3	7.2
8	0.25	6	95	15.3 ± 1.2	4.9
9	0.5	6	95	12.1 ± 0.9	3.0
10	0.125	12	95	15.6 ± 1.3	6.7
11	0.25	12	95	13.3 ± 0.9	4.2
12	0.5	12	95	10.6 ± 0.9	2.4

Kumar *et al.*[65] using the results of Turkevich *et al.*[34] Chow and Zukoski[82], Freund and Spiro[185] and Frens[83] showed that when increasing the Na_3Ct concentration, the particle size was unaffected for a wide range of $[Na_3Ct]/[HAuCl_4]$ ratio. In the current study, increasing the $Citrate$ concentration while keeping the temperature and the $HAuCl_4$ concentration constant, there was an approximately 2 nm drop on the mean particle size (Table 5-3). Particle size is inversely proportional to the amount of HCt^{2-} (the dominant species at pH ~ 5.6), therefore the higher its concentration, the smaller the final particle size for a given precursor concentration (i.e. the particle size drop

from 15.3 nm to 13.3 nm by increasing the reactant molar ratio from 6/1 to 12/1 while the gold precursor was constant at 0.25 mM and temperature equal to 95 ^{o}C)[40].

As it can be seen from Table 5-1, when the reactant molar ratio increased from 6/1 to 12/1 – for given gold precursor concentration $HAuCl_4$ – the Na_3Ct/H_3Ct molar ratio decreased so as the final pH of the colloidal solution to be ~ 5.6. The change of the Na_3Ct/H_3Ct molar ratio due to the increase of $[Citrate]$ is related to the species being present during the reaction, as discussed in the next Section (5.3.3.2). The reaction time is affected by the final pH of the Au NPs solution (remained equal to ~ 5.6), thus it was not affected by increasing the reactant molar ratio from 6/1 to 12/1 for given gold precursor concentration (the observed increase was less than 1 min which fell within the reproducibility of the measurements).

The particle size was unaffected when the temperature increased between 85 – 95 ^{o}C (observed difference was less than 1 nm under given conditions). However, the reaction time decreased significantly by increasing the synthesis temperature and the decrease was higher at low the gold precursor concentration. For example, as it is shown in Table 5-3, there was 5 min difference in the reaction time for $[HAuCl_4]$ = 0.125 mM and $[Citrate]/[HAuCl_4]$ = 6/1 between 85 ^{o}C and 95 ^{o}C, while the difference was only 2 min for $[HAuCl_4]$ = 0.5 mM and $Citrate/HAuCl_4$ = 6/1 at 95 ^{o}C. The effect of temperature on particle size and reaction time of Au NPs synthesis is complex, as temperature affects the speciation of the gold precursor and as well as the reduction of Au(III) to Au^0 monomers. Increasing the temperature, the reduction rate of $AuCl_{4-x}(OH)_x^-$ complexes to Au^0 and the nucleation rate increase, and at the same time the equilibrium of the gold complexes changes due to the reduction of the $AuCl_4^-$ (the species of the highest reactivity). Of course, changing the species equilibrium and nucleation rate, the growth stage is also influenced; increasing the temperature for constant Au^0 concentration leads to the formation of less seeds of larger size[38]. Previous studies by Takiyama *et al.*[212] and Wuithschick *et al.*[38] have described that particle size increases by increasing the temperature from 60 ^{o}C to 100 ^{o}C, however, their analysis concerned the use of only the Na_3Ct as reducing agent. In this study the reducing agent was the mixture of Na_3Ct and H_3Ct maintaining the pH = ~ 5.6, which could affected the equilibrium of the gold and citrate complexes, as well as influencing the reaction rates of the reduction and nucleation steps, minimising the effect of temperature on particle size between 85 – 95 ^{o}C.

The RSM determining the effect of each factor on the final particle size (d_{calc}) and reaction time (t_{calc}) are given in Equations 5-12 and 5-13. The developed models were refined from the initial second order regression equations by eliminating the linear, interaction and quadratic terms of low significance ($p-value$ > 0.05) as described in Section C.5 in Appendix C.

$$d_{calc} = 24.41 - 44.6X_1 - 0.29X_2 + 49.07{X_1}^2 \quad \text{Eq. 5-12}$$

$$t_{calc} = 49.79 - 16.04X_1 - 0.42X_3 \quad \text{Eq. 5-13}$$

Where X_1: $[HAuCl_4]$ (mM), X_2: $[Citrate]/[HAuCl_4]$ and X_3: Temperature (^oC).

Table 5-4 includes the coefficients and the $p-values$ of the factors in Equation 5-12 – which describes the particle size of the Au NPs – and it shows that the two significant factors determining the Au NPs size were the gold precursor concentration$[HAuCl_4]$ (X_1, $p-value$ = $2.9\cdot10^{-6}$) and the $[Citrate]/[HAuCl_4]$ (X_2, $p-value$ = 0.00154). The statistical analysis showed that the quadratic term of the gold precursor concentration had also a significant influence on the particle size (${X_1}^2$, $p-value$ = 0.00487). The three-dimensional (3D) plot in Figure 5-4 was constructed to assess the change of the response surface (particle size) by varying the gold precursor concentration and the reactant molar ratio. The developed model is in accordance with the one-factor-at-time (OFAT) analysis, where increasing the gold precursor concentration or the reactant molar ratio lead to Au NPs size decrease. However, the relationship between the variables and the desired response is not linear due to the quadratic term of the gold precursor concentration.

Table 5-4 Coefficients and $p-values$ of the factors for the linear and quadratic effects of the developed response surface model for the mean gold nanoparticle size (see Equation 5-12). X_1: $[HAuCl_4]$ (mM) and X_2: $[Citrate]/[HAuCl_4]$.

Factor (X_{ij})	Coefficient (β_{ij})	$p-value$
Intercept	24.41	$5.8\cdot10^{-10}$
X_1	-44.6	$2.9\cdot10^{-6}$
X_2	-0.29	0.00154
${X_1}^2$	49.07	0.00487

Assessing the goodness of fit via the ANOVA test for the particle size model (Table 5-5), the R^2 was equal to 0.9521 implying the high accuracy of the developed model[209]. The adjusted R^2 coefficient was similar to the R^2 (R^2_{adj} = 0.9341) indicating a good agreement between the experimental and the calculated results[205]. As it can be seen from Table 5-5, comparing the $F-value$ of the model with the *critical* $F-value$ for the 95 % confidence, the $F-value$ of the developed model was 52.95 > $F_{0.95}(3,8)$ = 4.07 indicating a good predictability ($p-value$ of model = $1.27 \cdot 10^{-5}$ < 0.05). Figure 5-5 shows the parity plot of the experimental versus the calculated particle size given by the model in Equation 5-12 indicating uniform scattering of the experimental against the calculated values, while all the experimental values lied within the 10 % marginal variance of the model.

Table 5-5 Analysis of variance (ANOVA) of the response surface model for the mean gold nanoparticle size (see Equation 5-12).

Source	$\boldsymbol{SS}$	$\boldsymbol{MS}$	$\boldsymbol{DF}$	$\boldsymbol{F-value}$	$\boldsymbol{p-value}$
Model	64.79	21.60	3	52.97	$1.27 \cdot 10^{-5}$
Residual	3.26	0.41	8		
Total	68.05		11		

$\boldsymbol{R^2}$ = 0.9521, $\boldsymbol{R^2_{adj}}$ = 0.9341, $\boldsymbol{F_{0.95}(3,8)}$ **= 4.07**

$\boldsymbol{SS}$, sum of squares; $\boldsymbol{MS}$, mean square; $\boldsymbol{DF}$, degree of freedom

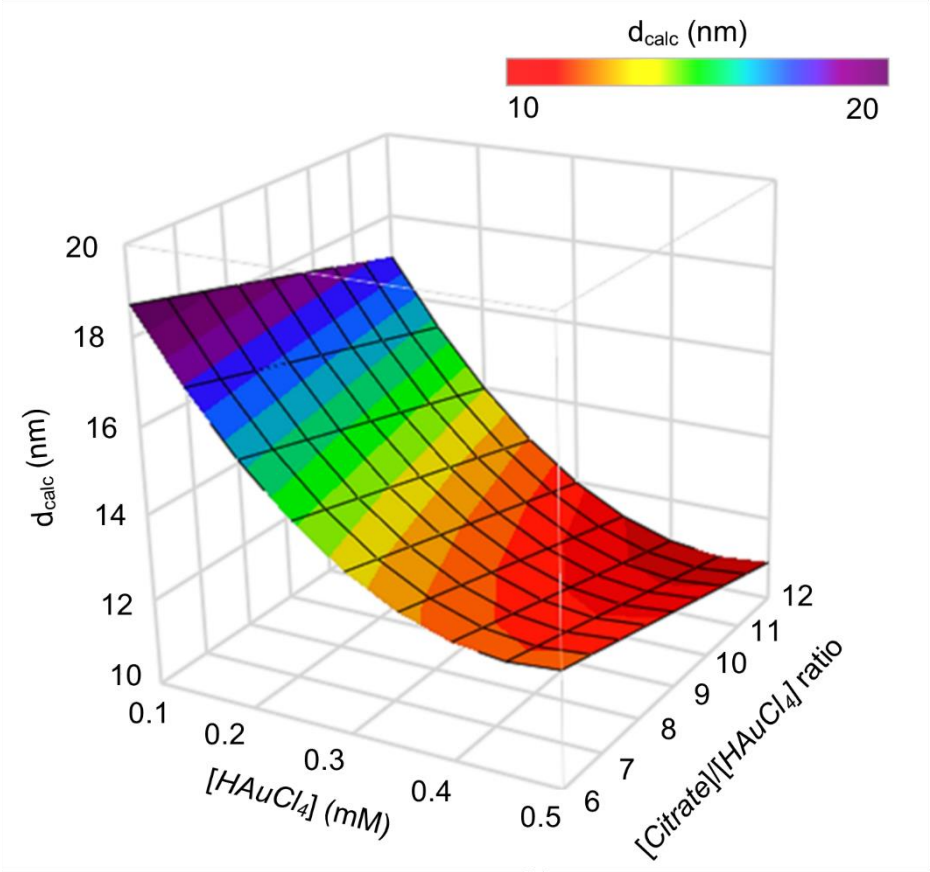

Figure 5-4 3D graph showing the effect of the gold precursor concentration ([$HAuCl_4$]) and reactant molar ratio ([$Citrate$]/[$HAuCl_4$]) on the gold nanoparticle size as calculated by the response surface model (d_{calc}) of Equation 5-12. The colour change from the red to purple corresponds to an increase of the particle size.

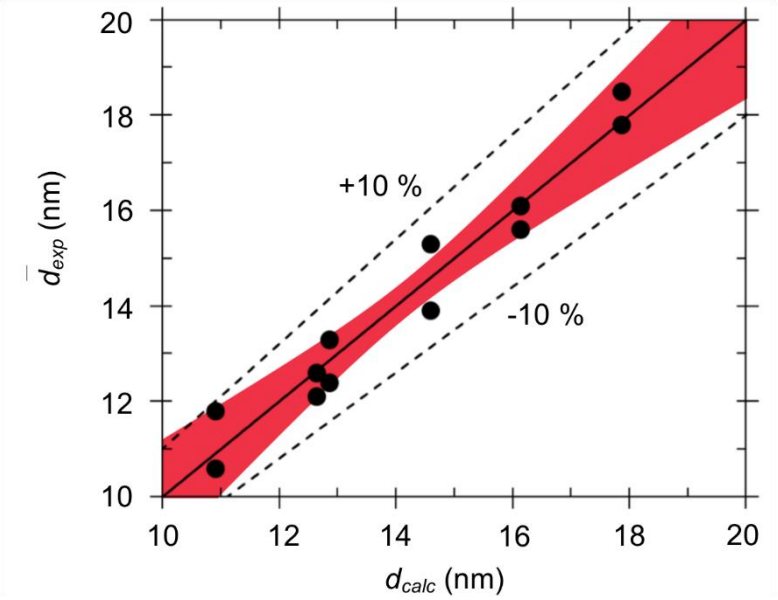

Figure 5-5 Parity plot of the experimental ($\bar{d}_{exp}$) versus the calculated (d_{calc}) particle size of the gold nanoparticles synthesis given by the response surface model. Dashed lines display the 10% deviation of the model from fitting line (solid line). Red coloured area displays the 95 % confidence of the model.

Regarding the reaction time model, Table 5-6 includes the coefficients and the $p - values$ of the factors in Equation 5-13 and it shows that the two significant factors determining the reaction time of the Au NPs synthesis were the gold precursor concentration $HAuCl_4$ (X_1, $p - value$ = 0.0001) and the reaction temperature (X_3, $p - value$ = 0.00074). In this model, there were no quadratic or synergetic terms, thus a linear relationship between the parameters and the response could be observed. The three-dimensional (3D) plot in Figure 5-6 is constructed to assess the change of the response surface (reaction time) by varying the gold precursor concentration and the reaction temperature. As it is shown from the 3D plot, increasing the gold precursor concentration or the reaction temperature the reaction time decreases, which agrees with the observations from the OFAT analysis.

Table 5-6 Coefficients and $p-values$ of the factors for the linear effects of the response surface model for the reaction time of gold nanoparticle synthesis (see Equation 5-13). X_1: $[HAuCl_4]$ (mM) and X_3:Temperature (°C).

Factor (X_{ij})	Coefficient (β_{ij})	$p-value$
Intercept	49.79	$9.0 \cdot 10^{-7}$
X_1	-16.04	0.0014
X_3	-0.42	0.0038

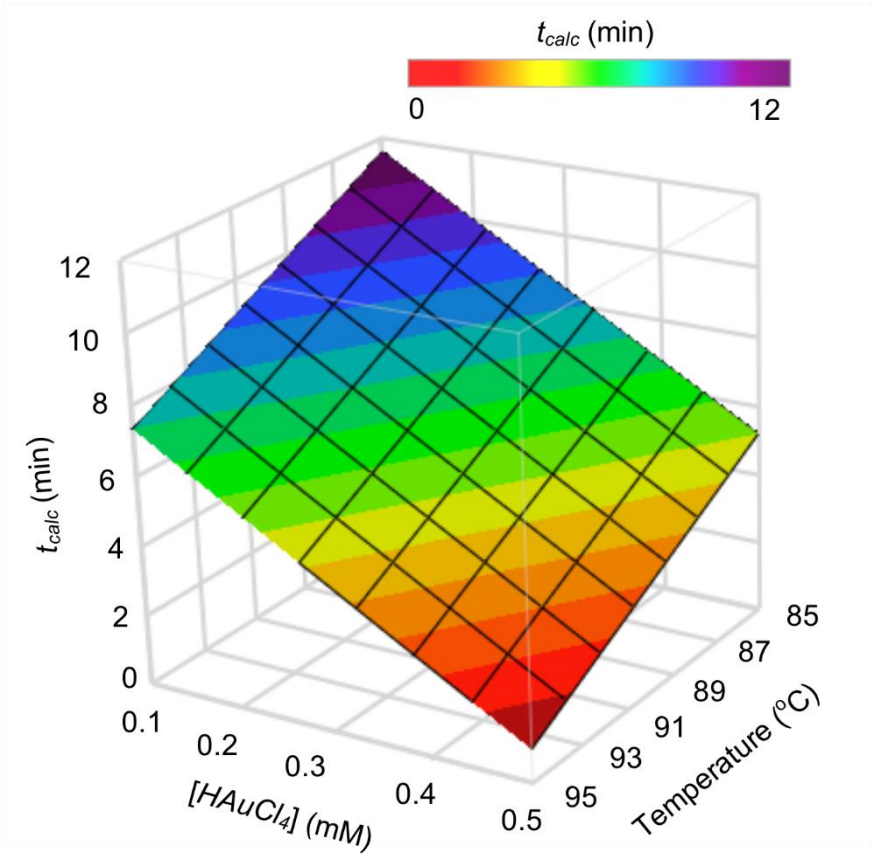

Figure 5-6 3D graph showing the effect of the gold precursor concentration ($[HAuCl_4]$) and temperature on the reaction time of gold nanoparticle synthesis (t_{calc}) as calculated by the response surface model of Equation 5-13. The colour change from the red to purple corresponds to an increase in reaction time of the synthesis.

Assessing the goodness of fit via the ANOVA test for the reaction time model (Table 5-7 and Section C.4 in Appendix C), the R^2 was equal to 0.80 indicating a model of sufficient accuracy[209]. At the same time, the adjusted R^2 coefficient was similar to the

R^2 (R^2_{adj} = 0.7543) indicating again a good agreement between the experimental and the calculated results of the response surface model[205]. As it can be seen from Table 5-7, comparing the $F-value$ of the model with the *critical* $F-value$ for the 95 % confidence, the $F-value$ of the developed model was 17.89 > $F_{0.95}(2,9)$ = 4.26 indicating a good predictability ($p-value$ of model = $7.31 \cdot 10^{-4}$ < 0.05). Figure 5-7 shows the parity plot of the refined experimental versus the calculated reaction time given by the model in Equation 5-13 indicating uniform scattering of the experimental against the calculated values. Unlike the developed model for particle size, a number of the experimental values lied on the margins or outside the derived 95 % significance area and the 10 % marginal variance of the model indicating higher residual values and explaining the lower R^2 compared with the particle size model. However, testing the model with and without these data points, it was observed that they did not skew the predictability of the model. In any case, the low $p-value$ of the developed correlation given by Equation 5-13 indicated adequate fitting.

Table 5-7 Analysis of variance (ANOVA) of the response surface model for the reaction time of gold nanoparticle synthesis (see Equation 5-13).

Source	$\boldsymbol{SS}$	$\boldsymbol{MS}$	$\boldsymbol{DF}$	$\boldsymbol{F-value}$	$\boldsymbol{p-value}$
Model	129.25	64.63	2	17.89	$7.31 \cdot 10^{-4}$
Residual	32.51	3.61	9		
Total	161.76		11		

$\boldsymbol{R^2}$ = 0.8000, $\boldsymbol{R_{adj}{}^2}$ = 0.7543, $\boldsymbol{F_{0.95}(2,9)}$ **= 4.26**

$\boldsymbol{SS}$, sum of squares; $\boldsymbol{MS}$, mean square; $\boldsymbol{DF}$, degree of freedom

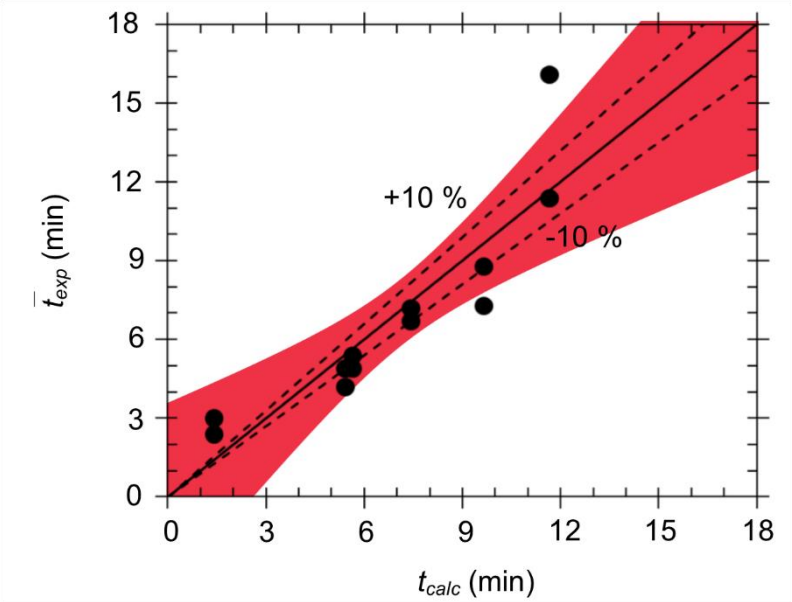

Figure 5-7 Parity plot of the experimental ($\bar{t}_{exp}$) versus the calculated (t_{calc}) reaction time of the gold nanoparticles synthesis given by the response surface model. Dashed lines display the 10% deviation of the model from fitting line (solid line). Red coloured area displays the 95 % confidence of each model.

5.3.3.2. Integrated predictive model with reactant speciation

The developed response surface models correlated the gold precursor concentration, reactant molar ratio and temperature with the particle size and reaction time. However, in this analysis the constraint was that the pH had to be ~ 5.6, so as the *Turkevich* synthesis to be within the "high reproducibility zone".[40] The pH was adjusted by varying the Na_3Ct and H_3Ct concentration in the mixture. Thus, an extended semi-empirical model was required to take into account the speciation of the gold precursor and the reducing agent and calculate the required amounts of Na_3Ct and H_3Ct in the mixture for a desired particle size.

In the model developed by Agunloye *et al.*[189] it was assumed the ionisation of precursor in water [189]:

$$HAuCl_4 \rightarrow AuCl_4^- + H^+ \qquad \text{Eq. 5-14}$$

Therefore, the concentrations of the hydroxylated species $AuCl_{3-x}(OH)_{1+x}^-$ were assumed negligible in the precursor solution at room temperature (ca. 25 ^oC).

Therefore the pH of the precursor solution was considered equal to $-\log_{10}[H^+] = -\log_{10}[HAuCl_4]$. However, the speciation of the precursor plays a significant role in the particle size and sample polydispersity. In order to estimate the pH of speciated gold at the desired concentration and reaction temperature, the gold precursor $HAuCl_4$ at various concentrations was heated at 95 °C for ~ 120 s – to ensure the speciation of the gold precursor[38] – quenched and cooled down at room temperature. In that way, it was attempted to estimate the H^+ concentration supplied by the gold speciation and the results are displayed in Figure 5-8. By quenching and measuring the pH rapidly it was attempted to minimise the rates of the reversible speciation reactions of the gold precursor and the pH measurements would be representative of the pH at 95 °C. It is worth noting that the pH measured (Figure 5-8) was 6 % – 10 % lower that the theoretically estimated from Equation 5-14. The theoretically expected pH was 3.90, 3.60 and 3.30 for 0.125 mM, 0.25 mM and 0.5 mM $[HAuCl_4]$, respectively. The difference was attributed to the polarisation of the water molecules due to the dissolved metal Au(III)[213, 214] which can lead to deprotonation of water (and increase of the solution pH) due to the attraction of the OH^- species by the metal cation[215]. The amount of H^+ (in mM) supplied by the $HAuCl_4$ was then calculated by the following regression equation (R^2 = 0.9716):

$$[H^+] = 0.3281 \cdot \ln[HAuCl_4] + 0.8843 \qquad \text{Eq. 5-15}$$

Where $[HAuCl_4]$ is the concentration of the gold precursor (mM).

On the other hand, the speciation of the $Citrate$ was estimated as follows[189]:

$$Na_3Ct \rightarrow 3Na^+ + Ct^{3-} \qquad \text{Eq. 5-16}$$

$$Ct^{3-} + H^+ \rightleftarrows HCt^{2-};\ 1/K_{R3} \qquad \text{Eq. 5-17}$$

$$HCt^{2-} + H^+ \rightleftarrows H_2Ct^-;\ 1/K_{R2} \qquad \text{Eq. 5-18}$$

$$H_2Ct^- + H^+ \rightleftarrows H_3Ct;\ 1/K_{R1} \qquad \text{Eq. 5-19}$$

Where the K_{Ri} is the equilibrium constant for each reaction at 25 °C and equal to K_{R1} = 7.41·10^{-4}, K_{R2} = 1.74·10^{-5} and K_{R3} = 3.98·10^{-7} [216].

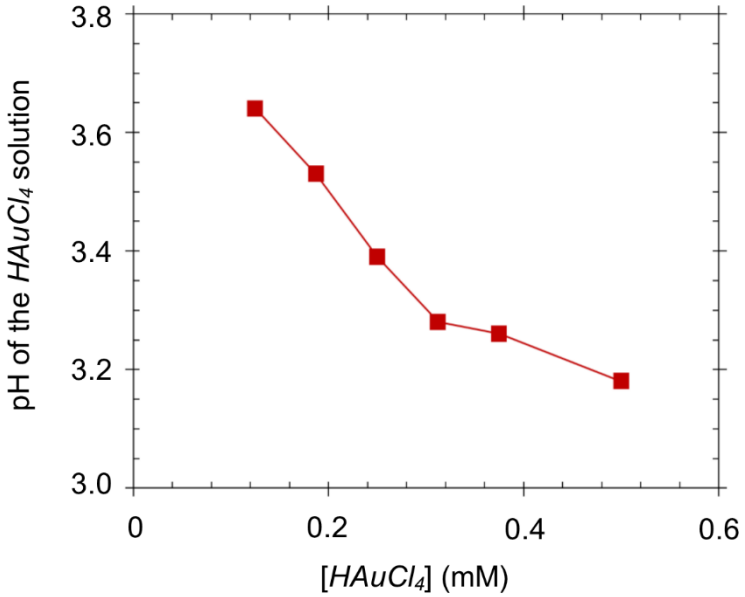

Figure 5-8 pH of the gold precursor solution at room temperature measured experimentally after heating and speciating at 95 °C and quenching rapidly. Solid line is used for visual aid.

In the present study, the reducing agent comprised of Na_3Ct and H_3Ct, as well as the deprotonated citrated species (Ct^{3-}, HCt^{2-} and H_2Ct^{-}). The speciation of the $Citrate$ at higher temperatures was not taken into account, since in the *direct Turkevich* method it is added in the gold speciated solution and the $Citrate$ speciation is fast (~ 2 s)[38]. Hence, the $Citrate$ speciation and reaction between the gold and citrate species is expected to start immediately upon the $Citrate$ addition in the preheated gold solution. The target pH of the solution at room temperature was 5.6 corresponding to $[H^+]$ = 2.5119·10^{-6} M.

5.3.3.3. Targeted gold nanoparticle synthesis

The developed model was initially tested for the targeted synthesis of the 10 nm, 15 nm and 20 nm Au NPs at 95 °C, by maximising the gold precursor concentration up to 0.5 mM – the maximum value of the $[HAuCl_4]$ used for the development of the model as discussed in Section 5.2.2 – (to achieve the highest possible productivity), while the $[Citrate]/[HAuCl_4]$ ratio was above 6/1. The model targets and restrictions for the calculation of the desired particle size based on the developed RSM (Equation 5-12) are summarised below:

$$\begin{cases} d_{calc} = \{10, 15, 20\} \\ X_1 = \max(0{,}0.5] \\ X_2 \geq 6 \end{cases} \quad \text{Eq. 5-20}$$

The proposed model was used for the calculation of the amount of Na_3Ct and H_3Ct for a given gold precursor concentration and reactant molar ratio, so as the final pH of the solution to be ~ 5.6. The required synthesis conditions estimated by the developed model are summarised in Table 5-8, however, the measured pH of the colloidal solution after the completion of the synthesis varied between 5.16 – 5.38 (Figure 5-9) – outside the "high reproducibility zone" of pH between 5.5- 6.0.

Table 5-8 Synthesis conditions determined by the response surface model and the extended mechanistic model for the targeted 10 nm, 15 nm and 20 nm gold nanoparticles synthesis (without the a factor).

Target Au NPs (nm)	Experimental conditions				
	$[HAuCl_4]$ (mM)	$[Citrate]/[HAuCl_4]$	$[H_3Ct]$ (mM)	$[Na_3Ct]$ (mM)	Temperature (^{o}C)
10	0.5	15/1	2.26	5.24	95
15	0.23	6/1	0.32	1.06	
20	0.065		0.13	0.26	

The observed discrepancies were assumed to be attributed to the speciation of either the gold precursor or the citrate species present in the synthesis. Figure C-11 (Appendix C) displays the absorbance at 313 nm for the gold precursor for different temperatures. Increasing the temperature, the absorbance decreases due to the hydroxylation of $AuCl_4^-$. In the experimental procedure to estimate the pH of the $HAuCl_4$ solution at high temperature, the solution was quenched and probably there was some change in the hydorxylated species prior or during the measurement. Another factor affecting the pH of the colloidal Au NPs solution could be the production of DCA in the synthesis mixture due to thermal decomposition of the $Citrate$ which could alter the speciation kinetics. Finally, despite the previous literature findings[40] suggesting sufficient calculation of the citrate speciation using the K_{Ri} values at 25 ^{o}C and not at 95 ^{o}C, calculations by Agunloye *et al.*[189] on the speciated citrate solution has shown that the pH of the reducing agent solution at 95

^{o}C can be overestimated by ~ 20 % by using the K_{Ri} values at 25 ^{o}C and not at 95 ^{o}C. All the above factors and uncertainties could affect the amount of H^+ in solution and subsequently the solution pH. As shown from Figure 5-9 (without the *α* factor) the discrepancy between the observed and the target pH was ~ 0.4 in average. A fitting factor a = 1.5849·10^{-6} M was applied on the calculation of the proton concentration in the final Au NPs solution to account for the observed discrepancy on the pH. Thereby the target proton concentration of the final model was equal to $[H^+]'$ = 2.5119·10^{-6} – a = 0.927·10^{-6} M and the calculated final pH from the model in that case was 6 resulting to higher $[Na_3Ct]/[H_3Ct]$ ratio in the required $Citrate$ for the desired synthesis. The required synthesis conditions estimated by the updated developed model (with the *α* factor) are summarised in Table 5-9 and the measured pH of the colloidal solution after the completion of the synthesis varied between 5.50 – 5.74 (Figure 5-9). Hence, the synthesis was within the "high reproducibility zone".

Table 5-9 Synthesis conditions determined by the updated response surface model and the extended mechanistic model for the targeted 10 – 20 nm gold nanoparticles synthesis with the a factor.

	Experimental conditions				
Target Au NPs (nm)	$[HAuCl_4]$ (mM)	$[Citrate]/[HAuCl_4]$	$[H_3Ct]$ (mM)	$[Na_3Ct]$ (mM)	Temperature (^{o}C)
10	0.5	15/1	1.65	5.85	95
12.5	0.5	6.5/1	0.59	2.66	
15	0.23	6/1	0.21	1.17	
17.5	0.135		0.126	0.684	
20	0.065		0.10	0.29	

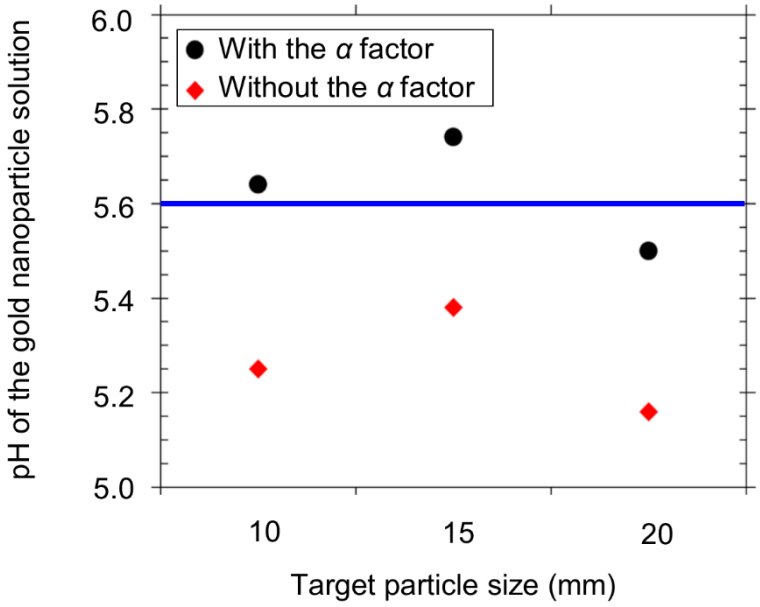

Figure 5-9 Experimentally measured pH of the synthesised gold nanoparticle solution. Synthesis conditions were derived from the developed model with and without the *α* factor. Blue line displays the target of pH = 5.6 for the "high reproducibility zone" of gold nanoparticle synthesis. *With the α factor:* 10 nm: [$HAuCl_4$], 0.5 mM; [H_3Ct], 1.65; [Na_3Ct], 5.85; temperature, 95 ^{o}C. 15 nm: [$HAuCl_4$], 0.23 mM; [H_3Ct], 0.21; [Na_3Ct], 1.17; temperature, 95 ^{o}C. 20 nm: [$HAuCl_4$], 0.065 mM; [H_3Ct], 0.10; [Na_3Ct], 0.29; temperature, 95 ^{o}C. *Without the α factor:* 10 nm: [$HAuCl_4$], 0.5 mM; [H_3Ct], 2.26; [Na_3Ct], 5.24; temperature, 95 ^{o}C. 15 nm: [$HAuCl_4$], 0.23 mM; [H_3Ct], 0.32; [Na_3Ct], 1.06; temperature, 95 ^{o}C. 20 nm: [$HAuCl_4$], 0.065 mM; [H_3Ct], 0.13; [Na_3Ct], 0.26; temperature, 95 ^{o}C.

The final extended model was used for the targeted synthesis of 10 – 20 nm citrate-capped Au NPs. The conditions for the desired syntheses are included in Table 5-9. The obtained nanoparticles were 10.8 ± 1.2 nm, 13.4 ± 1.0 nm, 15.0 ± 1.0 nm, 16.6 ± 1.4 nm, 18.4 ± 1.5 nm, corresponding to the target nanoparticle sizes of 10 nm, 12.5 nm, 15 nm 17.5 nm and 20 nm, respectively, given by the TEM imaging. Figure 5-10a summarises the experimental versus the calculated particle sizes, where the synthesised Au NPs fell within the 10 % margins of the developed model. Also, Figures 5-10 b – f display the TEM images of the high quality spherical nanoparticles of 10 nm, 12.5 nm, 15 nm 17.5 nm and 20 nm, respectively. The produced Au NPs can be characterised as monodisperse since their coefficient of variation was in general less than 10 %. The synthesis reproducibility was evaluated via DCS

analysis of the targeted synthesis in triplicates confirming the high reproducibility of the developed model as the variance of the reproducibility of the average particle size was less than 10 % (Figure C-12). Therefore, the extended statistical model can be used for the tuned synthesis of monodispersed 10 – 20 nm citrate-capped Au NPs.

Upon calculating the required synthesis conditions (gold precursor concentration and concentration of the Na_3Ct and H_3Ct), the synthesis reaction time was calculated based on the RSM from Equation 5-13 at 95 ^{o}C. The results are shown in Figure 5-10, where a discrepancy between the experimentally measured and calculated reaction time can be observed. According to the developed model, the reaction time increases for larger particle sizes because of the lower concentration of the gold precursor. The calculated reaction time was 2 min, 2 min, 5 min, 7 min and 8 min for the synthesis of 10 nm, 12.5 nm, 15 nm 17.5 nm and 20 nm, respectively. However, after analysing the UV-Vis spectra in time (Figure C-13, Appendix C), the average experimentally measured reaction time was lower than the calculated values despite the good fitting of the model via the *F-test* (Section 5.3.3.1). Also, the discrepancy increased by increasing the targeted particle size from ~ 6 s (for 10 nm) to 4 min (for 20 nm). Nevertheless, despite the observed discrepancies, the developed RSM model could provide an estimation for the required time for the targeted Au NPs synthesis and minimise the experimental time for 10 – 20 nm Au NPs from ~ 30 min[74, 200] to less than 10 min.

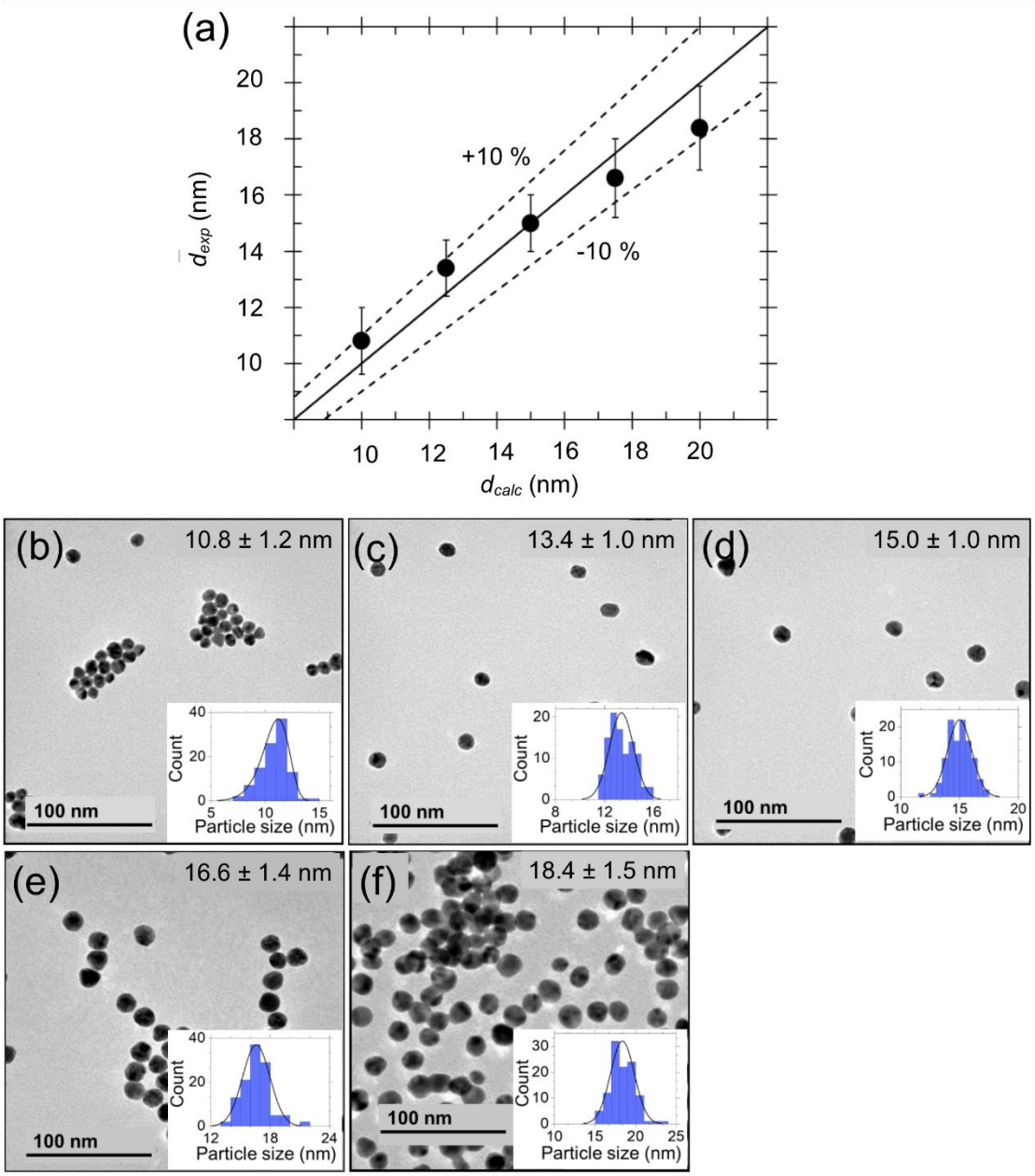

Figure 5-10 a) Experimental ($\bar{d}_{exp}$) versus the calculated (d_{calc}) targeted gold nanoparticles given by the final extended model (with the fitting factor a) Dashed lines display the 10% deviation from the model fitting line (solid line). Error bars correspond to the standard deviation of the particle distribution. b-f) TEM images of the targeted gold nanoparticles 10 nm, 12.5 nm, 15 nm, 17.5 nm and 20 nm, respectively. The histograms on the bottom-right corners in (b) – (f) present the frequency distribution of the particle size. Upper-right corner in (b) – (f) display the experimental values $\bar{d}_{exp}$ ± σ_d (nm). Experimental conditions for the 10 – 20 nm gold nanoparticle synthesis (with the *α* factor) are shown in Table 5-9.

The observed discrepancies in the RSM model for the reaction time could result from kinetic-related parameters concerning the Au NPs that have not been taken into account in the statistical model, such as the effect of DCA[217]. They could be related to the reaction rates of the precursor reduction and passivation step for the nucleation and growth steps, as well as the evolution and consumption of the various gold precursor and citrate species in time, which were excluded in this analysis as the reaction time was calculated by the plateau of the absorbance of the SPR band. Thus, a more rigorous mechanistic approach (similar to the previous literature work on particle size[189]) alongside a model-based design of experiments (MBDoE) could highlight these parameters and aid the development of an extended mechanistic model to improve the predictability of the statistical correlation on the required reaction time. Comparing the results from the particle size and the reaction time models, it can be concluded that the developed model could successfully predict the conditions for the targeted synthesis of high quality and monodisperse Au NPs.

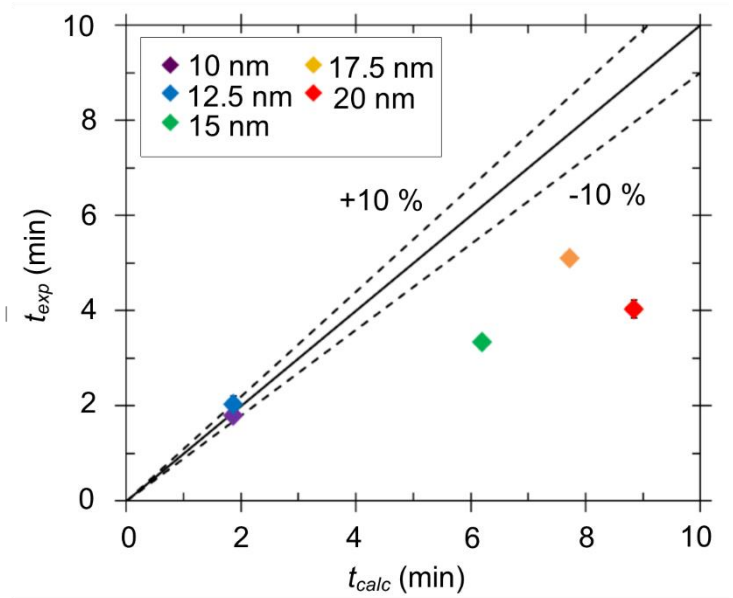

Figure 5-11 Experimental ($\bar{t}_{exp}$) versus the calculated (t_{calc}) reaction time for the targeted gold nanoparticles synthesis (10 nm – 20 nm). Dashed lines display the 10% deviation of the model from fitting line (solid line).

5.4. Conclusions

In this chapter the targeted synthesis of high quality and monodisperse gold nanoparticle was investigated. Following the previously published findings, there is a "highly reproducible zone" for gold nanoparticle synthesis at pH ~ 5.6, which is associated with the gold precursor and citrate species taking part in the reaction. In the classical *Turkevich* synthesis method, where only Na_3Ct is present as a reducing agent, the order of reactant addition plays a significant role on the final particle size and reaction time, resulting in ~ 4 nm decrease on the particle size by changing the reactant addition order from *direct* and *inverse Turkevich* method. At the same time, in the pH-adjusted system where pH was equal to ~ 5.6 (using a mixture of Na_3Ct and H_3Ct), there was no significant change between the two *Turkevich* methods, associated with the pH and the resulting gold species present. Adjusting the pH to ~ 5.6 resulted also in faster reaction times (reaction time increased from 5.3 minutes (for pH=5.6) to 49 min (for pH=7.9 min) due to the higher ratio of $AuCl_4^-/AuCl_{4-x}(OH)_x^-$ present in the lower pH mixture. Thus, a predictive model for the targeted gold nanoparticle synthesis was constructed focusing on the pH-adjusted *Turkevich* method. The developed model consisted of two response surface models correlating the particle size with the gold precursor concentration and the reactant molar ratio and the reaction time with the gold precursor concentration and the reaction temperature. The response surface models allowed in-depth understanding on the variability and influence of each factor on the desired investigated response, showing that temperature had no significant effect on the particle size between 85 – 95 ^{o}C, while the reaction time did not change by increasing the reactant molar ratio. An extended semi-empirical model was developed taking into account the speciation of gold precursor and *Citrate* solution for the calculation of the required concentrations of Na_3Ct and H_3Ct to adjust the solution pH to ~ 5.6. The developed model successfully predicted the conditions for the desired synthesis of 10 – 20 nm Au NPs, however, it overpredicted the required reaction time up to 45 % depending on the target particle size. The aforementioned results provide guidelines on the synthesis of targeted, high quality and monodisperse citrate-capped gold nanoparticles and the developed model could act as a tool to engineer the process for the desired Au NPs synthesis.

CHAPTER 6. Continuous citrate-capped gold nanoparticle synthesis in a two-phase flow reactor

The development of a platform was investigated for the synthesis of aqueous colloidal 10 – 20 nm gold nanoparticles (Au NPs) in a continuous flow capillary reactor. The use of a two-phase flow system – using heptane as the continuous phase – prevented the particle deposition on the reactor walls while improving the residence time distribution. Two synthesis pathways were tested where the inlet streams were either preheated to ensure reactant speciation, or the reactants were mixed at room temperature prior to droplet formation. Furthermore, mixing time and droplet size was evaluated to ensure sufficient reactant mixing prior to nanoparticle synthesis. The discrepancy between the target and the experimental acquired particles was lower when the reactants were mixed at room temperature. An inline hydrophobic membrane separator provided successful separation and collection of the aqueous phase comprising the colloidal Au NPs and the heptane in flow. A continuous synthesis for up to 2 hours was investigated as a proof of concept for the development of a manufacturing platform using an inline UV-Vis spectrometer for live monitoring of the particle size and process yield. The synthesis was stable and reproducible over time for gold precursor concentration above 0.23 mM (after mixing), resulting in average particle size between 12 – 15 nm, however, for lower precursor concentrations (0.065 mM), the particle size decreased over time, from 22 – 14 nm. Although the yield was lower than 100 % due to observed fouling on the PTFE membrane, the yield was higher as the inlet flow rates increased, due to lower residence time of the colloidal solution in the separator. Recycling of the heptane was addressed, showing that re-using the collected heptane without further purification, increased the polydispersity of the colloidal solutions (~ 23 %). The results of this study address the challenges for the translation of the synthesis from batch to flow and provide the tools for the development of a continuous manufacturing platform for gold nanoparticles synthesis.

6.1. Introduction

In the past years, there have been several attempts for the translation of the batch-base Au NPs synthesis towards continuous flow processing. Wagner and Köhler[99] used a continuous flow microreactor for the reduction of the gold precursor ($HAuCl_4$) with ascorbic acid for the synthesis of 5 – 50 nm Au NPs capped with polyvinylpyrrolidone (PVP). However, they identified that during the process there was particle deposition (fouling) on the reactor walls, hindering the particle quality. Huang *et al.*[96] addressed the issue by analysing the observed particle deposition in fluorinated capillary reactors, showing that fouling consisted of unreacted gold-reducing agent complexes and Au^0 – namely "dark fouling" – and synthesised Au NPs – namely "pink fouling". Kulkarni and Sebastian Cabeza[109] introduced a two-phase flow systems using toluene as the continuous phase (the colloidal Au NPs were formed in the aqueous disperse phase) – avoiding the fouling on the hydrophobic capillary walls, but they observed the absorption of the particles in the liquid-liquid interface. Sebastian Cabeza *et al.*[44] used both hydrophilic and hydrophobic platforms for the synthesis of aqueous Au NPs in two-flow systems and the particle synthesis was affected by the droplet hydrodynamic characteristics, the mixing in the formed droplets or slugs and the residence time distribution in the reactor[43, 108]. Two phase flow has already been studied for the continuous synthesis of gold or other type of nanoparticle synthesis [44, 46, 49, 151, 218, 219]. Using a two-phase flow system prevents fouling, while it improves the residence time distribution which is crucial for the synthesis of monodisperse nanoparticles[43, 44]. In recent years, there has been also an increase in research towards the application of quality control systems[220, 221] (such as online UV-Vis absorption spectroscopy[191, 222]) to ensure the manufacturing of high quality particles and the transition of nanoparticle synthesis from lab-scale towards commercialisation.

The aim of the work is the synthesis of 10 – 20 nm citrate-capped Au NPs in a two-phase flow system, using heptane as the continuous phase to prevent the particle deposition on the reactor walls. The droplet size and the reactant mixing and speciation are addressed and an inline UV-Vis spectrometer allows live monitoring of the quality of the synthesised nanoparticles and evaluates the stability and yield of the manufacturing process. An inline membrane separator has been implemented in

the system for the separation and collection of the two phases in flow (the aqueous phase comprising the colloidal Au NPs and the organic phase).

6.2. Experimental section

6.2.1. Materials and methods

The reactants used were citric acid ($C_6H_8O_7 \cdot H_2O$, Sigma-Aldrich), trisodium citrate ($Na_3C_6H_5O_7 \cdot 2H_2O$, Fisher Scientific), Gold (III) chloride trihydrate ($HAuCl_4 \cdot 3H_2O$, Sigma-Aldrich) and n-heptane (≥99%, $CH_3(CH_2)_5CH_3$) and were of analytical grade. Basic Blue 3 ($C_{20}H_{26}ClN_3O$, Sigma-Aldrich) was used for the evaluation of droplet size and mixing in the formed droplets. Ultra-pure water (15 MΩ·cm) was used for all aqueous solutions throughout the experimental series. Polytetrafluoroethylene (PTFE) tubing (1 mm ID, VICI Jour) was used for all fluidic tubing and ferrules and fittings made of polyether ether ketone (PEEK) (Upchuch) were used for all required connections in the experimental set-up. The online UV-Vis absorption measurements were carried out using a USB2000+UV-VIS-E spectrometer (Ocean Optics) connected to a DT-MINI-2-GS deuterium/tungsten lamp light source (Ocean Optics) via the appropriate fibre optics. For the UV-Vis absorption spectra, the sample passed through a 390 µL flow-through quartz cell (176.700-QS, 10 mm optical path length, Hellma Ltd), and spectral analysis was performed in the range of 200-800 nm. The cuvette was cleaned with ultra-pure water and ethanol (Sigma Aldrich) after each experimental run, to ensure there was no remaining sample in the cuvette which could lead to particle deposition on the cuvette walls.

The synthesised nanoparticles were characterised (offline) via UV-Vis absorption spectroscopy, pH measurement, transmission electron microscopy (TEM) imaging (Jeol 2010–200 kV), differential centrifugal sedimentation (DCS) (CPS 24 000 Disc Centrifuge, CPS Instruments) and microwave plasma-atomic emission spectrometer (MP-AES) (4200 MP-AES, Agilent). For the UV-Vis absorption spectra, the Au NPs sample (~3 ml) was placed in a polypropylene cuvette cell and spectral analysis was performed in the range of 200-800 nm. The pH measurements were performed with a SevenCompact pH meter S220 (Mettler Toledo) equipped with an InLab Micro glass electrode (Mettler Toledo). TEM samples were prepared by dipping a drop of the stable sample solution onto a carbon film 200 mesh copper grid (C200 Cu, EM Resist Ltd) and let it dry in air. Particle counts from the TEM image analysis was performed

via Pebbles software to ensure accurate and unbiased particle sizing[177]. The Au NPs samples were analysed via DCS (~ 0.1 ml injected per sample). The assumed nanoparticle density for the DCS analysis was 12.3 g/ml as it was shown to provide comparable results with TEM image analysis for the range of 8 – 30 nm citrate-capped Au NPs[49]. In order to evaluate the conversion of the Au NPs synthesis process, two samples of equal volume were obtained from the collected solution; the one sample was precipitated using 1 M $NaCl$ solution and filtered (using a 0.2 μm pore cellulose-acetate filter, Sartorius Stedim Biotech) and then the filtrate along with the second sample were dried in an over at 105 ^{o}C. The dried filtrate and second sample were diluted in a solution of 1:9 (by volume) aqua regia:water and the conversion was calculated by the difference in the gold concentration between the filtrate and the second sample. The yield was also calculated by the ratio of the gold concentration in the second sample over the target gold concentration after mixing.

6.2.2. Experimental set-up

Gold nanoparticles were synthesised in a continuous two-phase flow system, where the colloidal gold nanoparticle solution consisted the disperse phase, while heptane acted as the continuous phase, in order to avoid the particle deposition in the walls of the PTFE capillary. In the citrate-reduction (*Turkevich*) method, the gold precursor ($HAuCl_4$) was reduced by a mixture of citric acid (H_3Ct) and trisodium citrate (Na_3Ct), so as the final pH of the sample was ~ 5.6. The precursor stock solution that was used was 5 mM $HAuCl_4$, while two freshly prepared stock solution of 50 mM H_3Ct and 50 mM Na_3Ct were mixed at specific ratios (noted hereafter as $Citrate$) for a given $HAuCl_4$ concentration. Firstly the two reacting solutions ($HAuCl_4$ and the appropriate mixture of H_3Ct:Na_3Ct were prepared by filling two glass syringes (25 ml, Scientific Glass Engineering) at predefined concentrations based on the developed statistical correlation in batch (see Chapter 5) for the synthesis of the targeted nanoparticle size (aqueous phase) (Table 6-1). A third glass syringe (50 ml, Scientific Glass Engineering) was filled with heptane (organic phase). The flow of the three solutions was regulated by two syringe pumps (PHD Ultra, Harvard Apparatus). The two aqueous solutions were delivered at the same flow rate ($\dot{V}_{HAuCl_4} = \dot{V}_{H_3Ct:Na_3Ct}$) and the inlet flow rate of each reactant ranged between 0.080 – 0.155 ml/min. The ratio between the total aqueous ($\dot{V}_{aqueous} = \dot{V}_{HAuCl_4} + \dot{V}_{H_3Ct:Na_3Ct}$) to organic flow rate ($\dot{V}_{organic}$) was 1:1 ($\dot{V}_{aqueous} = \dot{V}_{organic}$) and the flow rate of the heptane stream

ranged between 0.158 – 0.310 ml/min. Two different set-ups were developed, where the reactants were either preheated before mixing (noted as "*hot mixed*") (shown in Figure 6-1) or the reactants were mixed at room temperatures (20 – 25 ^{o}C) before entering the heated reactor (noted as "*cold mixed*") (shown in Figure 6-2). In the "*hot mixed*" system, the three streams were preheated at the targeted temperature (95 ^{o}C) to allow reactant speciation. The mixing of the two reactants was realised by using of a PEEK cross-junction with 0.5 mm through-hole (Upchurch) in which the two aqueous streams – at the same flow rate – were at 90^{o} with the heptane, to ensure uniform and stable aqueous droplets. The organic phase was used to prevent the particle deposition (fouling) on the reactor wall and the cross-junction.

Table 6-1 $HAuCl_4$, H_3Ct and Na_3Ct concentrations (after mixing) for targeted gold nanoparticle synthesis and pH value ~ 5.6.

Experimental set	Target Au NPs (nm)	Experimental conditions			
		$[HAuCl_4]$ (mM)	$[H_3Ct]$ (mM)	$[Na_3Ct]$ (mM)	Temperature (^{o}C)
A	10	0.5	1.65	5.85	95
B	15	0.23	0.21	1.17	
C	20	0.065	0.10	0.29	

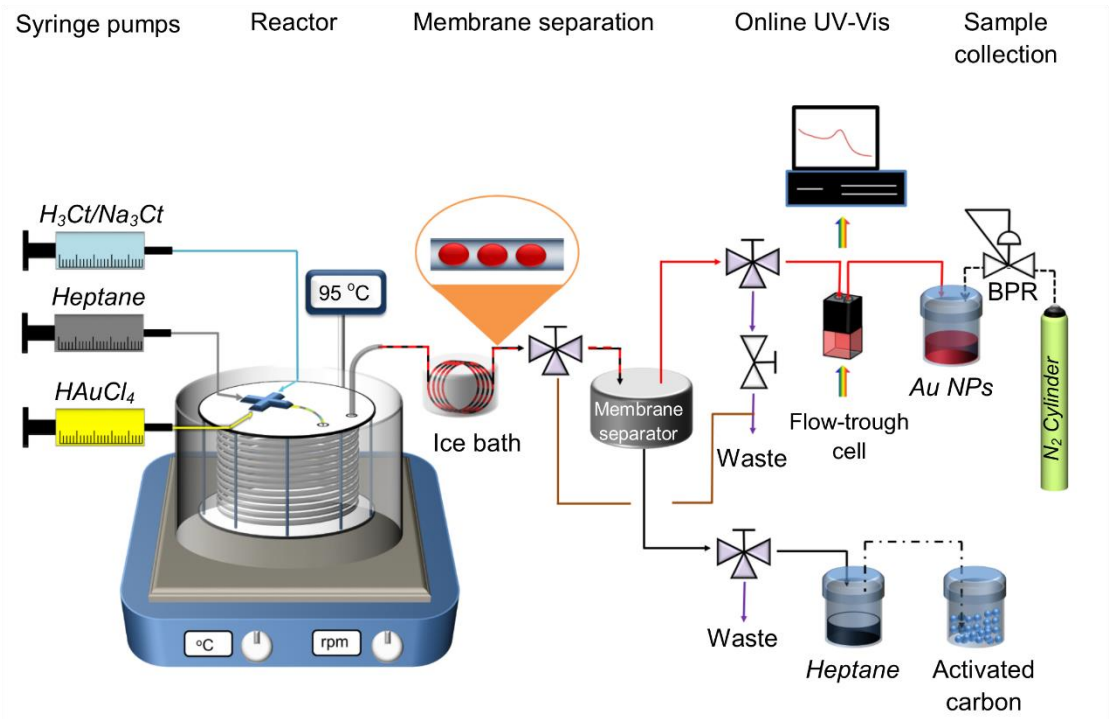

Figure 6-1 Setup of the "*hot mixed*" two-phase continuous synthesis system of citrate-capped gold nanoparticles using heptane as the continuous phase. The reactants ($HAuCl_4$ and H_3Ct:Na_3Ct) were preheated before mixing.

In the "*cold mixed*" system, the two reactants were mixed at room temperature; the coiled mixer consisted of a PTFE capillary of 0.21 ml volume (inner diameter: 0.5 mm, outer diameter: 1.59 mm, length: 1.07 m, VICI Jour). A T-junction with 0.5 mm through-hole (Upchurch) on the outlet of the mixer allowed the droplet generation using heptane as the segmenting fluid. In both systems, the droplets passed through a 2.25 ml coiled capillary reactor (inner diameter: 1 mm, outer diameter: 1.59 mm, length: 2.87 m, VICI Jour) made of PTFE. A glycerol bath on a hot plate with an integrated magnetic stirrer (Stuart UC152D, Cole-Parmer Ltd) was used for the regulation of the synthesis temperature. The temperature homogeneity in the glycerol bath was evaluated by immersing an external thermocouple at various positions and depths during the synthesis process; there were no temperature variations of more than 1 ^{o}C from the set temperature of 95 ^{o}C. Upon exiting the reactor, the droplets were cooled down to room temperature before entering the membrane separator in which the top stream contained only the aqueous phase of the Au NPs and the bottom stream contained only the organic phase. To prevent the deposition of unreacted particles on the membrane separator, a by-pass stream directed the two-phase flow from the reactor outlet to a waste bottle. A flow-through cell was

connected on the aqueous stream for the online monitoring of the UV-Vis spectra of the Au NPs solution. A 2.3 bara pressure was established with a backpressure regulator (BPR) (max. 4 bar K-type, Swagelok) connected to a nitrogen cylinder (BOC) to avoid boiling and bubble formation inside the capillary reactor. Collection vessels of the organic phase were connected with a vial filled with activated carbon to prevent heptane vapours from escaping in the environment.

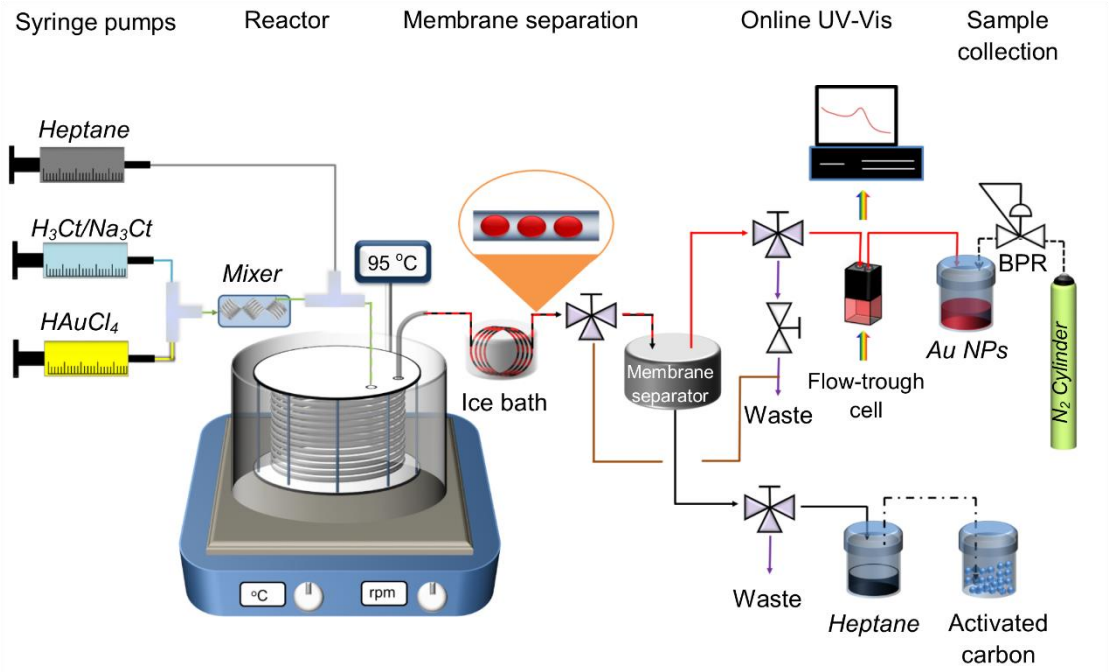

Figure 6-2 Setup of the "*cold mixed*" two-phase continuous synthesis system of citrate-capped gold nanoparticles using heptane as the continuous phase. The reactants ($HAuCl_4$ and H_3Ct:Na_3Ct) were mixed at room temperature using a coiled mixer.

6.3. Results & discussion

6.3.1. Hydrodynamic characterisation of reactant mixing

In the "*hot mixed*" system, the gold precursor ($HAuCl_4$) and the reducing agent (mixture of H_3Ct: Na_3Ct) were mixed in a cross-junction with the simultaneous flow of heptane to avoid fouling on the reactor walls, resulting in segmented flow in the PTFE capillary. In order to evaluate the droplet size, stability and extent of mixing of the reactants used in this study, a study was constructed using an aqueous solution of blue dye of standard concentration (75 mg/l) for the aqueous phase and heptane as the organic phase. In a two-phase flow system, droplet size increases by applying

a backpressure due to the increase on the hydrostatic pressure of the continuous phase (i.e. heptane), while the respective pressure on the disperse phase (i.e. water) remains constant[223]. As the aqueous phase enters the cross-junction and the droplet forms, the hydrostatic pressure of the continuous phase increases and reaches a peak when the droplet is ready to break-up[223]. Thereafter the pressure of the continuous phase decreases until the next aqueous segment to enter the junction. Hence, by applying 2.3 bara backpressure to the system, the hydrostatic pressure on the continuous phase is expected to increase resulting in more elongated aqueous segments.

A representative schematic of the mixing characterisation of the droplet is shown in Figure 6-3a, where the blue dye solution was mixed with water with the simultaneous flow of heptane at 90^{o} angle in the cross-junction. The mixing and the segmented flow of blue dye solution-heptane in the PTFE capillary was characterised using an inverted microscope (IX150, Olympus) monitoring the droplet size from 4 cm to 20 cm from the cross-junction outlet[*] (Section D.1.1, Appendix D). During gold nanoparticle synthesis, gold deposition can occur on the reactor walls in the absence of a hydrophobic film separating the aqueous phase from the PTFE material[96]. As PTFE is hydrophobic[191] and the heptane was the carrier phase, water convex segments were formed, while a liquid film was formed between the aqueous droplets and the capillary walls due to the wetting of the hydrophobic PTFE surface by the organic phase. By varying the flow rates of the aqueous and organic phases, the droplet size and standard deviation were evaluated, since the aim of the study was small and uniform droplets to ensure the residence time distribution would approximate the plug-flow reactor[43] and the synthesis would result in reproducible and monodisperse colloidal gold nanoparticle solution in flow. The droplet length is affected by the velocities of the aqueous and organic streams and ratio between the aqueous and organic flow rates[224], while increasing the aqueous flow rate the droplet length increases due to the lower shear stress exerted on the aqueous droplet by the continuous phase[223]. Yue *et al.*[191] examined the effect of the aqueous-to-organic flow rate ratio in a PTFE capillary microreactor, showing that increasing the flow rate ratio the length of the aqueous droplet increases in comparison with the length of the organic liquid slug. At the same time, for $\dot{V}_{Aqueous} = \dot{V}_{Organic}$ ($\dot{V}_{organic}$ is the flow

[*] *The image analysis for the droplet size and extent of mixing was performed by Dr Anand N. P. Radhakrishnan, Department of Chemical Engineering, University College London.*

rate of the organic inlet steam) the lengths of the aqueous droplet and the organic liquid slug are almost equal[191]. In this study, the water and the blue dye aqueous solution were delivered at the same flow rate ($\dot{V}_{water}$= $\dot{V}_{blue}$ = $\frac{\dot{V}_{aqueous}}{2}$) and the aqueous-to-organic flow rate ratio ($\dot{V}_{Heptane}$) was kept constant and equal to 1:1 ($\dot{V}_{Aqueous} = \dot{V}_{Heptane}$), to ensure equally spaced aqueous droplets and heptane slugs and avoid droplet coalescence[225].

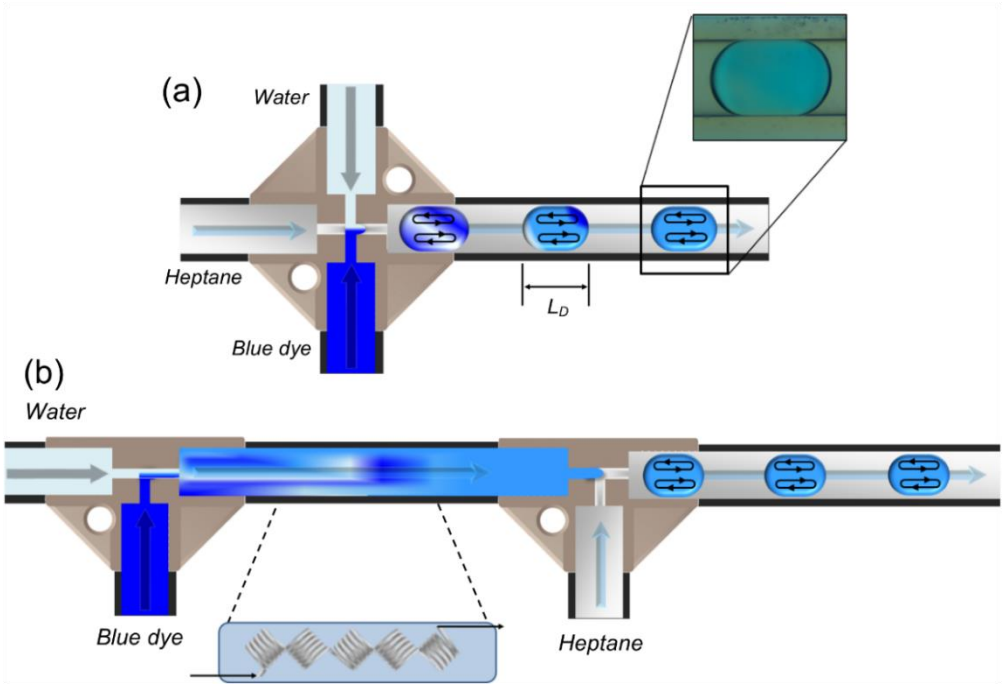

Figure 6-3 Schematic representation of the mixing profile and the segmented flow in the PTFE capillary in the a) "*hot mixed*" and the b) "*cold mixed*" system. In (a), the aqueous blue dye solution and water were mixed in the formed droplets. Mixing was enhanced due to the internal vortexes in the fluid flow. The droplet size (L_D) were characterised via image analysis. Magnified area: Formed droplet in the capillary as shown in the inverted microscope, where extent of mixing was equal to ~ 1. In (b), the aqueous streams were mixed at room temperature using a T-unction followed by a coiled tube prior to the formation of the aqueous droplets using heptane as continuous phase in the PTFE capillary.

The aqueous droplet size (L_D) was estimated via the regression model developed by Wang *et al.*[226], taking into account the flow rate ratio of the two streams:

$$\frac{L_D}{d_t} = 0.898 + 0.653\frac{wf}{1-wf} \qquad \text{Eq. 6-1}$$

where d_t is the diameter of the capillary and wf is the water fraction and it is equal to the ratio of the aqueous and organic flow rates ($wf = \frac{\dot{V}_{aqueous}}{\dot{V}_{aqueous}+\dot{V}_{organic}}$).

Figures 6-4 a-d show the droplet size and standard deviation of the droplet length for increasing flow rates ($\dot{V}_{Aqueous}$ and $\dot{V}_{Heptane}$). The total flow rates of the two phase flow increased from 0.315 ml/min to 1.26 ml/min, while keeping their ratio constant and equal to 1:1. The calculated droplet length (Equation 6-1) for all studied flow rates was 1.6 mm, while average droplet length – from the image analysis shown in Figure 6-4 – was ~ 1.4 mm, indicating an approximately 10% discrepancy between the experimental and the calculated droplet length. At the same time, increasing the total inlet flow rate from 0.315 ml/min to 0.63 ml/min (Figure 6-4 a-c), the average droplet length (experimental size) remained the same (~ 1.4 mm) since $\dot{V}_{Aqueous} = \dot{V}_{Heptane}$. However, above 0.42 ml/min total inlet flow rate the standard deviation of the droplet size increased – σ_D was 0.15 – 0.25 mm for 0.63 ml/min total inlet flow rate – related to the droplet instability and coalescence at higher flow velocities. The coalescence of the droplets could be result of the increased shear stress exerted from the continuous to disperse phase and the increase of the pressure drop on the two phase flow at higher velocities[223, 227]. This phenomenon was more visible in case of 1.26 ml/min total inlet flow rate (Figure 6-4d), where the average droplet size ranged between 1.1 – 1.5 mm with 17 – 30 % polydispersity.

For the given flow rates (and subsequently the flow velocity of the aqueous-organic system) the capillary number (Ca), the Weber number (We) and the Bond (Bo) were evaluated to identify the effect of the viscous, inertial and gravitational forces over the interfacial tension between the two phases (Section D.1.2, Appendix D). The analysis showed that their values were very small (Ca < 0.0001, We < 0.001, Bo ≈ 0.01), for the studied flow rates, indicating that the interfacial tension in the liquid-liquid system was dominant over the viscous, inertial and gravitational forces. Also, the organic liquid film surrounding the aqueous droplet was negligible (δ = 3.5 – 7 μm for the studied flow rates) and there was ~ 1% difference between the velocity of the formed droplets and the velocity of the aqueous inlet stream. Therefore the droplet velocity could be approximated equal to the flow velocity of the aqueous mixture (Section D.1.2, Appendix D).

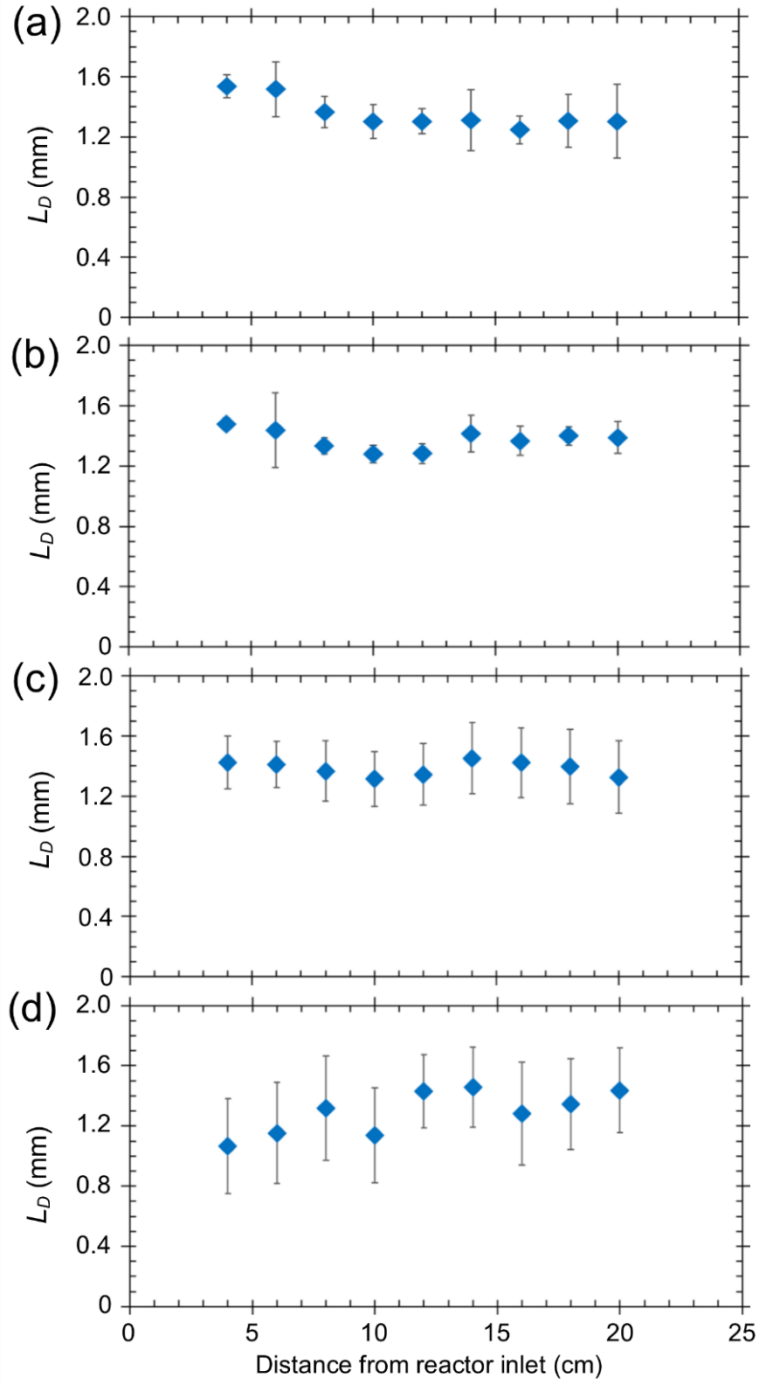

Figure 6-4 Length of the aqueous droplets formed (L_D) – calculated by image analysis – under segmented flow using a cross-junction (0.5 mm through-hole) connected to a PTFE capillary (inner diameter: 1 mm). The total flow rates of the two phase flow was equal to a) 0.315 ml/min, b) 0.42 ml/min, c) 0.63 ml/min and 1.26 ml/min, while the flow rates of water and blue dye aqueous solution were equal ($\dot{V}_{Water}$= $\dot{V}_{Blue}$). The ratio between the total aqueous ($\dot{V}_{Aqueous} = \dot{V}_{Water}$+ $\dot{V}_{Blue}$) to organic flow rate ($\dot{V}_{Heptane}$) remained 1:1 ($\dot{V}_{Aqueous} = \dot{V}_{Heptane}$) in all cases. Error bars refer to the standard deviation of the droplet length.

Figure 6-5 shows the extent of mixing over time for the studied flow rates, given by the image analysis of the formed droplets along the capillary length for different flow rates. The grey area represents the extent of mixing (ε_m) above 95 %, given by the ratio of the standard deviation of the pixel value in the formed aqueous droplet and the standard deviation of the pixel value of the perfectly mixed aqueous droplet (Section D.1.2, Appendix D)[228]:

$$\varepsilon_m = 1 - \frac{S_{droplet} - S_{mixed\ droplet}}{S_{droplet} + S_{mixed\ droplet}} \qquad \text{Eq. 6-2}$$

where $S_{droplet}$ is the standard deviation of the grey pixel value in the formed aqueous droplets and $S_{mixed\ droplet}$ is the standard deviation of the grey pixel value of the perfectly mixed aqueous droplet.

The mixing length (and of course the mixing time taking into account the inlet flow velocities) was defined as the distance (or required time) from the cross-junction outlet, where the extent of mixing ε_m was equal to 95 % homogeneity in the droplet (threshold for completion of the mixing)[228-230]. For the studied flow rates, the *mixing length* L_{95} was similar and varied between 7 cm (Figure 6-5a) to ~ 10 cm (Figure 6-5 b-d). However, taking into account the flow velocities and the L_{95}, the time required for 95 % can be calculated. Increasing the total inlet flow rate from 0.315 ml/min to 1.26 ml/min, the required time for reaching 95 % ε_m decreased from 12 s to 7s. The rapid mixing can be explained by internal recirculation vortices in the droplets[108] (or "twirling") which results from the shear stress of the stationary wall to the moving liquid inside the droplet[231]. Also, the high Péclet number values in the aqueous droplets (Pe^* = 3,730 – 14,921 for $\dot{V}_{Aqueous}$ = 0.158 - 0.63 ml/min) (Table D-2, Appendix D) means that the advection forces were dominant over the molecular diffusion[232, 233]. The aforementioned study allowed an insight on the operating inlet flow rate conditions for the formation of stable, uniform size droplets, as well as the required mixing length or time in each case.

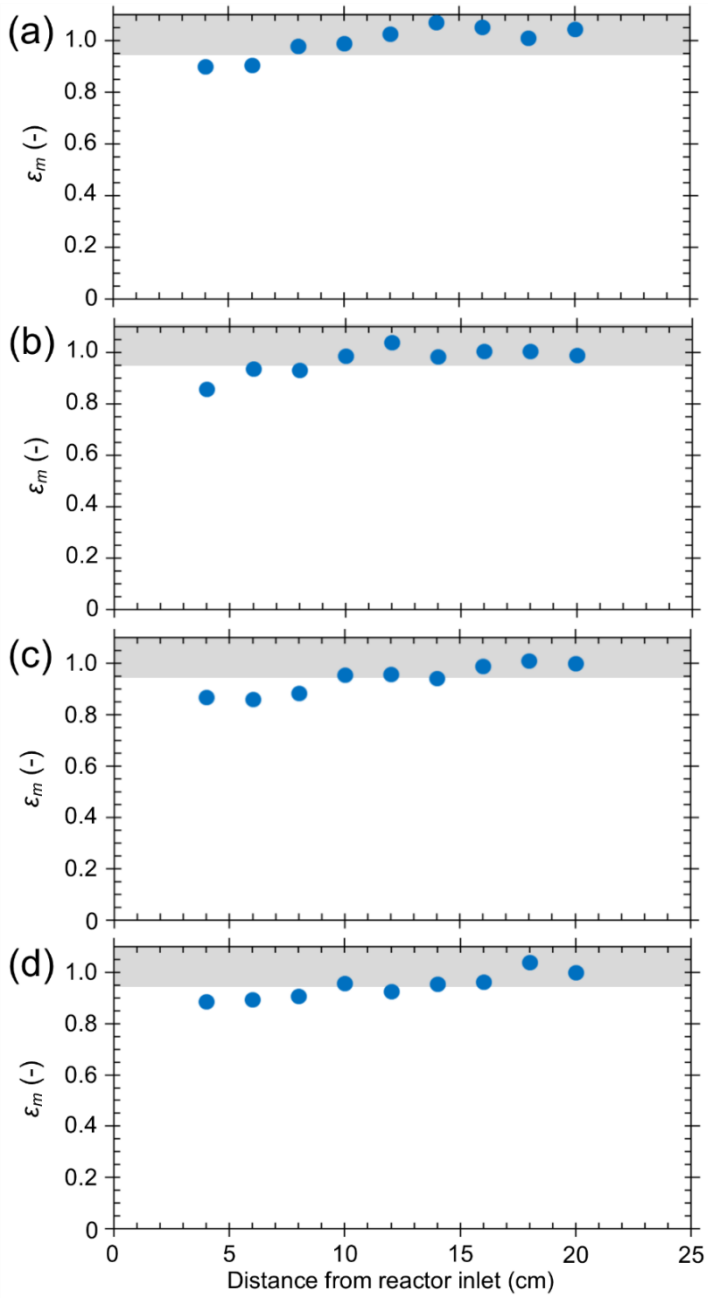

Figure 6-5 Extent of mixing (ε_m) – calculated by image analysis – in the aqueous droplets formed under segmented flow using a cross-junction (0.5 mm through-hole) connected to a PTFE capillary (inner diameter: 1 mm). The grey area represents the extent of mixing above 95 %, given by the ratio of the standard deviation of the pixel value in the formed aqueous droplet and the standard deviation of the pixel value of the perfectly mixed aqueous droplet. The total flow rates of the two phase flow was equal to a) 0.315 ml/min, b) 0.42 ml/min, c) 0.63 ml/min and 1.26 ml/min, while the flow rates of water and blue dye aqueous solution were equal ($\dot{V}_{Water}$= $\dot{V}_{Blue}$). The ratio between the total aqueous ($\dot{V}_{Aqueous} = \dot{V}_{Water}$+ $\dot{V}_{Blue}$) to organic flow rate ($\dot{V}_{Heptane}$) remained 1:1 ($\dot{V}_{Aqueous} = \dot{V}_{Heptane}$) in all cases.

For the case of "*cold mixed*" system, the reactants ($HAuCl_4$ and mixture of $H_3Ct{:}Na_3Ct$) were mixed at room temperature in a PTFE capillary, prior to segmentation with heptane (see schematic representation in Figure 6-3b). Varying the inlet aqueous flow rate ratio from 0.05 – 1 ml/min, the aqueous phase flow can be characterised as laminar since the Reynolds number varied between 2 – 48. τ_{conv} represents the time required for the stream to flow from the capillary inlet to outlet, and τ_{diff} represents the time required for the diluted species to diffuse across the half width of the capillary (Equations 6-3 and 6-4, respectively)[234, 235]. In order to evaluate the mixing efficiency of the two aqueous streams, the τ_{conv} and τ_{diff} characteristic times were estimated assuming only a straight capillary of 1 mm inner diameter. The aqueous flow rates varied between 0.1 – 1 ml/min, and the calculations were conducted for both the blue dye solution and the gold precursor ($HAuCl_4$) due to the different values in their diffusivities. As in the case of the "*hot mixed*" system, $\dot{V}_{aqueous} = \dot{V}_{water} + \dot{V}_{blue}$, while the molecular diffusivity of gold precursor was equal to $D_{m,HAuCl_4}$= 1.4·10^{-9} m^2/s[236] at 25 ^{o}C.

$$\tau_{conv} = \frac{L}{u_0} \qquad \text{Eq. 6-3}$$

where L is the length of the capillary and u_0 is the average fluid velocity.

$$\tau_{diff} = \frac{\left(\frac{1}{2} d_t\right)^2}{2D_m} \qquad \text{Eq. 6-4}$$

where d_t is the inner diameter of the capillary and D_m is the molecular diffusivity of the dilute species.

As shown in Figure 6-6, increasing the average fluid velocity (aqueous inlet flow rate), the τ_{diff} of the gold precursor ($\tau_{diff,HAuCl_4}$) remained constant and equal to 22 s, while the τ_{conv} decreased from ~ 250 s (for 0.05 ml/min) to 13 s for (for 1 ml/min). For the cases where $\tau_{conv} < \tau_{diff}$, there is not enough time for the solutes to diffuse to the water stream, while when $\tau_{conv} \geq \tau_{diff}$, the solute would have sufficient time to diffuse and the radial concentration would be uniform across the

channel. For 0.55 ml/min aqueous inlet flow rate $\tau_{conv} \approx \tau_{diff}$, indicating that for aqueous inlet flow rates up to 0.55 ml/min there would be sufficient time for the complete diffusion and mixing of the reacting species at room temperature.

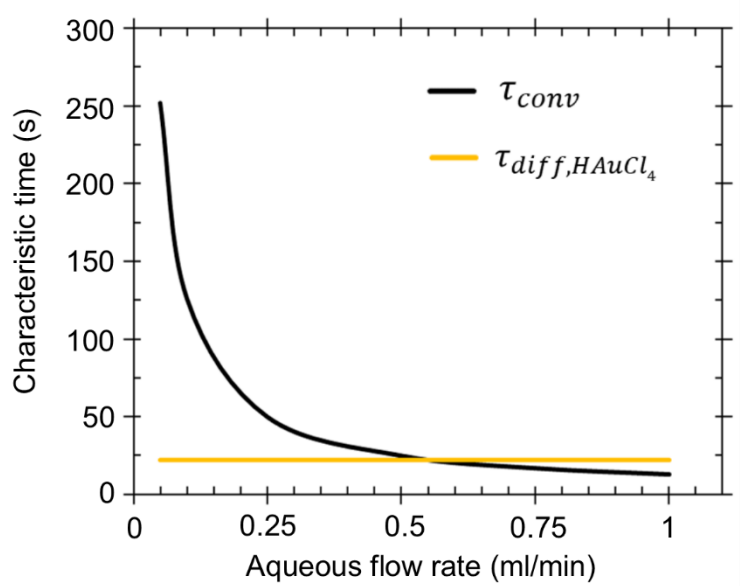

Figure 6-6 Estimation of the τ_{conv} corresponding to the time required for the downstream convection from the tube inlet to outlet and τ_{diff} representing the required time for the diffusion of the gold precursor ($\tau_{diff,HAuCl_4}$), respectively, across the half width of the capillary. Inner diameter, 1 mm; capillary length, 1.07 m; diffusivity of gold precursor at 25 ^{o}C, $D_{m,HAuCl_4}$= 1.4·10^{-9} m^2/s [236].

6.3.2. Study of operating conditions of membrane separator

For the separation of the organic phase (heptane) from the aqueous solution containing the synthesised Au NPs, a bespoke in-house designed membrane separator made of PEEK* was installed in line using a hydrophobic PTFE membrane (average pore size: 0.2 μm, Sterlitech Corporation) (Figure 6-7). Previous literature studies have implemented and investigated the use of PTFE membrane separators in continuous flow syntheses as they present a series of advantages over other mean of separations (gravity separators and microcapillary arrays)[237-239]: (1) PTFE offers a large chemical compatibility and it can be implemented in a wide area of chemical syntheses. (2) They are scalable up to small-scale flow chemistry applications and

* *The bespoke membrane separator was designed by Dr Enhong Cao, Department of Chemical Engineering, University College London.*

therefore a suitable candidate for the development of continuous manufacturing platforms. (3) The membrane separators are easy to fabricate and use and they can be reused as they are more durable than the microcapillary separators. (4) Due to the small average pore diameter (0.1 – 10 μm), they can be used for the separation of liquids with low interfacial tensions.

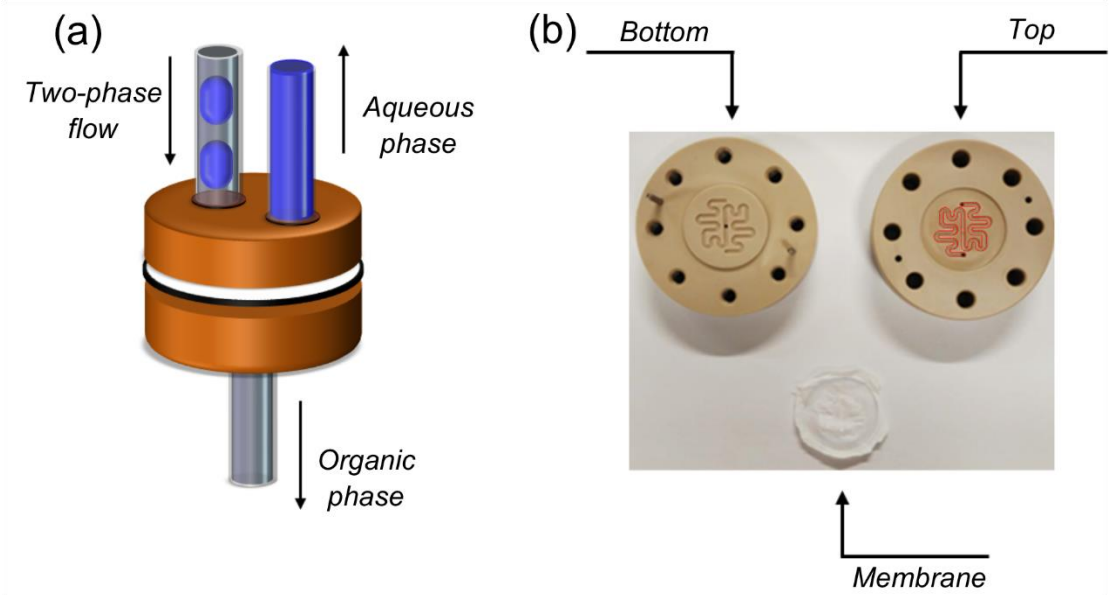

Figure 6-7 a) Schematic representation of the PEEK membrane separator used for the separation of the aqueous and organic phase (heptane) of the two-phase flow system. The aqueous phase is represented by the blue dye solution. b) Image of the internal parts of the membrane separator showing the top and bottom parts, the area of separation highlighted in red (channel dimensions on each part: length: 80 mm, width: 1 mm, height: 0.5 mm) and the PTFE membrane used in this study (average pore size, 0.2 μm).

The membrane separator was tested in a range of inlet flow rates and backpressures to map the optimum operating conditions for the successful inline separation of the heptane and aqueous Au NPs solution. An experimental visual inspection was conducted using blue dye and heptane to evaluate the liquid-liquid separation (or the retention and breakthrough), within a range of different inlet flow rates and applied pressures. The total flow rate ($\dot{V}_{total}$) varied between 0.1 – 1.0 ml/min, where $\dot{V}_{Blue} = \dot{V}_{Heptane} = {}^{\dot{V}_{Total}}/_{2}$. The applied pressure on the system (on the aqueous phase outlet) ranged between 0 – 2 barg using a K-type backpressure regulator from Swagelok, while the heptane phase outlet was opened at ambient pressure. The

pressure in the aqueous stream was monitored using a digital pressure test gauge (Druck DPI 104, General Electric). There was a 0.2 barg pressure drop on the system from the aqueous phase outlet to the pressure test gauge for the maximum inlet flow rate used ($\dot{V}_{total}$ = 1.0 ml/min), while the maximum applied pressure did not exceed the 2 barg to avoid breakage of glass collection vials on the outlet of the membrane separator (Duran 100 ml, Schott). The experimental results indicated successful separation of the two immiscible liquids within the studied flow rates and the applied pressures indicating that the PTFE membrane could be used as an inline separator for the separation of the heptane and the aqueous Au NPs solution on the outlet of the capillary reactor.

Previous studies have investigated and reported the existence of particle deposition on the capillary and reactor walls during the single phase synthesis of gold nanoparticles[96, 99, 105]. Huang *et al.*[96] conducted an in-depth investigation on the fouling of Au NPs on fluorinated capillaries. Based on their findings, there are two type of fouling, namely the "*dark fouling*" consisting of Au^0, gold ions and citrate-gold complexes due to adsorption on the reactor wall, and the "*pink fouling*" consisting of irreversibly attached formed Au NPs due to van der Waals forces. In this study, after the liquid-liquid separation it is possible that the formed Au NPs might attach on the PTFE membrane causing fouling and loss of material as well as clogging of the membrane after prolonged operation. The synthesis of Au NPs in flow was investigated via the "*hot mixed*" system, with and without the use of the membrane separator – once the system had reached steady-state – to identify if fouling takes place, as well as the effect of the membrane separator on the final particle size and shape. Figure 6-8a shows the offline UV-Vis absorption spectra of the synthesized Au NPs with and without the PTFE membrane separator after operating for one residence time (6.5 min), while Figures 6-8b and 6-8c show the TEM images of the formed particles with and without the membrane separator, respectively. In both cases – with and without the membrane separator – the absorption spectra were identical indicating that there was no loss of material on the membrane separator. The particle size (based on TEM) was similar and equal to 12.8 ± 1.4 nm and 13.1 ± 1.2 nm with and without the membrane separator, respectively. As previously discussed by Yang *et al.*[238] and Heider *et al.*[240], fouling can occur after prolong hours of use of the membrane separator for pharmaceutical products. The Au NPs synthesis process continued for up to 4 hours to evaluate if fouling occurs on the membrane in time and the membrane separator was opened showing that there was

fouling on the PTFE membrane, after visual inspection (Figure 6-9). Fouling was, also, observed on the top part of the membrane separator, which was coming in contact with the aqueous colloidal solution. It is worth noting that fouling was severe on the inlet of the two-phase flow in the membrane separator, confirming the rapid liquid-liquid separation.

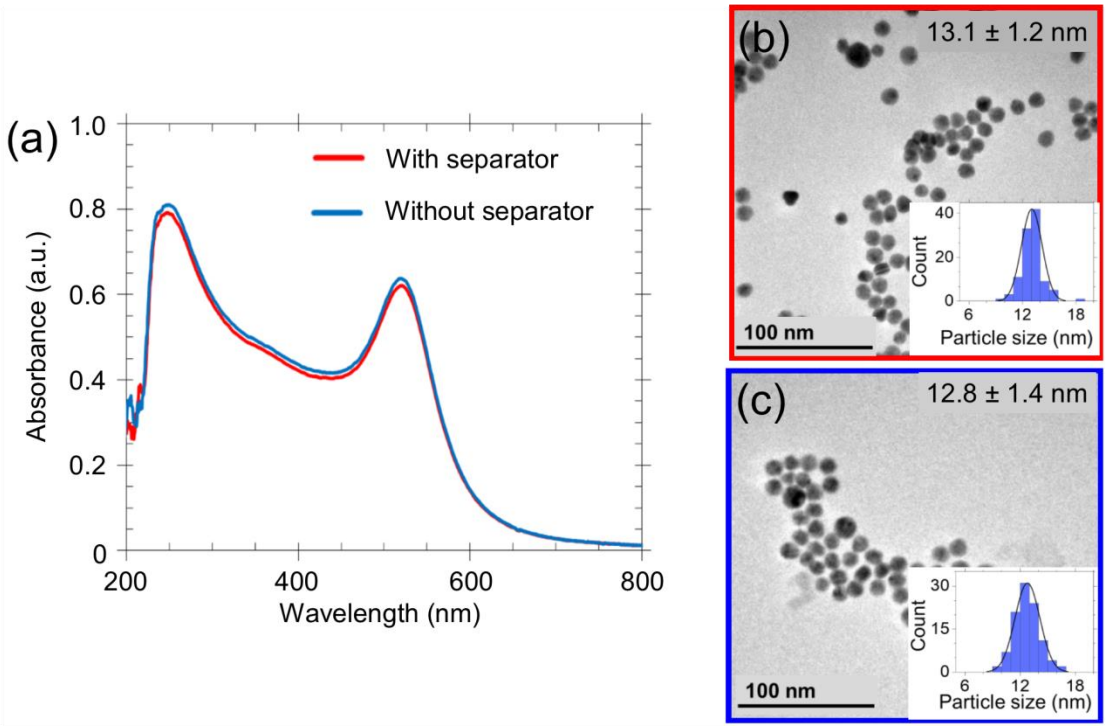

Figure 6-8 Offline analysis of the synthesised gold nanoparticles in flow via the "*hot mixed*" method with and without the membrane separator. The operating time with the membrane separation was one residence time (6.5 min). a) UV-Vis absorption spectra and TEM imaging b) with and c) without the membrane separator. Histograms in (b) and (c) show the particle size distribution obtained by TEM. Reactant concentration after mixing: [$HAuCl_4$], 0.23 mM; [H_3Ct], 0.21 mM; [Na_3Ct], 1.17 mM; temperature, 95 ^{o}C; $\dot{V}_{HAuCl_4} = \dot{V}_{H_3Ct:Na_3Ct}$, 0.09 ml/min; $\dot{V}_{Heptane}$, 0.174 ml/min; reactor volume, 2.25 ml; residence time, 6.5 min; average pore size of the PTFE membrane, 0.2 μm.

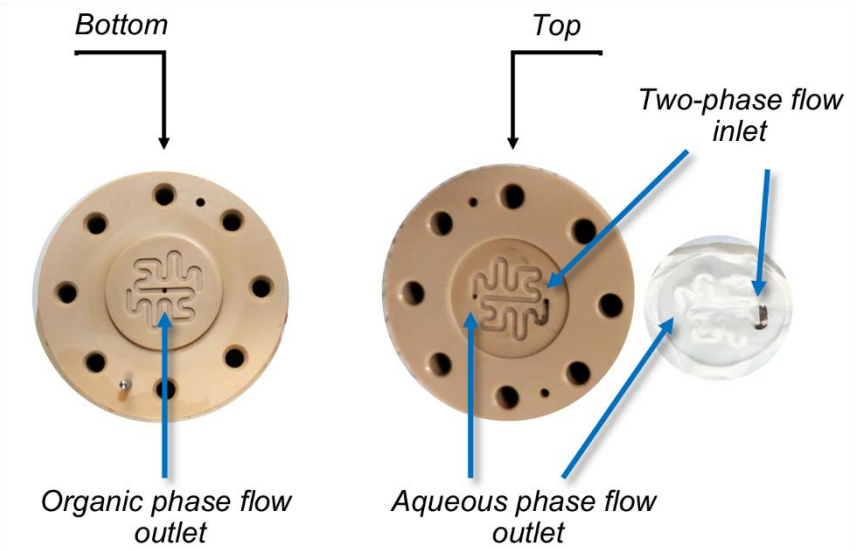

Figure 6-9 Top and bottom part of the membrane separator made of PEEK. Fouling observed on the PTFE membrane and the top part of the separator, after 4 hours of continuous operation for the synthesis of gold nanoparticles in flow via the "*hot mixed*" method. Reactant concentration after mixing: [$HAuCl_4$], 0.23 mM; [H_3Ct], 0.21 mM; [Na_3Ct], 1.17 mM; temperature, 95 °C; $\dot{V}_{HAuCl_4} = \dot{V}_{H_3Ct:Na_3Ct}$, 0.09 ml/min; $\dot{V}_{Heptane}$, 0.174 ml/min; reactor volume, 2.25 ml; residence time, 6.5 min; average pore size of the PTFE membrane, 0.2 μm.

6.3.3. Synthesis of gold nanoparticles in flow

The use of a liquid-liquid biphasic system prevented the particle deposition on the capillary walls due to the immiscible liquid film forming between the aqueous droplet and the reactor walls, while the segmented flow can approximate the plug-flow reactor (PFR) regime, since every aqueous droplet acts as an independent batch reactor[241]. Based on the droplet stability study (Figure 6-4), the flow rates of the aqueous stream (mixture of the gold precursor and the reducing agent) and the heptane could not be higher than 0.315 ml/min each, since above that value the droplets were unstable and they coalesced (Figures 6-4c and 6-4d). On the other hand, the lower the inlet flow rates, the longer the required time to reach 95 % extent of mixing in the droplets. Therefore, the lower value of the total inlet flow rate was 0.315 ml/min (Figure 6-5). The two developed synthesis routes (via *"hot mixed"* and *"cold mixed"*) were tested for the synthesis of 10 – 20 nm Au NPs, while the conditions for each size were given by the developed regression model in Chapter 5. The concentrations of every reactant are shown in Table 6-1, while the flow rates of

every stream are shown in Table 6-2. The chosen flow rates ensured that reactants would be mixed and the nominal residence time in the capillary reactor was enough for the synthesis to complete, as well as the Au NPs were stable upon collection.

Table 6-2 Flow rates of the $HAuCl_4$, $H_3Ct{:}Na_3Ct$ and heptane steams and the nominal residence time in the 2.25 ml reactor for the synthesis of 10 – 20 nm gold nanoparticles via both "*hot mixed*" and "*cold mixed*" methods.

Experimental set	Target Au NPs size (nm)	$\dot{V}_{HAuCl_4}$ (ml/min)	$\dot{V}_{H_3Ct:Na_3Ct}$ (ml/min)	$\dot{V}_{Heptane}$ (ml/min)	Nominal residence time (min)
A	10	0.155	0.155	0.310	3.6
B	15	0.09	0.09	0.174	6.5
C	20	0.08	0.08	0.158	7.1

Figure 6-10 shows the synthesised particle size distribution and UV-Vis spectra for the targeted synthesis of the 10 nm, 15 nm and 20 nm via the "*hot mixed*" method. Despite successful targeted synthesis in batch (see Chapter 5), there seems to be a large discrepancy between the targeted Au NPs size and the experimentally derived values for the 10 nm and 20 nm (particle size via DCS for A, B and C was 13.1 ± 0.9 nm, 14.7 ± 1.8 nm and 11.1 ± 1.9 nm, respectively). This discrepancy can also be confirmed by the TEM images of the synthesised particles, whereas the obtained particle sizes were 13.5 ± 1.1 nm, 15.6 ± 1.9 nm and 13.3 ± 2.0 nm, for the targeted synthesis of 10 nm, 15 nm and 20 nm, respectively (Figures 6-10 c-e). Additionally, Figure 6-11 shows the particle size distribution and UV-Vis spectra of the 10 – 20 nm Au NPs synthesis via the "*cold mixed*" synthesis method. The particle size via DCS for A, B and C was 12.2 ± 0.9 nm, 15.2 ± 1.0 nm and 19.3 ± 1.6 nm, respectively, while the obtained particle sizes given by TEM imaging were 12.1 ± 2.6 nm, 14.0 ± 1.4 nm and 18.1 ± 1.8 nm, for the targeted synthesis of 10 nm, 15 nm and 20 nm, respectively (Figures 6-11 c-e).

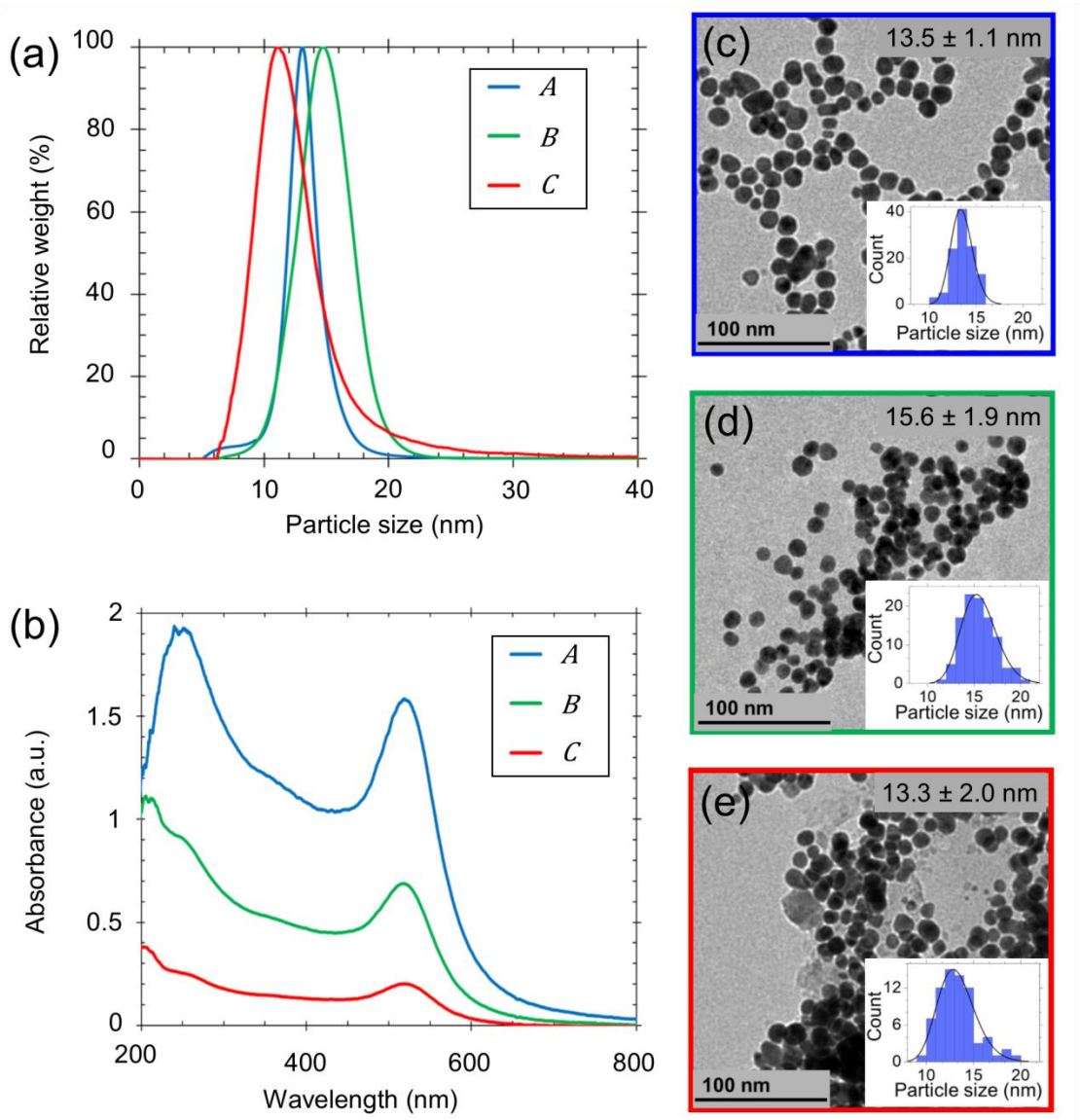

Figure 6-10 a) Particle size distribution (obtained by DCS) and b) UV-Vis spectra of the 10 – 20 nm gold nanoparticles synthesised via the "*hot mixed*" method. c-e) TEM images of the 10 – 20 nm gold nanoparticles for experimental set A – C, respectively. Histograms in (c)-(e) display the particle size distribution obtained by TEM. Reactor volume, 2.25 ml. *A:* $[HAuCl_4]$, 0.5 mM; $[H_3Ct]$, 1.65 mM; $[Na_3Ct]$, 5.85 mM; temperature, 95 °C; $\dot{V}_{HAuCl_4} = \dot{V}_{H_3Ct:Na_3Ct}$, 0.155 ml/min; $\dot{V}_{Heptane}$, 0.310 ml/min. *B:* $[HAuCl_4]$, 0.23 mM; $[H_3Ct]$, 0.210 mM; $[Na_3Ct]$, 1.17 mM; temperature, 95 °C; $\dot{V}_{HAuCl_4} = \dot{V}_{H_3Ct:Na_3Ct}$, 0.09 ml/min; $\dot{V}_{Heptane}$, 0.174 ml/min. *C:* $[HAuCl_4]$, 0.065 mM; $[H_3Ct]$, 0.10 mM; $[Na_3Ct]$, 0.29 mM; temperature, 95 °C; $\dot{V}_{HAuCl_4} = \dot{V}_{H_3Ct:Na_3Ct}$, 0.080 ml/min; $\dot{V}_{Heptane}$, 0.158 ml/min.

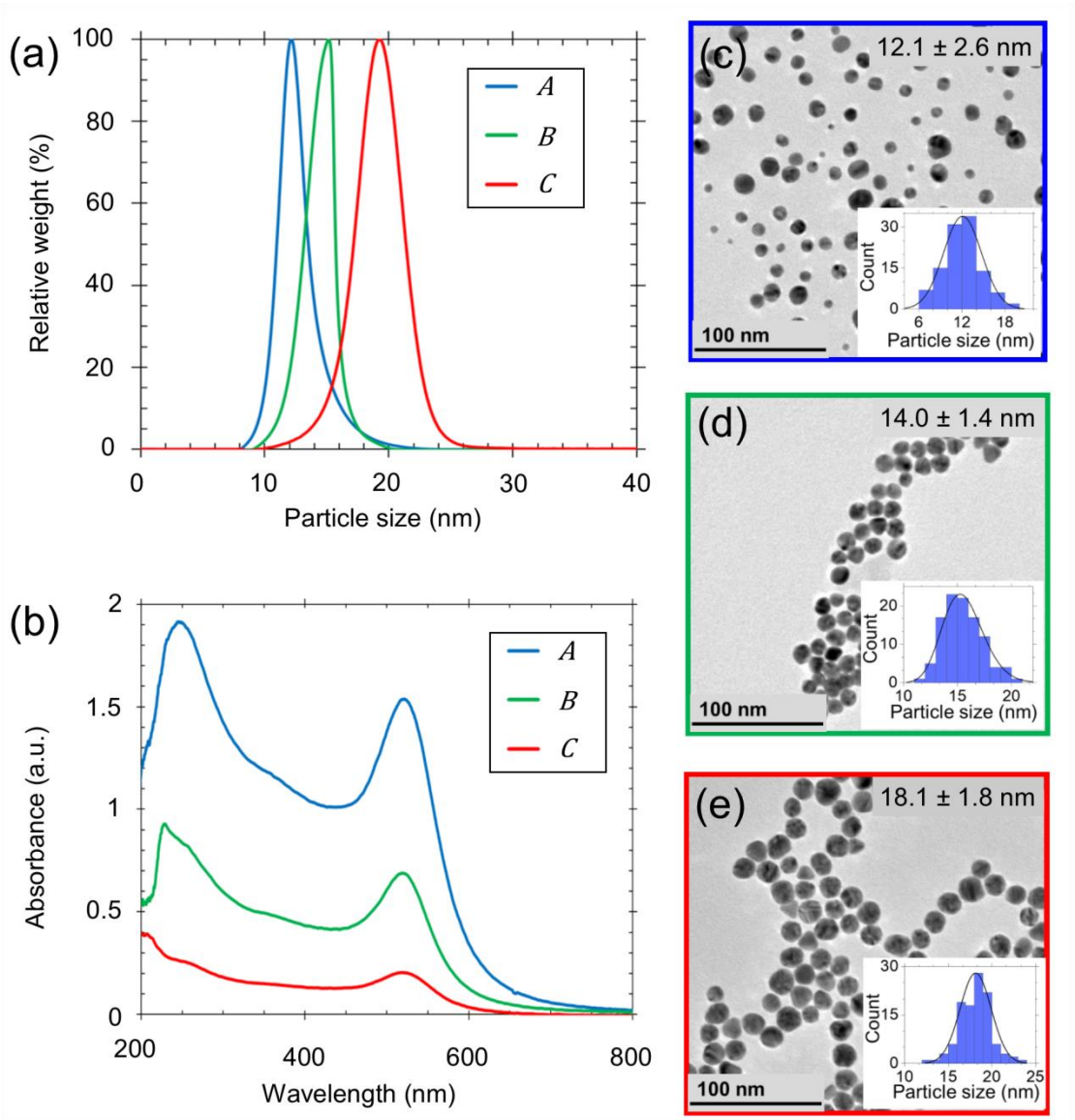

Figure 6-11 a) Particle size distribution (obtained by DCS) and b) UV-Vis spectra of the 10 – 20 nm gold nanoparticles synthesised via the "*cold mixed*" method. c-e) TEM images of the 10 – 20 nm gold nanoparticles for experimental set A – C, respectively. Histograms in (c)-(e) display the particle size distribution obtained by TEM. Reactor volume, 2.25 ml. *A:* $[HAuCl_4]$, 0.5 mM; $[H_3Ct]$, 1.65 mM; $[Na_3Ct]$, 5.85 mM; temperature, 95 °C; $\dot{V}_{HAuCl_4} = \dot{V}_{H_3Ct:Na_3Ct}$, 0.155 ml/min; $\dot{V}_{Heptane}$, 0.310 ml/min. *B:* $[HAuCl_4]$, 0.23 mM; $[H_3Ct]$, 0.210 mM; $[Na_3Ct]$, 1.17 mM; temperature, 95 °C; $\dot{V}_{HAuCl_4} = \dot{V}_{H_3Ct:Na_3Ct}$, 0.09 ml/min; $\dot{V}_{Heptane}$, 0.174 ml/min. *C:* $[HAuCl_4]$, 0.065 mM; $[H_3Ct]$, 0.10 mM; $[Na_3Ct]$, 0.29 mM; temperature, 95 °C; $\dot{V}_{HAuCl_4} = \dot{V}_{H_3Ct:Na_3Ct}$, 0.080 ml/min; $\dot{V}_{Heptane}$, 0.158 ml/min.

The observed discrepancies between the targeted sizes and the experimentally obtained Au NPs in both methods could be a result of the reactant mixing and the temperature profile along the reactor length, as well as the interfacial interaction between the aqueous phase and heptane. In case of the "*hot mixed*" system, the reactants and heptane were at 95 ^{o}C when mixed in the cross-junction, due to pre-heating of the streams. The reaction should start the moment the two reactants come into contact in the formed droplets. However, as shown from Figure 6-5, it required 8 – 12 s for acceptable mixing in the aqueous droplets translating to 3 – 4 % of the mean residence time in the capillary reactor. Despite the rapid mixing in comparison with the mean residence time in the reactor, the reaction could be initiated in the formed aqueous droplets the moment the streams were mixed and the particle size would be influenced by the concentration gradient in the formed droplets, which affects the nucleation and growth reaction rates[189]. At the same time, particles could assemble and agglomerate on the liquid-liquid interface of the aqueous droplets; the phenomenon is called interfacial absorption and it is stimulated by the minimisation of the interfacial energy due to the self-assembly of the particles on the interface[242]. Interfacial absorption during colloidal synthesis on the liquid-liquid interface has been reported in the literature[107, 218, 242-244], leading to asymmetric particle sizes and structures, and it is more dominant in higher reactant concentrations or larger formed particle sizes[109].

Kulkarni and Sebastian Cabeza[109] have examined the Au NPs synthesis in a segmented flow capillary reactor made of PTFE using toluene as the continuous phase, showing that the formed Au NPs are also likely to be assembled in the rear-end of the droplet, as the pressure gradient is lower than in the front of the droplet. Huang *et al.*[107] have studied a series of organic liquids for the Au NPs synthesis in segmented flow reactors, reporting that heptane has exhibited the least influence on the interfacial absorption amongst difference alkanes used. The aforementioned reasons could explain the discrepancies between the experimental and the target particle sizes in Figures 6-10c and 6-10e, as well as the long tail on particle size distribution observed on the C curve (Figure 6-10a). It is worth mentioning that the experimental run C (Tables 6-1 and 6-2) presented the highest polydispersity (~ 15 %) on the particle size distribution. This could be related to the low flow rates used and subsequently the longer mixing time required, sine the reactants were pre-heated and the synthesis would initiate once the reactants would come into contact.

Concerning the "*cold mixed*" system, the reactants were mixed at room temperature prior to segmentation; $\tau_{conv} \geq \tau_{diff}$ for the two reactants in the aqueous phase in all the flow rates of the aqueous stream used (Figure 6-6 and Table 6-2). Despite the previously reported fouling being formed on the capillary walls[96], there was no observed particle deposition on the PTFE walls due to the lower reaction rates at room temperature; Figure D-3 (Appendix D) shows the mixing stage, where fouling can be observed after the reactants were left in the capillary overnight. Hereafter, the observed discrepancies between the experimental and the 10 – 20 nm Au NPs sizes for the experimental run A, B and C (Figure 6-11) can be attributed again on the interfacial absorption on the liquid-liquid interface, similarly to the "*hot mixed* system" and the temperature profile along the capillary reactor. In both systems – "*hot mixed*" and "*cold mixed*" – the flow rates and reactants concentrations used were similar (shown in Table 6-2). Figure D-4 (Appendix D) shows the temperature profile for a single phase of water and heptane throughout the PTFE capillary (inner diameter: 1 mm) at high flow rate ($\dot{V}_{Heptane} = \dot{V}_{Aqueous}$ = 0.5 ml/min). The targeted temperature of 95 ^{o}C was achieved after ~ 20 cm for the water and 10 cm for the heptane, which translates to 3 – 6 % of the overall reactor length (~ 286 cm). However, in this work, a two-phase flow system was introduced, where the heat transfer to the aqueous phase is enhanced due to the internal vortices and the recirculation in the moving aqueous droplets[245-247]. Thus, the temperature in the aqueous droplet and the heptane slug was expected to reach 95 ^{o}C faster than compared to the single-phase system and the longitudinal temperature profile would not affect the Au NPs synthesis process to a great extent.

Interestingly, since the synthesis was conducted in flow, the possible variations on the pH could be result of fluctuations during the process or in the formed droplets The study of Contreras-Trigo *et al.*[248] has shown that small variation on the pH in the citrate reduction method (from 4.7 to 5.3) can alter the average particle size between ~ 14.0 nm – 15.5 nm, due to the shift on the gold complex and citrate species taking part in the reactions at different pH[40]. The pH of the solution could, also, be affected by reactant speciation due to the temperature profile along the reactor length, as described above; the speciation equilibrium of the gold complex shifts to more hydroxylated species at higher temperatures[38, 249]. It is worth noting, that the synthesised particles in the "*cold mixed*" system were within the targeted range of 10 – 20 nm Au NPs, despite the lack of reactant speciation due to preheating. These

results are in agreement with the batch data (see Chapter 5), showing that when the pH was ~ 5.6 the particle size was similar in the *direct*, *inverse* and *both speciated Turkevich* method because of the speciation process upon the reactant mixing.

6.3.4. Proof of concept for a continuous manufacturing platform

To establish an online quality control system and developing a continuous manufacturing set-up[31], the syringe pumps were replaced by milliGAT HF piston pumps (Global FIA) and an inline UV-Vis spectrometer was positioned on the aqueous stream outlet of the membrane separator. The Au NPs colloidal solution passed through a flow-through cell and the UV-Vis absorbance spectra were recorder in time[191] (Section D.5, Appendix D) The process stability was evaluated by recording the position (λ_{SPR}) and the absorbance (A_{SPR}) of the surface plasmon resonance (SPR) peak, while the particle size (in nm) was estimated via the Mie-theory based model developed by Haiss *et al.*[88] for particle sizes above 5 nm:

$$d_{est} = \exp\left(B_1 \frac{A_{SPR}}{A_{450}} - B_2\right) \quad \text{Eq. 6-5}$$

where A_{SPR} is the absorbance of the SPR peak, A_{450} is the absorbace at 450 nm wavelength of the UV-Vis spectra, and B_1 and B_2 are the experimentally derived fitting factors equal to 3 and 2.2, respectively.

The position of the SPR peak is characteristic of the particle size and shape, however, increasing the sample polydispersity could broaden the peak or cause red-shifting[84]. Additionally, the yield of the Au NPs synthesis process was estimated via the UV-Vis spectra using the Beer-Lambert law as described by Hendel *et al.*[84] and Yue *et al.*[191] The concentration of the Au^0 in the colloidal solution was calculated via the absorbance of the samples at 400 nm (A_{400}) and the yield (Y_d) was estimated by the ratio of the concentration of the Au^0 in the colloidal solution over the concentration of gold after mixing:

$$A_{400} = \varepsilon_{ext,400} \cdot [Au^0] \cdot l \quad \text{Eq. 6-6}$$

$$Y_d = \frac{[Au^0]}{[HAuCl_4]} \qquad \text{Eq. 6-7}$$

where A_{400} is the absorbance of the UV-vis spectra at 400 nm, $\varepsilon_{ext,400}$ is the extinction coefficient of the synthesised Au NPs sample (ranging between 2.29 – 2.38 L/mol·cm for 10 – 20 nm citrate-capped Au NPs)[84], $[Au^0]$ is the concentration of the Au^0 in the colloidal solution, l is the length of the flow-through cuvette used in the UV-Vis measurement (1 cm) and $[HAuCl_4]$ is the concentration of the gold precursor after mixing.

Figures 6-12 – 6-13 show the particle size within 2 hours of continuous operation, obtained via TEM imaging and DCS and the calculated values from Equations 6-5 – 6-7 via UV-Vis spectroscopy for the particle size between 10 – 20 nm Au NPs size using the *"cold mixed"* method. Figures D-5 – D-7 (Appendix D) show that the position of the SPR peak in all syntheses was located between 515 nm – 525 nm, indicating the formation of spherical gold nanoparticles of 10 – 20 nm in size[88]. The particle size and the process yield was measured experimentally via DCS, TEM and MP-AES to evaluate the accuracy of the online monitoring using the UV-Vis spectra. In case of the experimental run A and B the Figures 6-12a and 6-13a show that the synthesis particles followed a monomodal distribution and the obtained sizes over time – via DCS – were 13.9 ± 3.5 nm, 12.6 ± 1.8 nm, 12.4 ± 2.0 nm, 12.4 ± 1.8 nm for run A and 14.7 ± 2.3 nm, 14.9 ± 2.2 nm, 14.9 ± 2.2 nm, 14.6 ± 2.1 nm for run B, at 30 min, 60 min, 90 min and 120 min, respectively. Similarly, the particle size obtained by TEM over the 2 hour run fluctuated around 12.9 nm (Figure 6-12) and 15.2 nm (Figure 6-13), respectively, which was similar to the particle size obtained in the first experimental test of the *"cold mixed"* method (Figure 6-11). It is worth noting that the particle size of the experimental run A and B over time obtained by TEM and DCS was similar and the aspect ratio of the colloidal solutions was ~ 1.1 indicating spherical particles. Comparing the aforementioned Au NPs for run A and B with the previously synthesised particles in Figure 6-11, the synthesis showed high reproducibility as there was less than 1 nm difference in particle size in each case. The variation of the particle size ranged between 10 – 12 %, as obtained by the TEM imaging over time, except for the particle size of the experimental run A at 30 min (Figure 6-12c), where the polydispersity was ~ 18 % and comparable to the high polydispersity observed for the initial attempt of the same experimental run (21 %)

shown in Figure 6-11b. The high polydispersity should be related to the discrepancy of the pH of the collected colloidal solution with the target pH of ~ 5.6, as the pH of the colloidal solution was ~ 5.3 when the particle size distribution was between 18 – 21 %. The discrepancy of the colloidal pH could be attributed to the reasons analysed in Section 6.3.3, including fluctuations on the flow rates and different speciation equilibrium due to the longitudinal temperature profile in the capillary reactor.

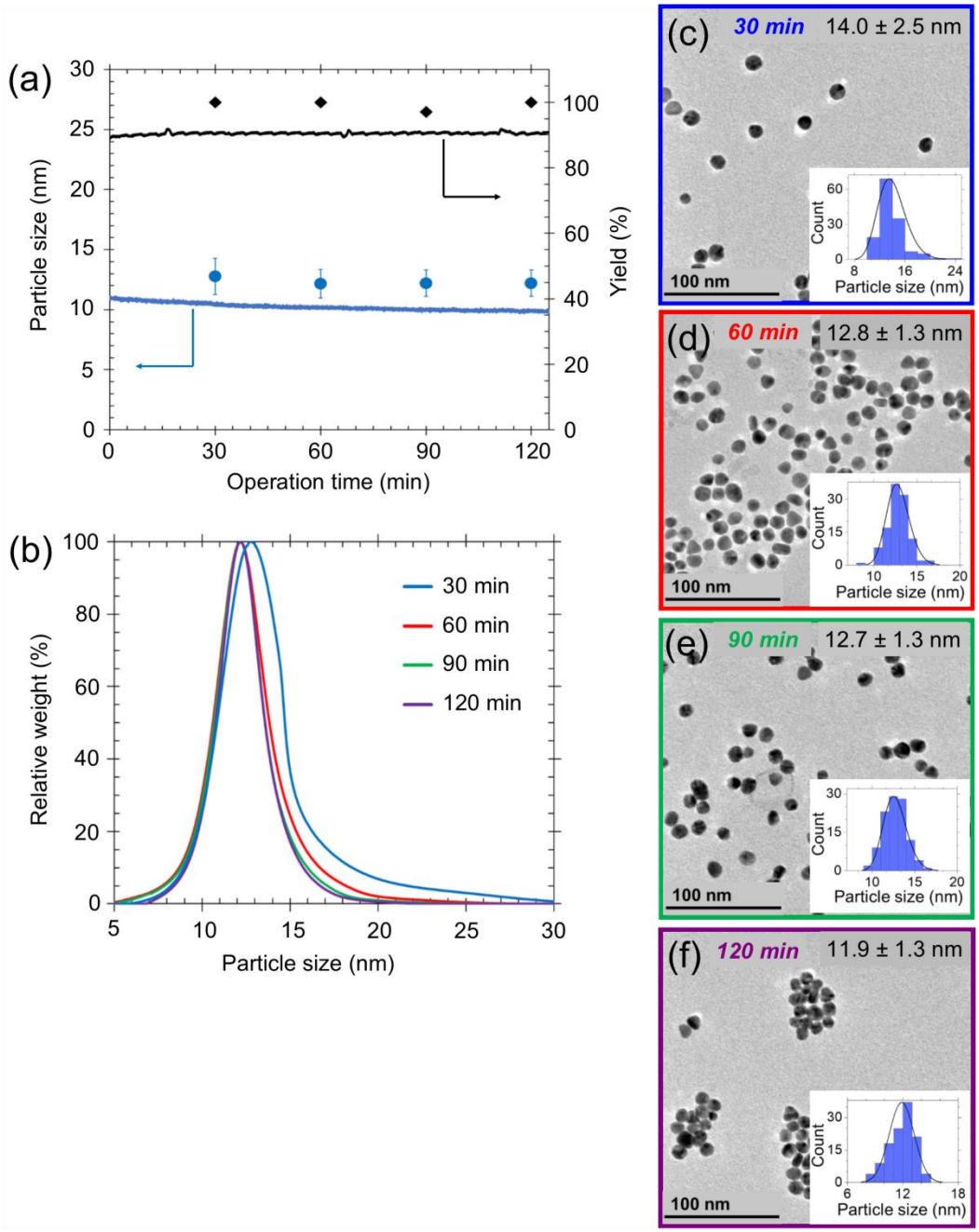

Figure 6-12 a) Particle size and yield of the gold nanoparticle synthesis via the "*cold mixed*" method for experimental run A (Tables 6-1 and 6-2) over 120 min operation time. Solid lines: experimental values obtained via online UV-Vis spectroscopy. Marks: experimental values obtained via TEM imaging (circles) and MP-AES (diamonds). b) Particle size distribution of the gold nanoparticles over 120 min operation time, obtained by DCS. c-f) TEM images of the gold nanoparticles, obtained via TEM imaging, after c) 30 min, d) 60 min, e) 90 min and f) 120 min operation time. Histograms in (c)-(f) display the particle size distribution obtained by TEM. Reactor volume, 2.25 ml. $[HAuCl_4]$, 0.5 mM; $[H_3Ct]$, 1.65 mM; $[Na_3Ct]$, 5.85 mM; temperature, 95 °C; $\dot{V}_{HAuCl_4} = \dot{V}_{H_3Ct:Na_3Ct}$, 0.155 ml/min; $\dot{V}_{Heptane}$, 0.310 ml/min.

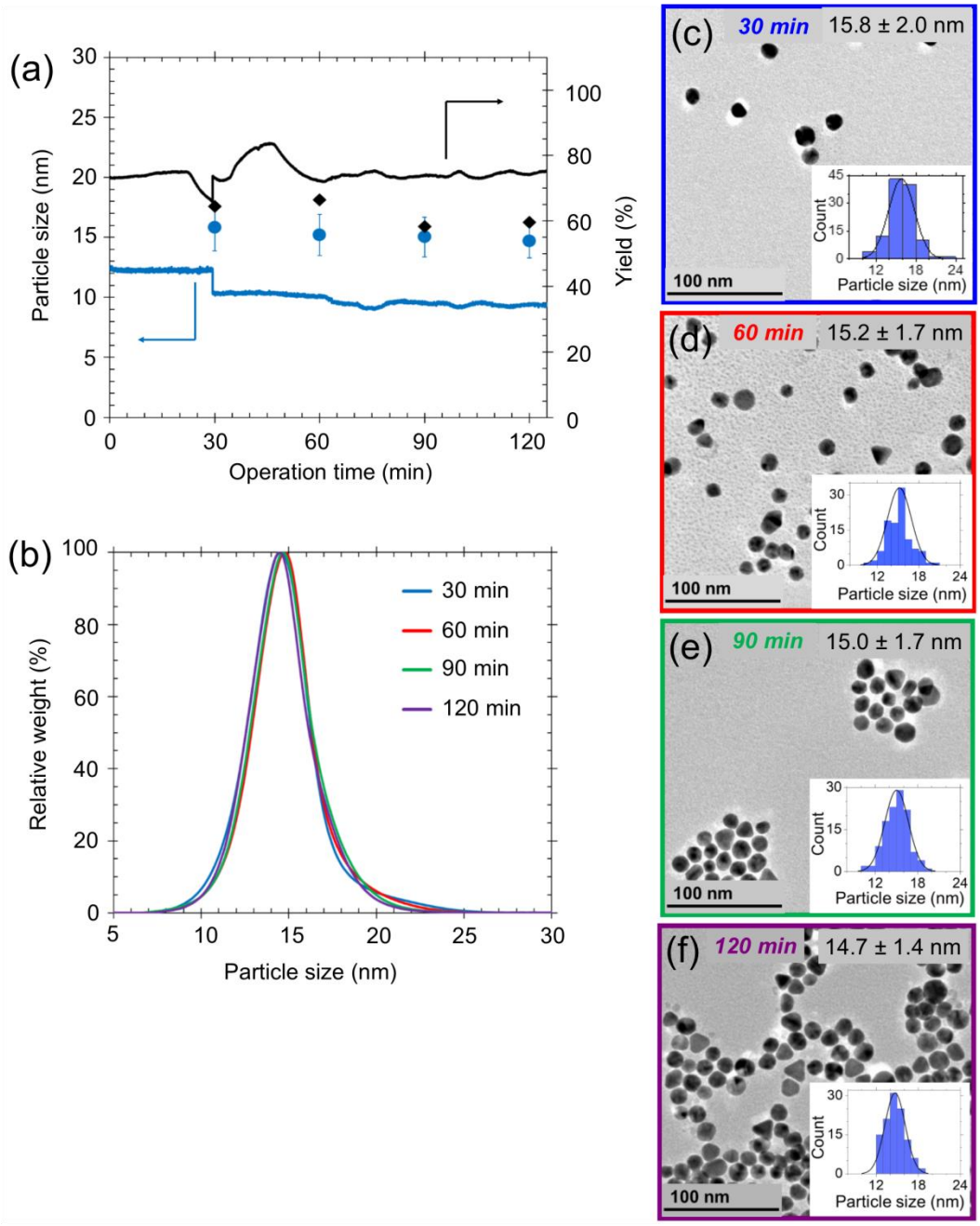

Figure 6-13 a) Particle size and yield of the gold nanoparticle synthesis via the "*cold mixed*" method for experimental run B (Tables 6-1 and 6-2) over 120 min operation time. Solid lines: experimental values obtained via online UV-Vis spectroscopy. Marks: experimental values obtained via TEM imaging (circles) and MP-AES (diamonds). b) Particle size distribution of the gold nanoparticles over 120 min operation time, obtained by DCS. c-f) TEM images of the gold nanoparticles, obtained via TEM imaging, after c) 30 min, d) 60 min, e) 90 min and f) 120 min operation time. Histograms in (c)-(f) display the particle size distribution obtained by TEM. Reactor volume, 2.25 ml. $[HAuCl_4]$, 0.23 mM; $[H_3Ct]$, 0.210 mM; $[Na_3Ct]$, 1.17 mM; temperature, 95 °C; $\dot{V}_{HAuCl_4} = \dot{V}_{H_3Ct:Na_3Ct}$, 0.09 ml/min; $\dot{V}_{Heptane}$, 0.174 ml/min.

The online UV-Vis showed a discrepancy between estimated particle size from Equation 6-5 and the experimental obtained data, as the particle size in Figure 6-12 ranged between 11.0 nm (at the beginning of the operation time) and 9.7 nm (120 min operation time), while the particle size in Figure 6-13 ranged between 12.4 nm (at the beginning of the operation time) and 9.4 nm (120 min operation time). Therefore, the estimated size (d_{est}) was underestimated by 16 – 37 % in comparison with the TEM imaging data. The model by Haiss *et al.*[88] was developed on spherical and monodisperse nanoparticles, thereof the polydispersity of the samples – as shown by both DCS and TEM imaging – could affect the evaluation limit and hinder the accuracy of the method due to the shift of the UV-Vis spectra[88, 89, 250]. Interestingly, in case of the experimental run C (Figure 6-14), as shown by the DCS over time, although Au NPs size after 30 min (21.6 ± 4.7 nm) was similar with the synthesised particles (run C) in Figure 6-11a, there was a decrease on the particle size along the 2 hour run to 16.1 ± 3.2 nm (60 min), 14.2 ± 2.3 nm (90 min) and 14 ± 2.5 nm (120 min). A similar trend can be observed on the estimated particle size by the online UV-Vis spectroscopy (Figure 6-14a). The estimated particle size in this case decreased from 27.9 nm to 13.4 nm. The decrease on the particle size along the 2 hour operation can be confirmed also by the blue-shifting of the SPR peak location from 526 nm to 524 nm (Figure D-7, Appendix D), since the SPR peak is also related to the particle size[88]. Nevertheless, it is uncertain the reason of the drop on the particle size over time. The particle size drop could be related to insufficient mixing and the temperature profile along the reactor length – due to the low flow rates used – or due to insufficient speciation of the feed precursor in the beginning of the operation and which speciated over time in the stock vial allowing the process to reach steady-state. The pH of the colloidal solution at 30 min operation time was measured equal to 4.15, while after 60 min, the pH of the colloidal solution was 5.35. Wuithschick *et al*.[38] stressed the boiling the gold precursor prior to the Au NPs synthesis in batch to ensure sufficient speciation, but this could not be possible in this configuration in flow due to fouling issues on the mixing stage. There seems to be a large discrepancy between the obtained size for 30 min operation time between DCS (21.0 ± 7.7 nm) and TEM (15.8 ± 2.0 nm). The discrepancy could be related to the influence of the agglomerated particles on the size distribution provided by DCS, since the instrument calculates the agglomerates as spheres with equivalent diameter and sedimentation time depending on the size, shape and configuration of every agglomerate[92].

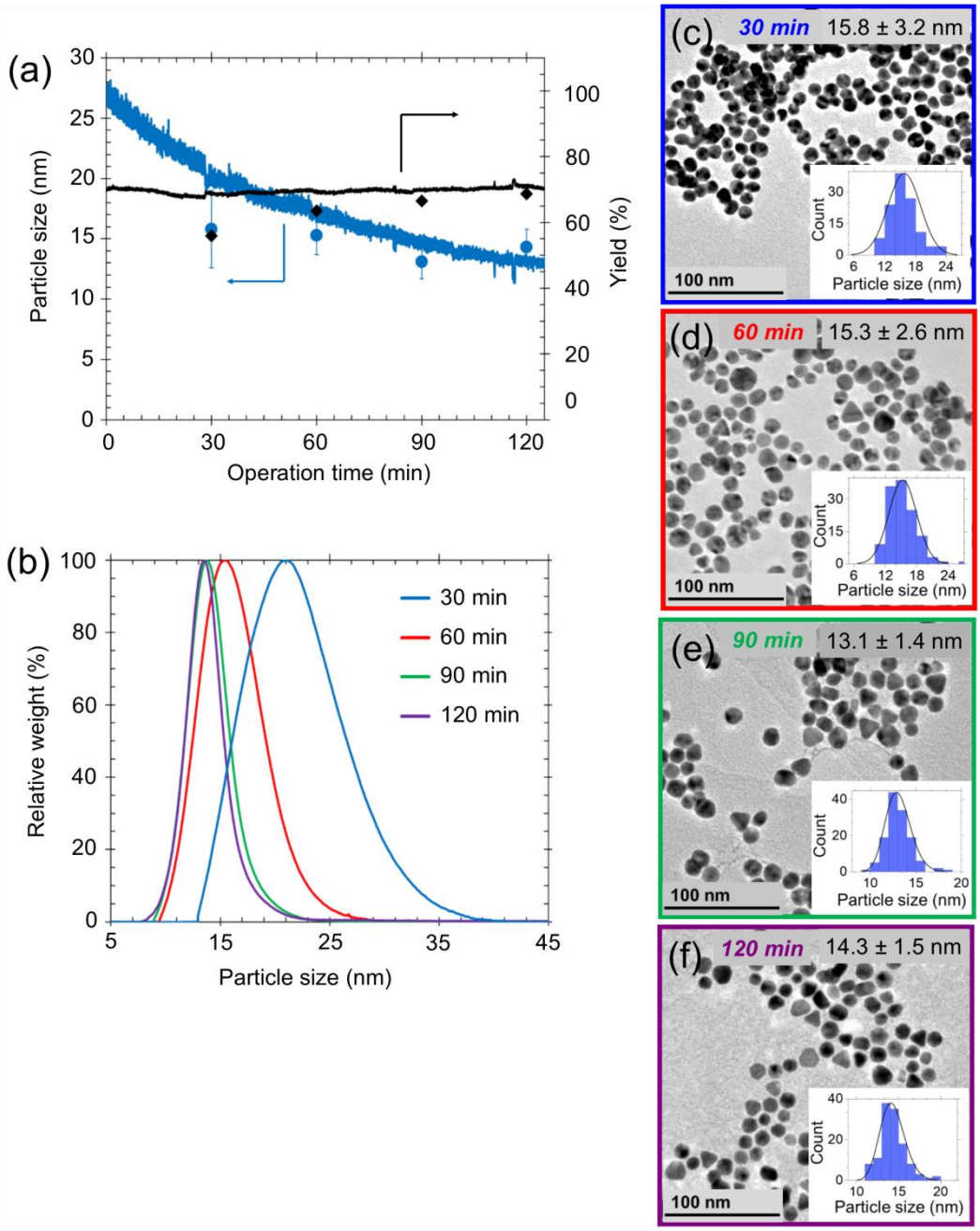

Figure 6-14 a) Particle size and yield of the gold nanoparticle synthesis via the "*cold mixed*" method for experimental run C (Tables 6-1 and 6-2) over 120 min operation time. Solid lines: experimental values obtained via online UV-Vis spectroscopy. Marks: experimental values obtained via TEM imaging (circles) and MP-AES (diamonds). b) Particle size distribution of the gold nanoparticles over 120 min operation time, obtained by DCS. c-f) TEM images of the gold nanoparticles, obtained via TEM imaging, after c) 30 min, d) 60 min, e) 90 min and f) 120 min operation time. Histograms in (c)-(f) display the particle size distribution obtained by TEM. Reactor volume, 2.25 ml. $[HAuCl_4]$, 0.065 mM; $[H_3Ct]$, 0.10 mM; $[Na_3Ct]$, 0.29 mM; temperature, 95 °C; $\dot{V}_{HAuCl_4} = \dot{V}_{H_3Ct:Na_3Ct}$, 0.080 ml/min; $\dot{V}_{Heptane}$, 0.158 ml/min.

At the same time, in order to evaluate the robustness of the *"cold mixed"* manufacturing platform over the 2 hour run, the yield of the Au NPs synthesis in time was evaluated using the Equation 6-6 via online UV-vis monitoring and experimentally via MP-AES. In all syntheses described above and shown in Figures 6-12 – 6-14, the conversion was between 94 – 99 %, confirming that the synthesis was completed within the targeted residence times in the capillary reactor (Table 6-2), as shown in Figure 6-15. It is worth noting that the lower conversion was observed for 30 min operation time for all experimental runs A – C, indicating that the synthesis required ~ 60 min to reach a steady state. As shown by Figure 6-12, the experimental yield over the 2 hour run ranged between 97 – 100 %. The estimated yield via online UV-Vis almost constant (< 1% fluctuation) and varied between 89 % – 92 %. Changing the operating conditions for the experimental run B and C over 2 hour synthesis (Figures 6-13 and 6-14), the estimated yield of the Au NPs via online UV-Vis decreased to ~ 70 %, while the discrepancy between the experimental and the estimated yield was again ~ 10 %. Observing the estimated yield over the 2 hour run in Figure 6-14 (solid black line), there was a large fluctuation at around 30 min, however, similar trend can be observed by the monitoring of the SPR peak (Figure D-7, Appendix) and it must be related to the sensitivity of the UV-Vis setup during sample collection.

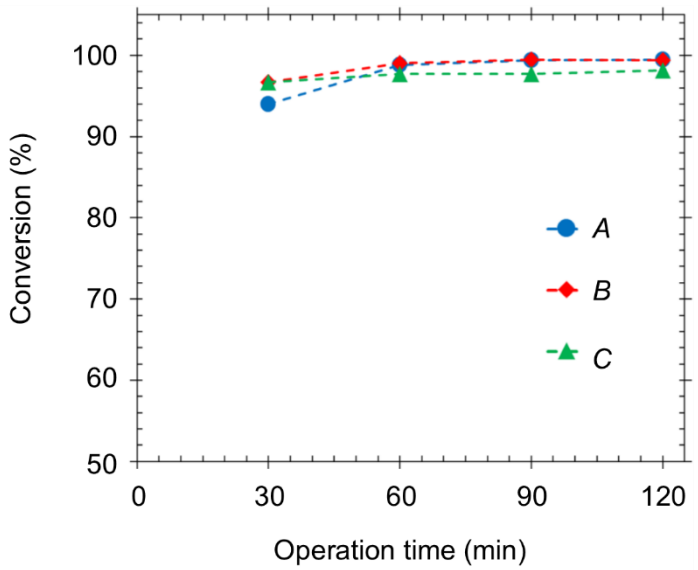

Figure 6-15 Conversion of the 10 – 20 nm gold nanoparticle synthesis (experimental run A – C) via the *"cold mixed"* method over 2 hour operation time, obtained by MP-AES. Operating conditions for the experimental run A – C are shown in Tables 6-1 and 6-2.

Since there was no fouling in the capillary walls, the deviation from the 100 % in yield should be related with the fouling on the membrane separator. The fouling was more severe in case of the experimental runs B and C, due to the lower inlet flow rates translating to longer residence times in the separator. It is worth noting that the accuracy of the yield estimated via the online UV-Vis monitoring is related with particle size and the sample polydispersity. The extinction coefficient increases with the particle size, affecting the absorbance A_{400}[84]. At the same time, the extinction coefficient is proportional to the particle size (and particle volume, d^3) and the sample concentration, hence the absorbance of the spectra (and subsequently the A_{400}) decreases by increasing the polydispersity of the sample[251, 252]. Hence, the observed lower values in the process yield could be related to the fouling in the membrane separator, as well as the quality of the colloidal solution. Nevertheless, the online model showed sufficient qualitative and quantitative agreement on particle size and yield, establishing that the online UV-Vis spectroscopy could be used as a quality control technique of live evaluation of the manufacturing process of Au NPs synthesis.

The recycling of the heptane used in the two-phase was also investigated, to study the potentials of re-using the organic phase – without additional purification steps – for the development of a sustainable manufacturing platform. Figure 6-16 shows the synthesis of the same experimental run B using fresh heptane (of high purity ≥ 99 %), while the collected heptane – exited from the membrane separator – was re-used for the same synthesis (Figure 6-16 a-b, *Recycled heptane*). As it can be observed from Figure 6-16a, when the recycled heptane was used for the same synthesis, the particle size increased by less than 1 nm, however, the polydispersity increased from 15 % to 23 % (the particle size was 14.7 ± 2.3 nm and 15.0 ± 3.4 nm, for fresh heptane and recycled heptane, respectively, obtained by DCS). The UV-Vis spectra of both syntheses (Figure 6-16b) were similar, despite the lower absorbance for the *Fresh heptane* run, which could be related to fouling in the PTFE membrane. Analysing the TEM images of the colloidal gold solution for fresh (Figure 6-16b) and recycled (Figure 6-16c) heptane as continuous phase, the synthesised Au NPs were spherical (particle aspect ratio was equal to ~ 1.1), while there was approximately 1 nm difference in size between DCS and TEM results. Figure D-8 (Appendix D) shows the UV-Vis spectra and TEM images of the recycled heptane. As it can be seen by the UV-Vis spectra (Figure D-8a), there were two peaks at 225 nm and 276 nm, similar to the peaks of gold species in aqueous solutions. The TEM images showed

the existence of gold nanoparticles or agglomerates (Figures D-8b and D-8c) which could result from transferring particles from aqueous phase to organic or deposited particles on the membrane which moved to heptane during separation. Another interesting point is the migration of polymer additives[253] (i.e. plasticisers) from the capillary walls to heptane, which could possibly enhance the interfacial absorption and result to the observed higher polydispesity. Of course, further experimental investigation on the impurities and mixtures in the recycled heptane is required (i.e. via infra-red spectroscopy or nuclear magnetic resonance), due to lack of information on the dilution of Au NPs or gold and citrate species in heptane.

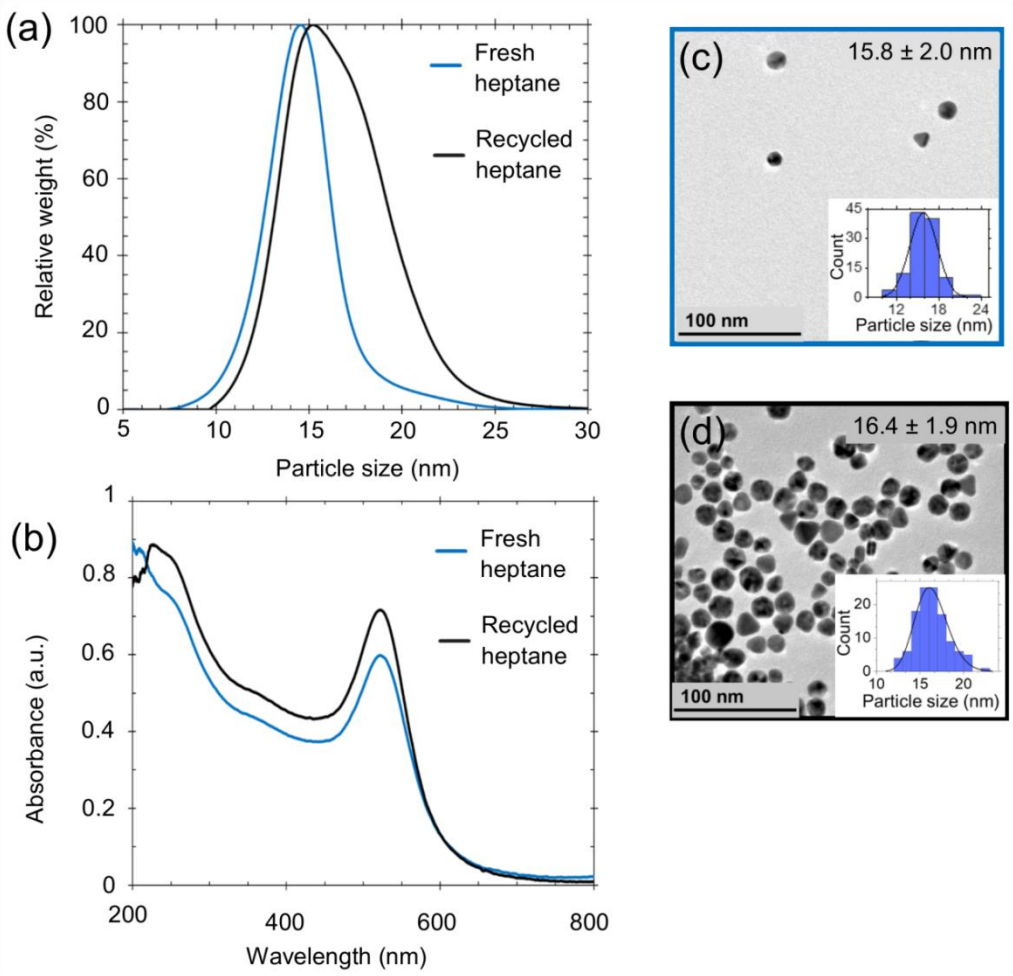

Figure 6-16 a) Particle size distribution (obtained by DCS) and b) UV-Vis spectra of the gold nanoparticles synthesised via the "*cold mixed*" method for experimental run B (Tables 6-1 and 6-2) using fresh and recycled heptane. c-d) TEM images of the gold nanoparticles, obtained via TEM imaging using c) fresh heptane and d) recycled heptane. Histograms in (c)-(d) display the particle size distribution given by TEM. Reactor volume, 2.25 ml. $[HAuCl_4]$, 0.23 mM; $[H_3Ct]$, 0.210 mM; $[Na_3Ct]$, 1.17 mM; temperature, 95 ^{o}C; $\dot{V}_{HAuCl_4} = \dot{V}_{H_3Ct:Na_3Ct}$, 0.09 ml/min; $\dot{V}_{Heptane}$, 0.174 ml/min.

6.4. Conclusions

This chapter describes the translation of the gold nanoparticle synthesis from batch to continuous flow. Reactant speciation is a vital step of the Au NPs synthesis process, influencing the reacting species participating in the reaction process. For that reason a two-phase flow system was used with and without pre-heating and speciating the reactants at the synthesis temperature (95 ^{o}C), where the heptane as continuous phase prevented the particle deposition on the reactor walls. At the same time, the formation of the aqueous droplets allowed the approximation of plug-flow reactor in each droplet, while an initial study on the reactant mixing and droplet size identified the range of the inlet flow rates. A PTFE membrane separator permitted the separation of the aqueous (containing the colloidal Au NPs) and the organic (heptane) streams in flow in a range of studied flow rates and system pressures, while the synthesised particles where monitored with the aid of an inline UV-Vis spectrometer on the aqueous outlet of the membrane separator. The synthesis experiments have shown that the lag time required for reactant mixing in the formed droplets and liquid-liquid interfacial absorption can hinder the synthesis – despite the reactant speciation in the *"hot mixed"* method – resulting in large discrepancies in particle size and polydispersity. Comparing with a similar system where the reactants were mixed at room temperature (*"cold mixed"* method), the particle sizes were within the range of 10 nm – 20 nm, showing that speciation via pre-heating is not compulsory when operating at pH equal to 5.6 in flow systems. The spectra acquisition via online monitoring over a 2 hour synthesis run allowed the estimation of the process stability via the surface plasmon resonance peak and the estimated size. Also, the process yield was evaluated both experimentally and via the online UV-Vis monitoring exhibiting a ~ 10 % discrepancy between the two evaluation methods. Finally, the heptane was recycled and re-used for the synthesis of ~ 15 % nm Au NPs, however, particle polydispersity increased – probably due to the existence of gold nanoparticles, gold species, as well as potential migration of polymer additives – identifying the importance of purifying steps prior to heptane recycling. The current system provides a new approach on continuous gold nanoparticle synthesis integrated with online monitoring for live quality control, and this study identifies the challenges and limitations for the continuous manufacturing of gold nanoparticles in flow.

CHAPTER 7. Conclusions and Future outlook

In the chapter, the highlights of this thesis are summarised, concerning the challenges investigated and the findings that emerged for the continuous gold nanoparticle synthesis under microwave and conventional heating. Attempts to translate the gold nanoparticle synthesis from batch to continuous manufacturing process is also discussed. Finally, key pathways by which multiple aspects of this research should be carried forward are identified and addressed in the Future Outlook section. This includes ways to address optimisation and scalability of the microwave-assisted process, design of a reactor based on a mechanistic kinetic model and routes towards autonomous manufacturing of gold nanoparticles in flow.

7.1. Conclusions

In order to develop a manufacturing platform for the continuous synthesis of gold nanoparticle in a robust and controllable manner, several challenges had to be addressed and overcome, including the exploration of novel pathways to implement milli-scale flow reactors. The outcomes of this doctoral thesis, in accordance with the drawn objectives, provide an insight on microwave heating as an alternative approach towards intensification of the continuous synthesis, while investigating the application – benefits and challenges – of continuous milli-fluidic tube reactors conjugated with microwave technology. Additionally, the developed empirical correlation for the targeted synthesis of colloidal gold nanoparticles could provide further guidance for developing continuous manufacturing set-ups for the synthesis of gold nanoparticles. The colloidal gold solutions can be further functionalised for biomedical applications, including point-of-care diagnosing platforms, lateral flow immunoassays and drug delivery.

In **Chapter 3**, the efficiency of microwave heating was investigated in continuous flow milli-scale reactors. Comparing with conventional heating, the temperature profile throughout the tube length was monitored while varying the process parameters - comprising the microwave power, inlet flow rate, tube orientation and system pressure. Increasing the input microwave power increased the longitudinal profile until it plateaued at a certain input value, related to the absorbed energy potential of the medium (water). Additionally, increasing the residence time (thereby decreasing the inlet flow rate) a higher longitudinal temperature was achieved, although after a certain inlet flow rate value the temperature remained unaffected by the decrease on the flow rate, due to the volumetric nature of microwave heating. A finite element model was developed to simulate the non-isothermal temperature profile in conjunction with the electric field profile in the tube, which contributed to a better understanding of the complexity of microwave heating in flow. However, the study revealed – despite the advantages – the drawbacks of the microwave technology in flow reactors related to the heating efficiency influenced by the reactor orientation towards the microwave port, as well as the perturbation of the electric field by the formed gas bubbles (due to evaporation) which decreases the heating efficiency. On the other hand, its efficiency was enhanced by increasing the system pressure, as this increased the boiling point of the medium and subsequently the microwave absorption potential.

The commercial single-mode microwave applicator and the PTFE tube used in **Chapter 3** was tested for the synthesis of gold nanoparticle in flow in **Chapter 4**. In order to explore the advantages of microwave radiation on the final product, a two-stage platform was built where nucleation-initiation took place in the first step under microwave heating, while the second step (where the residence time was constant at 20 min) allowed the growth to the final particle size under conventional heating. Particle size varied between 20 – 25 nm when the microwave power increased from 0 W to 25 W in the two-stage platform due to the longitudinal temperature profile in the microwave reactor. The study showed that non-thermal effects should not be considered related to enhancement of the synthesis reaction, due to the electromagnetic absorbance on the formed particles (Au NPs are particles with low electric conductivity) while at the microwave frequency spectrum the microwave absorbance on the medium (water) is dominant. Similarly to the outcomes of **Chapter 3**, the synthesis was unaffected by varying the residence time under microwave heating, as the temperature profile inside the reactor remained constant. However, this study revealed some major challenges on the application of the microwave heating for the synthesis of Au NPs in flow, related to the combined effect of the pure convective flow behaviour inside the reactor, the non-uniform longitudinal temperature profile and the loss of reactants and particles due to fouling on the reactor walls. These effects led to uncontrolled particle nucleation and growth under microwave heating affecting particle size and particle dispersity (the particle size distribution ranged between 18 – 20%).

Despite the increasing research on the gold nanoparticle synthesis in flow, there is limited kinetic information for the reactor design due to the perplexity and the nature of the citrate reduction mechanism. In **Chapter 5**, two empirical correlations were developed (based on two response surface models) for the estimation of synthesis parameters for the targeted synthesis of 10 – 20 nm Au NPs and the required reaction as functions of reactant concentrations and temperature. There is a “highly reproducible zone” for the citrate reduction gold nanoparticle synthesis at pH ~ 5.6, related to the dominant gold precursor ($AuCl_{4-x}(OH)_x^-$, where x = 0 – 4) and citrate species ($H_xCt^{(3-x)-}$, where x = 0 – 3) present in the reaction. Thus, the pH of the synthesis was adjusted using a mixture of Na_3Ct and H_3Ct (for a given $[HAuCl_4]$), while precursor or reducing agent speciation did not have any significant effect on the particle size. At the same time, increasing the synthesis pH, both the particle size and the polydispersity increased, while the required reaction time increased from 5.3

minutes (for pH=5.6) to 49 min (for pH=7.9 min). Particle size was affected by the reactant concentrations, while temperature variation between 85 – 95 ^{o}C had no significant effect ($p - value$ > 0.05). The response surface model for the required reaction time (taking into account the gold precursor concentration and temperature) overpredicted the required time up to 45 % depending on the target particle size, indicating the importance of further investigation on the evolution of Au NPs in time. Nevertheless, the developed models provide adequate information for the required conditions for the desired synthesis of spherical 10 – 20 nm Au NPs within less than 5 min at 95 ^{o}C, which can be used as a tool for the design of continuous flow synthesis systems.

The empirical correlations developed in **Chapter 5** provided essential information for the design and commission of a continuous manufacturing milli-fluidic system (such as reactor volume, respective flow rates, targeted concentrations, and temperature) for the translation of monodisperse 10 – 20 nm Au NPs synthesis from batch to flow using conventional heating. The findings and challenges that arose from **Chapter 4** identified that the residence time distribution in the reactor and the particle deposition in the reactor walls play a pivotal role in the size and quality of the synthesised Au NPs. At the same time, particle size and polydispersity was similar comparing microwave to conventional heating. Hence, these results led to the use of a two-phase flow system using heptane as the continuous phase and the aqueous colloidal gold particle in the disperse phase (water droplets), ensuring narrow residence time distribution and subsequently the formation of monodisperse particles while avoiding the fouling on the capillary walls. Two set-ups were developed with and without reactant speciation in flow (based on the finding from **Chapter 5**), where a parametric evaluation on mixing and droplet size was conducted for the choice of the target flow rates. Despite the platform optimisation, interfacial absorption was found to affect the final particle size, increasing the particle size and polydispersity. Reactant speciation caused large discrepancy from the target size, due to the mixing time required for the gold precursor and the citrate in the formed droplets to mix, while the reaction would initiate upon the droplet formation. A hydrophobic (PTFE) membrane separator placed in line with a flow-through UV-Vis spectrometer proved to be a robust downstream phase separation unit to separate the colloidal aqueous stream from heptane, thereby facilitating a novel online quality control system recording the particle size and stability and productivity in time. Finally, assessing the sustainability of the system, the heptane was recycled and re-used for the same Au NPs synthesis,

however, the polydispersity of the colloidal solution increased (~ 23%), indicating the need for further purification steps on the organic phase prior to recycling.

7.2. Future outlook

There are several challenges to be addressed and expand the academic and industrial research for the synthesis of gold nanoparticles.

7.2.1. Use of two-phase flow systems under microwave heating

The work in **Chapter 4** concluded that the large polydispersity (~18%) of the synthesised Au NPs under microwave heating was related to the temperature profile, the residence time distribution and the fouling on the reactor walls. **Chapter 3** showed that the non-isothermal temperature profile is a characteristic of the flow reactors under microwave heating, while the issue of narrow residence time distribution and fouling was resolved in **Chapter 6** with the aid of a two-phase flow system. The introduction of a liquid-liquid system (with immiscible liquids) in the capillary reactor under microwave heating could provide the same benefit as in the conventional heating. It is worth noting that the introduction of liquids of different dielectric properties in the microwave reactors could cause depolarisation of the electric field – non-polar solvents cause reflectance of the electromagnetic field – decreasing the efficiency of the microwave heating[131]. Due to the effect of the organic-to-aqueous flow rate ratio and the system pressure on the droplet length, a suitable parametric study on the aqueous droplets and organic slugs by varying these parameters would identify the appropriate experimental conditions to achieve the maximum length on the aqueous droplets. Hence, the length of the organic slug would be minimised to decrease the perturbation of the electric field, while maintaining a PFR-like RTD in the elongated aqueous droplets. Concerning the temperature profile and the efficiency of the microwave reactors, the use of custom single mode rectangular waveguides could minimise the power loss (minimise the reflected power)[60]. Using a series of stub tuners and a sliding short circuit, bespoke rectangular waveguides can tune the electric field intensity in the reactor affecting the temperature profile, as well[61, 254]. Thus, with the use of appropriate control in the microwave reactors, they can be used efficiently for the continuous synthesis of aqueous gold nanoparticles in flow.

7.2.2. Scale-up of microwave-assisted manufacturing systems

Aligning with the objectives of the thesis (see **Chapter 1**) on developing a continuous manufacturing platform for Au NPs synthesis, microwave reactors are considered an excellent tool for scale-up as the microwave heating is volumetric in nature. Increasing the volumetric capacity of the reactor, under constant microwave power, the higher the absorbed energy, while the temperature profile can be tuned with the appropriate components of the rectangular waveguide (stub tuners, solid-state conductor for power generation and sliding short circuit) and the inlet flow rates. There have been several approaches suggested in the literature on scale-out and scale-up techniques. Designing the microwave applicator to include microwave cavities in series[62] and parallel[63], the microwave power is directed in a series of microwave waveguides with separate reactors, scaling-out the process to multiple capillary and milli-scale reactors. On the other hand, the load volume could increase (increasing the tube diameter) while decreasing the microwave frequency of the power generator (below the 2.45 GHz) to achieve the same temperature uniformity and heating efficiency, since the penetration depth of the microwave radiation is inversely proportional to its frequency[161]. The performance of these systems can be tested to evaluate the temperature in the reactors and microwave efficiency in each case.

7.2.3. Mechanistic kinetic model for the citrate-reduction method

Despite the several attempts in the literature, the previously developed mathematical models are not adequate for the design of continuous flow reactors for the targeted Au NPs synthesis, due to the complicated nature of the citrate reduction mechanism. The response surface and the semi-empirical statistical correlations developed in **Chapter 5** accounted for the particle size of 10 – 20 nm Au NPs, as well as the respective reaction time of the synthesis – where it showed discrepancies between experimental and calculated results in **Chapter 6**. Additionally, the aforementioned correlations did not account for the change in the particle size over time. Previous literature models attempted to evaluate the reaction kinetics resulted in low predictability due to lack of respective data in time[65, 194], while modified models have shown the importance of taking into account the reactant speciation for the estimation of the reactions taking place[40, 189]. The combination of these models with respect to the evaluation of the particle size and distribution in time (either

experimentally using a platform with inline UV-Vis spectroscopy as in **Chapter 6** for optical extinction spectroscopy[255] and/or SAXS data[85]), could optimise the synthesis kinetis[189]. Hence a mechanistic model based on flow-derived data would lead to a suitable reactor design for the targeted Au NPs in continuous flow reactors.

7.2.4. Two-stage seeded-growth process for larger gold nanoparticle sizes

The properties and applicability of Au NPs are affected by both the particle size and shape. Considering the potential application and needs for larger sizes Au NPs, the developed set-ups (**Chapter 6**) could be optimised to accommodate a seeded-growth process, where the 10 – 20 nm particles could function as the seeds[74, 256, 257] for the synthesis of monodisperse Au NPs > 20 nm in size. The use of the separator in line provides the possibility of the process operating either in series or as in a discontinuous process. In case of operating in series, the outlet of the membrane separator would act as an inlet for the growth process, although the emerging challenges would be the pressure drop in the process, as well as the number of steps required for the growth of the Au NPs seeds to the targeted size[74]. On the other hand, in a discontinuous process, the collected monodisperse Au NPs seeds would have to be stored for sufficient time until its demand for the synthesis of larger sizes, thereby demanding stability. The *Turkevich* method offers the capability of the two-stage process which can be engineered taking into account the process characteristics and the number of the required steps. By identifying the required steps for the targeted size seeded-growth synthesis, the developed set-up in **Chapter 6** can be modified accordingly so as to produce the seeds (10 – 20 nm Au NPs) and then using these particles as a feed for the final growth to the larger particles (> 20 nm Au NPs).

7.2.5. Development of autonomous manufacturing platforms for gold nanoparticle synthesis

Ongoing research focuses the sustainability evaluation of nanomanufacturing processes and practises, due to the increasing interest and application of nanomaterials in various sectors[221]. At the same time, manufacturing practises are shifting towards “Industry 4.0”, implementing higher degree of automation and data acquisition via online monitoring connected to a centralised processing unit (so-called

Internet of Things)[258]. This methodology offers greater accuracy and efficiency due to the real-time data collection, while the automation ensures the self-sufficiency of the set-up. The platform developed in **Chapter 6** can be considered as an initial launching pad for a comprehensive manufacturing system, where additional components can be added on the platform including inline pH metering systems, pressure sensors and flow metes; all components should be connected to a central computing unit for live data analysis (Figure 7-1). Considering the semi-empirical statistical correlations in **Chapter 5**, the platform could operate autonomously for the targeted on-demand synthesis of Au NPs, while the online quality control monitoring system would include automatic shut-down procedures to avoid contamination of the collected colloidal solution and ensure operation safety in case of manufacturing instability. Taking into account the discrepancy between the estimated particle size via online UV-Vis spectroscopy and the respective experimental values, a multivariable partial least square (PLS) regression model[259, 260] or a Mie theory–based model[255] would enhance the online size estimation. Hence, unlike current batch processes, production would pause or stop automatically to avoid any contamination, ensuring the high quality of the final Au NPs[31].

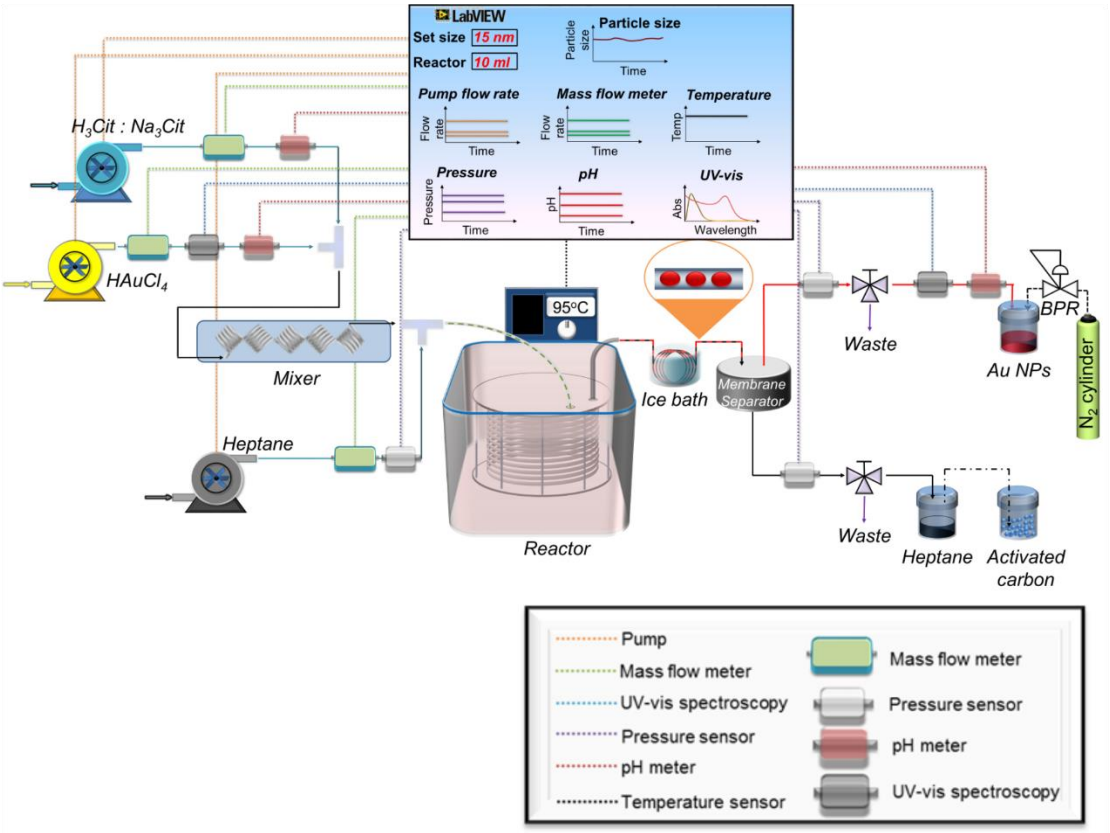

Figure 7-1 Automated manufacturing platform for the continuous synthesis of gold nanoparticles, with mass flow meters on the inlet streams and inline monitoring using pH metering systems, pressure and temperature sensors and UV-Vis spectrometers with simultaneous particle size estimation of the colloidal solution.

References

1. Park, J.; Joo, J.; Kwon, S. G.; Jang, Y.; Hyeon, T., Synthesis of monodisperse spherical nanocrystals. *Angew Chem Int Ed Engl* **2007,** 46, (25), 4630-60.
2. Nikoobakht, B.; Wang, J.; El-Sayed, M. A., Surface-enhanced Raman scattering of molecules adsorbed on gold nanorods: Off-surface plasmon resonance condition. *Chemical Physics Letters* **2002,** 366, (1), 17-23.
3. Smitha, S. L.; Gopchandran, K. G.; Smijesh, N.; Philip, R., Size-dependent optical properties of Au nanorods. *Progress in Natural Science: Materials International* **2013,** 23, (1), 36-43.
4. Li, P.-C.; Wang, C.-R. C.; Shieh, D.-B.; Wei, C.-W.; Liao, C.-K.; Poe, C.; Jhan, S.; Ding, A.-A.; Wu, Y.-N., In vivo photoacoustic molecular imaging with simultaneous multiple selective targeting using antibody-conjugated gold nanorods. *Opt. Express* **2008,** 16, (23), 18605-18615.
5. Huang, X.; El-Sayed, I. H.; Qian, W.; El-Sayed, M. A., Cancer cell imaging and photothermal therapy in the near-infrared region by using gold nanorods. *Journal of the American Chemical Society* **2006,** 128, (6), 2115-2120.
6. Zhang, T.; Zhao, H.; He, S.; Liu, K.; Liu, H.; Yin, Y.; Gao, C., Unconventional route to encapsulated ultrasmall nanoparticles for high-temperature catalysis gold. *ACS Nano* **2014,** 8, (7), 7297-7304.
7. Kim, B. H.; Hackett, M. J.; Park, J.; Hyeon, T., Synthesis, characterization, and application of ultrasmall nanoparticles. *Chemistry of Materials* **2014,** 26, (1), 59-71.
8. Macdonald, T. J.; Wu, K.; Sehmi, S. K.; Noimark, S.; Peveler, W. J.; du Toit, H.; Voelcker, N. H.; Allan, E.; MacRobert, A. J.; Gavriilidis, A.; Parkin, I. P., Thiol-capped gold nanoparticles swell-encapsulated into polyurethane as powerful antibacterial surfaces under dark and light conditions. *Scientific Reports* **2016,** 6, 39272.
9. Yang, Y.-C.; Wang, C.-H.; Hwu, Y.-K.; Je, J.-H., Synchrotron X-ray synthesis of colloidal gold particles for drug delivery. *Materials Chemistry and Physics* **2006,** 100, (1), 72-76.
10. Boisselier, E.; Astruc, D., Gold nanoparticles in nanomedicine: Preparations, imaging, diagnostics, therapies and toxicity. *Chemical Society Reviews* **2009,** 38, (6), 1759-1782.
11. Posthuma-Trumpie, G. A.; Korf, J.; van Amerongen, A., Lateral flow (immuno)assay: Its strengths, weaknesses, opportunities and threats. A literature survey. *Analytical and Bioanalytical Chemistry* **2009,** 393, (2), 569-582.
12. Rong-Hwa, S.; Shiao-Shek, T.; Der-Jiang, C.; Yao-Wen, H., Gold nanoparticle-based lateral flow assay for detection of staphylococcal enterotoxin B. *Food Chemistry* **2010,** 118, (2), 462-466.
13. Cordeiro, M.; Ferreira Carlos, F.; Pedrosa, P.; Lopez, A.; Baptista, P. V., Gold nanoparticles for diagnostics: Advances towards points of care. *Diagnostics (Basel, Switzerland)* **2016,** 6, (4), 43.
14. Ghosh, P.; Han, G.; De, M.; Kim, C. K.; Rotello, V. M., Gold nanoparticles in delivery applications. *Advanced Drug Delivery Reviews* **2008,** 60, (11), 1307-1315.
15. Ngo, V. K. T.; Nguyen, H. P. U.; Huynh, T. P.; Tran, N. N. P.; Lam, Q. V.; Huynh, T. D., Preparation of gold nanoparticles by microwave heating and application of spectroscopy to study conjugate of gold nanoparticles with antibodyE. coliO157:H7. *Advances in Natural Sciences: Nanoscience and Nanotechnology* **2015,** 6, (3), 035015.

16. Hall, J. B.; Dobrovolskaia, M. A.; Patri, A. K.; McNeil, S. E., Characterization of nanoparticles for therapeutics. *Nanomedicine* **2007,** 2, (6), 789-803.
17. Gangwar, R. K.; Dhumale, V. A.; Kumari, D.; Nakate, U. T.; Gosavi, S. W.; Sharma, R. B.; Kale, S. N.; Datar, S., Conjugation of curcumin with PVP capped gold nanoparticles for improving bioavailability. *Materials Science and Engineering: C* **2012,** 32, (8), 2659-2663.
18. Zong, J.; Cobb, S. L.; Cameron, N. R., Short elastin-like peptide-functionalized gold nanoparticles that are temperature responsive under near-physiological conditions. *Journal of Materials Chemistry B* **2018,** 6, (41), 6667-6674.
19. Fakayode, O. J.; Kruger, C. A.; Songca, S. P.; Abrahamse, H.; Oluwafemi, O. S., Photodynamic therapy evaluation of methoxypolyethyleneglycol-thiol-SPIONs-gold-meso-tetrakis(4-hydroxyphenyl)porphyrin conjugate against breast cancer cells. *Materials Science and Engineering: C* **2018,** 92, 737-744.
20. Li, Z.; Jin, R.; Mirkin, C. A.; Letsinger, R. L., Multiple thiol-anchor capped DNA–gold nanoparticle conjugates. *Nucleic Acids Research* **2002,** 30, (7), 1558-1562.
21. Aioub, M.; Austin, L. A.; El-Sayed, M. A., Chapter 2 - Gold nanoparticles for cancer diagnostics, spectroscopic imaging, drug delivery, and plasmonic photothermal therapy. In *Inorganic Frameworks as Smart Nanomedicines*, Grumezescu, A. M., Ed. William Andrew Publishing: 2018; pp 41-91.
22. Ahmadi, S.; Kamaladini, H.; Haddadi, F.; Sharifmoghadam, M. R., Thiol-capped gold nanoparticle biosensors for rapid and sensitive visual colorimetric detection of klebsiella pneumoniae. *Journal of Fluorescence* **2018,** 28, (4), 987-998.
23. León Félix, L.; Sanz, B.; Sebastián, V.; Torres, T. E.; Sousa, M. H.; Coaquira, J. A. H.; Ibarra, M. R.; Goya, G. F., Gold-decorated magnetic nanoparticles design for hyperthermia applications and as a potential platform for their surface-functionalization. *Scientific Reports* **2019,** 9, (1), 4185.
24. Ma, C.; Shao, H.; Zhan, S.; Hou, P.; Zhang, X.; Chai, Y.; Liu, H., Bi-phase dispersible Fe3O4@Au core–shell multifunctional nanoparticles: synthesis, characterization and properties. *Composite Interfaces* **2019,** 26, (6), 537-549.
25. Villa, A.; Wang, D.; Su, D. S.; Prati, L., New challenges in gold catalysis: Bimetallic systems. *Catalysis Science & Technology* **2015,** 5, (1), 55-68.
26. Liu, L.; Tai, X.; Zhou, X.; Hou, J.; Zhang, Z., Bimetallic Au–Ni alloy nanoparticles in a metal–organic framework (MIL-101) as efficient heterogeneous catalysts for selective oxidation of benzyl alcohol into benzaldehyde. *Journal of Alloys and Compounds* **2019,** 790, 326-336.
27. Mallikarjuna, K.; Bathula, C.; Dinneswara Reddy, G.; Shrestha, N. K.; Kim, H.; Noh, Y.-Y., Au-Pd bimetallic nanoparticles embedded highly porous Fenugreek polysaccharide based micro networks for catalytic applications. *International Journal of Biological Macromolecules* **2019,** 126, 352-358.
28. Niu, Z.; Cui, F.; Yu, Y.; Becknell, N.; Sun, Y.; Khanarian, G.; Kim, D.; Dou, L.; Dehestani, A.; Schierle-Arndt, K.; Yang, P., Ultrathin Epitaxial Cu@Au Core–Shell Nanowires for Stable Transparent Conductors. *Journal of the American Chemical Society* **2017,** 139, (21), 7348-7354.
29. Tomitaka, A.; Ota, S.; Nishimoto, K.; Arami, H.; Takemura, Y.; Nair, M., Dynamic magnetic characterization and magnetic particle imaging enhancement of magnetic-gold core–shell nanoparticles. *Nanoscale* **2019,** 11, (13), 6489-6496.
30. Li, Y.; DiStefano, J. G.; Murthy, A. A.; Cain, J. D.; Hanson, E. D.; Li, Q.; Castro, F. C.; Chen, X.; Dravid, V. P., Superior plasmonic photodetectors based on Au@MoS2 core–shell heterostructures. *ACS Nano* **2017,** 11, (10), 10321-10329.

31. Stavis, S. M.; Fagan, J. A.; Stopa, M.; Liddle, J. A., Nanoparticle manufacturing – Heterogeneity through processes to products. *ACS Applied Nano Materials* **2018,** 1, (9), 4358-4385.
32. Brust, M.; Walker, M.; Bethell, D.; Schiffrin, D. J.; Whyman, R., Synthesis of thiol-derivatised gold nanoparticles in a two-phase liquid-liquid system. *Journal of the Chemical Society, Chemical Communications* **1994**, (7), 801-802.
33. Martin, M. N.; Basham, J. I.; Chando, P.; Eah, S.-K., Charged gold nanoparticles in non-polar solvents: 10-min synthesis and 2D self-assembly. *Langmuir* **2010,** 26, (10), 7410-7417.
34. Turkevich, J.; Stevenson, P. C.; Hillier, J., A study of the nucleation and growth processes in the synthesis of colloidal gold. *Discussions of the Faraday Society* **1951,** 11, (0), 55-75.
35. Brown, K. R.; Walter, D. G.; Natan, M. J., Seeding of colloidal Au nanoparticle solutions. 2. Improved control of particle size and shape. *Chemistry of Materials* **2000,** 12, (2), 306-313.
36. Li, Y.; Zhang, P.; Duan, J.; Ai, S.; Li, H., One-step seeded growth of monodisperse, quasi-spherical, Tris-stabilized gold nanocrystals with sizes from 17 to 325 nm. *CrystEngComm* **2017,** 19, (2), 318-324.
37. Chen, H.; Zhou, K.; Zhao, G., Gold nanoparticles: From synthesis, properties to their potential application as colorimetric sensors in food safety screening. *Trends in Food Science & Technology* **2018,** 78, 83-94.
38. Wuithschick, M.; Birnbaum, A.; Witte, S.; Sztucki, M.; Vainio, U.; Pinna, N.; Rademann, K.; Emmerling, F.; Kraehnert, R.; Polte, J., Turkevich in new robes: Key questions answered for the most common gold nanoparticle synthesis. *ACS Nano* **2015,** 9, (7), 7052-7071.
39. Piella, J.; Bastús, N. G.; Puntes, V., Size-controlled synthesis of sub-10-nanometer citrate-stabilized gold nanoparticles and related optical properties. *Chemistry of Materials* **2016,** 28, (4), 1066-1075.
40. Kettemann, F.; Birnbaum, A.; Witte, S.; Wuithschick, M.; Pinna, N.; Kraehnert, R.; Rademann, K.; Polte, J., Missing piece of the mechanism of the turkevich method: The critical role of citrate protonation. *Chemistry of Materials* **2016,** 28, (11), 4072-4081.
41. Liu, X.; Atwater, M.; Wang, J.; Huo, Q., Extinction coefficient of gold nanoparticles with different sizes and different capping ligands. *Colloids Surf B Biointerfaces* **2007,** 58, (1), 3-7.
42. Rahman, M.; Rebrov, E., Microreactors for gold nanoparticles synthesis: From faraday to flow. *Processes* **2014,** 2, (2), 466-493.
43. Panariello, L.; Mazzei, L.; Gavriilidis, A., Modelling the synthesis of nanoparticles in continuous microreactors: The role of diffusion and residence time distribution on nanoparticle characteristics. *Chemical Engineering Journal* **2018,** 350, 1144-1154.
44. Sebastian Cabeza, V.; Kuhn, S.; Kulkarni, A. A.; Jensen, K. F., Size-controlled flow synthesis of gold nanoparticles using a segmented flow microfluidic platform. *Langmuir* **2012,** 28, (17), 7007-7013.
45. Wojnicki, M.; Luty-Błocho, M.; Hessel, V.; Csapó, E.; Ungor, D.; Fitzner, K., Micro droplet formation towards continuous nanoparticles synthesis. *Micromachines* **2018,** 9, (5), 248.
46. Lazarus, L. L.; Riche, C. T.; Marin, B. C.; Gupta, M.; Malmstadt, N.; Brutchey, R. L., Two-phase microfluidic droplet flows of ionic liquids for the synthesis of gold and silver nanoparticles. *ACS Appl Mater Interfaces* **2012,** 4, (6), 3077-83.
47. Kurihara, K.; Kizling, J.; Stenius, P.; Fendler, J. H., Laser and pulse radiolytically induced colloidal gold formation in water and in water-in-oil microemulsions. *Journal of the American Chemical Society* **1983,** 105, (9), 2574-2579.

48. Shang, Y.; Min, C.; Hu, J.; Wang, T.; Liu, H.; Hu, Y., Synthesis of gold nanoparticles by reduction of HAuCl4 under UV irradiation. *Solid State Sciences* **2013,** 15, 17-23.
49. du Toit, H.; Macdonald, T. J.; Huang, H.; Parkin, I. P.; Gavriilidis, A., Continuous flow synthesis of citrate capped gold nanoparticles using UV induced nucleation. *RSC Adv.* **2017,** 7, (16), 9632-9638.
50. Okitsu, K.; Ashokkumar, M.; Grieser, F., Sonochemical synthesis of gold nanoparticles: Effects of ultrasound frequency. *The Journal of Physical Chemistry B* **2005,** 109, (44), 20673-20675.
51. Pong, B. K.; Elim, H. I.; Chong, J. X.; Ji, W.; Trout, B. L.; Lee, J. Y., New insights on the nanoparticle growth mechanism in the citrate reduction of gold(III) salt: Formation of the au nanowire intermediate and its nonlinear optical properties. *Journal of Physical Chemistry C* **2007,** 111, (17), 6281-6287.
52. Seol, S. K.; Kim, D.; Jung, S.; Hwu, Y., Microwave synthesis of gold nanoparticles: Effect of applied microwave power and solution pH. *Materials Chemistry and Physics* **2011,** 131, (1-2), 331-335.
53. Bayazit, M. K.; Yue, J.; Cao, E.; Gavriilidis, A.; Tang, J., Controllable synthesis of gold nanoparticles in aqueous solution by microwave assisted flow chemistry. *ACS Sustainable Chemistry & Engineering* **2016,** 4, (12), 6435-6442.
54. Rana, K. K.; Rana, S., Microwave reactors: A brief review on its fundamental aspects and applications. *Open Access Library Journal* **2014,** 1, (6), 1-20.
55. Seol, S. K.; Kim, D.; Jung, S.; Chang, W. S.; Bae, Y. M.; Lee, K. H.; Hwu, Y., Effect of citrate on poly(vinyl pyrrolidone)-stabilized gold nanoparticles formed by PVP reduction in microwave (MW) synthesis. *Materials Chemistry and Physics* **2012,** 137, (1), 135-139.
56. Tsuji, M.; Hashimoto, M.; Nishizawa, Y.; Tsuji, T., Preparation of gold nanoplates by a microwave-polyol method. *Chemistry Letters* **2003,** 32, (12), 1114-1115.
57. Shen, M.; Du, Y.; Hua, N.; Yang, P., Microwave irradiation synthesis and self-assembly of alkylamine-stabilized gold nanoparticles. *Powder Technology* **2006,** 162, (1), 64-72.
58. Horikoshi, S.; Abe, H.; Sumi, T.; Torigoe, K.; Sakai, H.; Serpone, N.; Abe, M., Microwave frequency effect in the formation of Au nanocolloids in polar and non-polar solvents. *Nanoscale* **2011,** 3, (4), 1697-702.
59. Patil, N. G.; Benaskar, F.; Meuldijk, J.; Hulshof, L. A.; Hessel, V.; Schouten, J. C.; Esveld, E. D. C.; Rebrov, E. V., Microwave assisted flow synthesis: Coupling of electromagnetic and hydrodynamic phenomena. *AIChE Journal* **2014,** 60, (11), 3824-3832.
60. Matsuzawa, M.; Togashi, S.; Hasebe, S., Isothermal reactor for continuous flow microwave-assisted chemical reaction. *Journal of Thermal Science and Technology* **2012,** 7, (1), 58-74.
61. Sturm, G. S. J.; Van Braam Houckgeest, A. Q.; Verweij, M. D.; Van Gerven, T.; Stankiewicz, A. I.; Stefanidis, G. D., Exploration of rectangular waveguides as a basis for microwave enhanced continuous flow chemistries. *Chemical Engineering Science* **2013,** 89, 196-205.
62. Patil, N. G.; Benaskar, F.; Rebrov, E. V.; Meuldijk, J.; Hulshof, L. A.; Hessel, V.; Schouten, J. C., Scale-up of microwave assisted flow synthesis by transient processing through monomode cavities in series. *Organic Process Research & Development* **2014,** 18, (11), 1400-1407.
63. Matsuzawa, M.; Togashi, S.; Hasebe, S., Basic examination of a pilot plant for continuous flow microwave-assisted chemical reaction combined with microreactors. *Journal of Thermal Science and Technology* **2011,** 6, (1), 69-79.
64. Horikoshi, S.; Serpone, N., Introduction to nanoparticles. In *Microwaves in Nanoparticle Synthesis*, Wiley-VCH Verlag GmbH & Co. KGaA: 2013; pp 1-24.

65. Kumar, S.; Gandhi, K. S.; Kumar, R., Modeling of formation of gold nanoparticles by citrate method. *Industrial & Engineering Chemistry Research* **2007,** 46, (10), 3128-3136.
66. Dzido, G.; Markowski, P.; Malachowska-Jutsz, A.; Prusik, K.; Jarzebski, A. B., Rapid continuous microwave-assisted synthesis of silver nanoparticles to achieve very high productivity and full yield: from mechanistic study to optimal fabrication strategy. *J Nanopart Res* **2015,** 17, 27.
67. Becker, R.; Döring, W., Kinetische Behandlung der Keimbildung in übersättigten Dämpfen. *Annalen der Physik* **1935,** 416, (8), 719-752.
68. Myerson, A. S.; Ginde, R., 2 - Crystals, crystal growth, and nucleation. In *Handbook of Industrial Crystallization (Second Edition)*, Myerson, A. S., Ed. Butterworth-Heinemann: Woburn, 2002; pp 33-65.
69. Polte, J., Fundamental growth principles of colloidal metal nanoparticles – A new perspective. *CrystEngComm* **2015,** 17, (36), 6809-6830.
70. Sosso, G. C.; Chen, J.; Cox, S. J.; Fitzner, M.; Pedevilla, P.; Zen, A.; Michaelides, A., Crystal nucleation in liquids: Open questions and future challenges in molecular dynamics simulations. *Chemical Reviews* **2016,** 116, (12), 7078-7116.
71. Bai, X.-M.; Li, M., Calculation of solid-liquid interfacial free energy: A classical nucleation theory based approach. *The Journal of Chemical Physics* **2006,** 124, (12), 124707.
72. LaMer, V. K., Nucleation in phase transitions. *Industrial & Engineering Chemistry* **1952,** 44, (6), 1270-1277.
73. LaMer, V. K.; Dinegar, R. H., Theory, production and mechanism of formation of monodispersed hydrosols. *Journal of the American Chemical Society* **1950,** 72, (11), 4847-4854.
74. Bastús, N. G.; Comenge, J.; Puntes, V., Kinetically controlled seeded growth synthesis of citrate-stabilized gold nanoparticles of up to 200 nm: Size focusing versus Ostwald ripening. *Langmuir* **2011,** 27, (17), 11098-11105.
75. Baghbanzadeh, M.; Carbone, L.; Cozzoli, P. D.; Kappe, C. O., Microwave-assisted synthesis of colloidal inorganic nanocrystals. *Angew Chem Int Ed Engl* **2011,** 50, (48), 11312-59.
76. Karpinski, P. H.; Wey, J. S., 6 - Precipitation processes. In *Handbook of Industrial Crystallization (Second Edition)*, Myerson, A. S., Ed. Butterworth-Heinemann: Woburn, 2002; pp 141-160.
77. Derjaguin, B.; Landau, L., Theory of the stability of strongly charged lyophobic sols and of the adhesion of strongly charged particles in solutions of electrolytes. *Progress in Surface Science* **1993,** 43, (1), 30-59.
78. Verwey, E. J. W.; Overbeek, J. T. G., *Theory of stability of lyophobic colloids*. Elsevier: Amsterdam, 1948.
79. Xia, Y.; Xiong, Y.; Lim, B.; Skrabalak, S. E., Shape-controlled synthesis of metal nanocrystals: Simple chemistry meets complex physics? *Angew Chem Int Ed Engl* **2009,** 48, (1), 60-103.
80. Chen, Z.; Mochizuki, D.; Wada, Y., Precisely controlled synthesis of metal nanoparticles under microwave irradiation. In *Microwaves in Nanoparticle Synthesis*, Wiley-VCH Verlag GmbH & Co. KGaA: 2013; pp 145-183.
81. Viswanath, B.; Kundu, P.; Halder, A.; Ravishankar, N., Mechanistic aspects of shape selection and symmetry breaking during nanostructure growth by wet chemical methods. *The Journal of Physical Chemistry C* **2009,** 113, (39), 16866-16883.
82. Chow, M. K.; Zukoski, C. F., Gold sol formation mechanisms: Role of colloidal stability. *Journal of Colloid and Interface Science* **1994,** 165, (1), 97-109.
83. Frens, G., Controlled nucleation for the regulation of the particle size in monodisperse gold suspensions. *Nature Physical Science* **1973,** 241, (105), 20-22.

84. Hendel, T.; Wuithschick, M.; Kettemann, F.; Birnbaum, A.; Rademann, K.; Polte, J., In situ determination of colloidal gold concentrations with UV–vis spectroscopy: limitations and perspectives. *Analytical Chemistry* **2014,** 86, (22), 11115-11124.
85. Polte, J.; Ahner, T. T.; Delissen, F.; Sokolov, S.; Emmerling, F.; Thünemann, A. F.; Kraehnert, R., Mechanism ofgold nanoparticle formation in the classical citrate synthesis method derived from coupled in situ XANES and SAXS evaluation. *Journal of the American Chemical Society* **2010,** 132, (4), 1296-1301.
86. Ji, X.; Song, X.; Li, J.; Bai, Y.; Yang, W.; Peng, X., Size control of gold nanocrystals in citrate reduction: The third role of citrate. *Journal of the American Chemical Society* **2007,** 129, (45), 13939-13948.
87. Usher, A.; McPhail, D. C.; Brugger, J., A spectrophotometric study of aqueous Au(III) halide–hydroxide complexes at 25–80°C. *Geochimica et Cosmochimica Acta* **2009,** 73, (11), 3359-3380.
88. Haiss, W.; Thanh, N.; Aveyard, J.; Fernig, D., Determination of size and concentration of gold nanoparticles from UV-vis spectra. *Analytical Chemistry* **2007,** 79, (11), 4215.
89. Amendola, V.; Meneghetti, M., Size evaluation of gold nanoparticles by UV−vis spectroscopy. *The Journal of Physical Chemistry C* **2009,** 113, (11), 4277-4285.
90. Oliveira, J. P.; Prado, A. R.; Keijok, W. J.; Ribeiro, M. R. N.; Pontes, M. J.; Nogueira, B. V.; Guimarães, M. C. C., A helpful method for controlled synthesis of monodisperse gold nanoparticles through response surface modeling. *Arabian Journal of Chemistry* **2017**.
91. Martínez, J. C.; Chequer, N. A.; González, J. L.; Cordova, T., Alternative metodology for gold nanoparticles diameter characterization using PCA technique and UV-vis spectrophotometry. *Nanoscience and Nanotechnology* **2013,** 2, (6), 184-189.
92. Minelli, C.; Sikora, A.; Garcia-Diez, R.; Sparnacci, K.; Gollwitzer, C.; Krumrey, M.; Shard, A. G., Measuring the size and density of nanoparticles by centrifugal sedimentation and flotation. *Analytical Methods* **2018,** 10, (15), 1725-1732.
93. Bird, E. B.; Stewart, W. E.; Lightfoot, E. N., *Tansport Phenomena*. 2 ed.; John Wiley & Sons: New York, USA, 2007.
94. Laidlaw, I.; Steinmetz, M., Introduction to differential sedimentation. In *Analytical Ultracentrifugation - Techniques and Methods*, Scott, D. J.; Harding, S. E.; Rowe, A. J., Eds. Royal Society of Chemistry: London, UK, 2005.
95. Kaech, A. *An introduction to electron microscopy instrumentation, imaging and preparation*; Center for Microscopy and Image Analysis, University of Zurich, 2013.
96. Huang, H.; Toit, H. d.; Besenhard, M. O.; Ben-Jaber, S.; Dobson, P.; Parkin, I.; Gavriilidis, A., Continuous flow synthesis of ultrasmall gold nanoparticles in a microreactor using trisodium citrate and their SERS performance. *Chemical Engineering Science* **2018,** 189, 422-430.
97. Pyrz, W. D.; Buttrey, D. J., Particle size determination using TEM: A discussion of image acquisition and analysis for the novice microscopist. *Langmuir* **2008,** 24, (20), 11350-11360.
98. deMello, J.; deMello, A., Microscale reactors: nanoscale products. *Lab on a Chip* **2004,** 4, (2), 11N-15N.
99. Wagner, J.; Köhler, J. M., Continuous synthesis of gold nanoparticles in a microreactor. *Nano Letters* **2005,** 5, (4), 685-691.
100. Köhler, J. M.; Wagner, J.; Albert, J., Formation of isolated and clustered Au nanoparticles in the presence of polyelectrolyte molecules using a flow-through Si chip reactor. *Journal of Materials Chemistry* **2005,** 15, (19), 1924-1930.

101. Wagner, J.; Tshikhudo, T. R.; Köhler, J. M., Microfluidic generation of metal nanoparticles by borohydride reduction. *Chemical Engineering Journal* **2008,** 135, S104-S109.
102. Ftouni, J.; Penhoat, M.; Addad, A.; Payen, E.; Rolando, C.; Girardon, J.-S., Highly controlled synthesis of nanometric gold particles by citrate reduction using the short mixing, heating and quenching times achievable in a microfluidic device. *Nanoscale* **2012,** 4, (15), 4450-4454.
103. Sugano, K.; Uchida, Y.; Ichihashi, O.; Yamada, H.; Tsuchiya, T.; Tabata, O., Mixing speed-controlled gold nanoparticle synthesis with pulsed mixing microfluidic system. *Microfluidics and Nanofluidics* **2010,** 9, (6), 1165-1174.
104. Krishna, K. S.; Li, Y.; Li, S.; Kumar, C. S. S. R., Lab-on-a-chip synthesis of inorganic nanomaterials and quantum dots for biomedical applications. *Advanced Drug Delivery Reviews* **2013,** 65, (11), 1470-1495.
105. Lohse, S. E.; Eller, J. R.; Sivapalan, S. T.; Plews, M. R.; Murphy, C. J., A simple millifluidic benchtop reactor system for the high-throughput synthesis and functionalization of gold nanoparticles with different sizes and shapes. *ACS Nano* **2013,** 7, (5), 4135-4150.
106. Baber, R.; Mazzei, L.; Thanh, N. T. K.; Gavriilidis, A., An engineering approach to synthesis of gold and silver nanoparticles by controlling hydrodynamics and mixing based on a coaxial flow reactor. *Nanoscale* **2017,** 9, (37), 14149-14161.
107. Huang, H.; du Toit, H.; Panariello, L.; Mazzei, L.; Gavriilidis, A., 4. Continuous synthesis of gold nanoparticles in micro- and millifluidic systems. In 2018; pp 157-220.
108. Ahmed, B.; Barrow, D.; Wirth, T., Enhancement of reaction rates by segmented fluid flow in capillary scale reactors. *Advanced Synthesis & Catalysis* **2006,** 348, (9), 1043-1048.
109. Kulkarni, A. A.; Sebastian Cabeza, V., Insights in the diffusion controlled interfacial flow synthesis of Au nanostructures in a microfluidic system. *Langmuir* **2017,** 33, (50), 14315-14324.
110. Duraiswamy, S.; Khan, S. A., Droplet-based microfluidic synthesis of anisotropic metal nanocrystals. *Small* **2009,** 5, (24), 2828-2834.
111. Carino, A.; Walter, A.; Testino, A.; Hofmann, H., Continuous synthesis of gold nanoparticles using the segmented flow tubular reactor (SFTR). *CHIMIA International Journal for Chemistry* **2016,** 70, (6), 457-457.
112. Leonelli, C.; Mason, T. J., Microwave and ultrasonic processing: Now a realistic option for industry. *Chemical Engineering and Processing: Process Intensification* **2010,** 49, (9), 885-900.
113. Pozar, D. M., *Microwave Engineering*. 4th Edition ed.; John Wiley & Sons: New Jersey, USA, 2012.
114. Stefanidis, G. D.; Muñoz, A. N.; Sturm, G. S. J.; Stankiewicz, A., A helicopter view of microwave application to chemical processes: Reactions, separations, and equipment concepts. *Reviews in Chemical Engineering* **2014,** 30, (3), 233-259.
115. Meredith, R., *Engineers' Handbook of Industrial Microwave Heating*. The Institution of Engineering and Technology: London, 1998.
116. Tsuji, M.; Hashimoto, M.; Nishizawa, Y.; Kubokawa, M.; Tsuji, T., Microwave-assisted synthesis of metallic nanostructures in solution. *Chemistry* **2005,** 11, (2), 440-52.
117. Huang, K. M.; Lin, Z.; Yang, X. Q., Numerical simulation of microwave heating on chemical reaction in dilute solution. *Progress In Electromagnetics Research* **2004,** 49, 273–289.
118. Horikoshi, S.; Serpone, N., Nanoparticle synthesis through microwave heating. In *Microwaves in Nanoparticle Synthesis*, Wiley-VCH Verlag GmbH & Co. KGaA: 2013; pp 75-105.

119. Nishioka, M.; Miyakawa, M.; Daino, Y.; Kataoka, H.; Koda, H.; Sato, K.; Suzuki, T. M., Single-mode microwave reactor used for continuous flow reactions under elevated pressure. *Industrial & Engineering Chemistry Research* **2013,** 52, (12), 4683-4687.
120. Patil, N. G.; Hermans, A. I. G.; Benaskar, F.; Meuldijk, J.; Hulshof, L. A.; Hessel, V.; Schouten, J. C.; Rebrov, E. V., Energy efficient and controlled flow processing under microwave heating by using a millireactor-heat exchanger. *AIChE Journal* **2012,** 58, (10), 3144-3155.
121. Oliveira, M. E. C.; Franca, A. S., Microwave heating of foodstuffs. *Journal of Food Engineering* **2002,** 53, (4), 347-359.
122. Yousefi, T.; Mousavi, S. A.; Saghir, M. Z.; Farahbakhsh, B., An investigation on the microwave heating of flowing water: A numerical study. *International Journal of Thermal Sciences* **2013,** 71, 118-127.
123. Sturm, G. S. J.; Verweij, M. D.; Van Gerven, T.; Stankiewicz, A. I.; Stefanidis, G. D., On the effect of resonant microwave fields on temperature distribution in time and space. *International Journal of Heat and Mass Transfer* **2012,** 55, (13-14), 3800-3811.
124. Zhu, J.; Kuznetsov, A. V.; Sandeep, K. P., Numerical modeling of a moving particle in a continuous flow subjected to microwave heating. *Numerical Heat Transfer, Part A: Applications* **2007,** 52, (5), 417-439.
125. Salvi, D.; Boldor, D.; Aita, G. M.; Sabliov, C. M., COMSOL Multiphysics model for continuous flow microwave heating of liquids. *Journal of Food Engineering* **2011,** 104, (3), 422-429.
126. Cherbański, R.; Rudniak, L., Modelling of microwave heating of water in a monomode applicator – Influence of operating conditions. *International Journal of Thermal Sciences* **2013,** 74, 214-229.
127. Tuta, S.; Palazoğlu, T. K., Finite element modeling of continuous-flow microwave heating of fluid foods and experimental validation. *Journal of Food Engineering* **2017,** 192, 79-92.
128. Zhu, J.; Kuznetsov, A. V.; Sandeep, K. P., Mathematical modeling of continuous flow microwave heating of liquids (effects of dielectric properties and design parameters). *International Journal of Thermal Sciences* **2007,** 46, (4), 328-341.
129. Salvi, D.; Boldor, D.; Ortego, J.; Aita, G. M.; Sabliov, C. M., Numerical modeling of continuous flow microwave heating: A critical comparison of COMSOL and ANSYS. *J Microw Power Electromagn Energy* **2010,** 44, (4), 187–197.
130. Robinson, J.; Kingman, S.; Irvine, D.; Licence, P.; Smith, A.; Dimitrakis, G.; Obermayer, D.; Kappe, C. O., Electromagnetic simulations of microwave heating experiments using reaction vessels made out of silicon carbide. *Phys Chem Chem Phys* **2010,** 12, (36), 10793-800.
131. Morgan, A. J. L.; Naylon, J.; Gooding, S.; John, C.; Squires, O.; Lees, J.; Barrow, D. A.; Porch, A., Efficient microwave heating of microfluidic systems. *Sensors and Actuators B: Chemical* **2013,** 181, 904-909.
132. Adnadjevic, B.; Jovanovic, J., *The effects of microwave heating on the isothermal kinetics of chemicals reactions and physicochemical processes*. IntechOpen: London, UK, 2011.
133. Horikoshi, S.; Abe, H.; Torigoe, K.; Abe, M.; Serpone, N., Access to small size distributions of nanoparticles by microwave-assisted synthesis. Formation of Ag nanoparticles in aqueous carboxymethylcellulose solutions in batch and continuous-flow reactors. *Nanoscale* **2010,** 2, (8), 1441-7.
134. Komorowska-Durka, M.; Dimitrakis, G.; Bogdał, D.; Stankiewicz, A. I.; Stefanidis, G. D., A concise review on microwave-assisted polycondensation reactions and curing of polycondensation polymers with focus on the effect of process conditions. *Chemical Engineering Journal* **2015,** 264, 633-644.

135. Baghurst, D. R.; Mingos, D. M. P., Superheating effects associated with microwave dielectric heating. *Journal of the Chemical Society, Chemical Communications* **1992**, (9), 674-677.
136. Ferrari, A.; Hunt, J.; Stiegman, A.; Dudley, G. B., Microwave-assisted superheating and/or microwave-specific superboiling (nucleation-limited boiling) of liquids occurs under certain conditions but is mitigated by stirring. *Molecules* **2015,** 20, (12), 21672-80.
137. Gillespie, P. M., Microwave chemistry – An approach to the assessment of chemical reaction hazards. *IChemE Symposium series no. 150* **23-25 November 2004**.
138. Sturm, G. S. J.; Verweij, M. D.; Stankiewicz, A. I.; Stefanidis, G. D., Microwaves and microreactors: Design challenges and remedies. *Chemical Engineering Journal* **2014,** 243, 147-158.
139. Zhu, X.; Zhang, Q.; Li, Y.; Wang, H., Facile crystallization control of LaF3/LaPO4:Ce, Tb nanocrystals in a microfluidic reactor using microwave irradiation. *Journal of Materials Chemistry* **2010,** 20, (9), 1766.
140. Hostetler, E. B.; Kim, K.-J.; Oleksak, R. P.; Fitzmorris, R. C.; Peterson, D. A.; Chandran, P.; Chang, C.-H.; Paul, B. K.; Schut, D. M.; Herman, G. S., Synthesis of colloidal PbSe nanoparticles using a microwave-assisted segmented flow reactor. *Materials Letters* **2014,** 128, 54-59.
141. Corradi, A. B.; Bondioli, F.; Ferrari, A. M.; Focher, B.; Leonelli, C., Synthesis of silica nanoparticles in a continuous-flow microwave reactor. *Powder Technology* **2006,** 167, (1), 45-48.
142. Blanco-Andujar, C.; Ortega, D.; Southern, P.; Pankhurst, Q. A.; Thanh, N. T., High performance multi-core iron oxide nanoparticles for magnetic hyperthermia: Microwave synthesis, and the role of core-to-core interactions. *Nanoscale* **2015,** 7, (5), 1768-75.
143. Dzido, G.; Jarzębski, A. B., Fabrication of silver nanoparticles in a continuous flow, low temperature microwave-assisted polyol process. *Journal of Nanoparticle Research* **2010,** 13, (6), 2533-2541.
144. Kang, X.; Sun, X.; Han, B., Synthesis of functional nanomaterials in ionic liquids. *Adv Mater* **2015**.
145. Kingston, H. M.; Haswell, S. J., *Microwave-enhanced chemistry : Fundamentals, sample preparation, and applications*. American Chemical Society: Washington D.C., USA, 1997.
146. Robinson, J.; Kingman, S.; Irvine, D.; Licence, P.; Smith, A.; Dimitrakis, G.; Obermayer, D.; Kappe, C. O., Understanding microwave heating effects in single mode type cavities-Theory and experiment. *Phys Chem Chem Phys* **2010,** 12, (18), 4750-8.
147. Nishioka, M.; Miyakawa, M.; Kataoka, H.; Koda, H.; Sato, K.; Suzuki, T. M., Continuous synthesis of monodispersed silver nanoparticles using a homogeneous heating microwave reactor system. *Nanoscale* **2011,** 3, (6), 2621-6.
148. Tu, W.; Liu, H., Continuous synthesis of colloidal metal nanoclusters by microwave irradiation. *Chemistry of Materials* **2000,** 12, (2), 564-567.
149. Bondioli, F.; Bonamartini Corradi, A.; Ferrari, A.; Leonelli, C., Synthesis of zirconia nanoparticles in a continuous-flow microwave reactor. *Journal of the American Ceramic Society* **2008,** 91, (11), 3746-3748.
150. Koziej, D.; Floryan, C.; Sperling, R. A.; Ehrlicher, A. J.; Issadore, D.; Westervelt, R.; Weitz, D. A., Microwave dielectric heating of non-aqueous droplets in a microfluidic device for nanoparticle synthesis. *Nanoscale* **2013,** 5, (12), 5468-75.
151. Kim, K.-J.; Oleksak, R. P.; Hostetler, E. B.; Peterson, D. A.; Chandran, P.; Schut, D. M.; Paul, B. K.; Herman, G. S.; Chang, C.-H., Continuous microwave-

assisted gas–liquid segmented flow reactor for controlled nucleation and growth of nanocrystals. *Crystal Growth & Design* **2014,** 14, (11), 5349-5355.
152. Kundu, S.; Lau, S.; Liang, H., Shape-Controlled Catalysis by Cetyltrimethylammonium Bromide Terminated Gold Nanospheres, Nanorods, and Nanoprisms. *The Journal of Physical Chemistry C* **2009,** 113, (13), 5150-5156.
153. Furlong, D. N.; Launikonis, A.; Sasse, W. H. F.; Sanders, J. V., Colloidal platinum sols. Preparation, characterization and stability towards salt. *Journal of the Chemical Society, Faraday Transactions 1: Physical Chemistry in Condensed Phases* **1984,** 80, (3), 571-588.
154. Uppal, M. A.; Kafizas, A.; Ewing, M. B.; Parkin, I. P., The effect of initiation method on the size, monodispersity and shape of gold nanoparticles formed by the Turkevich method. *New Journal of Chemistry* **2010,** 34, (12), 2906.
155. Jachuck, R. J. J.; Selvaraj, D. K.; Varma, R. S., Process intensification: oxidation of benzyl alcohol using a continuous isothermal reactor under microwave irradiation. *Green Chem.* **2006,** 8, (1), 29-33.
156. Calabrese, M. L.; d'Ambrosio, G.; Massa, R.; Petraglia, G., A high-efficiency waveguide applicator for in vitro exposure of mammalian cells at 1.95 GHz. *IEEE Transactions on Microwave Theory and Techniques* **2006,** 54, (5), 2256 - 2264.
157. Bogdal, D.; Bednarz, S.; Łukasiewicz, M.; Kasprzyk, W., Intensification of oxidation and epoxidation reactions—Microwave vs. conventional heating. *Chemical Engineering and Processing - Process Intensification* **2018,** 132, 208-217.
158. Cherbański, R.; Molga, E., Intensification of desorption processes by use of microwaves—An overview of possible applications and industrial perspectives. *Chemical Engineering and Processing: Process Intensification* **2009,** 48, (1), 48-58.
159. Werth, K.; Lutze, P.; Kiss, A. A.; Stankiewicz, A. I.; Stefanidis, G. D.; Górak, A., A systematic investigation of microwave-assisted reactive distillation: Influence of microwaves on separation and reaction. *Chemical Engineering and Processing: Process Intensification* **2015,** 93, 87-97.
160. Cecilia, R.; Kunz, U.; Turek, T., Possibilities of process intensification using microwaves applied to catalytic microreactors. *Chemical Engineering and Processing: Process Intensification* **2007,** 46, (9), 870-881.
161. Sturm, G. S. J.; Stefanidis, G. D.; Verweij, M. D.; Van Gerven, T. D. T.; Stankiewicz, A. I., Design principles of microwave applicators for small-scale process equipment. *Chemical Engineering and Processing: Process Intensification* **2010,** 49, (9), 912-922.
162. Link, G.; Ramopoulos, V., Simple analytical approach for industrial microwave applicator design. *Chemical Engineering and Processing - Process Intensification* **2018,** 125, 334-342.
163. Sturm, G. S. J.; Verweij, M. D.; Van Gerven, T.; Stankiewicz, A. I.; Stefanidis, G. D., On the parametric sensitivity of heat generation by resonant microwave fields in process fluids. *International Journal of Heat and Mass Transfer* **2013,** 57, (1), 375-388.
164. COMSOL Inc, CFD Module Users Guide v 5.2a. **2016**.
165. Salvi, D.; Ortego, J.; Arauz, C.; Sabliov, C. M.; Boldor, D., Experimental study of the effect of dielectric and physical properties on temperature distribution in fluids during continuous flow microwave heating. *Journal of Food Engineering* **2009,** 93, (2), 149-157.
166. Uematsu, M.; Frank, E. U., Static dielectric constant of water and steam. *Journal of Physical and Chemical Reference Data* **1980,** 9, (4), 1291-1306.
167. Kaatze, U., Complex permittivity of water as a function of frequency and temperature. *Journal of Chemical & Engineering Data* **1989,** 34, (4), 371-374.

168. Kaatze, U., Reference liquids for the calibration of dielectric sensors and measurement instruments. *Measurement Science and Technology* **2007,** 18, (4), 967-976.
169. Schornack, L. G.; Eckert, C. A., Effect of pressure on the density and dielectric constant of polar solvents. *The Journal of Physical Chemistry* **1970,** 74, (15), 3014-3020.
170. Dunn, L. A.; Stokes, R. H., Pressure and temperature dependence of the electrical permittivities of formamide and water. *Transactions of the Faraday Society* **1969,** 65, (0), 2906-2912.
171. Owen, B. B.; Miller, R. C.; Milner, C. E.; Cogan, H. L., The dielectric constant of water as a function of temperature and pressure. *The Journal of Physical Chemistry* **1961,** 65, (11), 2065-2070.
172. Rosen, J. S., Refractive indices and dielectric constants of liquids and gases under pressure. *The Journal of Chemical Physics* **1949,** 17, (12), 1192-1197.
173. Owen, B. B.; Brinkley, S. R., The effect of pressure upon the dielectric constants of liquids. *Physical Review* **1943,** 64, (1-2), 32-36.
174. Bradley, D. J.; Pitzer, K. S., Thermodynamics of electrolytes. 12. Dielectric properties of water and Debye-Hueckel parameters to 350 ^{o}C and 1 kbar. *The Journal of Physical Chemistry* **1979,** 83, (12), 1599-1603.
175. Floriano, W. B.; Nascimento, M. A. C., Dielectric constant and density of water as a function of pressure at constant temperature. *Brazilian Journal of Physics* **2004,** 34, 38-41.
176. Liu, F.-K.; Ker, C.-J.; Chang, Y.-C.; Ko, F.-H.; Chu, T.-C.; Dai, B.-T., Microwave heating for the preparation of nanometer gold particles. *Japanese Journal of Applied Physics* **2003,** 42, (Part 1, No. 6B), 4152-4158.
177. Mondini, S.; Ferretti, A. M.; Puglisi, A.; Ponti, A., Pebbles and PebbleJuggler: Software for accurate, unbiased, and fast measurement and analysis of nanoparticle morphology from transmission electron microscopy (TEM) micrographs. *Nanoscale* **2012,** 4, (17), 5356-5372.
178. Hanson, G. W.; Monreal, R. C.; Apell, S. P., Electromagnetic absorption mechanisms in metal nanospheres: Bulk and surface effects in radiofrequency-terahertz heating of nanoparticles. *Journal of Applied Physics* **2011,** 109, (12), 124306.
179. Corr, S. J.; Raoof, M.; Mackeyev, Y.; Phounsavath, S.; Cheney, M. A.; Cisneros, B. T.; Shur, M.; Gozin, M.; McNally, P. J.; Wilson, L. J.; Curley, S. A., Citrate-capped gold nanoparticle electrophoretic heat production in response to a time-varying radiofrequency electric-field. *J Phys Chem C Nanomater Interfaces* **2012,** 116, (45), 24380-24389.
180. Li, D.; Jung, Y. S.; Tan, S.; Kim, H. K.; Chory, E.; Geller, D. A., Negligible absorption of radiofrequency radiation by colloidal gold nanoparticles. *J Colloid Interface Sci.* **2011,** 358, (1), 47-53.
181. Sahu, P.; Prasad, B. L. V., Time and temperature effects on the digestive ripening of gold nanoparticles: Is there a crossover from digestive ripening to Ostwald ripening? *Langmuir* **2014,** 30, (34), 10143-10150.
182. Lin, X. M.; Sorensen, C. M.; Klabunde, K. J., Digestive ripening, nanophase segregation and superlattice formation in gold nanocrystal colloids. *Journal of Nanoparticle Research* **2000,** 2, (2), 157-164.
183. Lee, D.-K.; Park, S.-I.; Lee, J. K.; Hwang, N.-M., A theoretical model for digestive ripening. *Acta Materialia* **2007,** 55, (15), 5281-5288.
184. Abid, J.-P. Laser induced synthesis and nonlinear optical properties of metal nanoparticles (Doctoral thesis). Ph.D. Thesis, Ecole Polytechnique Federale de Lausanne, Lausanne, Switzerland, 2003.
185. Freund, P. L.; Spiro, M., Colloidal catalysis: The effect of sol size and concentration. *The Journal of Physical Chemistry* **1985,** 89, (7), 1074-1077.

186. Damilos, S.; Radhakrishnan, A. N. P.; Dimitrakis, G.; Tang, J.; Gavriilidis, A., Experimental and computational investigation of heat transfer in a microwave-assisted flow system. *Chemical Engineering and Processing - Process Intensification* **2019,** 142, 107537.
187. Welch, B. L., The generalization of 'student's' problem when several different population varlances are involved. *Biometrika* **1947,** 34, (1-2), 28-35.
188. Besenhard, M. O.; Baber, R.; LaGrow, A. P.; Mazzei, L.; Thanh, N. T. K.; Gavriilidis, A., New insight into the effect of mass transfer on the synthesis of silver and gold nanoparticles. *CrystEngComm* **2018,** 20, (44), 7082-7093.
189. Agunloye, E.; Panariello, L.; Gavriilidis, A.; Mazzei, L., A model for the formation of gold nanoparticles in the citrate synthesis method. *Chemical Engineering Science* **2018,** 191, 318-331.
190. de la Hoz, A.; Díaz-Ortiz, Á.; Moreno, A., Microwaves in organic synthesis. Thermal and non-thermal microwave effects. *Chemical Society Reviews* **2005,** 34, (2), 164-178.
191. Yue, J.; Falke, F. H.; Schouten, J. C.; Nijhuis, T. A., Microreactors with integrated UV/Vis spectroscopic detection for online process analysis under segmented flow. *Lab on a Chip* **2013,** 13, (24), 4855-4863.
192. Gobert, S. R. L.; Kuhn, S.; Braeken, L.; Thomassen, L. C. J., Characterization of milli- and microflow reactors: mixing efficiency and residence time distribution. *Organic Process Research & Development* **2017,** 21, (4), 531-542.
193. Levenspiel, O., Chemical Reaction Engineering (3rd Edition). In John Wiley & Sons.
194. Agunloye, E.; Gavriilidis, A.; Mazzei, L., A mathematical investigation of the Turkevich organizer theory in the citrate method for the synthesis of gold nanoparticles. *Chemical Engineering Science* **2017,** 173, 275-286.
195. Rossi, D.; Gargiulo, L.; Valitov, G.; Gavriilidis, A.; Mazzei, L., Experimental characterization of axial dispersion in coiled flow inverters. *Chemical Engineering Research and Design* **2017,** 120, 159-170.
196. Klutz, S.; Kurt, S. K.; Lobedann, M.; Kockmann, N., Narrow residence time distribution in tubular reactor concept for Reynolds number range of 10–100. *Chemical Engineering Research and Design* **2015,** 95, 22-33.
197. Shalom, D.; Wootton, R. C. R.; Winkle, R. F.; Cottam, B. F.; Vilar, R.; deMello, A. J.; Wilde, C. P., Synthesis of thiol functionalized gold nanoparticles using a continuous flow microfluidic reactor. *Materials Letters* **2007,** 61, (4), 1146-1150.
198. Grzelczak, M.; Perez-Juste, J.; Mulvaney, P.; Liz-Marzan, L. M., Shape control in gold nanoparticle synthesis. *Chemical Society Reviews* **2008,** 37, (9), 1783-1791.
199. Zabetakis, K.; Ghann, W. E.; Kumar, S.; Daniel, M.-C., Effect of high gold salt concentrations on the size and polydispersity of gold nanoparticles prepared by an extended Turkevich–Frens method. *Gold Bulletin* **2012,** 45, (4), 203-211.
200. Schulz, F.; Homolka, T.; Bastús, N. G.; Puntes, V.; Weller, H.; Vossmeyer, T., Little adjustments significantly improve the turkevich synthesis of gold nanoparticles. *Langmuir* **2014,** 30, (35), 10779-10784.
201. van Rossum, G., *Python tutorial, technical report CS-R9526*. Centrum voor Wikunde en Informatica (CWI): Amsterdam, 1995.
202. van der Walt, S.; Colbert, S. C.; Varoquaux, G., The NumPy array: A structure for efficient numerical computation. *Computing in Science & Engineering* **2011,** 13, (2), 22-30.
203. Hunter, J. D., Matplotlib: A 2D graphics environment. *Computing in Science & Engineering* **2007,** 9, (3), 90-95.
204. Oliphant, T. E., Python for scientific computing. *Computing in Science & Engineering* **2007,** 9, (3), 10-20.
205. Montgomery, D. C., *Design and analysis of experiments*. 8 ed.; John Wiley & Sons: New Jersey, USA, 2013.

206. Jafarzadeh, N. K.; Sharifnia, S.; Hosseini, S. N.; Rahimpour, F., Statistical optimization of process conditions for photocatalytic degradation of phenol with immobilization of nano TiO2 on perlite granules. *Korean Journal of Chemical Engineering* **2011,** 28, (2), 531-538.
207. Ba-Abbad, M. M.; Chai, P. V.; Takriff, M. S.; Benamor, A.; Mohammad, A. W., Optimization of nickel oxide nanoparticle synthesis through the sol–gel method using Box–Behnken design. *Materials & Design* **2015,** 86, 948-956.
208. Nagarwal, R. C.; Srinatha, A.; Pandit, J. K., In situ forming formulation: development, evaluation, and optimization using 3^3 factorial design. *AAPS PharmSciTech* **2009,** 10, (3), 977.
209. Lazić, Z. R., *Design of experiments in chemical engineering: A practical guide*. John Wiley & Sons: New Jersey, USA, 2004; p 607-610.
210. Li, C.; Li, D.; Wan, G.; Xu, J.; Hou, W., Facile synthesis of concentrated gold nanoparticles with low size-distribution in water: temperature and pH controls. *Nanoscale Research Letters* **2011,** 6, (1), 440.
211. Tran, M.; DePenning, R.; Turner, M.; Padalkar, S., Effect of citrate ratio and temperature on gold nanoparticle size and morphology. *Materials Research Express* **2016,** 3, (10), 105027.
212. Takiyama, K., Formation and aging of precipitates. VIII. Formation of monodisperse particles (1) gold sol particles by sodium citrate method. *Bulletin of the Chemical Society of Japan* **1958,** 31, (8), 944-950.
213. Heinz, H.; Jha, K. C.; Luettmer-Strathmann, J.; Farmer, B. L.; Naik, R. R., Polarization at metal–biomolecular interfaces in solution. *Journal of Royal Society Interface* **2010,** 8, (55), 220-232.
214. Krekeler, C.; Delle Site, L., Lone pair versus bonding pair electrons: the mechanism of electronic polarization of water in the presence of positive ions. *J Chem Phys* **2008,** 128, (13), 134515.
215. Salazar-Salinas, K.; Baldera-Aguayo, P. A.; Encomendero-Risco, J. J.; Orihuela, M.; Sheen, P.; Seminario, J. M.; Zimic, M., Metal-ion effects on the polarization of metal-bound water and infrared vibrational modes of the coordinated metal center of mycobacterium tuberculosis pyrazinamidase via quantum mechanical calculations. *The Journal of Physical Chemistry B* **2014,** 118, (34), 10065-10075.
216. Serjeant, E. P.; Dempsey, B., *Ionisation Constants of organic acids in aqueous solution. International union of pure and applied chemistry (IUPAC)*. Pergamon Press: New York, 1979; Vol. 23.
217. Gao, Y.; Torrente-Murciano, L., Mechanistic insights of the reduction of gold salts in the Turkevich protocol. *Nanoscale* **2020,** 12, (4), 2740-2751.
218. Zhang, L.; Wang, Y.; Tong, L.; Xia, Y., Synthesis of colloidal metal nanocrystals in droplet reactors: The pros and cons of interfacial adsorption. *Nano Letters* **2014,** 14, (7), 4189-4194.
219. Shestopalov, I.; Tice, J. D.; Ismagilov, R. F., Multi-step synthesis of nanoparticles performed on millisecond time scale in a microfluidic droplet-based system. *Lab Chip* **2004,** 4, (4), 316-21.
220. Długosz, O.; Banach, M., Continuous production of silver nanoparticles and process control. *Journal of Cluster Science* **2019,** 30, (3), 541-552.
221. Naidu, S.; Sawhney, R.; Li, X., A methodology for evaluation and selection of nanoparticle manufacturing processes based on sustainability metrics. *Environmental Science & Technology* **2008,** 42, (17), 6697-6702.
222. Cattaneo, S.; Althahban, S.; Freakley, S. J.; Sankar, M.; Davies, T.; He, Q.; Dimitratos, N.; Kiely, C. J.; Hutchings, G. J., Synthesis of highly uniform and composition-controlled gold–palladium supported nanoparticles in continuous flow. *Nanoscale* **2019,** 11, (17), 8247-8259.

223. Garstecki, P.; Fuerstman, M. J.; Stone, H. A.; Whitesides, G. M., Formation of droplets and bubbles in a microfluidic T-junction—Scaling and mechanism of break-up. *Lab on a Chip* **2006,** 6, (3), 437-446.
224. Shui, L.; Eijkel, J. C.; van den Berg, A., Multiphase flow in microfluidic systems - Control and applications of droplets and interfaces. *Adv Colloid Interface Sci* **2007,** 133, (1), 35-49.
225. Kašpar, O.; Koyuncu, A. H.; Pittermannová, A.; Ulbrich, P.; Tokárová, V., Governing factors for preparation of silver nanoparticles using droplet-based microfluidic device. *Biomedical Microdevices* **2019,** 21, (4), 88.
226. Wang, J.; Wang, J.; Feng, L.; Lin, T., Fluid mixing in droplet-based microfluidics with a serpentine microchannel. *RSC Advances* **2015,** 5, (126), 104138-104144.
227. Angeli, P.; Gavriilidis, A., Hydrodynamics of Taylor flow in small channels: A review. *Proceedings of the Institution of Mechanical Engineers, Part C: Journal of Mechanical Engineering Science* **2008,** 222, (5), 737-751.
228. P. Radhakrishnan, A. N.; Marques, M. P. C.; Davies, M. J.; O'Sullivan, B.; Bracewell, D. G.; Szita, N., Flocculation on a chip: A novel screening approach to determine floc growth rates and select flocculating agents. *Lab on a Chip* **2018,** 18, (4), 585-594.
229. Tan, R.-K.; Eberhard, W.; Büchs, J., Measurement and characterization of mixing time in shake flasks. *Chemical Engineering Science* **2011,** 66, (3), 440-447.
230. Melton, L. A.; Lipp, C. W.; Spradling, R. W.; Paulson, K. A., Dismt - Determination of mixing time through color changes. *Chemical Engineering Communications* **2002,** 189, (3), 322-338.
231. Tice, J. D.; Song, H.; Lyon, A. D.; Ismagilov, R. F., Formation of droplets and mixing in multiphase microfluidics at low values of the reynolds and the capillary numbers. *Langmuir* **2003,** 19, (22), 9127-9133.
232. Tanthapanichakoon, W.; Matsuyama, K.; Aoki, N.; Mae, K., Design of microfluidic slug mixing based on the correlation between a dimensionless mixing rate and a modified Peclet number. *Chemical Engineering Science* **2006,** 61, (22), 7386-7392.
233. Rhee, M.; Burns, M. A., Drop mixing in a microchannel for lab-on-a-chip platforms. *Langmuir* **2008,** 24, (2), 590-601.
234. Bruus, H., *Theoretical Microfluidics*. Oxford University Press: Oxford, 2008.
235. Nguyen, N.-T.; Wu, Z., Micromixers—A review. *Journal of Micromechanics and Microengineering* **2004,** 15, (2), R1-R16.
236. Hariri, M. B.; Dolati, A.; Moakhar, R. S., The potentiostatic electrodeposition of gold nanowire/nanotube in HAuCl4 solutions based on the model of recessed cylindrical ultramicroelectrode array. *Journal of The Electrochemical Society* **2013,** 160, (6), D279-D288.
237. Adamo, A.; Heider, P. L.; Weeranoppanant, N.; Jensen, K. F., Membrane-based, liquid–liquid separator with integrated pressure control. *Industrial & Engineering Chemistry Research* **2013,** 52, (31), 10802-10808.
238. Yang, L.; Weeranoppanant, N.; Jensen, K. F., Characterization and modeling of the operating curves of membrane microseparators. *Industrial & Engineering Chemistry Research* **2017,** 56, (42), 12184-12191.
239. Kralj, J. G.; Sahoo, H. R.; Jensen, K. F., Integrated continuous microfluidic liquid–liquid extraction. *Lab on a Chip* **2007,** 7, (2), 256-263.
240. Heider, P. L.; Born, S. C.; Basak, S.; Benyahia, B.; Lakerveld, R.; Zhang, H.; Hogan, R.; Buchbinder, L.; Wolfe, A.; Mascia, S.; Evans, J. M. B.; Jamison, T. F.; Jensen, K. F., Development of a multi-step synthesis and workup sequence for an integrated, continuous manufacturing process of a pharmaceutical. *Organic Process Research & Development* **2014,** 18, (3), 402-409.

241. Jongen, N.; Donnet, M.; Bowen, P.; Lemaître, J.; Hofmann, H.; Schenk, R.; Hofmann, C.; Aoun-Habbache, M.; Guillemet-Fritsch, S.; Sarrias, J.; Rousset, A.; Viviani, M.; Buscaglia, M. T.; Buscaglia, V.; Nanni, P.; Testino, A.; Herguijuela, J. R., Development of a continuous segmented flow tubular reactor and the "scale-out" concept – In search of perfect powders. *Chemical Engineering & Technology* **2003,** 26, (3), 303-305.
242. Lin, Y.; Skaff, H.; Emrick, T.; Dinsmore, A. D.; Russell, T. P., Nanoparticle assembly and transport at liquid-liquid interfaces. *Science* **2003,** 299, (5604), 226.
243. Binder, W. H., Supramolecular assembly of nanoparticles at liquid–liquid interfaces. *Angewandte Chemie International Edition* **2005,** 44, (33), 5172-5175.
244. Cecchini, M. P.; Turek, V. A.; Paget, J.; Kornyshev, A. A.; Edel, J. B., Self-assembled nanoparticle arrays for multiphase trace analyte detection. *Nature Materials* **2012,** 12, 165.
245. Gupta, R.; Fletcher, D. F.; Haynes, B. S., CFD modelling of flow and heat transfer in the Taylor flow regime. *Chemical Engineering Science* **2010,** 65, (6), 2094-2107.
246. Dai, Z.; Guo, Z.; Fletcher, D. F.; Haynes, B. S., Taylor flow heat transfer in microchannels—Unification of liquid–liquid and gas–liquid results. *Chemical Engineering Science* **2015,** 138, 140-152.
247. Gupta, R.; Leung, S. S. Y.; Manica, R.; Fletcher, D. F.; Haynes, B. S., Hydrodynamics of liquid–liquid Taylor flow in microchannels. *Chemical Engineering Science* **2013,** 92, 180-189.
248. Contreras-Trigo, B.; Díaz-García, V.; Guzmán-Gutierrez, E.; Sanhueza, I.; Coelho, P.; Godoy, S. E.; Torres, S.; Oyarzún, P., Slight pH fluctuations in the gold nanoparticle synthesis process influence the performance of the citrate reduction method. *Sensors* **2018,** 18, (7), 2246.
249. Peck, J. A.; Tait, C. D.; Swanson, B. I.; Brown, G. E., Speciation of aqueous gold(III) chlorides from ultraviolet/visible absorption and Raman/resonance Raman spectroscopies. *Geochimica et Cosmochimica Acta* **1991,** 55, (3), 671-676.
250. Khlebtsov, N. G., Determination of size and concentration of gold nanoparticles from extinction spectra. *Analytical Chemistry* **2008,** 80, (17), 6620-6625.
251. Amendola, V.; Pilot, R.; Frasconi, M.; Maragò, O. M.; Iatì, M. A., Surface plasmon resonance in gold nanoparticles: A review. *Journal of Physics: Condensed Matter* **2017,** 29, (20), 203002.
252. Mulvaney, P., Surface plasmon spectroscopy of nanosized metal particles. *Langmuir* **1996,** 12, (3), 788-800.
253. Hahladakis, J. N.; Velis, C. A.; Weber, R.; Iacovidou, E.; Purnell, P., An overview of chemical additives present in plastics: Migration, release, fate and environmental impact during their use, disposal and recycling. *Journal of Hazardous Materials* **2018,** 344, 179-199.
254. Manno, R.; Sebastian, V.; Mallada, R.; Santamaria, J., 110th Anniversary: Nucleation of Ag nanoparticles in helical microfluidic reactor. Comparison between microwave and conventional heating. *Industrial & Engineering Chemistry Research* **2019,** 58, (28), 12702-12711.
255. Andalibi, M. R.; Wokaun, A.; Bowen, P.; Testino, A., Kinetics and mechanism of metal nanoparticle growth via optical extinction spectroscopy and computational modeling: The curious case of colloidal gold. *ACS Nano* **2019**.
256. Jenkins, J. A.; Wax, T. J.; Zhao, J., Seed-mediated synthesis of gold nanoparticles of controlled sizes to demonstrate the impact of size on optical properties. *Journal of Chemical Education* **2017,** 94, (8), 1090-1093.

257. Leng, W.; Pati, P.; Vikesland, P. J., Room temperature seed mediated growth of gold nanoparticles: mechanistic investigations and life cycle assesment. *Environmental Science: Nano* **2015,** 2, (5), 440-453.
258. Lasi, H.; Fettke, P.; Kemper, H.-G.; Feld, T.; Hoffmann, M., Industry 4.0. *Business & Information Systems Engineering* **2014,** 6, (4), 239-242.
259. Geladi, P.; Kowalski, B. R., Partial least-squares regression: A tutorial. *Analytica Chimica Acta* **1986,** 185, 1-17.
260. de Jong, S., SIMPLS: An alternative approach to partial least squares regression. *Chemometrics and Intelligent Laboratory Systems* **1993,** 18, (3), 251-263.
261. Curet, S.; Bellincanta Begnini, F.; Rouaud, O.; Boillereaux, L., Modeling microwave heating during batch processing of liquid sample in a single mode cavity. In *COMSOL Conference*, Grenoble, 2015; pp 1-16.
262. Engineering ToolBox (2003) Emissivity coefficients materials. [online] Available at: https://www.engineeringtoolbox.com/emissivity-coefficients-d_447.html [Accessed 27 February 2019].
263. Perry, R. H.; Green, D. W.; Maloney, J. O., *Perry's Chemical Engineers' Handbook*. 7th ed.; McGraw-Hill: New York, 1999.
264. Yaws, C. L., *Transport Properties of Chemicals and Hydrocarbons, 2nd edition*. 2nd ed.; Gulf Professional Publishing: Oxford, 2014.
265. Porch, A.; Slocombe, D.; Edwards, P. P., Microwave absorption in powders of small conducting particles for heating applications. *Phys Chem Chem Phys* **2013,** 15, (8), 2757-63.
266. Keblinski, P.; Cahill, D. G.; Bodapati, A.; Sullivan, C. R.; Taton, T. A., Limits of localized heating by electromagnetically excited nanoparticles. *J. Appl. Phys.* **2006,** 100, 054305.
267. Bergman, T. L.; Lavine, A. S.; Incropera, F. P.; Dewitt, D. P., *Fundamentals of Heat and Mass Transfer*. 7 ed.; John Wiley & Sons: Hoboken, NJ, USA, 2011.
268. Engineering ToolBox (2003) Thermal conductivity of common materials and gases. [online] Available at: https://www.engineeringtoolbox.com/thermal-conductivity-d_429.html [Accessed 16 October 2019].
269. Capretto, L.; Cheng, W.; Hill, M.; Zhang, X., Micromixing within microfluidic devices. In *Microfluidics: Technologies and Applications*, Lin, B., Ed. Springer Berlin Heidelberg: Berlin, Heidelberg, 2011; pp 27-68.
270. Schneider, C. A.; Rasband, W. S.; Eliceiri, K. W., NIH Image to ImageJ: 25 years of image analysis. *Nature methods* **2012,** 9, (7), 671-675.
271. Schindelin, J.; Arganda-Carreras, I.; Frise, E.; Kaynig, V.; Longair, M.; Pietzsch, T.; Preibisch, S.; Rueden, C.; Saalfeld, S.; Schmid, B.; Tinevez, J.-Y.; White, D. J.; Hartenstein, V.; Eliceiri, K.; Tomancak, P.; Cardona, A., Fiji: An open-source platform for biological-image analysis. *Nature Methods* **2012,** 9, (7), 676-682.
272. Baroud, C. N.; Gallaire, F.; Dangla, R., Dynamics of microfluidic droplets. *Lab Chip* **2010,** 10, (16), 2032–2045.
273. Davies, M. J.; Marques, M. P. C.; Radhakrishnan, A. N. P., Chapter 2 Microfluidics Theory in Practice. In *Microfluidics in Detection Science: Lab-on-a-chip Technologies*, The Royal Society of Chemistry: 2015; pp 29-60.
274. Goebel, A.; Lunkenheimer, K., Interfacial tension of the water/n-alkane interface. *Langmuir* **1997,** 13, (2), 369-372.
275. Chen, J.-D., Measuring the film thickness surrounding a bubble inside a capillary. *Journal of Colloid and Interface Science* **1986,** 109, (2), 341-349.
276. Fairbrother, F.; Stubbs, A. E., 119. Studies in electro-endosmosis. Part VI. The “bubble-tube” method of measurement. *Journal of the Chemical Society (Resumed)* **1935**, (0), 527-529.

277. Besenhard, M. O.; Hohl, R.; Hodzic, A.; Eder, R. J. P.; Khinast, J. G., Modeling a seeded continuous crystallizer for the production of active pharmaceutical ingredients. *Crystal Research and Technology* **2014,** 49, (2-3), 92-108.
278. Eder, R. J. P.; Radl, S.; Schmitt, E.; Innerhofer, S.; Maier, M.; Gruber-Woelfler, H.; Khinast, J. G., Continuously seeded, continuously operated tubular crystallizer for the production of active pharmaceutical ingredients. *Crystal Growth & Design* **2010,** 10, (5), 2247-2257.

Appendix A. Experimental and computational investigation of heat transfer in a microwave-assisted flow system

A.1. Dielectric properties of water

A.1.1. Measurement of dielectric properties at atmospheric pressure

The relative complex permittivity of water, $\varepsilon_r = \varepsilon' - \varepsilon'' j$ (dielectric constant: ε' and dielectric loss: ε''), was evaluated experimentally between 20-95 ^{o}C and atmospheric pressure, as bubbling occurred above 95 ^{o}C. A coaxial dielectric probe (87070E, Agilent Technologies) connected to a network analyser (PNA-L, Agilent Technologies) was inserted in a 100 ml water sample. E-cal software (Agilent Technologies) was used for the calculation of the dielectric properties at a frequency span of 1-10 GHz (Table A-1).

Table A-1 Experimental measurements of the relative complex permittivity of ultra-pure water for different temperatures at atmospheric pressure at 2.45 GHz frequency using a coaxial probe, following the methodology described by Robinson *et al.*[146].

Temperature, T (^{o}C)	**Relative complex permittivity, ε_r (-)**
20	78.6 - 10.5j
25	77.3 - 9.4j
30	76.2 - 8.6j
35	74.6 - 7.5j
40	73.0 - 6.7j
45	71.7 - 6.2j
50	70.6 - 5.8j
55	69.4 - 5.4j
60	68.0 - 5.0j
65	65.9 - 4.5j
70	64.2 - 4.2j
75	63.0 - 4.0j
80	61.8 - 3.9j
85	60.5- 3.7j
90	59.3- 3.5j
95	59.2- 3.4j

A.1.2. Calculation of dielectric properties as a function of temperature and pressure

In order to model the system at elevated pressures, the effect of pressure on the water dielectric properties was investigated. Table A-2 shows the dielectric properties of water calculated from literature empirical correlations. Based on the comparison of the two correlations considered, there is no significant increase of the dielectric constant by increasing the system pressure from 1 bara to 2.3 bara, at different temperatures.

Table A-2 Calculated dielectric constant of water at 1 bara and 2.3 bara and at various temperatures, based on the empirical correlations of Bradley & Pitzer[174] and Floriano & Nascimento[175].

Temperature	System pressure	*Bradley & Pitzer*	*Floriano & Nascimento*
0 ^{o}C	1 bara	87.57	87.78
	2.3 bara	87.57	87.79
25 ^{o}C	1 bara	78.05	78.45
	2.3 bara	78.05	78.45
50 ^{o}C	1 bara	69.46	69.91
	2.3 bara	69.46	69.91
75 ^{o}C	1 bara	61.74	62.24
	2.3 bara	61.74	62.25

To the best of our knowledge, there are no experimental data of the dielectric constant and dielectric loss of water at 2.3 bara. The boiling point of water at this pressure is 125 ^{o}C; thus, as shown on Figure A-1, the experimentally measured dielectric properties from Table A-1 were extrapolated up to 120 ^{o}C since bubbling was observed above that temperature, while the dielectric loss was assumed equal to zero at 125 ^{o}C due to the phase change. A linear interpolation was then performed between ε'' at 120 ^{o}C to $\varepsilon'' = 0$ at 125 ^{o}C by COMSOL.

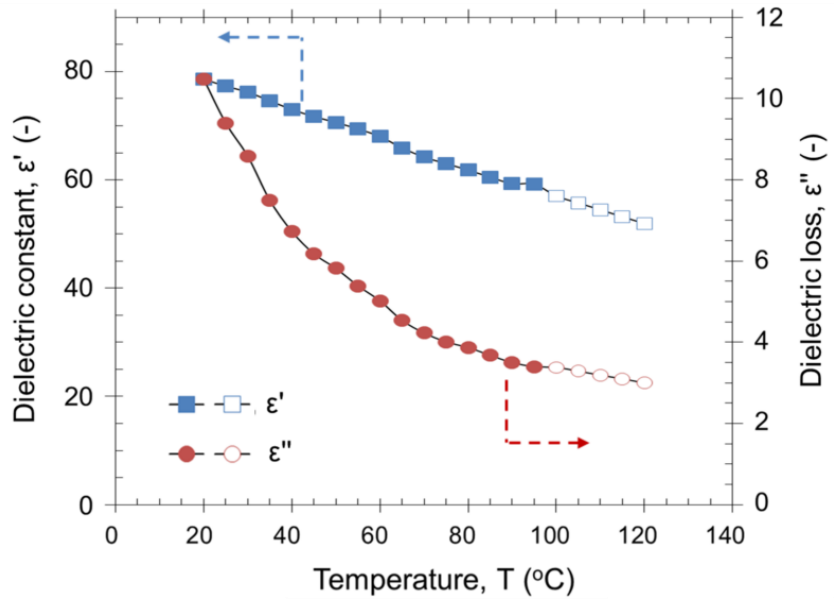

Figure A-1 Experimentally measured dielectric properties of water at atmospheric pressure (filled marks) and the extrapolated values (empty marks) for the estimation of the dielectric properties at 2.3 bara pressure (water boiling point at 2.3 bara is 125 ^{o}C). Lines are used for visualisation.

A.2. Dielectric properties of water

The effect of the fibre optic probe inside the tube was evaluated prior to the parametric investigation of the operational parameters on the temperature profile. In this work, the study the electric field (Figure A-2) and the temperature profile (Figure A-3) were simulated in the tube and the support structure with and without the fibre optic temperature probe, using COMSOL Multiphysics. The probe was positioned at the 5 points for temperature measurements by inserting it from the tube outlet, while in all cases the water flow rate was 0.7 ml/min. The fibre optic probe was considered as a solid cylinder of glass of ~ 1.7 mm diameter ($\varepsilon_{r,glass} = 4.6 - 0.01j$, $C_{p,glass} = 840$ J/kg·K)[123, 146].

The electric field intensity at the measurement points was different in the presence or absence of the fibre optic probe. When the fibre optic probe was at point 3, the electric field intensity on the tip was $1.03 \cdot 10^4$ V/m, while the intensity at the same position without the probe was ~ $0.56 \cdot 10^4$ V/m. These results are in accordance with previous studies in batch vessels, discussing the influence of fibre optic probe in microwave-assisted studies[126]. However, the simulated temperatures at the temperature measurement points were similar in the presence or absence of the probe, similar to the study by Robinson *et al.*[146]. The negligible temperature difference with or without the inserted fibre optic showed that heat was dissipated uniformly in the medium, despite the local heating of the tip of the probe.

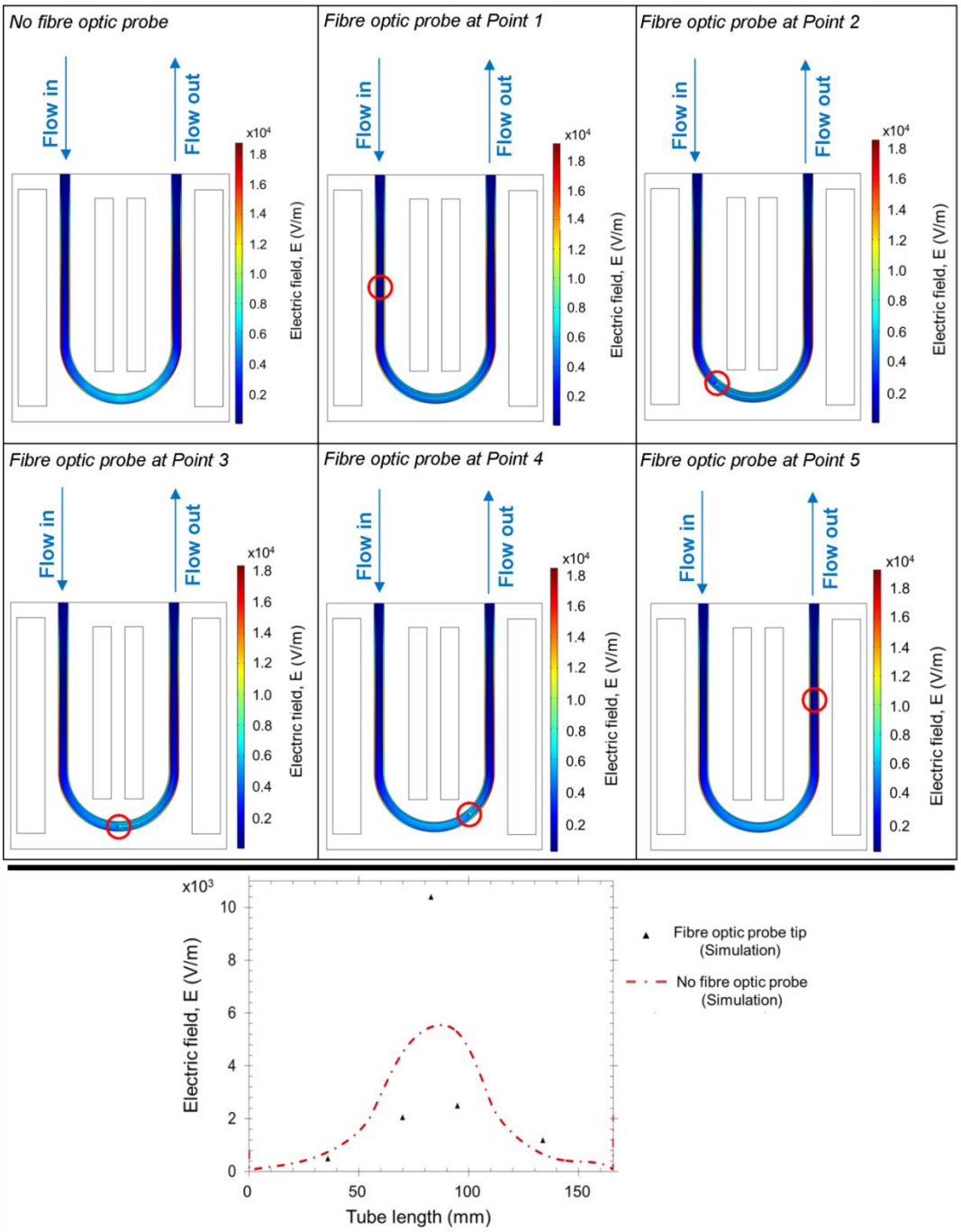

Figure A-2 Top: Computational results of the electric field profile inside the U-shape tube without the fibre optic temperature probe and with the probe positioned at the 5 points for temperature measurements by inserting the probe from the tube outlet (point 1: 36 mm, point 2: 70 mm, point 3: 83 mm, point 4: 95 mm, point 5: 135 mm from tube inlet). The tip of the fibre optic probe is noted with a red circle. Bottom: Simulated electric field profile over the tube length without the fibre optic probe (dash-dotted line) and at the measurement points when the fibre optic probe was included in the simulations (triangle marks). Microwave power, 35 W; frequency, 2.45 GHz; flow rate, 0.7 ml/min; tube orientation: parallel-to-port; system pressure, 1 bara.

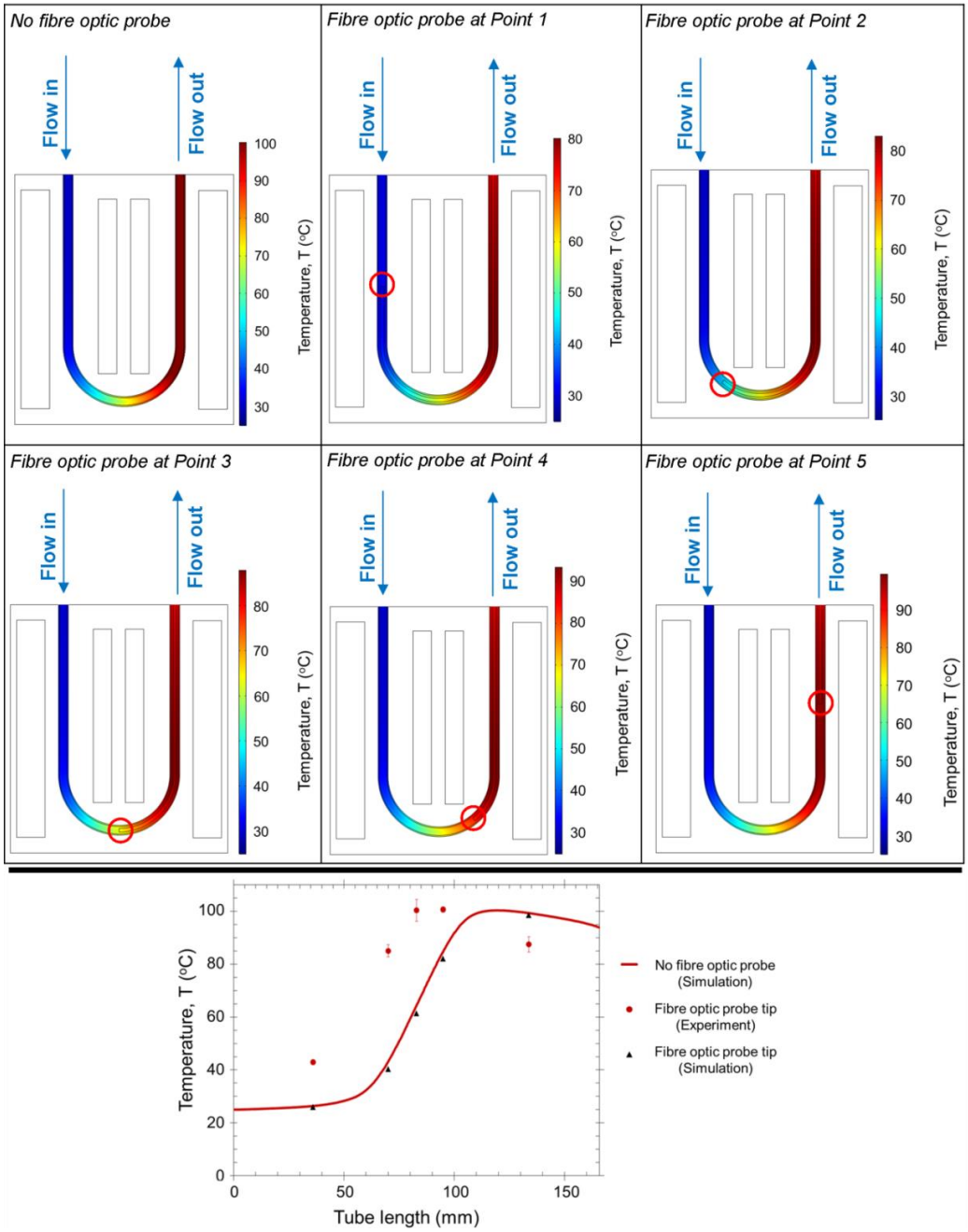

Figure A-3 Top: Computational results of the temperature profile inside the U-shape tube without the fibre optic temperature probe and with the probe positioned at the 5 points for temperature measurements by inserting the probe from the tube outlet (point 1: 36 mm, point 2: 70 mm, point 3: 83 mm, point 4: 95 mm, point 5: 135 mm from tube inlet). The tip of the fibre optic probe is noted with a red circle. Bottom: Experimental (circle marks) and simulated temperature profile along the tube length without the fibre optic probe (solid line) and at the measurement points when the fibre optic probe was included in the simulations (triangle marks). Microwave power, 35 W; frequency 2.45 GHz; flow rate, 0.7 ml/min; tube orientation: parallel-to-port; system pressure, 1 bara.

A.3. COMSOL model description

For the evaluation of the electric field and temperature profiles throughout the tube length and the absorbed microwave power by the flowing water, a FEM model was developed in COMSOL Multiphysics consisting of two steps, Step 1 and Step 2. In Step 1, the electric field inside the microwave cavity was evaluated via the *Electromagnetic Waves, Frequency Domain* module. Step 1 included six domains (the metal cavity, the contained PTFE protective ring, the air, the PTFE support structure, the PTFE tube and the water flowing inside the tube). In Step 2, the temperature profile in the water was evaluated by coupling the *Heat Transfer* and *Laminar Flow* modules. Step 2 included three domains (the PTFE support structure, the PTFE tube and the water).

Step 1

In Step 1 of COMSOL Multiphysics simulation, the following assumptions were made:

- The dielectric properties of air and PTFE were constant
- The microwave energy absorbed by the air was negligible

Model equations

- Time-harmonic electromagnetic field distribution in the metal cavity, PTFE protective ring, air, PTFE support structure, PTFE tube and water domains :

$$\nabla \times \mu_r^{-1}(\nabla \times \boldsymbol{E}) - k_o^2 \varepsilon_r \boldsymbol{E} = 0 \qquad \text{Eq. A-1}$$

where $k_o = \omega\sqrt{(\varepsilon_o \mu_o)} = \frac{\omega}{c}$ is the wave number of free space, ε_o is the permittivity of free space, μ_0 is the permeability of the free space, ω is the angular frequency, c is the speed of light in the free space, μ_r is the relative permeability, ε_r is the relative permittivity, and $\boldsymbol{E}$ is the electric field vector. Maximum element size in free space was set at 0.0244 m (1/5 of the electromagnetic wavelength in vacuum).

Model boundary conditions

- The inside surfaces of the waveguide were assumed to behave as perfect electric conductor:
  $\boldsymbol{n} \times \boldsymbol{E} = 0$, on the inside waveguide surfaces
- The electric field excitation at the magnetron port is given by:

$E_z = \left(\sqrt{\frac{4Z_{TE}P_{in}}{A}}\right) sin\left(\frac{\pi y}{L_y}\right)$, normal to the magnetron port

Here, $\boldsymbol{n}$ is the normal vector, the x-direction is normal to the port, the y-direction is parallel to the port width and the z-direction is parallel to the port height, L_y is the dimension of the broad side of the launching waveguide section, A is the area of the launching waveguide section (magnetron port dimensions are 44 mm x 87 mm), P_{in} the input microwave power and $Z_{TE} = \frac{\lambda_g}{\lambda}\sqrt{\frac{\mu_r \cdot \mu_0}{\varepsilon_r \cdot \varepsilon_0}}$ is the wave impedance; the last parameter depends on the properties of the material ($\lambda = {}^{c}/_{f}$ and λ_g are the wavelengths of microwaves in free space and rectangular waveguide, respectively and f the operating microwave frequency). Based on its dimensions, the waveguide is defined as TE_{10} mode [123] translating to transverse electric (TE) waves that have no electric field component in the propagating direction. In this case the wavelength in the rectangular waveguide is given by $\lambda_g = \frac{\lambda}{\sqrt{1-\left({}^{\lambda}/_{L_y}\right)^2}}$.

Step 2

In Step 2 of COMSOL Multiphysics simulation, the following assumptions were made:

- The thermal conductivity of the PTFE was constant
- Water was assumed as incompressible fluid

Model equations

- Energy balance in the water domain:

$$\rho_{water} C_{p,water}(\boldsymbol{u} \cdot \nabla T_{water}) = k_{water}\nabla^2 T_{water} + P_d \qquad \text{Eq. A-2}$$

where the microwave power density in water is given by:

$$P_d = 2\pi f \varepsilon_o \varepsilon''_{water} |\boldsymbol{E}|^2 \qquad \text{Eq. A-3}$$

- Energy balance in the PTFE tube and support structure domains:

$$k_{PTFE}\nabla^2 T_{PTFE} = 0 \qquad \text{Eq. A-4}$$

- Momentum balance in the water domain:

$$\rho_{water}[\boldsymbol{u} \cdot \nabla \boldsymbol{u}] - \eta_{water}\nabla \cdot [\nabla \boldsymbol{u} + (\nabla \boldsymbol{u})^T] + \nabla p = 0 \qquad \text{Eq. A-5}$$

- Continuity equation in the water domain:

$$\rho_{water}(\nabla \cdot \boldsymbol{u}) = 0 \qquad \text{Eq. A-6}$$

where ε_o is the permittivity of free space, ε'' is the dielectric loss factor, f is the operating microwave frequency, $|\boldsymbol{E}|$ is the electric field intensity, ρ is the density, C_p is the specific heat capacity, k is the thermal conductivity, $\boldsymbol{u}$ is the water velocity field vector inside the tube, η is the dynamic viscosity, p is the pressure and T is the temperature.

Model boundary conditions

- The water temperature at the tube inlet was set as:
  $T_{water} = T_0$, at tube inlet
- No heat flux was assumed at the tube outlet:
  $-\boldsymbol{n} \cdot k_{water} \nabla T_{water} = 0$, at tube outlet
- The heat flux at the interface between the water and the PTFE tube were matched:
  $k_{water} \nabla T_{water} = k_{PTFE} \nabla T_{PTFE}$, at inner tube wall
- The temperature at the interface between the water and the PTFE tube were matched:
  $T_{water} = T_{PTFE}$, at inner tube wall
- The heat loss from the PTFE wall and support structure to the ambient environment due to natural convection and radiation was given by:

$-\boldsymbol{n} \cdot k_{PTFE} \nabla T_{PTFE} = h_{air}(T_{air} - T_{PTFE}) + \varepsilon_{PTFE} \sigma \left({T^4}_{air} - {T_{PTFE}}^4 \right)$, at PTFE surface

- The water velocity at the tube inlet was set as:
  $\boldsymbol{u} = u_0$, at tube inlet
- No slip condition was assumed at the inside walls of the tube:
  $\boldsymbol{u} = 0$, at inner tube wall
- The relative pressure was assumed to be zero at the tube outlet :
  $p_0 = 0$, at tube outlet

Here, $\boldsymbol{n}$ is the normal vector and p_0 is the relative pressure. Input parameters for the COMSOL model (for Step 1 and Step 2) are given in Table A-3 and the thermal properties of water are given in Table A-4.

Table A-3 Input parameters for the COMSOL model (Step 1 and Step 2).

Symbol	Value	Unit	Description
		Step 1	
c	$2.998 \cdot 10^{9}$	m/s	Speed of light in free space
f	$2.45 \cdot 10^{9}$ – $2.47 \cdot 10^{9}$	Hz	Frequency in the microwave cavity
L_{tube}	$166 \cdot 10^{-3}$	m	Tube length
P_{in}	5 – 35	W	Input microwave power
ε_o	$8.854 \cdot 10^{-12}$	F/m	Permittivity of free space
ε'_{water}	78.6	-	Dielectric constant of water at 20 ^{o}C
ε''_{water}	10.5	-	Dielectric loss of water at 20 ^{o}C
ε'_{PTFE}	2.1	-	Dielectric constant of PTFE
ε''_{PTFE}	0	-	Dielectric loss of PTFE
ε'_{air}	1	-	Dielectric constant of air
ε''_{air}	0	-	Dielectric loss of air
μ_o	$4\pi \cdot 10^{-7}$	H/m	Permeability of free space
$\mu_{r,water}$	1	-	Relative permeability of water
$\mu_{r,PTFE}$	1	-	Relative permeability of PTFE
$\mu_{r,air}$	1	-	Relative permeability of air
		Step 2	
$C_{p,water}$	see Table S4	J/kg·K	Heat capacity of water
h_{air} [261]	5	W/m^2·K	Heat transfer coefficient of air
k_{PTFE}	0.24	W/m·K	Thermal conductivity of PTFE
k_{water}	see Table S4	W/m·K	Thermal conductivity of water
L_{tube}	$166 \cdot 10^{-3}$	m	Tube length
V_{in}	0.5 – 1.5	cm^3/min	Inlet flow rate
R_{tube}	$1.2 \cdot 10^{-3}$	m	Tube inner radius
T_0	20	^{o}C	Water temperature at the tube inlet
u_0	1.84 – 5.53	mm/s	Water inlet velocity

Table A-3 continued

Symbol	Symbol	Symbol	Symbol
ε_o	$8.854 \cdot 10^{-12}$	F/m	Permittivity of free space
ε_{PTFE} [262]	0.92	-	Surface emissivity of PTFE
ε'_{water}	see Table S1, Figure S1	-	Dielectric constant of water
ε''_{water}	see Table S1, Figure S1	-	Dielectric loss of water
η_{water}	see Table S4	Pa·s	Dynamic viscosity of water
ρ_{water}	see Table S4	kg/m^3	Density of water
σ	$5.6704 \cdot 10^{-8}$	$W/m^2 \cdot K^4$	Stefan-Boltzmann constant

Table A-4 Thermal properties of water for the COMSOL model (Step 2).

Density [263]:	$-0.0031\mathrm{T}^2 + 1.5392\mathrm{T} + 810.7$ (kg/m^3)
Dynamic viscosity [264]:	$10^{\left(-0.00001599\mathrm{T}^2+0.021641\mathrm{T}+\left(\frac{1949}{\mathrm{T}}\right)-14.62\right)}$ (Pa·s)
Heat capacity [263]:	$-0.00009\mathrm{T}^3 + 0.1054\mathrm{T}^2 - 39.619\mathrm{T} + 9021.6$ (J/kg·K)
Thermal conductivity [264]:	$-0.0000056209\mathrm{T}^2 + 0.0047054\mathrm{T} - 0.2987$ (W/m·K)

Temperature range: 293.15 – 373.15 K; Temperature in K.

Appendix B. Investigation of citrate-capped gold nanoparticle synthesis in continuous flow microwave-assisted reactors

B.1. Microwave absorption on gold nanoparticles

A preliminary experimental study was conducted in order to evaluate the effect of the presence of citrate-capped gold nanoparticles (Au NPs) on the microwave absorption of the reacting mixture. In this study, the temperature ramping of the aqueous solutions was monitored up to 95 ^{o}C at ambient pressure in batch, containing either the reacting mixture for the gold nanoparticle synthesis ($HAuCl_4$ and Na_3Cit) or only the trisodium citrate in the same concentration. The same microwave equipment (Discover SP, CEM) was utilised and temperature was measured via the built-in infrared sensor on the equipment focusing on the bottom of the 10 ml reaction vessel made of borosilicate glass supplied by the manufacturer.

Based on the findings shown in Figure B-1 for the aforementioned study, the temperature ramping was similar in all cases varying between 0.32 – 0.37 ^{o}C/s either with reaction taking place or when only the trisodium citrate was present. The temperature ramping was comparable to the respective value for ultra-pure water only (~ 0.39 ^{o}C/s) as water has a dominant role on the microwave absorbance from aqueous solutions[178]. An additional study was conducted in order to establish if the continuous synthesis and the presence of gold nanoparticles could affect the microwave absorption and subsequently the temperature of the aqueous solution. Similarly to the experimental procedure protocol developed by Bayazit *et al.*[53], a K-type thermocouple was placed at 6 cm from the outlet of the microwave reactor setup – as described in Section 2.2 of the main text – and recorded the temperature for 50 min. Maximum temperature in both the synthesis solution and the trisodium citrate solution in the same concentration was ~ 90 ^{o}C, while temperature was constant and fluctuated around 88 ^{o}C in both systems (Figure B-2).

These observations were in accordance with the previously published literature findings describing the low to negligible enhancement of heating rate of gold nanoparticles in aqueous solution under radiofrequency heating[179, 180]. Gold nanoparticles are considered to be ineffective under microwave heating due to their low magnetic loss and their small size which results to low power dissipation due to electric dipole absorption[265]. According to the work of Keblinski *et al.*[266], particles surfaces can be locally heated, however, considering the low concentration of the gold nanoparticles and the strong microwave absorption on the surrounding medium

in the studied frequency range (at 2.45 GHz frequency which is within the specification of the utilised equipment), the final temperature of the solution is dominated by the microwave absorption on the medium.

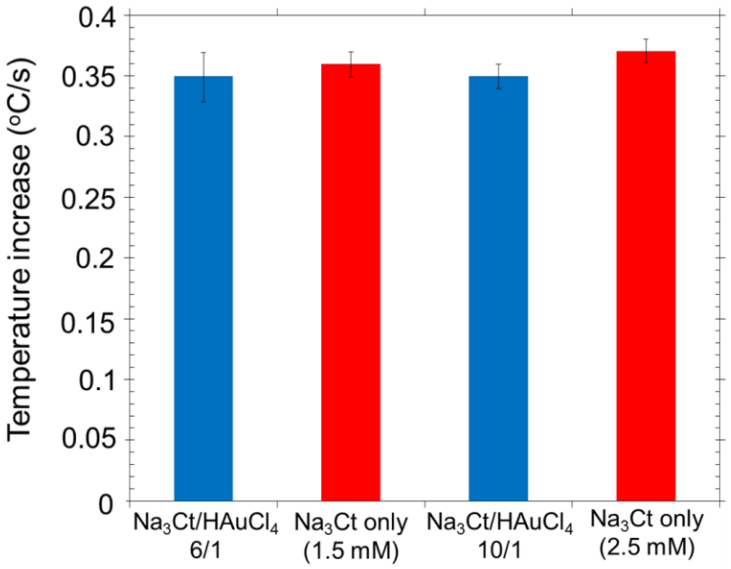

Figure B-1 Temperature increase of the reacting mixture $HAuCl_4/Na_3Ct$ and Na_3Ct only in the same concentration in batch. [$HAuCl_4$], 0.25 mM; volume, 3 ml; microwave power, 10 W. Error bars correspond to the standard deviation of the experimental measurements at each point.

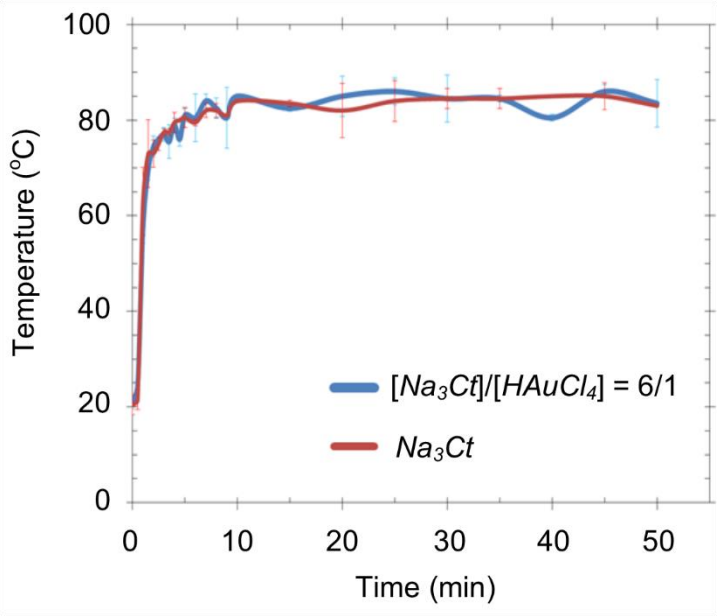

Figure B-2 Temperature recorded via a K-type thermocouple placed at 6 cm from the outlet of the reactor in case of the reacting mixture for gold nanoparticles synthesis ($HAuCl_4$ and Na_3Ct) and only Na_3Cit in the same concentration. Reacting solution: [$HAuCl_4$], 0.25 mM; [Na_3Ct], 1.5 mM ([Na_3Ct]/ [$HAuCl_4$]: 6/1); Citrate solution: [Na_3Ct], 1.5 mM; total inlet flow rate, 0.7 ml/min; microwave power, 15 W. Error bars correspond to the standard deviation of the experimental measurements at each point.

B.2. Estimation of the temperature on the outlet of the microwave reactor

The temperature of the solution exiting the microwave reactor was measure via a K-type thermocouple inserted from the tube outlet and positioned at 5 cm from the reactor outlet. Thereby, the temperature on the outlet of the PTFE tube after exiting the microwave applicator was estimated using the following heat transfer model using the MATLAB software (version R2019a, MathWorks)[53, 267]. The medium properties were assumed equal to water due to the low concentration of the colloidal Au NPs.

For a small section of the PTFE tube (dL), the temperature change of the medium (water) can be calculated via the heat transfer rate through the tube wall[267]:

$$dQ = \pi d_{outer} K (T - T_{amb}) dL \qquad \text{Eq. B-1}$$

where the heat transfer coefficient K was given by[267]:

$$K = \left[\frac{1}{h_{int}} \frac{d_{outer}}{d_{inner}} + \frac{d_{outer}}{2k_{tubing}} \ln \frac{d_{outer}}{d_{inner}} + \frac{1}{h_{ext}} \right]^{-1} \qquad \text{Eq. B-2}$$

And the thermal energy balance of the medium[267]:

$$dQ = \rho \dot{V} Cp dT \qquad \text{Eq. B-3}$$

Where Q is the heat energy, d_{outer} is the outer tube diameter, d_{inner} is the inner tube diameter, ρ is the density of the medium, Cp is the specific heat capacity of the medium, k_{tubing} is the thermal conductivity of the PTFE tube, $\dot{V}$ is the flow rate of the medium, T is the cross-sectional average temperature of the medium, T_{amb} is the ambient air temperature, L is the reactor length and h_{ext} is the external heat transfer coefficient (natural convection).

Therefore, the temperature over the tube section was calculated from Equation B-1 – B-3, resulting in the equation:

$$\frac{dT}{dL} = \frac{\pi d_{outer}}{\rho \dot{V} Cp} K(T - T_{amb}) \qquad \text{Eq. B-4}$$

For fully–developed laminar flow systems in circular tubes, the Nusselt number is[267]:

$$Nu = \frac{h_{int} d_{inner}}{k} \qquad \text{Eq. B-5}$$

where d_{inner} is the inner tube diameter, k is the thermal conductivity of the medium and h_{int} is the internal heat transfer coefficient.

The Nusselt number (Nu) was assumed constant and equal to 4.36 (constant heat flux)[267]. Table B-1 shows calculated temperature on the outlet of the microwave reactor, based on the calculations on the heat loss to the surrounding air up to the measurement point by the inserted thermocouple (reactor length: 5 cm), for different input microwave powers using the one-stage synthesis process. The boiling point of water at 2.3 bar[263] is 125 ^{o}C, however, the boiling point can increase up to 4 ^{o}C as results of limited bubble nucleation sites to trigger the liquid to gas transition (superheating effect)[135]. Figure B-3 shows the TEM images of the synthesised gold nanoparticles at 25 – 45 W input microwave power using the one-stage microwave-assisted synthesis.

Table B-1 Calculated temperature at the outlet (T_{exit}) of the PTFE tube reactor on the exit of the microwave applicator using the measured temperature at 5 cm (T_{5cm}) from the microwave reactor outlet.

Input microwave power	T_{exit} (°C)	T_{5cm} (°C)
25 W	120	109
30 W	123	113
36 W	125	115
40 W	126	116
45 W	128	117

d_{inner} = 2 mm; d_{outer} = 3.2 mm; $\dot{V}$ = 4 ml/min; T_{amb} = 25 °C; L = 5 cm; h_{ext} = 10 W/m^{2}K[267]; k_{tubing} = 0.25 W/mK[268]; k_{water} = 0.69 W/mK (120 °C)[263]; Cp_{water} = 4,239 J/kgK (120 °C)[263]; ρ_{water} = 945 kg/m^3 (120 °C)[263].

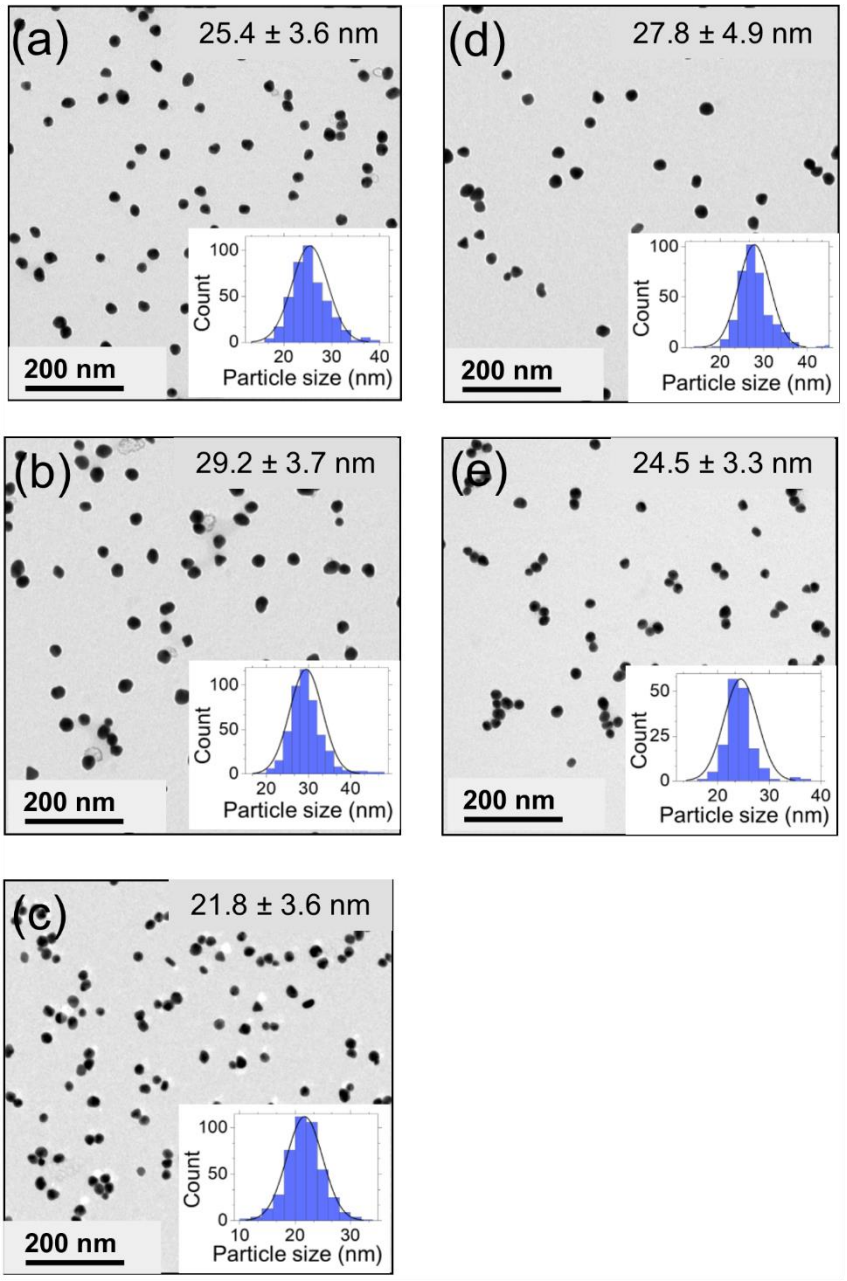

Figure B-3 TEM image of the gold nanoparticles synthesised at a) 25 W, b) 30 W, c) 36 W, d) 40 W and e) 45 W input microwave power in a one-stage microwave assisted synthesis. Histograms display the particle size distribution given by TEM. Reactor volume, 6 ml; Inlet flow rate, 4 ml/min; residence time, 90s; [$HAuCl_4$] (after mixing), 0.25 mM; [Na_3Ct] (after mixing), 1.5 mM; system pressure, 2.3 bara.

B.3. Estimation of the yield under different input microwave powers

The yield of the gold nanoparticles synthesis in the two stage process under different input microwave power (0 – 25 W) was estimated using the Beer-Lambert law as described by Hendel *et al.*[84] and Yue *et al.*[191] The concentration of the Au^0 was calculated via the absorbance of the samples at 400 nm from the spectra obtained by UV-Vis spectroscopy:

$$A_{400} = \varepsilon_{ext} \cdot C_{Au^0} \cdot l \qquad \text{Eq. B-6}$$

where A_{400} is the absorbance of the UV-vis spectra at 400 nm, ε_{ext} is the extinction coefficient of the synthesised Au NPs sample (ranging between 2.29 – 2.38 L/mol·cm for 10 – 20 nm citrate-capped Au NPs)[84], C_{Au^0} is the concentration of the Au^0 and l is the length of the cuvette used in the UV-Vis absorbance measurement (1 cm). Therefore, by dividing the concentration of the Au^0 over the initial concentration of the gold precursor after mixing the process yield could be estimated (Figure B-4). The yield of the two-stage process increased from 65 % (for 0 W – only conventional heating) up to ~ 79 % (for 5 – 25 W).

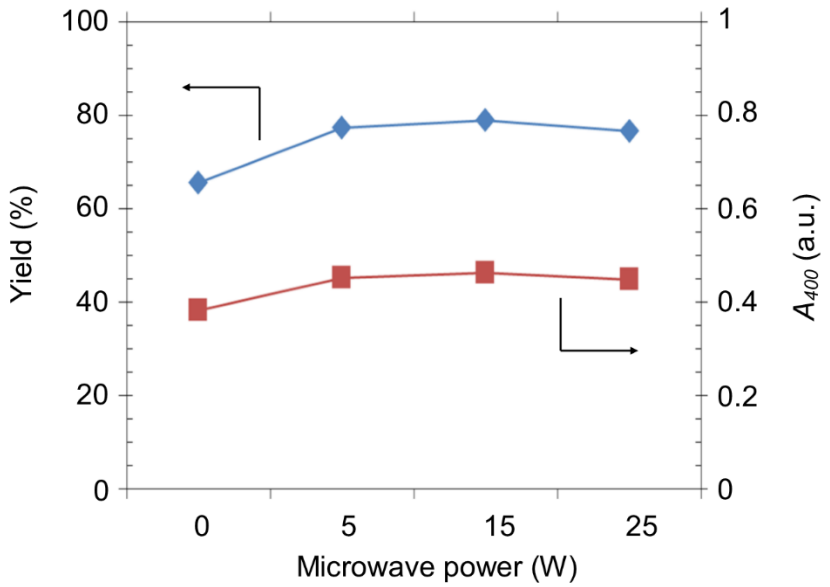

Figure B-4 Absorbance of the UV-Vis spectra at 400 nm (A_{400}) and yield of gold nanoparticles obtained during the two-stage synthesis with different input microwave powers (5 – 25 W) and under only conventional heating (0 W), calculated via the UV-Vis spectra of the stabilised solutions. [$HAuCl_4$] (after mixing), 0.25 mM; [Na_3Ct] (after mixing), 1.5 mM; total inlet flow rate, 0.5 ml/min; microwave heating reactor volume, 0.75 ml, residence time in microwave reactor, 90 s; conventional heating reactor volume, 10 ml, residence time in conventional heating reactor, 20 min; temperature in conventional heating reactor, 90 ^{o}C; system pressure, 2.3 bara. Solid lines were used for visual aid.

B.4. Evaluation of residence time distribution in the microwave heating and conventional heating reactor

The evaluation of residence time distribution in the microwave heating (MWH) and the conventional heating (CH) reactors are included in Table B-2. The flow can be characterised as laminar in both reactors since the Reynolds number varied between 3.8 – 7.1 for the studied total inlet flow rates (0.375 – 0.7 ml/min). Particularly for the CH reactor, the tube was commissioned in a coiled formation, however, the Dean number was less than 3 (for all three different growth reactors of 7.5 – 14 ml in volume which were utilised to maintain the residence time in the growth stage at 20 min). This indicated that the centrifugal forces were insignificant and could not enhance the mixing[195]. Therefore, the coiled formation and the centrifugal forces were not taken into account in this study. In order to investigate the operating flow regime inside the MWH and the CH reactors, 3 different nanoparticle sizes were chosen (5 nm, 10 nm and 20 nm Au NPs). This methodology allowed the visualisation of the effect of particle size on the diffusivity and subsequently ensure the appropriate flow regime, since the gold nanoparticles grow in size over the tube length. Additionally, the operating flow regimes were calculated for the gold precursor ($HAuCl_4$) only. As shown in Table B-2, the diffusivity of the gold nanoparticles decreased by increasing the particle size and in all cases it was ~ 2 orders of magnitude smaller than the respective diffusivities of the reactants. From the calculated Bodenstein number – for each reactor and flow rate – and the mapping reported by Levenspiel[193], the solution with the gold nanoparticles fell within the pure convection or the intermediate regime, indicating that the convective forces were prevailing over the diffusive forces for all particle sizes. In all of the cases, the physical properties of the solution containing the synthesised nanoparticles were assumed similar to water due to the low particle content.

Table B-2 Evaluation of residence time distribution in the microwave heating (MWH) and the conventional heating (CH) reactors.

					MWH reactor		***CH reactor***		
Item	**Total inlet flow rate (ml/min)**	**Diffusion coefficient (m^2/s)**	**Reynolds number**	**Bodenstein number**	d_t=2.4 mm L=165 mm **Volume: 0.75 ml**	**Dean number**	d_t=2.4 mm L=1.658 m **Volume: 7.5 ml**	d_t=2.4 mm L=2.210 m **Volume: 10 ml**	d_t=2.4 mm L=3.095 m **Volume: 14 ml**
Equation		$D_m = k_B T/(6\pi\mu R)$	Re	$Bo = ud_t/D_m$	L/d_t	$De = Re/\sqrt{\lambda}$	L/d_t	L/d_t	L/d_t
$HAuCl_4$	0.7	$1.40\cdot10^{-9}$ [a]	7.1	$4.51\cdot10^{3}$	$7.00\cdot10^{1}$	1.2	-	-	$1.29\cdot10^{3}$
	0.5		5.1	$3.22\cdot10^{3}$	$7.00\cdot10^{1}$	0.9	-	$9.21\cdot10^{2}$	-
	0.375		3.8	$2.42\cdot10^{3}$	$7.00\cdot10^{1}$	0.7	$6.91\cdot10^{2}$	-	-
2 nm Au NPs	0.7	$2.47\cdot10^{-10}$ [b]	7.1	$2.55\cdot10^{4}$	$7.00\cdot10^{1}$	1.2	-	-	$1.29\cdot10^{3}$
	0.5		5.1	$1.82\cdot10^{4}$	$7.00\cdot10^{1}$	0.9	-	$9.21\cdot10^{2}$	-
	0.375		3.8	$1.37\cdot10^{4}$	$7.00\cdot10^{1}$	0.7	$6.91\cdot10^{2}$	-	-
10 nm Au NPs	0.7	$4.95\cdot10^{-11}$ [b]	7.1	$1.28\cdot10^{5}$	$7.00\cdot10^{1}$	1.2	-	-	$1.29\cdot10^{3}$
	0.5		5.1	$9.11\cdot10^{4}$	$7.00\cdot10^{1}$	0.9	-	$9.21\cdot10^{2}$	-
	0.375		3.8	$6.83\cdot10^{4}$	$7.00\cdot10^{1}$	0.7	$6.91\cdot10^{2}$	-	-
20 nm Au NPs	0.7	$2.47\cdot10^{-11}$ [b]	7.1	$2.55\cdot10^{5}$	$7.00\cdot10^{1}$	1.2	-	-	$1.29\cdot10^{3}$
	0.5		5.1	$1.82\cdot10^{5}$	$7.00\cdot10^{1}$	0.9	-	$9.21\cdot10^{2}$	-
	0.375		3.8	$1.37\cdot10^{5}$	$7.00\cdot10^{1}$	0.7	$6.91\cdot10^{2}$	-	-

k_B = $1.38\cdot10^{-23}$ m^2kg/s_2K: Boltzmann constant; T = 298.15: solution temperature; μ = $8.82\cdot10^{-4}$ Pa·s: water dynamic viscosity at 20 °C[263]; R : particle radius

ρ = 997 kg/m^3: water density at 20 °C[263]; d_t = inner tube diameter; u : liquid velocity in the tube; L : reactor length; $\lambda = d_s/d_t$: ratio of the diameter of the cylindrical support structure (d_s = 80 mm) over the diameter of the tube reactor.

a : Given by Hariri *et al.*[236]

b : Calculated by the Stokes-Einstein equation[269]

B.5. Particle deposition (fouling) in the PTFE tube under microwave heating

Figure B-5 shows the U-shape PTFE tube reactor (Figures B-5 a-b) and the coiled PTFE tube of the growth stage (Figures B-5 c-d). Comparing the pictures of the reactors before (Figures B-5a and B-5c) and after gold nanoparticle synthesis (Figures B-5b, B-5d), the particle deposition (fouling) can be identified along the reactor length. Similar to the work of Huang *et al.*[96], there was “dark fouling” close to the entrance of the entrance (inlet) of the U-shape reactor consisting of positively charged gold ions and citrate-gold complexes adsorbed on the negatively charged PTFE tube wall due to electrostatic attraction. However, along the reactor length, the colour of the fouling became similar to the elemental gold, resulting in high loss of unreacted material on the PTFE surface and explaining the low yield of the Au Ps synthesis displayed in Figure B-4. The observed fouling in the coiled reactor of the growth stage was speculated resulting from the deposition of synthesised Au NPs due to the attraction on the PTFE tube wall by van der Waals forces.

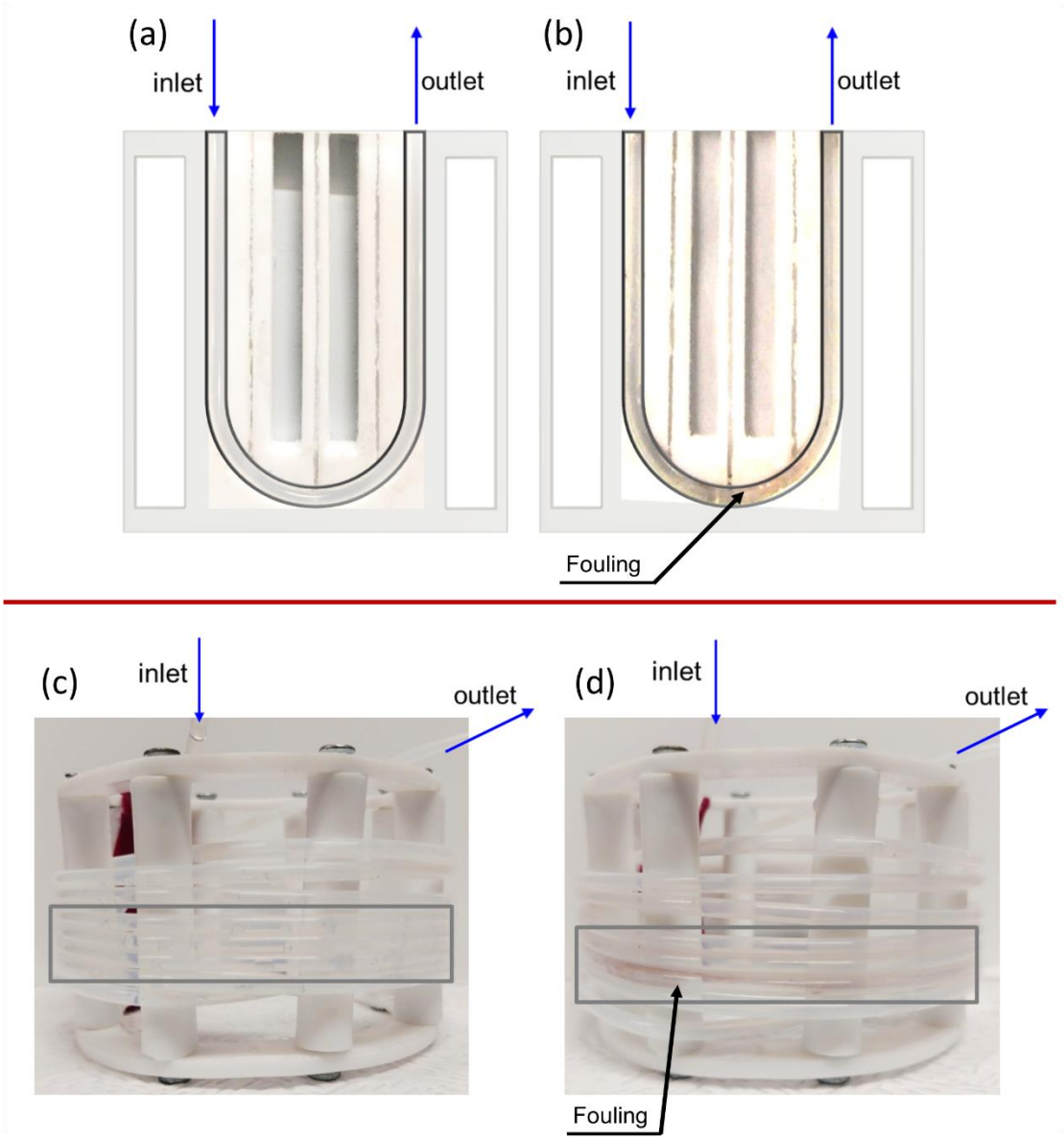

Figure B-5 Comparison of the U-shape tube reactor a) before and b) after gold nanoparticle synthesis under microwave heating and of the controllable growth stage coiled reactor c) before and d) after the synthesis under conventional heating. After the synthesis, particle deposition (fouling) appeared on the tube walls. The area, where fouling appeared, is highlighted by the grey shape.

Appendix C. Development of a predictive model for the targeted synthesis of citrate-capped gold nanoparticles

C.1. *In situ* gold precursor and citrate speciation

The $AuCl_4^-$ complex of the gold precursor ($AuCl_4$) exhibits a peak at 313 nm wavelength of the UV-Vis spectra[38]. During the Au NPs synthesis under the pH-adjusted *direct Turkevich* synthesis, the peak was monitored in time to evaluate the precursor behaviour during speciation, reactant addition and nanoparticle synthesis. Figure C-1 displays the absorbance peak at 313 nm (A_{313}). The overall synthesis can be divided in 4 phases related to the peak and its absorbance:

- In Phase I (0 – 1 min) the absorbance was equal to 0, as there was only the heated medium (water) at 95 ^oC.
- In Phase II (1 – 3 min) there was a sudden increase in the absorbance peak due to the addition of the gold precursor stock solution (stock solution concentration: 5 mM). Immediately the absorbance decreased and plateaued within the first 30 s upon addition (absorbance at 1 – 1.5 min), due to the speciation of the $AuCl_4^-$ complex towards the hydroxylated species ($AuCl_{3-x}(OH)_{1+x}^-$) and the ratio $AuCl_4^-/AuCl_{3-x}(OH)_{1+x}^-$ decreased.
- In Phase III (3 – 4 min) the absorbance at 313 nm dropped due to the addition of the reducing agent (mixture of Na_3Ct and H_3Ct, stock solution concentration: 50 mM). The addition of the reducing agent increased the pH from ~ 3.3 to ~ 5.6 causing further hydroxylation of the gold species (minimising the $AuCl_4^-/AuCl_{3-x}(OH)_{1+x}^-$ ratio).
- In Phase IV (4 – 10 min) the reaction took place between the gold and the citrate species leading to the nucleation and growth phases of the gold nanoparticle synthesis. As the gold nanoparticles started to form, the absorbance of the colloidal solution increased, leading to an increase on the absorbance at 313 nm. During the synthesis, the Au(III) was reduced to the Au^0 monomers. The reaction was completed within ca. 7.5 min from the beginning of Phase I (*time* = 0 s), where absorbance was plateaued signifying the required reaction time of the synthesis.

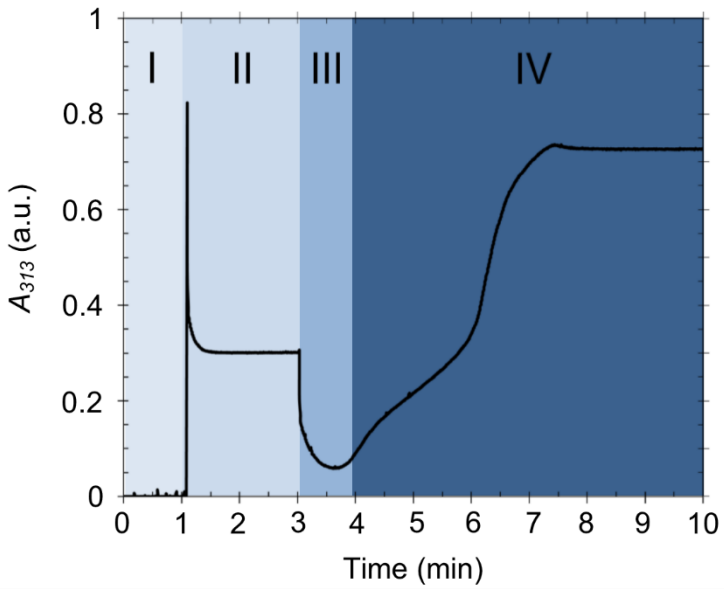

Figure C-1 Absorbance of the gold precursor peak at 313 nm (A_{313}) via *in situ* UV-Vis spectrometry during speciation and gold nanoparticle synthesis for the pH-adjusted *direct Turkevich* method. Phase I: Heating of only the water solution. Phase II: Addition of the concentrated gold precursor ($HAuCl_4$, 5 mM) and rapid speciation. Phase III: Addition of the concentrated $Citrate$ mixture (Na_3Ct and H_3Ct, 50 mM). Phase IV: Gold nanoparticle synthesis. Reaction was completed when the absorbance at 313 nm plateaued. Gold precursor concentration $HAuCl_4$ (after mixing), 0.25 mM; H_3Ct (after mixing), 0.54 mM; Na_3Ct (after mixing), 2.46 mM; temperature, 95 ^{o}C.

Figure C-2 shows the evolution of the surface absorbance (A_{SPR}) and the wavelength of the surface plasmon resonance peak (λ_{SPR}) of the UV-Vis spectra in time for the pH-adjusted (H_3Ct:Na_3Ct) and Na_3Ct only *direct, inverse* and *both speciated Turkevich* synthesis method. The evolution of the A_{SPR} in time in all conditions followed the same trend as small angle X-ray scattering (SAXS) data by Polte *et al.*[85] and Wuithschick *et al.*[38]. These results showed that Au NPs synthesis and growth does not follow the nucleation, formation of nanowires or fluffy particles and subsequent fragmentation or size reduction to spherical particles as proposed by Pong *et al.*[51] and Chow and Zukoski[82] but it follows the 4-step growth mechanism of Au NPs synthesis proposed by Polte's group[38, 69, 85]. In the latter mechanism, following the formation of nuclei and seeds, the remaining Au(III) is attracted by the electric double layer (EDL) of the seed particles and the reduction of Au(III) to Au^0 and growth of the particles takes place on the EDL. The reaction time for the gold

nanoparticle synthesis at each conditions was estimated by the time where A_{SPR} and λ_{SPR} plateaued.

Figures C-3a and C3b display the A_{313} over time for pH-adjusted *direct*, *both speciated* and *inverse Turkevich* methods noting the addition of the reactants in time, while Figure C-3c shows the A_{SPR} of the UV-vis spectra, respectively in all methods. As displayed in Figure C-1, upon addition of the gold precursor there was a sudden increase followed by an immediate drop due to the hydroxylation of the gold species. It is worth noting that in case of *inverse Turkevich* method, A_{313} was equal to 0 until 2 min since the citrate species displayed no peak at that wavelength. Comparing between the absorbance spectra at 313 nm (Figures C-3 a,b) and at the SPR peak (Figure C-3c), the formation of the gold nanoparticle can be observed at ~ 4 min, where the absorbance is all Figures C-3 started to increase. Also, in all Figures, the absorbance plateaued at the same time ca. 8 min signalling the completion of the reaction. Finally, the UV-Vis spectra of the pH-adjusted *direct, inverse* and *both speciated Turkevich* methods were similar explaining the negligible difference on the particle size and dispersity shown in Figure 5-2 in the main text.

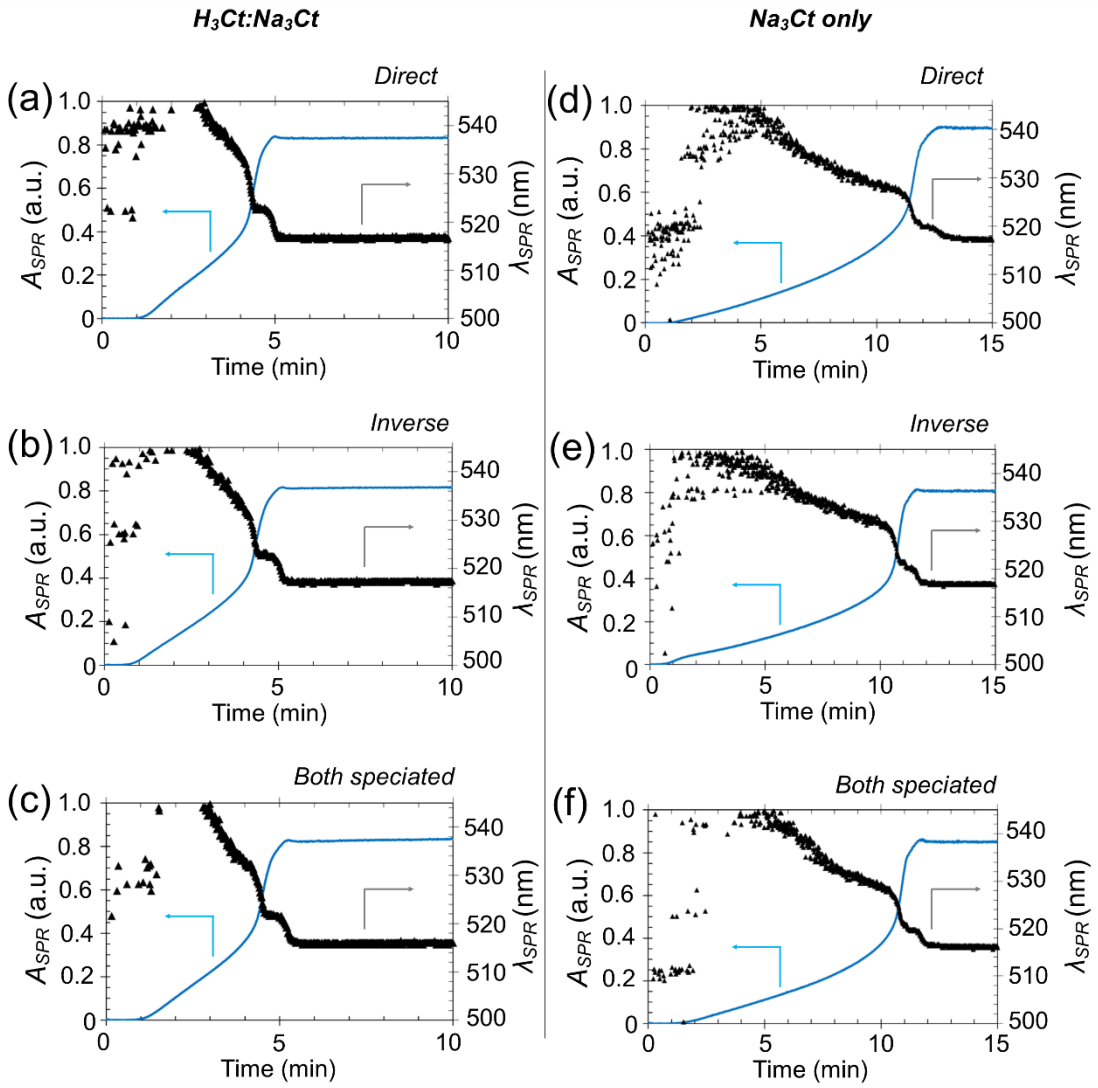

Figure C-2 Absorbance (A_{SPR}) and wavelength (λ_{SPR}) of the surface plasmon resonance peak in time in the (a-c) pH-adjusted *Turkevich* method (H_3Ct:Na_3Ct) and (d-f) normal *Turkevich* method (Na_3Ct only) for (a,d) *direct*, (b,f) *inverse* and (c,f) *both speciated Turkevich* synthesis via *in situ* UV-Vis spectrometry. Gold precursor concentration $HAuCl_4$ (after mixing), 0.25 mM; reducing agent, H_3Ct:Na_3Ct mixture concentration (after mixing): [H_3Ct] = 0.15 mM, [Na_3Ct] = 1.35 mM or Na_3Ct only concentration (after mixing): [Na_3Ct] = 1.5 mM; temperature, 95 ^{o}C.

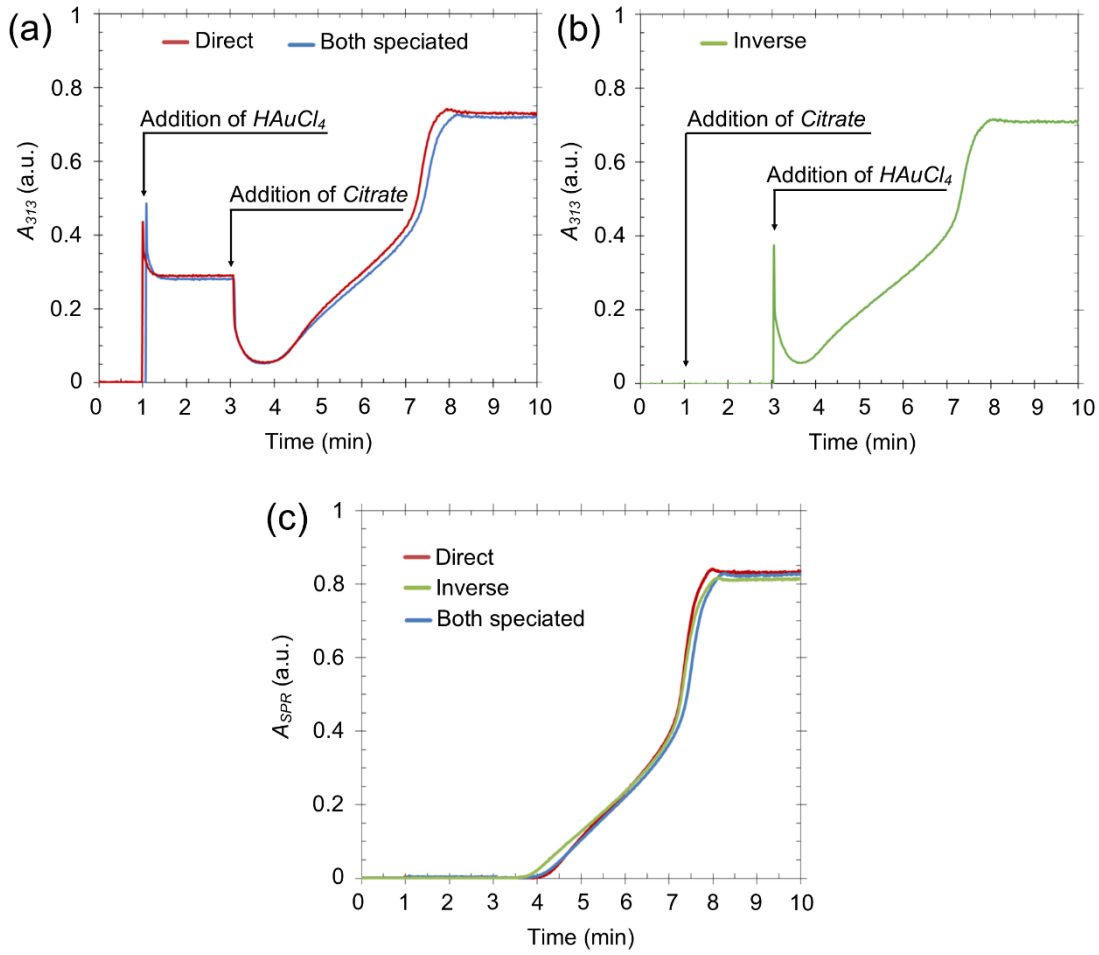

Figure C-3 Absorbance of the gold precursor peak at 313 (A_{313}) during speciation and gold nanoparticle synthesis for the pH-adjusted a) *direct, both speciated* and b) *inverse Turkevich* methods, as well as c) the absorbance of the surface plasmon resonance peak (A_{SPR}) in time via *in situ* UV-Vis spectrometry. Gold precursor concentration $HAuCl_4$ (after mixing), 0.25 mM; H_3Ct (after mixing), 0.15 mM; Na_3Ct (after mixing), 1.35 mM; temperature, 95 ^{o}C.

C.2. Reproducibility of the gold nanoparticle synthesis

Figure C-4 shows the reproducibility study for the of gold nanoparticle synthesis for the pH-adjusted *direct* (Figure C-4a), *inverse* and (Figure C-4b) *both speciated* (Figure C-4c) *Turkevich* methods. Comparing the two repeats in each method (as shown by the solid and the dashed lines), confirmed the analysis and observations of Kettemann *et al.*[40] of the high reproducibility of the gold nanoparticle synthesis at pH ~ 5.6.

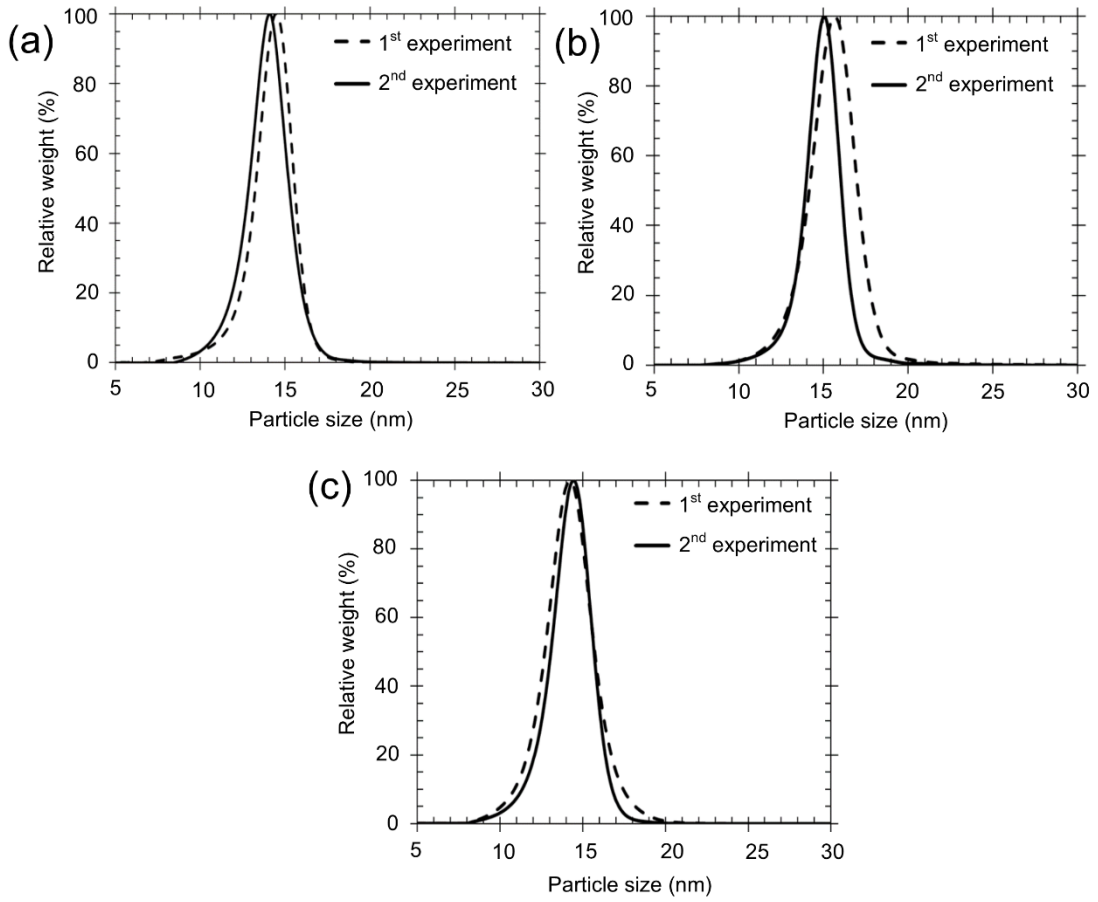

Figure C-4 Reproducibility study of the particle size distribution of gold nanoparticle synthesis for the pH-adjusted a) *direct*, b) *indirect* and c) *both speciated Turkevich* methods obtained by DCS. Gold precursor concentration $\boldsymbol{HAuCl_4}$ (after mixing), 0.25 mM; $\boldsymbol{H_3Ct}$ (after mixing), 0.15 mM; $\boldsymbol{Na_3Ct}$ (after mixing), 1.35 mM; temperature, 95 ^{o}C.

C.3. Effect of solution pH on the surface plasmon resonance peak of synthesised gold nanoparticles

Figure C-5 shows the evolution of the surface absorbance (A_{SPR}) and the wavelength of the surface plasmon resonance peak (λ_{SPR}) of the UV-Vis spectra in time at different solution pH (5.6 – 7.9) via the *direct Turkevich* synthesis method. Similarly to the study discussed in Section C1, the evolution of the A_{SPR} in time in all conditions followed the same trend as small angle X-ray scattering (SAXS) data by Polte *et al.*[85] and Wuithschick *et al.*[38] showing that particle growth followed the 4-step growth mechanism of Au NPs synthesis proposed by Polte's group[38, 69, 85]. The reaction time for the gold nanoparticle synthesis at each conditions was estimated by the time where A_{SPR} and λ_{SPR} plateaued.

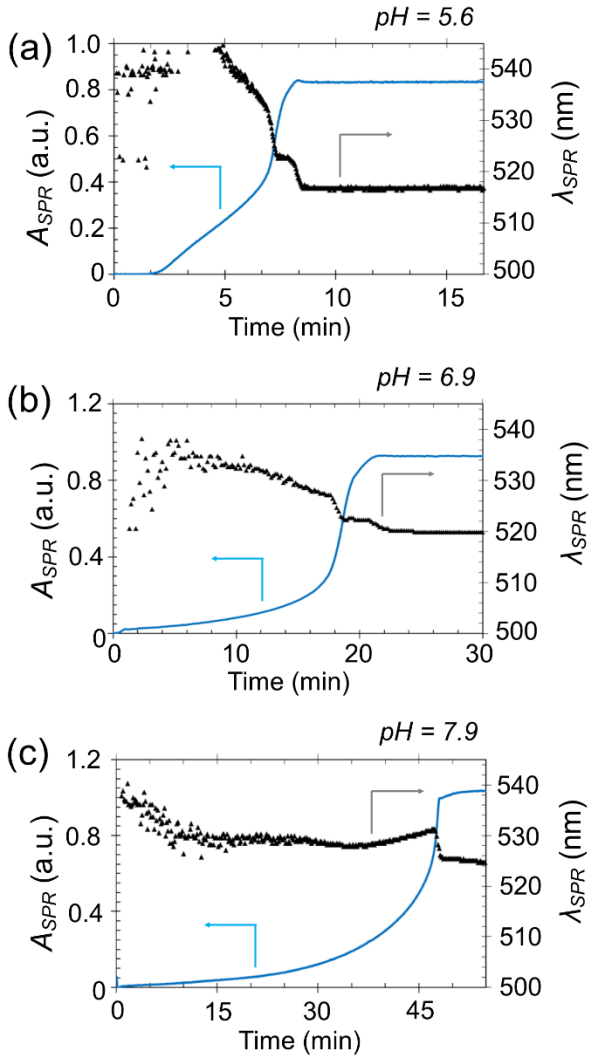

Figure C-5 Absorbance (A_{SPR}) and wavelength (λ_{SPR}) of the surface plasmon resonance peak in time in the pH-adjusted *direct Turkevich* method at a) pH = 5.6, b) pH = 6.9 and c) pH = 7.9 via *in situ* UV-Vis spectrometry. Gold precursor concentration $HAuCl_4$ (after mixing), 0.25 mM; reducing agent (H_3Ct:Na_3Ct mixture) concentration (after mixing), [H_3Ct] = 0.54 mM, [Na_3Ct] = 2.46 mM, temperature, 95 ^{o}C.

C.4. Particle size and reaction time of gold nanoparticle synthesis

The results of the TEM imaging of the 12 experiments based on the factorial analysis described in Section 5.2.2 in the main text are shown in Table C-1. The synthesised particles were monodisperse with average coefficient of variance ranging between 7 % – 12 %. Figures C-6 and C-7 show the TEM images of the synthesised particles mentioned in Table C-1 for $[Citrate]/[HAuCl_4]$ equal to 6/1 and 12/1, respectively. Figures C-8 and C-9 show the reaction time and the evolution of the surface absorbance (A_{SPR}) and the wavelength of the surface plasmon resonance peak (λ_{SPR}) of the UV-Vis spectra in time of the synthesised particles mentioned in Table C-1, in respect to the increasing gold precursor concentration for different $[Citrate]/[HAuCl_4]$ ratio.

Table C-1 Mean particle size ($\bar{d}_{exp}$), standard deviation of the particle size distribution (σ_d) and the respective coefficient of variance (CV) of the synthesised gold nanoparticles (obtained by TEM imaging) via the pH-adjusted *direct Turkevich* method, by varying the gold precursor concentration $[HAuCl_4]$ (mM) concentration and $[Citrate]/[HAuCl_4]$ ratio at different reaction temperatures (given by TEM imaging). Experimental conditions are shown in Table 5-1 in the main text.

$[HAuCl_4]$ (mM)	$[Citrate]/[HAuCl_4]$	Results of the gold nanoparticle synthesis					
		85 °C			95 °C		
		$\bar{d}_{exp}$ (nm)	σ_d (nm)	CV (%)	$\bar{d}_{exp}$ (nm)	σ_d (nm)	CV (%)
0.125	6/1	18.5	1.7	9	17.8	1.3	7
0.25		13.9	1.6	12	15.3	1.2	8
0.5		12.6	1.0	8	12.1	0.9	7
0.125	12/1	16.1	1.8	11	15.6	1.3	8
0.25		12.4	1.1	9	13.3	0.9	7
0.5		11.8	0.8	7	10.6	0.9	8

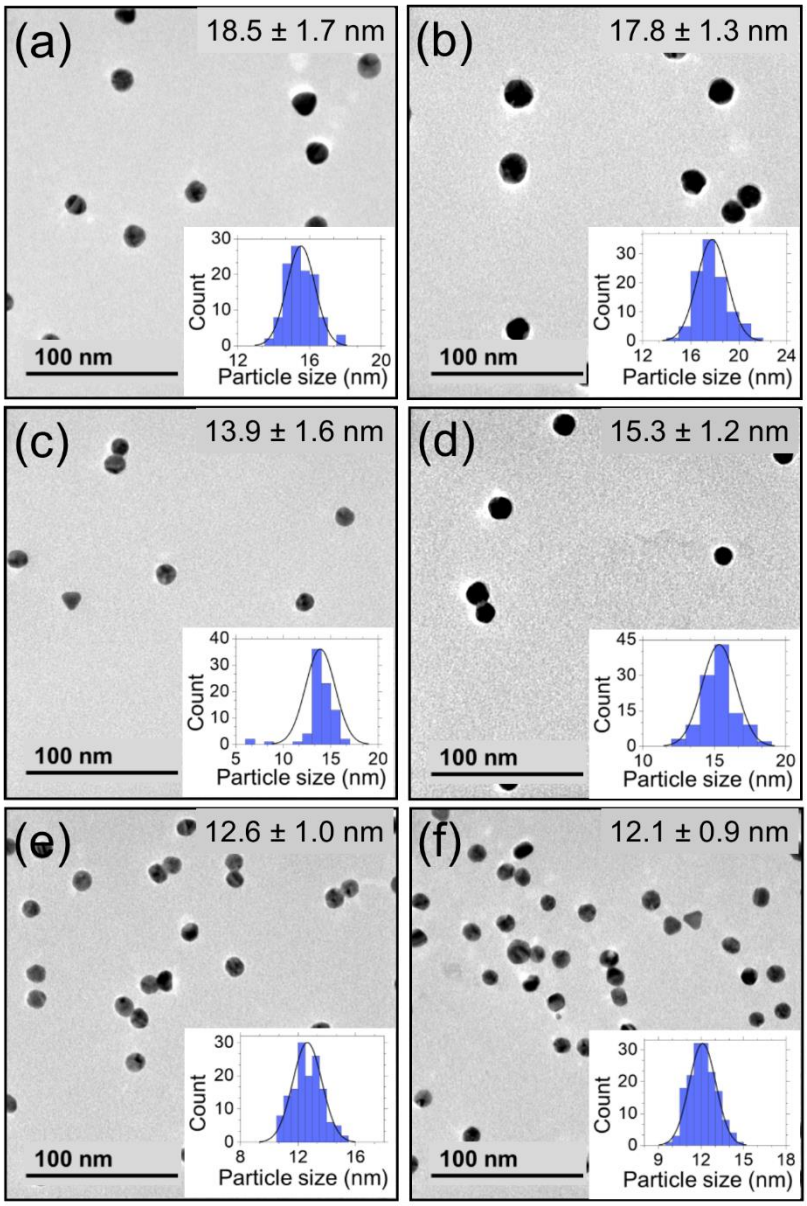

Figure C-6 TEM images of the synthesised gold nanoparticles via the pH-adjusted *direct Turkevich* method at 85 °C ((a), (c) and (e)) and 95 °C ((b), (d) and (f)). The histograms on the bottom-right corners present the frequency distribution of the particle size. Upper-right corner display the experimental $\bar{d}_{exp} \pm \sigma_d$ (nm) of the particles. Gold precursor concentration $HAuCl_4$ (after mixing), 0.125 mM ((a) and (b)), 0.25 mM ((c) and (d)) and 0.5 mM ((e) and (f)); $[Citrate]/[HAuCl_4]$ ratio, 6/1. Experimental conditions are shown in Table 5-1 in the main text.

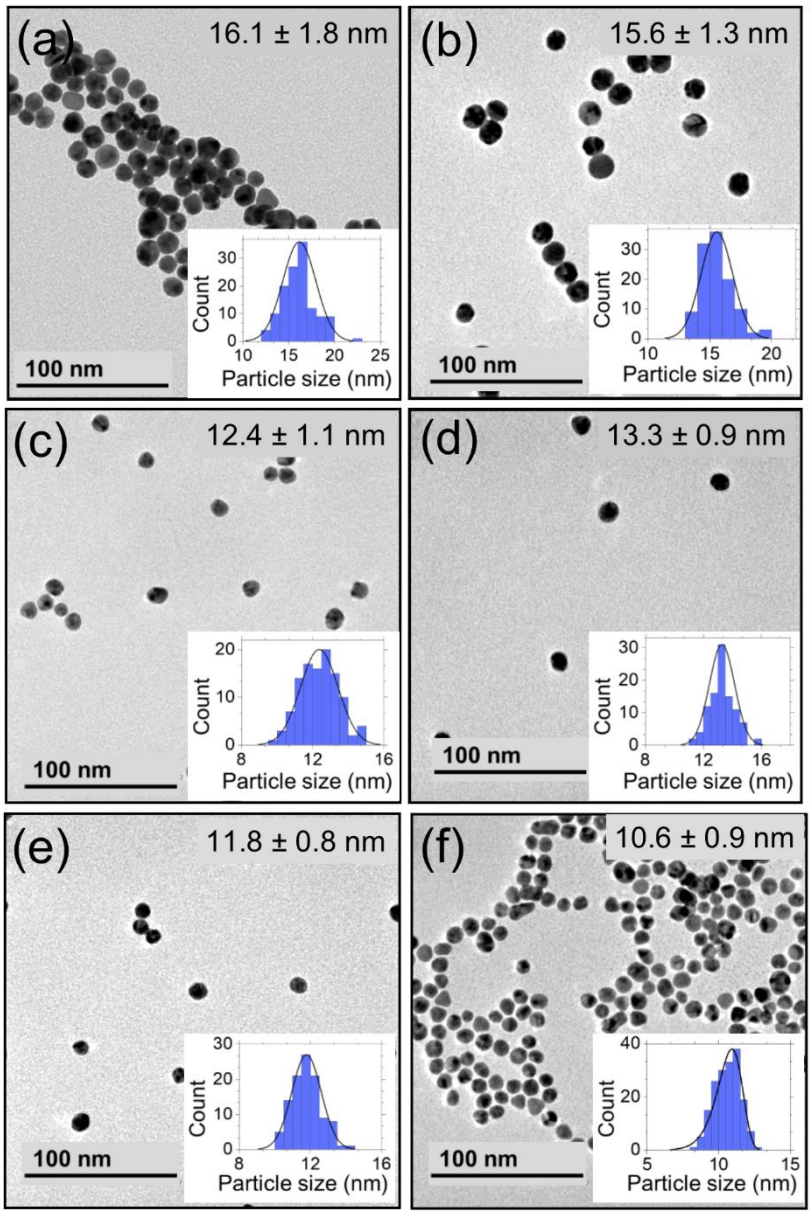

Figure C-7 TEM images of the synthesised gold nanoparticles via the pH-adjusted *direct Turkevich* method at 85 °C ((a), (c) and (e)) and 95 °C ((b), (d) and (f)). The histograms on the bottom-right corners present the frequency distribution of the particle size. Upper-right corner display the experimental $\bar{d}_{exp} \pm \sigma_d$ (nm) of the particles. Gold precursor concentration $HAuCl_4$ (after mixing), 0.125 mM ((a) and (b)), 0.25 mM ((c) and (d)) and 0.5 mM ((e) and (f)); $[Citrate]/[HAuCl_4]$ ratio, 12/1. Experimental conditions are shown in Table 5-1 in the main text.

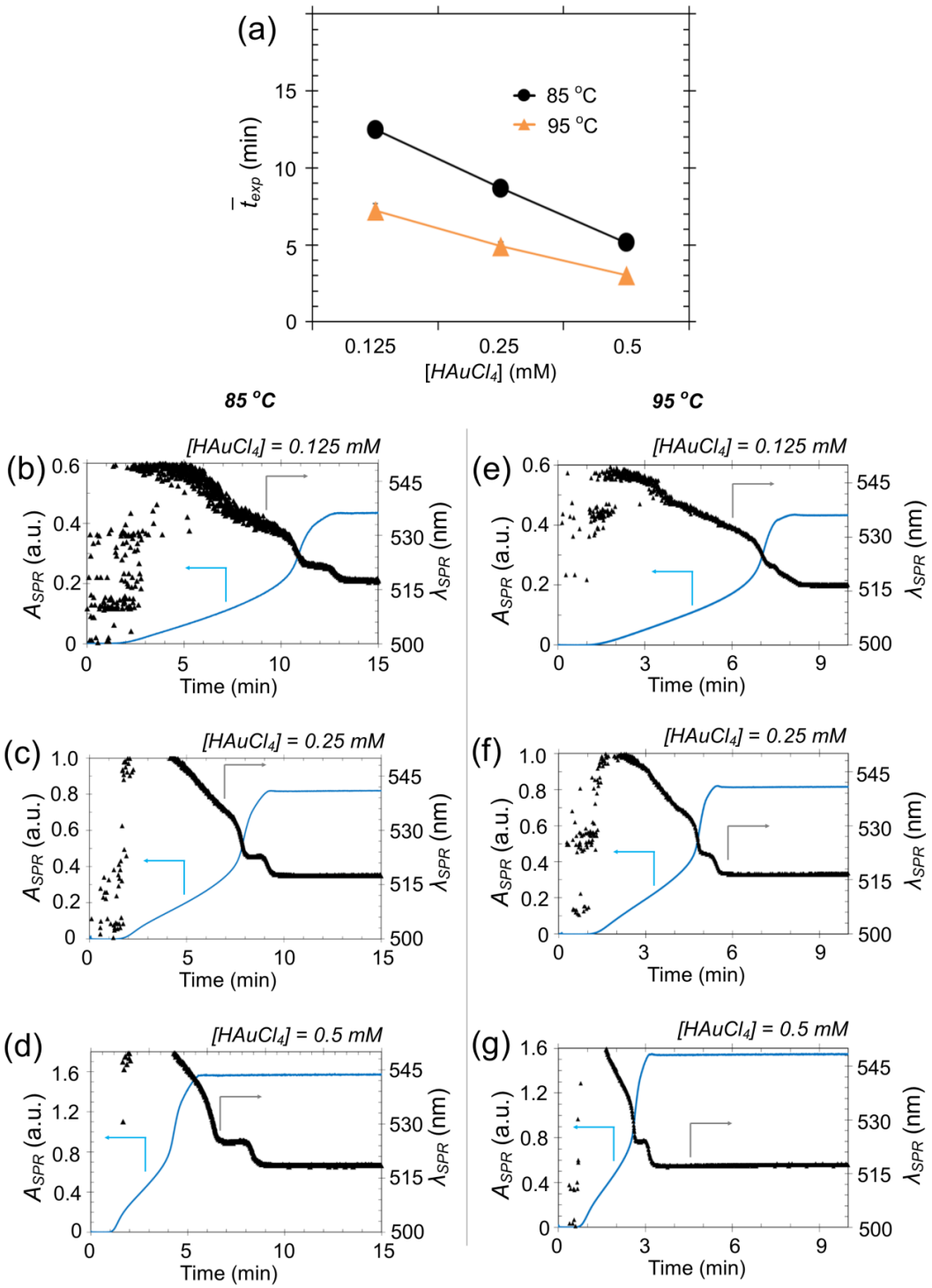

Figure C-8 a) Average reaction time ($\bar{t}_{exp}$) and b-g) absorbance (A_{SPR}) and wavelength (λ_{SPR}) of the surface plasmon resonance peak in time in the pH-adjusted *direct Turkevich* method via *in situ* UV-Vis spectrometry. Gold precursor concentration $HAuCl_4$ (after mixing), 0.125 mM ((b) and (e)), 0.25 mM ((c) and (f)) and 0.5 mM ((d) and (g)); $[Citrate]/[HAuCl_4]$ ratio, 6/1. Error bars in (s) correspond to the standard deviation of the reaction time. Experiment were performed in triplicates. Experimental conditions are shown in Table 5-1 in the main text.

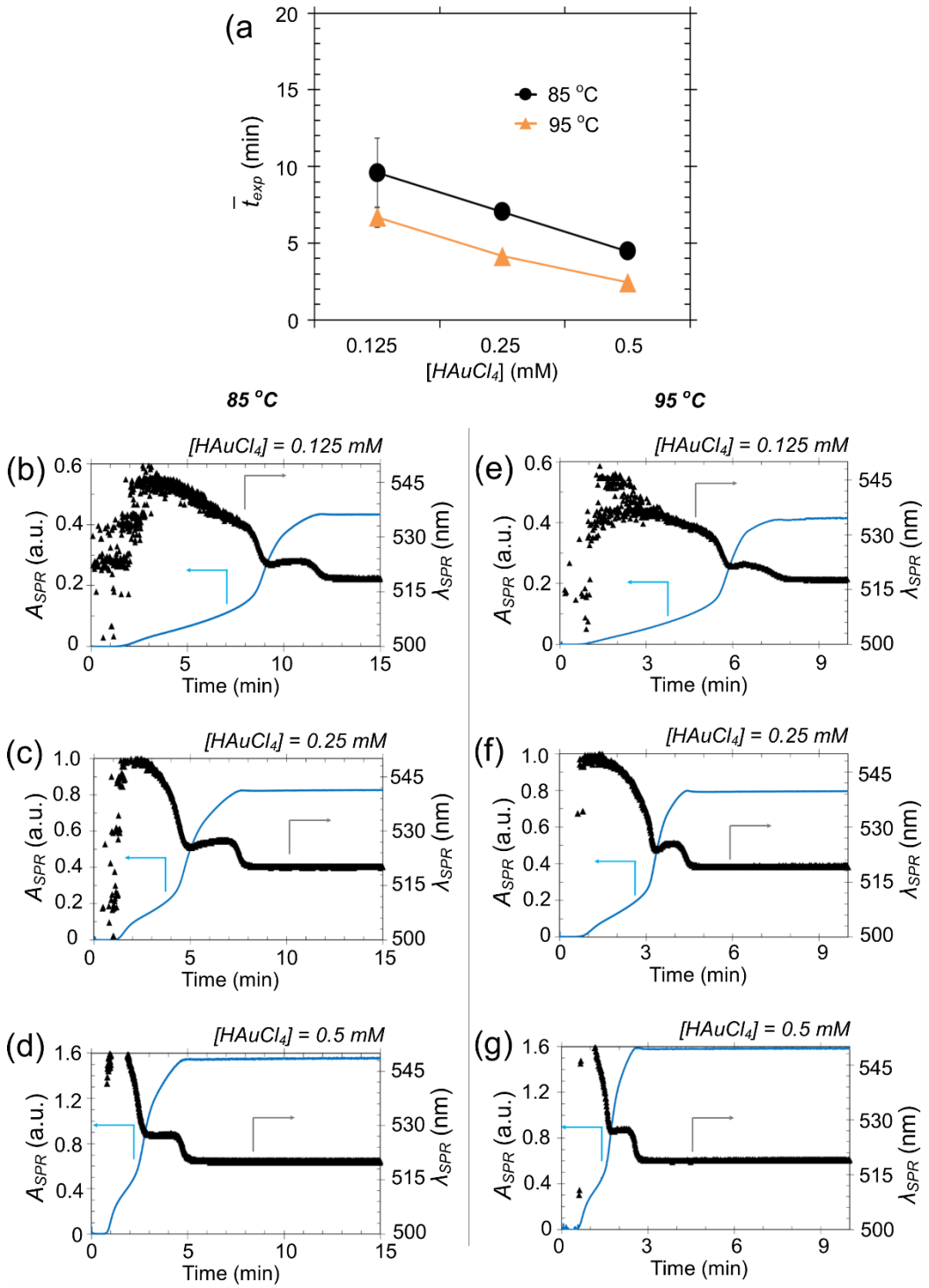

Figure C-9 a) Average reaction time ($\bar{t}_{exp}$) and b-g) absorbance (A_{SPR}) and wavelength (λ_{SPR}) of the surface plasmon resonance peak in time in the pH-adjusted *direct Turkevich* method via *in situ* UV-Vis spectrometry. Gold precursor concentration $HAuCl_4$ (after mixing), 0.125 mM ((b) and (e)), 0.25 mM ((c) and (f)) and 0.5 mM ((d) and (g)); $[Citrate]/[HAuCl_4]$ ratio, 12/1. Error bars in (a) correspond to the standard deviation of the reaction time. Experiment were performed in triplicates. Experimental conditions are shown in Table 5-1 in the main text.

C.5. Statistical analysis of the regression models

The responses obtained from the factorial study (gold nanoparticle size and reaction time) were subjected to second-order regression models. The developed models were tested by an analysis of variance (ANOVA) at 95% confidence level, where the $p-value$ denoted the significance of each factor (for $p-value$ < 0.05, the factor had significant contribution on the response). The regression models allowed deeper understanding on the interaction between the variables. The two response surface method (RSM) models for the particle size (d) and reaction time (t) are given below:

$$d = 17.61 - 33.63X_1 + 0.07X_2 + 0.09X_3 + 0.5X_1X_2 - 0.17X_1X_3 - 0.01X_2X_3 + 49.07{X_1}^2 \quad \text{Eq. C-1}$$

$$t = 108.60 - 157.69X_1 - 2.93X_2 - 0.98X_3 + 0.83X_1X_2 + 1.05X_1X_3 + 0.03X_2X_3 + 61.07{X_1}^2 \quad \text{Eq. C-2}$$

Where X_1: $HAuCl_4$ (mM), X_2: $Citrate/HAuCl_4$ and X_3: Temperature (^{o}C).

Regarding the RSM for the estimation of the particle size, R^2 was equal to 0.9663 demonstrating model of high validity. The adjusted R^2 coefficient was similar to the R^2 (R^2_{adj} = 0.9074) indicating good agreement between the experimental and the calculated results. Table C-2 includes the coefficients and the $p-values$ of the factors in Equation C-1 – which describes the particle size of the Au NPs – and it shows that the two significant factors determining the Au NPs size were the [$HAuCl_4$] (X_1, $p-value$ = 0.00062) and the reactant ratio [$Citrate$]/[$HAuCl_4$] (X_2, $p-value$ = 0.01923), while temperature had negligible contribution on the determination of the particle size (X_3, $p-value$ = 0.77351). The statistical analysis showed that the quadratic term of the gold precursor concentration had also a significant influence on the particle size (${X_1}^2$, $p-value$ = 0.03139), while there were no significant effects arising from the interactions between the three factors ($X_1 \cdot X_2$, $p-value$ = 0.34875; $X_1 \cdot X_3$, $p-value$ = 0.57376; $X_2 \cdot X_3$, $p-value$ = 0.72223). Figure C-10a shows the parity plot of the experimental versus the calculated particle size for the RSM model provided by Equation C-1, indicating uniform scattering of the experimental against

the calculated values. All the experimental values lied within the 10 % marginal variance of the model due to the large numbers of factors which increase the confidence of the model regardless of the significant contribution of each factor. The factors of low significance (with $p-value$ > 0.05) were eliminated and the ANOVA analysis of the refined model is presented in Section 5.3.3.1 in the main text.

Table C-2 Coefficients and $p-values$ of the factors for linear, quadratic and interaction effects of the initial response surface screening model for the particle size. X_1: [$HAuCl_4$] (mM), X_2: [$Citrate$]/[$HAuCl_4$] and X_3: Temperature (°C).

Factor (X_{ij})	Coefficient (β_{ij})	$p-value$
Intercept	17.61	$8.6 \cdot 10^{-6}$
X_1	-33.36	0.00062
X_2	0.07	0.01923
X_3	0.09	0.77351
$X_1 \cdot X_2$	0.50	0.34875
$X_1 \cdot X_3$	-0.17	0.57376
$X_2 \cdot X_3$	-0.01	0.72223
${X_1}^2$	49.07	0.03139

Regarding the RSM for the estimation of the reaction time, the R^2 was equal to 0.9679 demonstrating model of high validity. The adjusted R^2 coefficient was similar to the R^2 (R^2_{adj} = 0.9116) indicating a good agreement between the experimental and the calculated results. Table C-3 includes the coefficients and the $p-values$ of the factors in Equation C-2 – which describes the reaction time of the Au NPs synthesis – and it shows that only the the gold precursor concentration [$HAuCl_4$] (X_1, $p-value$ = 0.00134), the reactant molar ratio [$Citrate$]/[$HAuCl_4$] (X_2, $p-value$ = 0.00027), and the reaction temperature (X_3, $p-value$ = 0.00372) were significant for the determination of the synthesis reaction time. At the same time, the reactant molar ratio [$Citrate$]/[$HAuCl_4$] (X_2, $p-value$ = 0.00027), and the reaction temperature (X_3, $p-value$ = 0.11933) and the quadratic term of the gold precursor concentration (${X_1}^2$, $p-value$ = 0.05501), as well as the interaction between the factors ($X_1 \cdot X_2$, $p-value$ = 0.30193; $X_1 \cdot X_3$, $p-value$ = 0.06700; $X_2 \cdot X_3$, $p-value$ = 0.28257) had no significant influence on the reaction time. Figure C-10b shows the parity plot of the experimental versus the calculated reaction time for the RSM model provided by

Equation C-2, indicating uniform scattering of the experimental against the calculated values. All the experimental values lied within the 10 % marginal variance of the model due to the large numbers of factors which increase the confidence of the model regardless of the significant contribution of each factor. The factors of low significance (with $p - value$ > 0.05) were eliminated and the ANOVA analysis of the refined model is presented in Section 5.3.3.1 in the main text.

Table C3. Coefficients and $p - values$ of the factors for linear, quadratic and interaction effects of the initial response surface screening model for the reaction time. X_1: [$HAuCl_4$] (mM), X_2: [$Citrate$]/[$HAuCl_4$] and X_3: Temperature (^{o}C).

Factor (X_{ij})	Coefficient (β_{ij})	$p - value$
Intercept	108.60	0.00160
X_1	-157.69	0.00134
X_2	-2.93	0.11933
X_3	-0.98	0.00372
$X_1 \cdot X_2$	0.83	0.30193
$X_1 \cdot X_3$	1.05	0.06700
$X_2 \cdot X_3$	0.03	0.28257
${X_1}^2$	61.07	0.05501

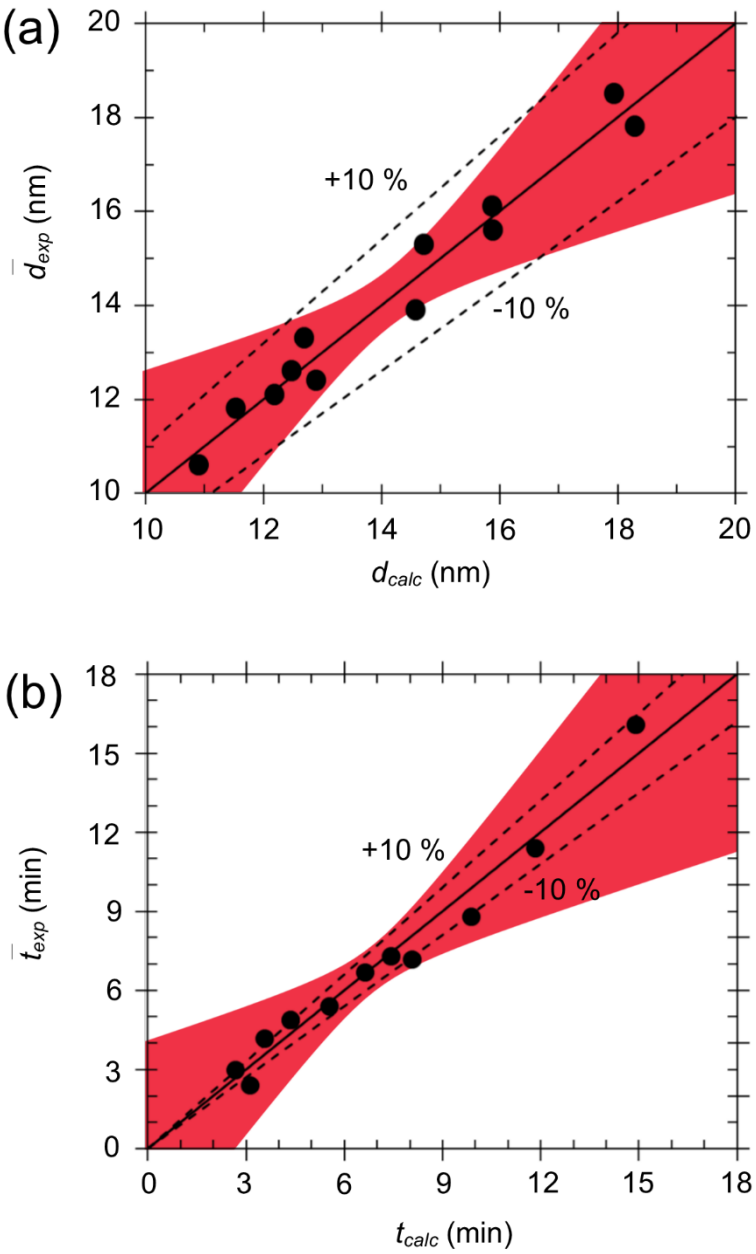

Figure C-10 Parity plot of a) the experimental ($\bar{d}_{exp}$) versus the calculated (d_{calc}) particle size and b) of the experimental ($\bar{t}_{exp}$) versus the calculated (t_{calc}) reaction time for the response surface model of gold nanoparticles synthesis prior to eliminations of factors of low significance (with $p - value$ > 0.05). Dashed lines display the 10% deviation of the model from fitting line (solid line). Red coloured area displays the 95 % confidence of the model.

C.6. Effect of temperature on gold speciation

Figure C-11 shows the absorbance of the gold precursor in the UV-Vis spectra at 313 nm wavelength at different temperatures, as shown by Wuithschick *et al.*[38]. Increasing the synthesis temperature, the gold speciation equilibrium shifts towards the hydroxylated species $AuCl_{3-x}(OH)_{1+x}^{-}$ [38]. This shift from $AuCl_4^-$ causes the drop in the absorbance of the UV-Vis spectra.

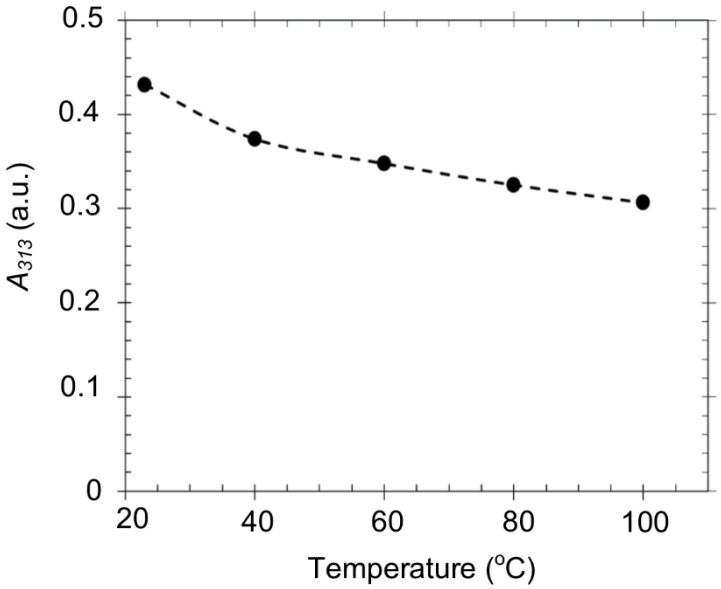

Figure C-11 Absorbance of the gold precursor peak at 313 nm (A_{313}) at different temperatures monitored via UV-Vis spectroscopy. Gold precursor concentration [$HAuCl_4$], 0.25 mM. Dashed line was used for visual aid. Adapted from Wuithschick *et al.*[38]

C.7. Experimental conditions for targeted gold nanoparticle synthesis

Table 5-8 shows the required synthesis conditions estimated by the developed model (without taking into account the fitting factor a = 1.5849·10^{-6}) for the targeted 10-20 nm gold nanoparticles synthesis. Measuring the pH of the colloidal solution after the completion of the synthesis for the above target sizes, the pH varied between 5.16 – 5.38 (Figure 5-9 of the main text) and therefore the synthesis was outside the "high reproducibility zone" described by Kettemann *et al.*[40]. After applying the fitting factor a, the target pH of the model increased to 6 and the synthesis conditions – the ratio and the concentrations of the H_3Ct and Na_3Ct – changed. Table 5-9 (in the main text) shows the required synthesis conditions estimated by the developed model (with the fitting factor a = 1.5849·10^{-6} M) for the targeted 10 – 20 nm gold nanoparticles synthesis. Measuring the pH of the colloidal solution after the completion of the synthesis for the above target sizes, the pH varied between 5.50 – 5.74 (within the "high reproducibility zone"). The fitting factor a accounted for the discrepancy between the target and the experimentally measured pH of the 10 – 20 nm Au NPs colloidal solutions. A more rigorous supplementary mechanistic model which correlates the reaction kinetics with the evolution and consumption of the species in time could improve the predictability of the RSM model and explain the observed discrepancies without the use of the fitting factor a. Figure C-12 shows standard deviation of the average particle size after 3 repeat of the targeted synthesis (10 nm, 12.5 nm, 15 nm, 17.5 nm and 20 nm). The graph displays the high reproducibility of the targeted synthesis, as the deviation between the three repeats for each targeted size was less than 7 %. Figure C-13 shows the reaction time and the evolution of the surface absorbance (A_{SPR}) and the wavelength of the surface plasmon resonance peak (λ_{SPR}) of the UV-Vis spectra in time of the targeted 10 – 20 nm Au NPs synthesis.

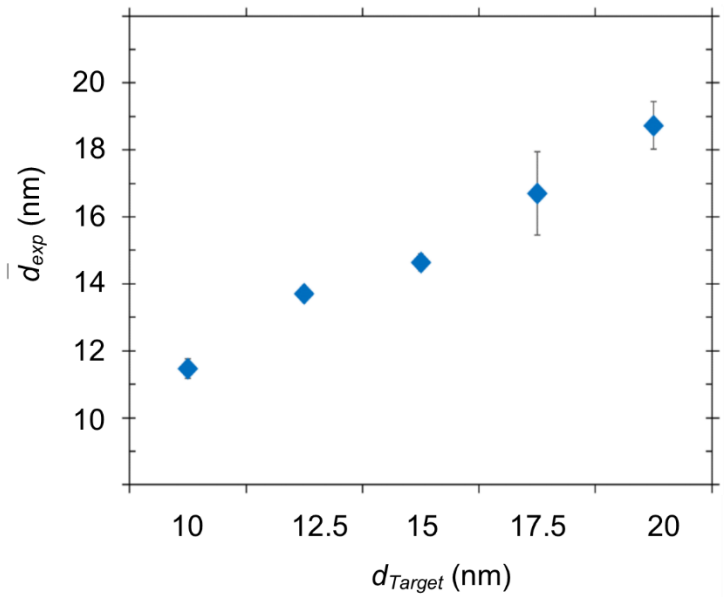

Figure C-12 Reproducibility and average particle size ($\overline{d}_{exp}$) of the targeted gold nanoparticle synthesis (d_{Target}) for 10 nm, 12.5 nm, 15 nm, 17.5 nm and 20 nm. Error bars correspond to the standard deviation of the average particle size. Experiments were repeated in triplicates. Experimental conditions are shown in Table 6-9 in the main text.

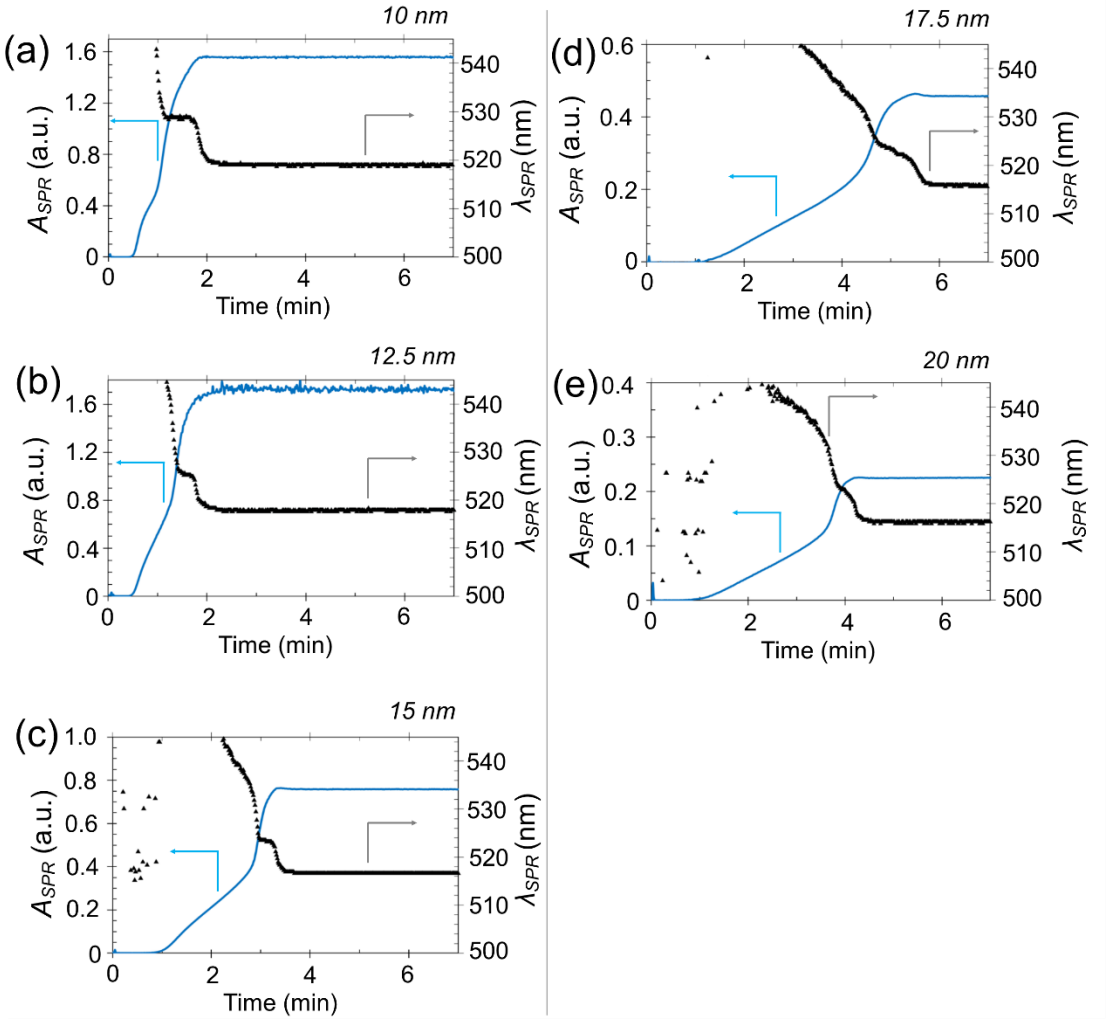

Figure C-13 Absorbance (A_{SPR}) and wavelength (λ_{SPR}) of the surface plasmon resonance peak in time in the targeted a) 10 nm, b) 12.5 nm, c) 15 nm, d) 17.5 nm and e) 20 nm gold nanoparticle synthesis Experimental conditions are shown in Table 5-9 in the main text.

Appendix D. Continuous citrate-capped gold nanoparticle synthesis in a two-phase flow reactor

D.1. Characterisation of the two-phase flow system

D.1.1. Droplet size and extent of mixing

The extent of mixing in the aqueous droplets in the two-phase flow system comprising of blue dye solution (75 mg/l Blue dye 3, Sigma Aldrich) and n-heptane (analytical grade, Sigma Aldrich), was characterised by analysing the images of the droplets captured using an inverted microscope (IX150, Olympus) equipped with a colour camera (Point Grey 2, FLIR) and a TH3 light source. The mixing study consisted of the evaluation of the aqueous droplets formed in a straight capillary, using a cross-junction (as described in Section 6.3.1. of the main text) at room temperature and 2.3 bara backpressure. The two aqueous streams (water and blue dye solution) were introduced at 90^{o} angle to the heptane phase (Figure 6-3a of the main text) flowing always at the same flow rate ($\dot{V}_{Water} = \dot{V}_{Blue} = \frac{\dot{V}_{Aqueous}}{2}$), while the total aqueous flow rate was equal to the flow rate of the heptane ($\dot{V}_{Aqueous} = \dot{V}_{Heptane}$). Four different total flow rates ($\dot{V}_{Total} = \dot{V}_{Aqueous} + \dot{V}_{Heptane}$) were tested (0.315, 0.420, 0.630 and 1.260 ml/min) – the aqueous-to-organic flow rate ratio was equal to 1:1 – and images of the two-phase flow in the capillary were taken every 2 cm from 4 cm from the cross-junction outlet up to 20 cm. Since PTFE capillary tube is translucent, a transparent fluorinated ethylene propylene (FEP) capillary was implemented (inner diameter: 1 mm, outer diameter: 1.59 mm, VICI-Jour), while in order to eliminate refraction problems in the liquid flows, the capillary was placed in a water-filled cuvette for refractive index matching.

The droplets formed along the straight capillary are shown in Figure D-1a. Images were captured in the red-green-blue (RGB) format (Figure D-1a). The red, green and blue colour channels of the images were split using the Fiji software package[270, 271] (ImageJ, NIH) and monochromatic images from the red channel were chosen, due to the highest absorbance by the blue dye at this wavelength (Figure D-1 b-d). Figure D-2 shows the grey pixel value along the centreline of the aqueous droplet – using the red colour channel – at 4 cm and 20 cm from the outlet of the cross-junction. The grey pixel value varies between 0 (black, maximum absorbance) and 255 (white, minimum absorbance) and it can be seen that the pixel value showed larger variation across the centreline in the unmixed droplet (Figure D-2a) in comparison with the perfectly mixed droplet (Figure D-2b). The extent of mixing and subsequently the

mixing length in the formed droplets at various flow rates was calculated via the ratio of the standard deviation of the grey pixel value in the whole aqueous droplet and the standard deviation of the grey pixel value in the perfectly mixed aqueous droplet[228]:

$$\varepsilon_m = 1 - \frac{S_{droplet} - S_{mixed\ droplet}}{S_{droplet} + S_{mixed\ droplet}} \qquad \text{Eq. D-1}$$

where $S_{droplet}$ is the standard deviation of the grey pixel value in the formed aqueous droplets and $S_{mixed\ droplet}$ is the standard deviation of the grey pixel value of the perfectly mixed aqueous droplet.

The mixing length (and of course the mixing time taking into account the inlet flow velocities) was defined as the distance (or required time) from the cross-junction outlet, where the extent of mixing ε_m was equal to 95 % homogeneity in the droplet. Additionally, the average length and the standard deviation of length of the formed droplets were calculated as the distance between the front and rear meniscus of the aqueous droplet.

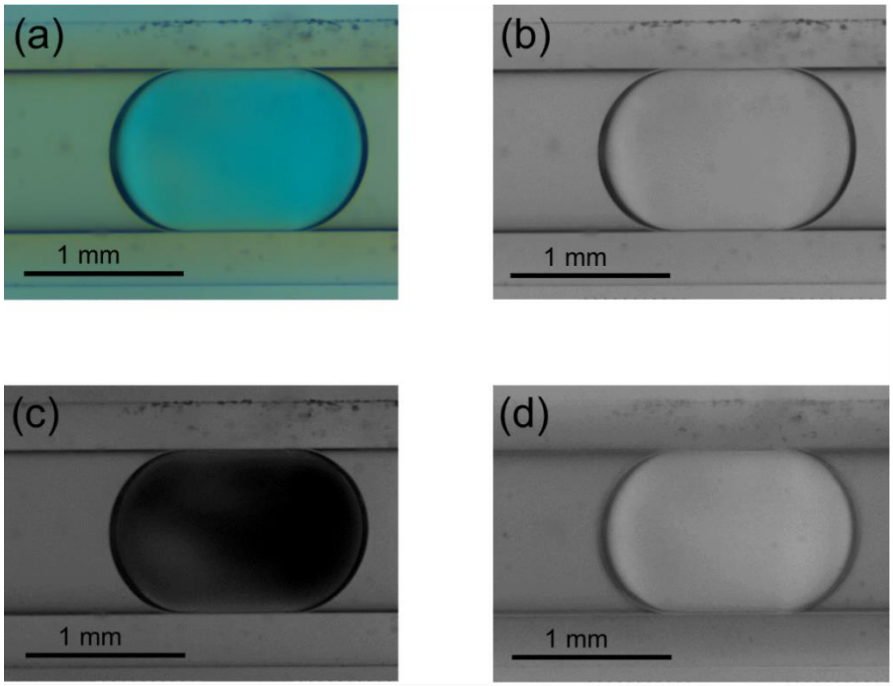

Figure D-1 Image of the perfectly mixed formed aqueous droplet in a) real colours as recorded by the camera, b) green colour channel, c) red colour channel and d) blue colour channel in the FEP capillary. $\dot{V}_{Water}$ = $\dot{V}_{Blue}$, 0.079 ml/min; $\dot{V}_{Heptane}$, 0.158 ml/min; inner diameter, 1 mm; outer diameter, 1.59 mm; system pressure, 2.3 bara.

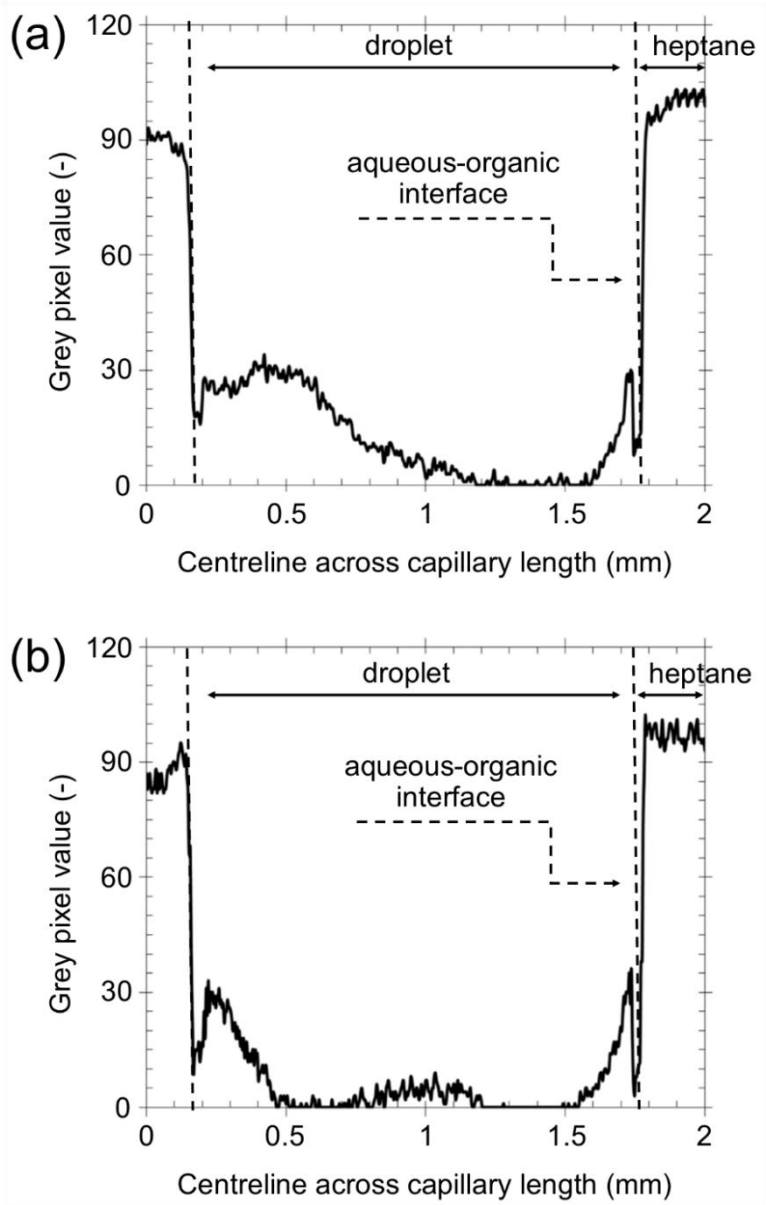

Figure D-2 Grey pixel value of the droplet – using the red colour channel – at a) 4cm and b) 20 cm from the outlet of the cross-junction. Pixel value varied between 0 (black, maximum absorbance) and 255 (white, minimum absorbance). $\dot{V}_{Water}$ = $\dot{V}_{Blue}$, 0.079 ml/min; $\dot{V}_{Heptane}$, 0.158 ml/min; FEP capillary; inner diameter, 1 mm; outer diameter, 1.59 mm; system pressure, 2.3 bara.

D.1.2. Characterisation of the liquid-liquid flow

In two-phase flow systems in hydrophobic capillaries, the velocity of the aqueous droplet can be affected by the length of the organic liquid film surrounding the droplet. There have been several dimensionless numbers proposed for the characterisation of the force-related phenomena in the capillary flow reactors: gravitational, viscous, inertial and interfacial forces, as well as the velocity of the aqueous bubble[224]:

The Reynolds number describes the ratio of inertial to viscous in the liquid-liquid flow. At low Reynolds numbers (< 2300) the flow is laminar, while the number is given by the following expression[227]:

$$Re = \frac{\rho_c u_m d_t}{\eta_c} \qquad \text{Eq. D-2}$$

where d_t is the inner capillary diameter, ρ_c is the density of the continuous phase, η_c is the dynamic viscosity of the continuous phase and u_m is the average superficial velocity of the two-phase flow.

The capillary number is related to the film thickness of the continuous phase around the droplet or slug of the dispersed phase. At low Ca values (Ca < 10^{-3}), the interfacial forces are dominant over the viscous stress resulting in uniform droplets of spherical ends[191, 272]:

$$Ca = \frac{u_m \eta_c}{\sigma} \qquad \text{Eq. D-3}$$

where u_m is the average superficial velocity of the two-phase flow, η_c is the dynamic viscosity of the continuous phase and σ is the interfacial force.

The Weber number describes the magnitude of inertial over the interfacial tension forces, given by the following expression[273]:

$$We = \frac{d_t u_c^2 \rho_c}{\sigma} \qquad \text{Eq. D-4}$$

where d_t is the inner capillary diameter, u is the superficial velocity of the continuous phase, ρ is the density of the continuous phase and σ is the interfacial tension.

For We = 1, the surface tension and the viscous forces are balanced, while as higher velocities the viscous forces increase (and We > 1), the surface tension is less important and the film thickness increases, eventually affecting the velocity of the formed droplets.

The magnitude of the gravitational forces over the surface tension is given by the Bond (or Eötvös) number, by the following expression[227]:

$$Bo = \frac{(\rho_d - \rho_c) g {d_t}^2}{\sigma} \qquad \text{Eq. D-5}$$

where d_t is the inner capillary diameter, g is the gravitational acceleration, ρ_d is the density of the disperse phase, ρ_c is the density of the continuous phase and is the interfacial force.

For systems where the Bo << 1, surface tension dominates over the gravitational forces and the effect of gravity can be neglected[234].

Considering a capillary with inner diameter equal to 1 mm, the Capillary (Ca), Weber (We) and Bond (Bo) number of the two-phase flow system were evaluated at different organic (and aqueous) inlet flow rates (Table D-1). In all cases, the respective values were Ca ~ 10^{-4} – 10^{-5}, We ~ 10^{-3} – 10^{-4} and Bo ~ 10^{-2}, indicating that the interfacial tension in the liquid-liquid system was dominant over the viscous, inertial and gravitational forces and the thickness of the liquid film surrounding the aqueous droplet was negligible.

Table D-1 Reynold (Re), capillary (Ca), Weber (We) and Bond (Bo) number of the two-phase flow system at different flow rates. Aqueous phase: blue dye solution. Organic phase: heptane. In all scenarios, $\dot{V}_{Aqueous} = \dot{V}_{Organic} = {}^{\dot{V}_{Total}}/_{2}$

$\dot{V}_{Total}$ (ml/min)	$\dot{V}_{Organic}$ (ml/min)	$u_{Organic}$ (mm/s)	Re	Ca	We	Bo
0.315	0.158	3.34	12	$2{\cdot}10^{-5}$	$1{\cdot}10^{-4}$	$6{\cdot}10^{-2}$
0.420	0.210	4.46	16	$3{\cdot}10^{-5}$	$3{\cdot}10^{-4}$	
0.630	0.315	6.68	24	$5{\cdot}10^{-5}$	$6{\cdot}10^{-4}$	
1.260	0.630	13.37	48	$1{\cdot}10^{-4}$	$2{\cdot}10^{-3}$	

d_t = 1 mm; ρ_{Water} = 997 kg/m^3 (25 ^{o}C)[263]; $\rho_{Heptane}$ = 684 kg/m^3 (20 ^{o}C)[263]; $\eta_{Heptane}$ = $3.76{\cdot}10^{-4}$ Pa·s (20 ^{o}C)[264]; σ = $5.19{\cdot}10^{-2}$ N/m[274]; g = 9.81 m/s^2.

It was assumed that the solution of the blue dye had similar physical properties with the pure water due to the low concentration used (75 mg/l).

The film thickness around the aqueous droplets for the range of capillary numbers in this study (Ca ~ 10^{-4} – 10^{-5}) is given by the following expression[275]:

$$\frac{\delta}{d_t} = 0.5(Ca)^{1/2} \qquad \text{Eq. D-6}$$

where d_t is the inner capillary diameter.

At the same time, the droplet velocity is given by the following expression, where m characterises the relative velocity of the droplet velocity and the aqueous stream[227]:

$$m = \frac{u_d - u_{Aqueous}}{u_d} \qquad \text{Eq. D-7}$$

where $u_{Aqueous}$ is the superficial velocity of the aqueous phase and $m = 1.0(Ca)^{1/2}$ [276].

The Péclet number (Pe) describes the correlation of the convective over the diffusive forces in the moving liquid. Tanthapanichakoon *et al.*[232] developed a modified Péclet

number (Pe^*) for the aqueous droplets in two-phase flow reactors, taking into account the droplet aspect ratio $\varepsilon_D = \frac{L_D}{d_t}$. For $Pe^* \gg 1$, the transport by convention is dominant over diffusion[225]:

$$Pe^* = \frac{Pe}{\varepsilon_D} = \frac{{}^{d_t u_d}/_{D}}{{}^{L_D}/_{d_t}} = \frac{d_t^2 u_d}{L_D D} \qquad \text{Eq. D-8}$$

where d_t is the inner capillary diameter, u_d is the droplet velocity, L_D is the droplet length and D is the molecular diffusivity of the dilute species.

The length of the film thickness, the droplet velocity and the modified Péclet number for the aqueous droplet at different inlet flow rates are given in Table D-2. Increasing the total flow rate from 0.315 ml/min to 1.26 ml/min, the film thickness ranged between 3.5 – 7 μm, while the difference between the droplet velocity was velocity of the aqueous stream was ~ 1 %. Additionally, the $Pe^* \gg 1$ for all aqueous and total inlet flow rates indicating that the convective forces dominate over molecular diffusion. Thereof, the film thickness around the droplets could be ignored in this study[191] and the total velocity of the two-phase flow could be approximated equal to the sum of the inlet velocity of the aqueous and organic streams.

Table D-2 Film thickness (δ) and droplet velocity (u_d) of the two-phase flow system at different flow rates. Aqueous phase: blue dye solution. Organic phase: heptane. In all scenarios, $\dot{V}_{Aqueous} = \dot{V}_{Organic} = {}^{\dot{V}_{Total}}/_{2}$. d_t = 1 mm.

$\dot{V}_{Total}$ (ml/min)	$\dot{V}_{Aqueous}$ (ml/min)	$u_{Aqueous}$ (mm/s)	m (-)	u_d (mm/s)	δ (μm)	Pe^*
0.315	0.158	3.34	$7{\cdot}10^{-3}$	3.37	3.5	3,730
0.420	0.210	4.46	$8{\cdot}10^{-3}$	4.49	4.0	5,921
0.630	0.315	6.68	$1{\cdot}10^{-2}$	6.75	4.9	7,460
1.260	0.630	13.37	$1{\cdot}10^{-2}$	13.56	7.0	14,921

It was assumed that the solution of the blue dye had similar physical properties with the pure water due to the low concentration used (75 mg/l).

D.2. Particle deposition (fouling) in the PTFE tubing of the mixer

Figure D-3 shows the PTFE capillary in the mixing stage for the mixing of the $HAuCl_4$ and $H_3Ct{:}Na_3Ct$ in the continuous gold nanoparticle synthesis via the "*cold mixed*" method. Particle deposition (fouling) can be identified along the capillary length, after leaving the reacting solution in the mixer overnight. Although the mixer was always at room temperature and it was used only for mixing, there were areas of "dark fouling" and "pink fouling" related to the electrostatic attraction of unreacted gold complexes and Au NPs[96]. However, during the synthesis, there was no fouling observed.

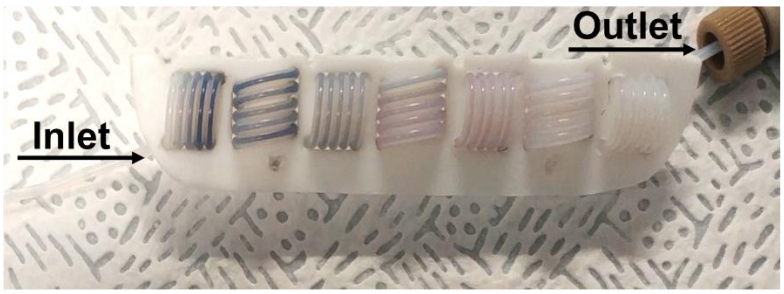

Figure D-3 Picture of the PTFE-made mixing stage used for reactant mixing ($HAuCl_4$ and $H_3Ct{:}Na_3Ct$) after leaving the mixer filled in with the reacting solution overnight. Particle deposition (fouling) appeared on the tube walls. Arrows indicate the inlet and the outlet of the reacting stream.

D.3. Temperature profile in the capillary reactor

The temperature profile in a single-phase flow through the PTFE capillary at a constant inlet flow rate (0.5 ml/min) was estimated for the case of water and heptane passing through the capillary using the MATLAB software (version R2019a, MathWorks)[277, 278]. For a small section of the PTFE tube (dL), the temperature change of the medium (water) can be calculated via the heat transfer rate through the tube wall[267]:

$$dQ = \pi d_{outer} K (T - T_{amb}) dL \qquad \text{Eq. D-9}$$

where the heat transfer coefficient K was given by[267]:

$$K = \left[\frac{1}{h_{int}} \frac{d_{outer}}{d_{inner}} + \frac{d_{outer}}{2k_{tubing}} \ln \frac{d_{outer}}{d_{inner}} + \frac{1}{h_{ext}} \right]^{-1} \qquad \text{Eq. D-10}$$

And the thermal energy balance of the medium[267]:

$$dQ = \rho \dot{V} Cp dT \qquad \text{Eq. D-11}$$

Where Q is the heat energy, d_{outer} is the outer tube diameter, d_{inner} is the inner tube diameter, ρ is the density of the medium, Cp is the specific heat capacity of the medium, k_{tubing} is the thermal conductivity of the PTFE tube, $\dot{V}$ is the flow rate of the medium, T is the cross-sectional average temperature of the medium, T_{amb} is the ambient glycerol temperature, L is the reactor length and h_{ext} is the external heat transfer coefficient.

Therefore, the temperature over the tube section was calculated from D-9 – D-11, resulting to the equation:

$$\frac{dT}{dL} = \frac{\pi d_{outer}}{\rho \dot{V} Cp} K (T - T_{amb}) \qquad \text{Eq. D-12}$$

For fully–developed laminar flow systems in circular tubes, the Nusselt number is[267]:

$$Nu = \frac{h_{int} d_{inner}}{k} \qquad \text{Eq. D-13}$$

where d_{inner} is the inner tube diameter, k is the thermal conductivity of the medium and h_{int} is the internal heat transfer coefficient.

For 0.5 ml/min inlet flow rate, the Reynolds number was very low for both water and heptane (12 and 19, respectively), indicating laminar flow. Hence, the Nusselt number (Nu) was assumed constant and equal to 3.651 (Graetz–Nusselt)[278]. Table D-3 shows the input parameter for the calculation of the temperature profile along the first 20 cm of the capillary (total reactor length: 287 cm). Due to uncertainty on the external heat transfer coefficient in the stirred glycerol bath (at 95 ^{o}C), h_{ext} varied between 500 – 20,000 W/m^{2}K (which is within the range of the external heat transfer coefficient for forced convection[267]) to evaluate the capillary length required for the medium to reach 95 ^{o}C. Figure D-4 shows the temperature profile from capillary inlet (where the medium was at 20 ^{o}C) until reaching 95 ^{o}C for different external heat transfer coefficients for water (Figure D-4a) and heptane (Figure D-4b) flow.

In case of water, the medium reached 95 ^{o}C within ~ 10 cm for h_{ext} equal to 1,500 W/m^{2}K and 20,000 W/m^{2}K and the required length increased to ~ 16 cm for h_{ext} equal to 500 W/m^{2}K. This translates to 3 % and 6 % of the overall reactor length, respectively and the temperature inside capillary reactor reached 95 ^{o}C within 10 – 15 s. On the other hand, using heptane as the medium, it reached 95 ^{o}C within ~ 4 cm for h_{ext} equal to 1,500 W/m^{2}K and 20,000 W/m^{2}K and the required length increased to ~ 8 cm for h_{ext} equal to 500 W/m^{2}K, probably due to the different heating properties of the two liquids. This translates to 1 % and 3 % of the overall reactor length, respectively and the temperature inside capillary reactor reached 95 ^{o}C within 4 – 8 s.

Table D-3 Input parameters for the calculation of the temperature profile in a single-phase flow through the PTFE capillary.

Material	ρ_i (kg/m^3)	k_i (W/mK)	Cp_i (J/kgK)
PTFE	-	0.25[268]	-
Heptane	684[263]	0.12[264]	2240[263]
Water	997[263]	0.60[264]	4193[263]

d_{inner} = 1 mm; d_{outer} = 1.59 mm; $\dot{V}$ = 0.5 ml/min; T_{amb} = 95 ^{o}C; T_{inlet} = 20 ^{o}C; L = 20 cm; h_{ext} = 500 – 20,000 W/m^{2}K[267].

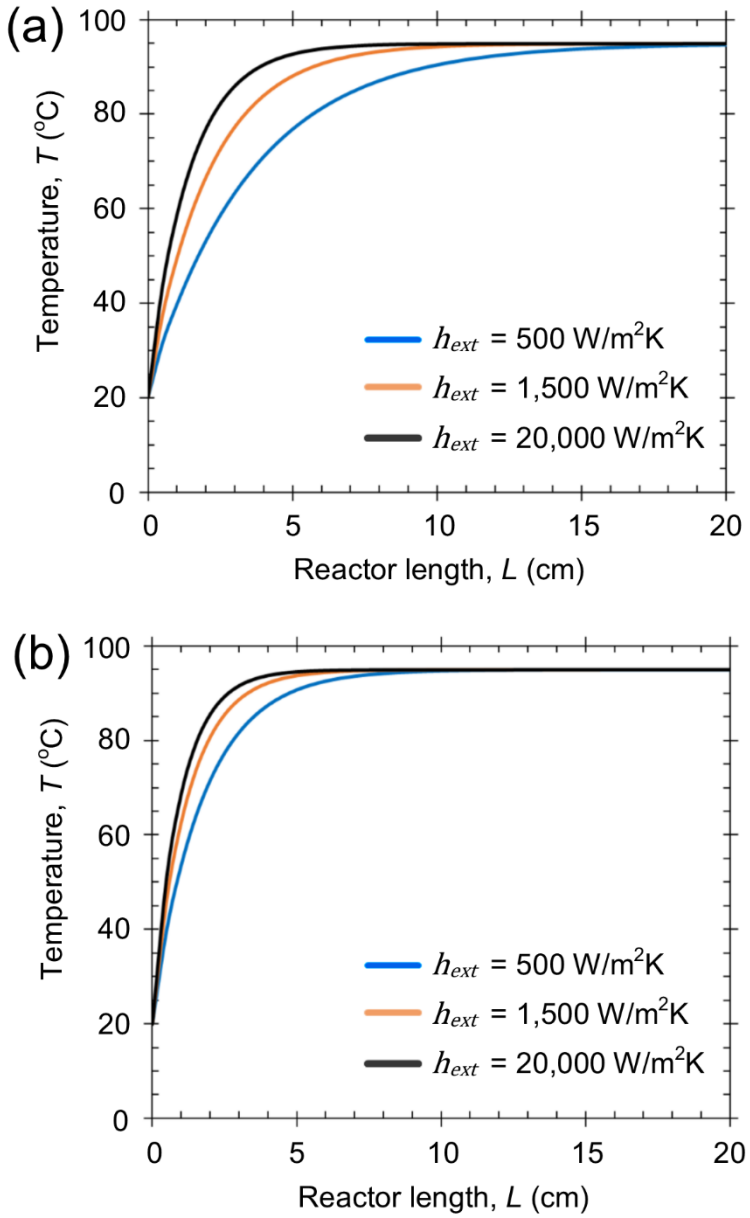

Figure D-4 Temperature profile in a single-phase flow through the PTFE capillary placed in a stirred glycerol bath, using a) water and b) heptane as the medium for different external heat transfer coefficients. Inlet flow rate, 0.5 ml/min; glycerol bath temperature, 95 °C; medium temperature on the inlet, 20 °C; inner capillary diameter, 1 mm; outer capillary diameter, 1.59 mm.

D.4. Online monitoring via UV-Vis spectroscopy

Figures D-5 – D-7 show the absorbance (A_{SPR}) and position (λ_{SPR}) of the surface plasmon resonance peak and the absorbance at 400 nm (A_{400}) and 450 nm (A_{450}) over the 2 hour continuous 10 – 20 nm gold nanoparticle synthesis via the "*cold mixed*" method. The position (wavelength) of the SPR peak is related to the particle size and is blue-shifting as the particle size decreases[88]. The absorbance of the UV-Vis spectra is proportional to the concentration of gold precursor (after mixing). The absorbance of the SPR peak and at 450 nm is related to particle size of the synthesised Au NPs[88] and the absorbance at 400 nm is related to concentration of the colloidal solution[84].

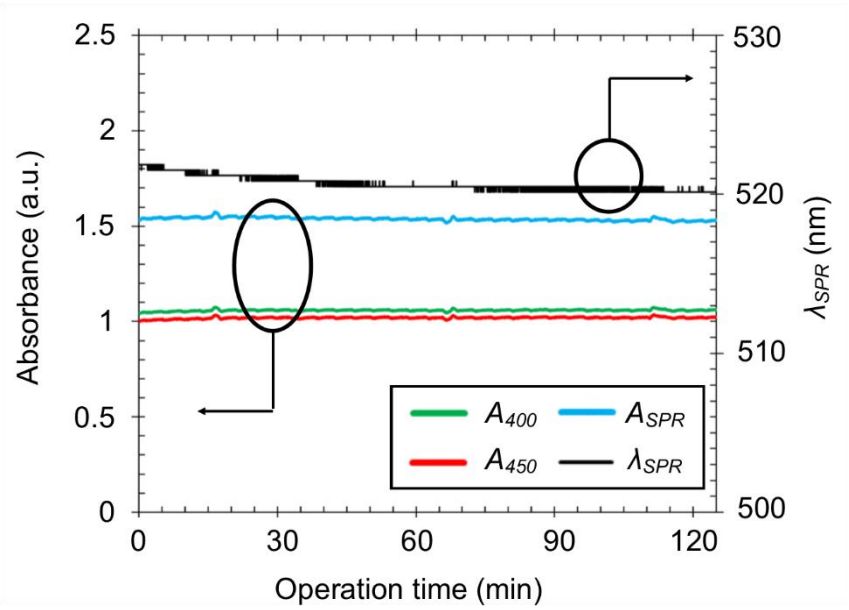

Figure D-5 Absorbance (A_{SPR}) and wavelength (λ_{SPR}) of the surface plasmon resonance peak and absorbance at 400 nm (A_{400}) and 450 nm (A_{450}) in the "*cold mixed*" method for experimental run A (Tables 6-1 and 6-2 in main text) over 120 min operation time. Reactor volume, 2.25 ml. [$HAuCl_4$], 0.5 mM; [H_3Ct], 1.65 mM; [Na_3Ct], 5.85 mM; temperature, 95 ^{o}C; $\dot{V}_{HAuCl_4} = \dot{V}_{H_3Ct:Na_3Ct}$, 0.155 ml/min; $\dot{V}_{Heptane}$, 0.310 ml/min.

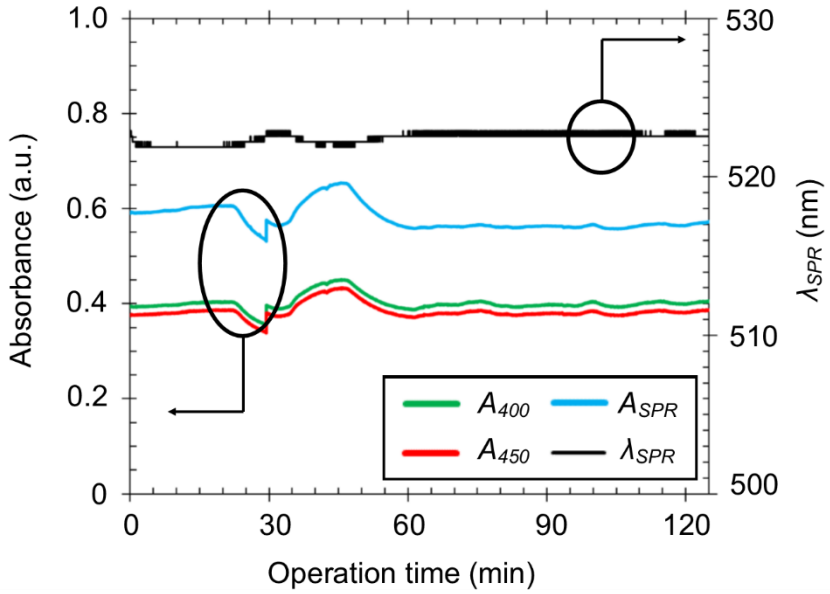

Figure D-6 Absorbance (A_{SPR}) and wavelength (λ_{SPR}) of the surface plasmon resonance peak and absorbance at 400 nm (A_{400}) and 450 nm (A_{450}) in the "*cold mixed*" method for experimental run B (Tables 6-1 and 6-2 in main text) over 120 min operation time. Reactor volume, 2.25 ml. [$HAuCl_4$], 0.23 mM; [H_3Ct], 0.210 mM; [Na_3Ct], 1.17 mM; temperature, 95 ^{o}C; $\dot{V}_{HAuCl_4} = \dot{V}_{H_3Ct:Na_3Ct}$, 0.09 ml/min; $\dot{V}_{Heptane}$, 0.174 ml/min.

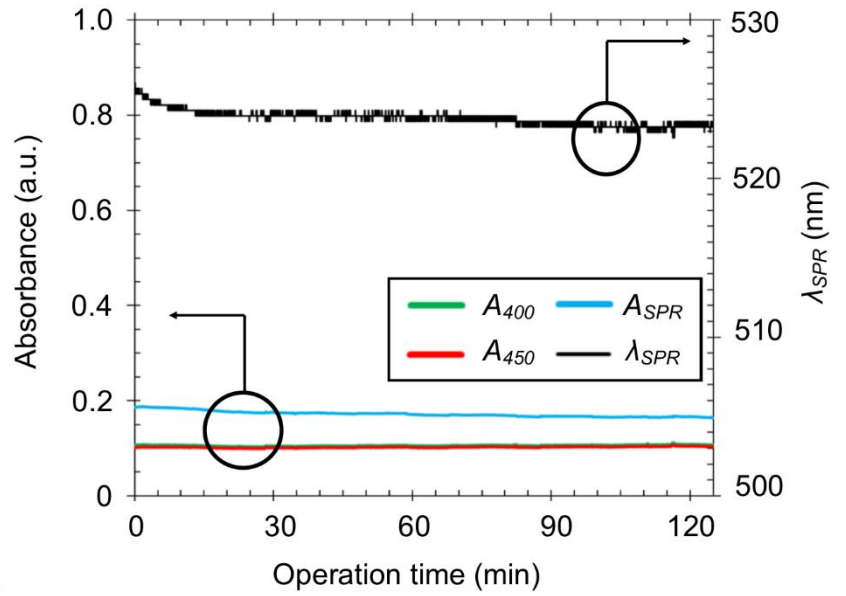

Figure D-7 Absorbance (A_{SPR}) and wavelength (λ_{SPR}) of the surface plasmon resonance peak and absorbance at 400 nm (A_{400}) and 450 nm (A_{450}) in the "*cold mixed*" method for experimental run C (Tables 6-1 and 6-2 in main text) over 120 min operation time. Reactor volume, 2.25 ml. [$HAuCl_4$], 0.065 mM; [H_3Ct], 0.10 mM; [Na_3Ct], 0.29 mM; temperature, 95 °C; $\dot{V}_{HAuCl_4} = \dot{V}_{H_3Ct:Na_3Ct}$, 0.080 ml/min; $\dot{V}_{Heptane}$, 0.158 ml/min.

D.5. Recycle of the heptane in the two-phase flow system

Figure D-8 shows the UV-Vis spectra and TEM images of the recycled heptane after the synthesis of the ~ 15 nm Au NPs following the experimental run B via the *"cold mixed"* method. The heptane was re-used without any purification step as the continuous phase in the same two-flow synthesis resulting in more polydisperse particles (15.0 ± 3.4 nm) as shown by the DCS. There were two peaks at 225 nm and 276 nm in the UV-Vis spectra, similar to the peaks of gold species in aqueous solutions, however, the absorbance of these peaks was very low (< 0.1 a.u.), indicating the low concentration of these species in the heptane (Figure D-8a). Additionally, the TEM images showed the existence of gold nanoparticles and agglomerates, resulting from either interfacial absorption and/or transferring particles from aqueous phase to organic during separation in the membrane separator (Figure D-8b and D-8c).

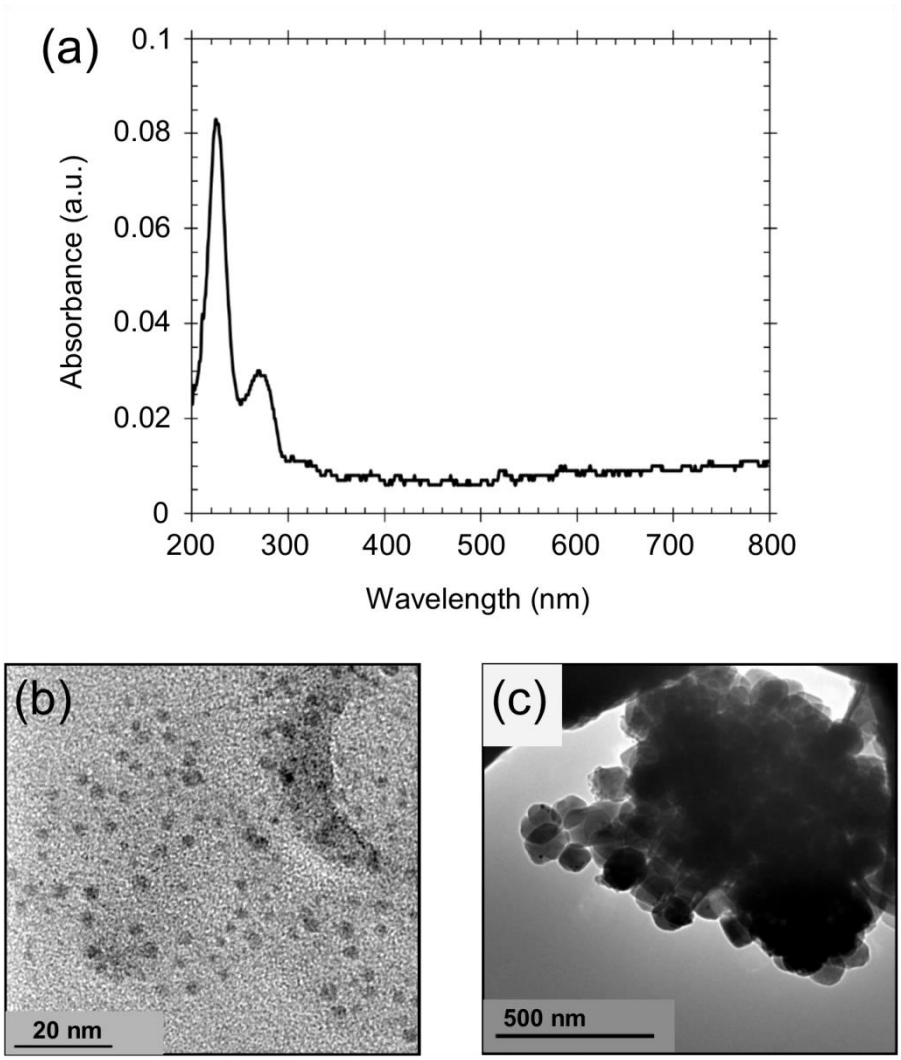

Figure D-8 a) UV-Vis spectra of the recycled heptane used in the "*cold mixed*" method for experimental run C (Tables 6-1 and 6-2 in main text, without further purification. b-c) TEM images of the recycled heptane showing the existence of gold nanoparticles and agglomerates dispersed in the heptane.